DEVELOPMENT OF OXIDATION RESISTANT MOLYBDENUM-SILICON-BORON COMPOSITES

A Dissertation
Presented to
The Academic Faculty

by

Peter E. Marshall

In Partial Fulfillment
of the Requirements for the Degree
Doctor of Philosophy in the
School of Material Science and Engineering

Georgia Institute of Technology
December, 2015

DEVELOPMENT OF OXIDATION RESISTANT MOLYBDENUM-SILICON-BORON COMPOSITES

Approved by:

Dr. Joe Cochran, Advisor
School of Material Science and Engineering
Georgia Institute of Technology

Dr. Robert Speyer
School of Material Science and Engineering
Georgia Institute of Technology

Dr. Thomas Sanders, Jr.
School of Material Science and Engineering
Georgia Institute of Technology

Dr. David McDowell
School of Mechanical Engineering
Georgia Institute of Technology

Dr. Arun Gokhale
School of Material Science and Engineering
Georgia Institute of Technology

Dr. Richard Neu
School of Mechanical Engineering
Georgia Institute of Technology

Date Approved: September 21, 2015

ACKNOWLEDGEMENTS

This research was made possible through funding from the Office of Naval Research contracts N00014-12-C-0412 and N00014-13-P-1181 with project monitors David Shifler, Steven Sullivan, and Robert Kowalik. I also greatly appreciate the support of Oliver Strbik at Deep Strings Technology and Carol Wedding at Imaging Systems Technology in perusing these STTR/SBIR contracts and in preparing the deliverables.

I would like to thank my adviser, Dr. Joe Cochran, for his unwavering support and optimistic approach to research. Regardless of any looming challenges, his can-do attitude kept our scientific endeavors going. I also greatly appreciate the day-to-day help of my lab and office-mates Will Daloz, Michael Middlemas, and Tammy McCoy. In particular, working shoulder to shoulder with Will in the lab and the numerous in depth discussions on our research was tremendously helpful. The opportunity to bounce ideas off him and to see a different perspective allowed us to tease apart and understand more of our complex results. In the lab and out, I thankful for the help of my fellow graduate students Siddharth Avachat, Justin Lamb, Judy Dickson, Brian Doyle, and Alex Bryant, both with research and as teaching assistants for the laboratory classes.

Finally, I wish to thank my family for their support and confidence in my endeavors as a graduate student. In spite of the great distances, they always expressed interest in my research, challenging me to come up with sound and understandable explanations. I greatly appreciate, and admire, their willingness to read portions of the document which follows.

TABLE OF CONTENTS

ACKNOWLEDGEMENTS . . . . . **iii**

LIST OF TABLES . . . . . **vii**

LIST OF FIGURES . . . . . **viii**

SUMMARY . . . . . **xiv**

1 INTRODUCTION **1**

2 LITERATURE REVIEW **7**

2.1 Molybdenum 7

2.1.1 Oxidation of Molybdenum 7

2.1.2 Brittle to Ductile Transition in Molybdenum Alloys 9

2.1.3 Embrittlment in Molybdenum Solid Solutions of Boron and Silicon 10

2.2 Molybdenum - Silicon - Boron System in the Molybdenum Rich Corner . . 12

2.2.1 Processing Techniques 13

2.2.2 Mechanical Properties 16

2.2.3 Oxidation Results and Models 19

2.3 Silica, Borosilicate, and other Glasses 31

2.3.1 Structure of Silicates, Borates, and Borosilicates 32

2.3.2 Silicate Viscosities 34

2.3.3 Oxygen Permeability and Diffusion 36

2.3.4 Molybdenum in Glasses 37

2.3.5 Volatile Losses from Glass Melts 38

2.4 Additional Relevant Systems 40

2.4.1 Crystalline Molybdates 40

2.4.2 Alkaline-Earth Aluminosilicates 41

3 EXPERIMENTAL METHODS **43**

3.1 Composite Production 43

3.1.1 Raw Materials 43

3.1.2 Slurry Formulation 44

3.1.3 Spray Drying 45

3.1.4 Consolidation and Firing 46
3.2 Characterization and Oxidation Testing 49
3.2.1 Microstructural Characterization 49
3.2.2 Oxidation Resistance 50
4 FRAMEWORK FOR COMPOSITE DEVELOPMENT 51
4.1 Composition of the Borosilicate Melt 53
4.2 Selection of Oxidation Temperature and Conditions 54
4.3 Interaction with Coatings 55
5 PROCESSING - MICROSTRUCTURE DEVELOPMENT 57
5.1 Pressureless Sintering without In-Line Hygrometer 58
5.1.1 Densification and Typical Microstructures 59
5.1.2 Detrimental Oxygen and Water Vapor Reactions 62
5.2 Pressureless Sintering with Hygrometer Analysis 66
5.2.1 Iterative Firing Improvements 68
5.3 Hot Isostatic Pressing 75
5.3.1 Encapsulated in Low-Carbon Steel 79
5.3.2 Encapsulated in Titanium 81
6 COMPOSITION TAILORING FOR OXIDATION RESISTANCE . . 84
6.1 Understanding Oxidation Behavior 84
6.2 Results of 1300℃ Oxidation Testing 86
6.2.1 Mo - 3wt%Si - 1wt%B with Iron and Nickel Minor Additions . . . 88
6.2.2 Variation in Si-to-B ratio with Cobalt, Iron, Manganese, and Yttria Additions 91
6.2.3 Results of Iron Additions 94
6.2.4 Results of Cobalt Additions 99
6.2.5 Results of Yttria Additions 113
6.2.6 Results of Manganese Additions 118
6.2.7 Results of HIP'ed Samples 131
6.2.8 Effect of Air Flow During Oxidation 136

7 THEORY OF OXIDATION RESISTANCE 143

7.1 Mechanisms of Oxidation Resistance 143

7.1.1 Stage One Oxidation 146

7.1.2 Stage One Transition 146

7.1.3 Stage Two Oxidation 149

7.1.4 Stage Two Transition 156

7.1.5 Stage Three 157

7.2 Environment Interaction 158

7.3 Design for Oxidation Resistance 162

7.3.1 Ratio of Silicon to Boron 162

7.3.2 Minor Additions 163

7.3.3 Matrix Volume Fraction 164

8 CONCLUSIONS 166

REFERENCES 171

LIST OF TABLES

3.1 Powder specifications for base Mo-Si-B composite formulation 44
3.2 Powders for composition modifications 44
3.3 Powders for $SrAl_2Si_2O_8$ production 44
6.1 Equivalent glass composition of adjusted, Mn modified Mo-Si-B samples . . 125

LIST OF FIGURES

1.1 Dependence of specific turbine core power on inlet temperature 2

2.1 Molybdenum - oxygen phase diagram 8

2.2 Cross section of molybdenum oxidized at 600℃ 8

2.3 The molybdenum - boron equilibrium phase diagram 11

2.4 The molybdenum - silicon equilibrium phase diagram 12

2.5 Silicon concentrations on grain boundaries and interiors 12

2.6 Molybdenum rich corner of the Mo-Si-B equilibrium phase diagram 13

2.7 Quasibinary Mo-T2 phase diagram 14

2.8 Liquidus projection of the Mo-Si-B system 14

2.9 Solidification microstructures of arc cast Mo-Si-B 15

2.10 Microstructures of powder processed Mo-Si-B 16

2.11 Mechanical properties of Mo-A15-T2 materials at various elevated temperatures 17

2.12 Bend testing of Mo-Si solid solution with yttria or zirconium additions . . . 18

2.13 Fracture toughness of Mo-A15-T2 materials as a function of temperature . 19

2.14 Creep resistance of mechanically alloyed Mo-9at%Si-8at%B 19

2.15 Larson-Miller parameter diagram of the Mo-A15-T2 creep resistance 20

2.16 Oxidation mechanisms of Mo-12at%Si-12at%B at various temperatures . . . 22

2.17 Surface appearance of Mo-14at%Si-10at%B during transient oxidation . . . 23

2.18 Cross section of the oxide scale formed on Mo-12.5at%Si-25at%B at 1200℃ 24

2.19 Volatile species of molybdenum and boron at 1350K 25

2.20 Surface appearance of Mo-3wt%Si-1wt%B oxidized at 816℃, left, and 1100℃ 26

2.21 Weight loss of mechanically alloyed Mo-9at%Si-8at%B during oxidation at various temperatures 26

2.22 Cross sections of mechanically alloyed Mo-9at%Si-8at%B oxidized at 820 and 1100℃ 27

2.23 Weight loss of mechanically alloyed Mo-9at%Si-8at%B with Zr during oxidation at various temperatures 28

2.24 Schematic of oxidation at 1300℃ for both base mechanically alloyed Mo-9at%Si-8at%B and it modified with Zr 28

2.25 High temperature oxidation on yttria modified, mechanically alloyed Mo-9at%Si-8at%B 29
2.26 Improved oxidation of cast Mo-2wt%Si-1wt%B from minor additions of iron 30
2.27 Oxidation of a pack-cemented Mo-Si-B coating on Mo-9at%Si-at%B at 1300℃ 30
2.28 Interaction between CMAS and Mo-Si-B coatings at 1200, 1300, and 1400℃ 31
2.29 Transmission electron microscopy images of air and vacuum bonded Kovar to borosilicate joints 34
2.30 Temperature dependence of viscosities for various ternary silica-alumina systems 35
2.31 Borosilicate viscosities at varying temperatures and for different compositions 36
2.32 Oxygen diffusion and permeation through liquid, glass, and crystalline silicates 37
2.33 Schematic of molybdenum location within a soda-lime borosilicate glass . . 38
2.34 Equilibrium vapor pressure of the three primary species over boria 39
2.35 Schematic of the volatile loss from a gas flow over a glass melt 40
2.36 Stability diagrams for cobalt, manganese, and nickel molybdates 41
2.37 Thermogravimetric analysis of $CaMoO_4$ and $MgMoO_4$ in argon 42
3.1 Spray dried powder 46
3.2 Schematic of furnace setup 48
3.3 Idealized temperature and dew point profiles 48
5.1 Microstructure of sintered molybdenum 60
5.2 Microstructure of sintered Mo-Si-B 60
5.3 Density verse sintering temperature of Mo-Mo_2B-SAS 61
5.4 Densities of various composites sintered at 1600℃ 62
5.5 Sintered Mo-Si-B with surface depletion 65
5.6 TGA traces for molybdenum and various Mo-Si-B compositions 66
5.7 Dew point trace for de-oxidizing molybdenum powder 69
5.8 Dew point trace for two step de-oxidation of molybdenum powder 70
5.9 Temperature, dew point, and cumulative water generation for early sample firings 71
5.10 Effect of ramp rate on cumulative water generation during de-oxidation . . 72
5.11 Effect of ramp and gas flow rates on dew point 73
5.12 Cumulative water generation verses temperature for the firings shown in 5.11 74

5.13 Cumulative water generation verses temperature for further increased gas flow rate 75

5.14 Cumulative water generation verses temperature with additional low temperature de-oxidation 76

5.15 Dew point traces showing little effect from an evacuation cycle 77

5.16 Temperature and dew point traces for a Mo-Si-B compact in a low-carbon steel can prior to HIP'ing 80

5.17 Microstructure of steel encapsulated Mo-Si-B composite HIP'ed at 1300℃ and 45ksi 80

5.18 Appearance of Mo-Si-B composited HIP'ed in a low-carbon steel can after oxidation at 1300℃ 81

5.19 Temperature and dew point traces for a Mo-Si-B as powder verses compact prior to HIP'ing 82

5.20 Microstructure of a Ti encapsulated Mo-Si-B composite HIP'ed at 1300℃ and 45ksi 83

6.1 Surface area normalized weight loss for 90 minutes of oxidation at 1300℃ of Mo-3wt%Si-1%B 87

6.2 Surface appearence of Mo-Si-B samples after 3 hours of 1300C oxidation . . 88

6.3 Reduced weight loss during oxidation from Fe and Ni additions 89

6.4 Cross section of oxidized Mo-3wt%Si-1wt%B with Ni addition at 1300℃ . . 90

6.5 Cross section of oxidized Mo-3wt%Si-1wt%B with Fe addition at 1300℃ . . 90

6.6 Effect of Si/B ratio and modifier on oxidation rate between 10 and 30 minutes 93

6.7 Effect of Si/B ratio and modifier on oxidation rate between 30 and 90 minutes 94

6.8 Effect of Si/B ratio and Fe content on oxidation rates 95

6.9 Surface appearance of oxidized Mo-Si-B with low Fe additions 96

6.10 Cross section view of oxidized Mo-Si-B with low Fe additions 97

6.11 Devitrified surface of oxidized Mo-Si-B with high Fe addition 98

6.12 Surface appearance of oxidized Mo-Si-B with moderate Fe additions and varying Si/B 100

6.13 Cross section view of oxidized Mo-Si-B with moderate Fe additions and varying Si/B 101

6.14 Effect of Si/B ratio on oxidation rates for Co modified Mo-Si-B 102

6.15 Effect of Si/B ratio on weight loss after 90 minutes of oxidation of Co modified Mo-Si-B 103

6.16 Surface appearance of Co modified Mo-Si-B with varying Si/B after 10 minutes of oxidation 104

6.17 Surface appearance of Co modified Mo-Si-B with varying Si/B after 90 minutes of oxidation 104

6.18 Cross section view of Co modified Mo-Si-B with differing Si/B after 90 minutes of oxidation 105

6.19 Surface appearance of Co modified Mo-Si-B after short oxidation times . . . 107

6.20 Oxidation weight loss of Co modified Mo-Si-B after exposure times from 1 to 90 minutes 108

6.21 Surface appearance of oxidized Co modified Mo-Si-B with a high Si/B after 10 minutes of oxidation 110

6.22 Effect of Co amount on weight loss during oxidation 113

6.23 Effect of Si/B ratio and Y_2O_3 content on oxidation rates 114

6.24 Surface appearance of Y_2O_3 modified Mo-Si-B with varying Si/B after 10 minutes of oxidation 115

6.25 Surface appearance of Y_2O_3 modified Mo-Si-B with varying Si/B after 90 minutes of oxidation 115

6.26 Effect of Y_2O_3 content on weight loss during oxidation 116

6.27 Oxidation weight loss of a Y_2O_3 modified sample and other Mo-Si-B compositions for up to 20 hours of exposure 117

6.28 Surface appearance of the Y_2O_3 modified Mo-Si-B in 6.27 after 90 minutes and 20 hours of exposure 118

6.29 Oxidation weight loss of two Y_2O_3 modified Mo-Si-B composites with differing αMo contents 118

6.30 Effect of Si/B ratio and Mn content on oxidation rates 120

6.31 Surface appearance of Mn modified Mo-Si-B with varying Si/B after 30 minutes of oxidation 121

6.32 Surface appearance of a Mn modified Mo-Si-B after 30 and 90 minutes of oxidation 122

6.33 Surface appearance of Mn modified Mo-Si-B with varying Si/B after 20 hours of oxidation 123

6.34 Surface appearance of oxidized Mn and SAS modified Mo-Si-B at various times from 10 mintues to 20 hours 125

6.35 Surface appearance and cross section of oxidized Mn and SAS modified Mo-Si-B after 20 hours of oxidation 126

6.36 Surface appearance of oxidized Mo-Si-B with high Mn addition at various times from 10 mintues to 20 hours 126

6.37 Surface appearance and cross section of oxidized Mo-Si-B with high Mn addition after 20 hours of oxidation 127

6.38 Firing and dew point traces for different Mn added samples 128

6.39 Sample weight loss during 90 minute pre-oxidation and subsequent oxidation at 800℃ 130

6.40 Surface appearance of pre-oxidized, Mn modified Mo-Si-B samples after 24 hours of oxidation at 800℃ 130

6.41 Cross section view of pre-oxidized Mo-Si-B with high Mn addition after 24 hours of oxidation at 800℃ 132

6.42 Cross section view of pre-oxidized, Mn and SAS modified Mo-Si-B after 24 hours of oxidation at 800℃ 132

6.43 Cross section views near the air interface of oxidized, Mo-Si-B composite HIP'ed in steel cans 133

6.44 Cross section views of oxidized, Mo-Si-B composite HIP'ed in steel cans . . 134

6.45 Cross section views of oxidized, Mo-Si-B composite HIP'ed in steel cans showing acicular molybdenum oxide 134

6.46 Surface appearance of Mo-Si-B composite HIP in a Ti can after oxidation at 1300℃ for 20 hours 135

6.47 Oxidation weight loss at 1300℃ in flowing air for both the HIP'ed Mo-Si-B can'ed in Ti and three pressurelessly sintered samples 136

6.48 Oxidation weight loss of Co modified Mo-Si-B under both static and flowing air at 1300℃ 138

6.49 Oxidation weight loss of Y_2O_3 modified Mo-Si-B under both static and flowing air at 1300℃ 140

6.50 Oxidation weight loss of Mn modified Mo-Si-B under both static and flowing air at 1300℃ 141

7.1 Schematic of the transition out of stage one oxidation 147

7.2 Cross section views of Co modified Mo-Si-B after 1 minute of oxidation at 1300℃ 149

7.3 Schematic of stage two oxidation 151

7.4 Cross section of Co modified Mo-Si-B containing bubbles after 1 and 6 minutes of oxidation 152

7.5 Cross section view of bubbles in Co modified Mo-Si-B after 90 minutes of oxidation 154

7.6 Cross section view of large bubbles in oxidized, non-modified and Mn modified Mo-Si-B 154

7.7 Cross section view of channel-type oxidation in Fe modified Mo-Si-B 155

7.8 Cross section view showing entrained pockets and multiple oxidation layers in Co and Fe modified Mo-Si-B 156

7.9 Cross section view of Mn modified Mo-Si-B with protective borosilicate surface layer 158

7.10 Schematic oxidation weight loss as a function of time for differing behaviors 159

7.11 Time dependent changes during theoretical Mo-Si-B oxidation 161

SUMMARY

The development of molybdenum - silicon - boron (Mo-Si-B) composites having a combination of high temperature strength, creep, and oxidation residence has the potential to substantially increase the efficiency of gas turbines. The refractory nature of the αMo, Mo_3Si (A15), and Mo_5SiB_2 (T2) phases results in good strength and creep resistance up to 1300℃. At this temperature, the formation of a borosilicate surface scale from the two intermetallic phases is able to provide oxidation resistance. However, realization of these advantages has been prevented by both a high brittle to ductile transition temperature and difficulty in forming the initial surface borosilicate to provide bulk oxidation resistance.

This dissertation addresses two factors pertaining to this material system: 1) improvements to powder processing techniques, and 2) development of compositions for oxidation resistance at 1300℃. The processing of Mo-Si-B composites is strongly tied to their mechanical properties by establishing the αMo matrix, limiting impurity content, and reducing silicon supersaturation. These microstructural aspects control the brittle to ductile transition temperature which has traditionally been too high for implementation of Mo-Si-B composites. The processing here built upon the previously developed powder processing with silicon and boron nitrides which allowed for a low oxygen content and sintering of fine starting powders. Adjustments were made to the firing cycle based upon dew point measurements made during the hydrogen de-oxidation stage. Under a relatively high gas flow rate, 90% of the total water generated occurred during a ramp of $2^{\circ C}/_{min}$ between 450 and 800℃ followed by a hold of 30 minutes.

The oxidation resistance of Mo-Si-B composites was studied for a wide range of compositions. Silicon to boron atomic ratios were varied from 1 to 5 and iron, nickel, cobalt, yttria, and manganese were included as minor additions. In all these compositions, the αMo volume fraction was kept over 50% to ensure the potential toughness of the composite. For the oxidized surface glass, a silica fraction of 80 to 85% was found to be necessary

for the borosilicate to have a sufficiently high viscosity and low oxygen permeability for oxidation resistance at 1300℃. For the Mo-Si-B bulk composition this corresponds to a Si/B atomic ration of 2 to 2.5. Higher viscosity compositions failed due to spallation of poorly attached, high silica scales. Lower viscosity compositions failed from continuous oxidation, either through open channels or repetitive MoO_3 bubble growth and popping. Additionally, around 1% manganese was necessary for initial spreading of the borosilicate at 1300℃. In conjunction with flowing air to prevent MoO_3 accumulation, oxidation weight loss rates below $0.05^{mg}/_{cm^2 \cdot hr}$ were measured. Finally, a theory is proposed here to describe the mechanisms responsible for the development of oxidation resistance. This theory involves three stages associated with: 1) generation of an initial surface borosilicate, 2) thickening of the borosilicate layer, and 3) slow parabolic oxidation controlled by the high silica surface scale.

CHAPTER 1

INTRODUCTION

Development of novel, higher temperature materials can satisfy the demand for improved gas turbine efficiency, a demand that may arise from high aviation fuel prices and the increased use of ground-based power turbines. Much of the historical performance of gas turbines has been dictated by the development of materials for service within the hot, high-pressure section of the engines, Figure 1.1. The theoretical efficiency of these engines is strongly dependent upon the peak internal temperature which, in real systems, is limited by the materials available for the turbine blades. The combination of high temperatures, high rotational speeds, and oxidizing atmospheres requires a material that is refractory, tough, creep and oxidation resistant.

While a number of common refractory materials can withstand the atmospheres, temperatures, and nominal stresses within a turbine, the very large number of fatigue cycles and the critical nature of the engine components have restricted the material options to those that are more mechanically forgiving, possessing high toughness and fatigue crack growth resistance. Of greatest importance to date are the alloys of nickel. While traditional alloying can develop oxidation resistant scales up to and beyond 1200℃, they suffer from traditional metallic creep which limits their upper use temperature in structural applications. With the development of superalloys however, the high temperature strength and creep resistance was dramatically improved, allowing for continuous operation above 1000℃ even though 1200℃ is 85% of nickel's homologous temperature. In their most extreme incarnation, single-crystal superalloy blades have operated near 1150℃ [69]. However, it is believed that this system has reached its limit and that continued increases in peak engine temperatures will require a fundamentally different material [30].

One such novel material system, upon which this research is focused, is based upon composites of molybdenum (Mo). As a refractory metal, molybdenum has both the strength

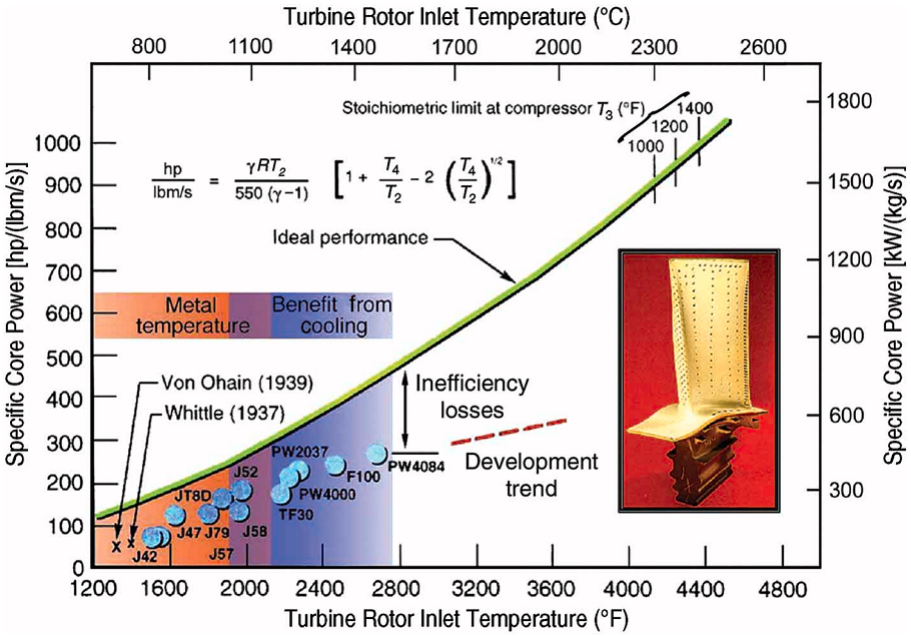

Figure 1.1: Inlet temperature dependence of jet turbine efficiency shown as specific core power. Both the ideal performance (green line) and specific production engines are shown [30].

and toughness to operate over the full range of temperatures in a gas turbine and with suitable alloying can have excellent creep resistance as well. However, above 500℃ the oxidation of pure molybdenum is poor as the primarily molybdenum dioxide scale begins to fail [38]. Above 800℃ the oxidation rate increases dramatically with the formation of liquid molybdenum trioxide. Unfortunately no single phase alloy of molybdenum has been discovered which imparts oxidation resistance while maintaining the favorable mechanical properties. To take advantage of these mechanical properties in anything other than inert or reducing environments, a composite is required whose secondary phase(s) provides a protective surface scale. Environmental barrier coatings may be the most direct way to obtain this, but they introduce their own challenges, such as matching thermal expansions. They also have a large risk of catastrophic failure due to the dramatic nature of molybdenum's oxidation. A molybdenum matrix composite with secondary phases that provide a protective surface layer mitigates many of the issues associated with coatings by producing a protective scale on any exposed surface.

Relatively few materials can provide oxidation resistance at 1200-1300℃ over hundreds

or thousands of hours due, in most cases, to either excessive oxygen diffusivity or high oxide volatility [8]. Complicating the oxidation resistance mechanism for continuous molybdenum matrix composites is the requirement that the protective scale must flow to cover the previously exposed molybdenum. In this aim, Mo-rich composites of silicon and boron were developed which, upon oxidation, formed a surface borosilicate melt [7]. Due to the unusually high viscosity of silica melts, a balance can be struck between rapid surface coverage and low oxygen permeability. Varying the boron to silicon ratio allows for tailoring the borosilicate viscosity to the operational temperature of the engine components.

Most molybdenum - silicon - boron (Mo-Si-B) composites to date have focused on compositions situated within a three phase field of αMo, Mo_5SiB_2 (also known as T2), and Mo_3Si (also known as A15). The aim of these compositions is to have just enough T2 and A15 to provide sufficient borosilicate glass during oxidation and rely upon the αMo for toughness. However, the high melting points of the three phases (αMo is the highest) and the sluggish kinetics, which are favorable for low creep in service, lead to processing challenges. In particular the high processing temperatures results in 3 to 5 atomic percent silicon dissolving into the αMo phase, which is then difficult to remove by subsequent processing. Work by Jain, Heilmaier, Saage, and others [55, 43, 96] has shown that just a few atomic percent silicon can dramatically embrittle molybdenum by segregating to both dislocation cores and grain boundaries, weakening them in much the same way as oxygen embrittles molybdenum alloys [87, 63]. Even with a high volume fraction of αMo, this level of dissolved silicon results in brittle, intergranular fracture and correspondingly low toughness up to at least 1000°C. The high brittle to ductile transition temperature (BDTT) is a serious obstacle to any structural use of these composites.

In spite of the high BDTT, the mechanical properties of Mo-Si-B composites above their transition to ductile behavior have been shown to be favorable with very good creep resistance and reasonable toughness [62, 70]. Three main challenges to the implementation of Mo-Si-B composites still exit. First, the temperature range of the favorable mechanical properties must be increased by lowering the BDTT. Second, the refractory nature of these phases makes processing difficult and in constant need of development. Casting results

in both detrimental solidification segregation and the highest silicon supersaturation [85]. Powder processing is preferred as it is well suited for forming a fine and homogeneous microstructure with an αMo matrix. The silicon supersaturation is then controlled by the consolidation temperature, with 1600℃ causing a BDTT around 1000℃ [77]. Third, the mechanism by which oxidation resistance occurs and the role of the borosilicate composition have not been investigated in depth making material optimization challenging. Oxidation of continuous matrix Mo-Si-B composites is complex with competition between the evolving MoO_3 gas and spreading borosilicate. Additionally, the sizable difference between the initial oxidation and long term resistance means that the borosilicate's role is challenging.

The work of this dissertation addresses the challenges to Mo-Si-B composites in two areas, improvements to powder processing techniques and development of compositions for oxidation resistance at 1300℃. The processing of Mo-Si-B composites is strongly tied to their mechanical properties by establishing the αMo matrix, limiting impurity content, and setting the level of silicon solution which may become supersaturated. The powder techniques developed by Middlemas [77] used fine powders and the nitrides of silicon and boron to create a fine, homogeneous Mo-Si-B composite with low impurities by sintering at 1600℃. Improvements were made here to the hydrogen removal of initial oxygen on the molybdenum powder during the early stages if firing. Additionally, the use of hot isostatic pressing at 1300℃ was demonstrated as a viable alternative to pressureless sintering at 1600℃.

The second area addressed here is the oxidation resistance. Samples having a wide range of compositions were used to both develop a theory for the oxidation of these materials and to identify compositions which were oxidation resistant at 1300℃. Compared to most published results, the preferred compositions here had higher silicon to boron ratios, resulting in higher viscosities, and a minor addition of manganese, which aided initial spreading of the borosilicate. The origin of this composition's superior performance was found within the second of three stages defined in the theory of oxidation resistance. During this stage, a thin borosilicate surface layer becomes thicker and experiences continuous bubbling of MoO_3. If the viscosity is too high, the borosilicate is poorly attached and fails by spall. If

the viscosity is too low, bubbles of MoO_3 never close and become channels of continuous oxidation. The high MoO_3 vapor pressure at 1300℃ requires a relatively high borosilicate viscosity and the presence of a modifier, such as manganese, to aid coverage.

In Chapter 2 a review of pertinent literature is given. Molybdenum, its alloys, and multiphase Mo-Si-B will be covered with regard to their mechanical and oxidation properties. A consistent aspect of these diverse materials is the sensitivity of the brittle to ductile transition temperature to solid solution hardening and grain boundary segregation of either oxygen or silicon. Beyond the mechanical properties, the oxidation resistance depends upon the behavior of the surface borosilicate. Therefore a review is also given of some borosilicate glasses focusing upon their structure and high temperature viscosity, permeability, and volatility.

Chapter 3 summarizes the experimental techniques and procedures used throughout this work. This extends from the raw materials used for powder processing through the sample firing and consolidation to the final characterization and oxidation testing. However, the details of the green body firing procedure are instead given in Chapter 5. The firing of the green body included considerable hydrogen reduction of molybdenum oxide prior to the intermetallic reactions and final sintering. Chapter 5 covers the iterative development of the de-oxidation portion of the firing utilizing dew point measurements and adjustments of the gas flow rate and firing schedule.

Before presenting the results of composition development for oxidation resistance, Chapter 4 provides the framework used to develop oxidation resistance while minimally impacting the potential mechanical properties. As is often noted by the published works in Chapter 2, the Mo-Si-B materials optimized for oxidation resistance verses strength and toughness are substantially different with nearly inverted microstructures (ie. metallic verses intermetallic matrices). A theoretical framework was thus used to define the development for oxidation resistance. Generally the work here is restricted to compositions having over 50 volume % αMo and oxidation is only evaluated at 1300℃ in air for up to 20 hours. The rational for selecting these oxidation conditions is based upon the belief that actual implementation of Mo-Si-B composites will rely upon protective coatings for the majority of a components life.

The bulk oxidation resistance is therefore intended as a damage tolerance (or graceful failure) type mechanism allowing for continued operation for a short time after damage occurs. The selection of 1300℃ is a slight increase over already proven Mo-Si-B performance and is around 150℃ higher than the maximum temperature for single crystal nickel superalloys.

The results of oxidation testing of numerous different compositions, as well as a theory proposed for the mechanism of oxidation resistance, are given in Chapter 6 and Chapter 7. The Mo-Si-B compositions evaluated had Si/B atomic ratios from 1 to nearly 5, all with an αMo volume fraction above 50%. Additionally, minor additions of iron, nickel, cobalt, yttria, and manganese were evaluated. Both the Si/B ratio and transition metal additions had a profound influence at 1300℃. The Si/B ratio needed for oxidation resistance was around 2.5, far higher than any other continuous αMo Mo-Si-B reported. Additionally, and believed to be specific to 1300℃, a minor addition of one of these transition metals is necessary for initial coverage of the borosilicate on the composite surface. However, all except manganese caused devitrification and large scale spallation between 30 and 90 minutes of oxidation. The combination of a Si/B ratio around 2.5 and manganese added at 0.5 atomic% is a promising candidate composition for oxidation resistance at 1300℃. Additionally, both the positive and negative effects of forced air are shown. Surprisingly, most compositions ultimately perform better under flowing air, having reduced oxidation rates after the borosilicate scale is formed. This is due to both the formation of a thicker borosilicate and greater removal of boria from that borosilicate surface.

CHAPTER 2

LITERATURE REVIEW

2.1 Molybdenum

The primary constituent of Mo-Si-B composites is the refractory metal molybdenum. As a refractory metal, molybdenum has a high melting point (2623℃), high thermal conductivity (138 $^{W}/_{m \cdot K}$), low thermal expansion (4.8 $^{ppm}/_{K}$), and high density (10.22 $^{g}/_{cm^2}$). While the high density is not favorable for turbine applications, the high melting point and thermal properties make molybdenum a desirable candidate for a high temperature, structural material [30]. However, like the other refractory metals, the oxidation resistance of molybdenum is limited to a very small temperature range. Successful Mo-Si-B development must mitigate the poor oxidation resistance of molybdenum with minimal detriment to the mechanical properties.

2.1.1 Oxidation of Molybdenum

The oxidation of molybdenum in air has three general regimes based upon the behavior of its two primary oxides, MoO_2 and MoO_3, though under certain conditions other phase can form, Figure 2.1 [10]. Below approximately 500℃ molybdenum itself is considered oxidation resistant as the MoO_2 present in the native oxide is an effective diffusion barrier [38, 106]. However, MoO_2 is not the equilibrium phase in air and at temperatures above 500℃ it oxidizes into MoO_3 at an increasingly rapid rate. Unlike the dioxide, MoO_3 is not refractory (having a melting point of 816℃) and has a correspondingly high oxygen diffusivity. In the temperature range between 500 and approximately 900℃, rapid and extensive MoO_3 formation occurs along with a significant volume expansion, Figure 2.2 [106]. Additionally, the vapor pressure of MoO_3 is very high (the boiling point is 1155℃) resulting in a high temperature change to oxidation weight loss once the volatilization of MoO_3 (primarily as molecular trimers) exceeds the rate of its formation [39].

Because of the high equilibrium vapor pressure of MoO_3, the oxidation of molybdenum

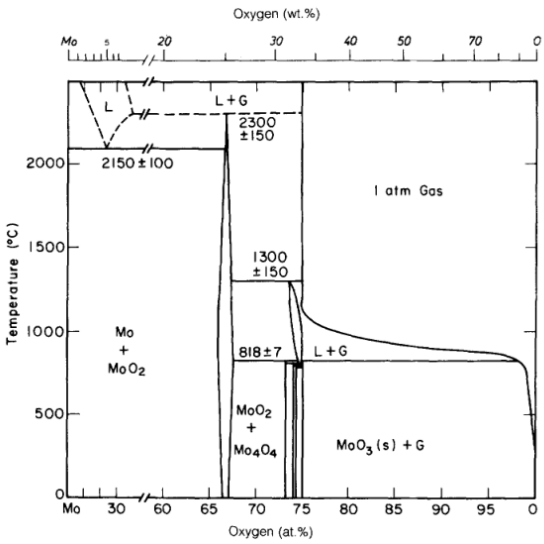

Figure 2.1: The molybdenum - oxygen phase diagram [10]

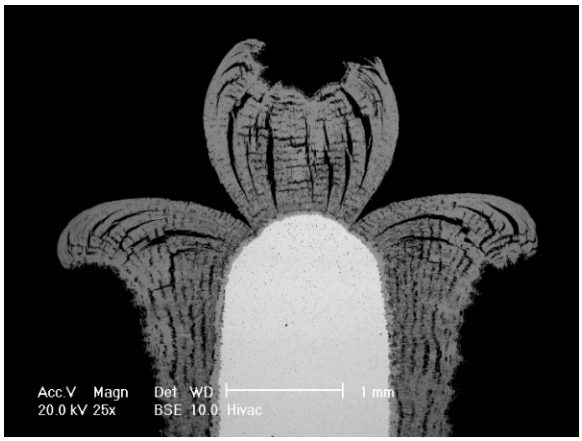

Figure 2.2: Cross section view of molybdenum alloy TZM oxidized in air at 600°C for 24 hours showing the sizable volume expansion due to MoO_2 and MoO_3 formation [106]

at high temperatures can become gas transport controlled. Gulbransen showed that in his specific testing setup, the increase in oxidation rate with increasing temperature slowed above a certain point. The outwardly growing "cloud" of MoO_3 impeded the inward gaseous diffusion of oxygen to the point that these transport rates became controlling [38]. For other applications, this conclusion means that gas flow rate, boundary layer thickness, and turbulent flows can have large effects upon the overall oxidation behavior.

In air and moist environments, including hydrogen reduction and combustion, water vapor can play a role in the oxidation of molybdenum. The species H_2MoO_4 has a higher equilibrium vapor pressure than MoO_3 at low and moderate temperatures [6]. This is used

advantageously in the production of high surface area molybdenum powder during hydrogen reduction of MoO_3. By operating at a moderate dew point, some of the reduction reactions occur rapidly in the gas phase and produce very fine solid precipitates [104]. However, during high temperature oxidation of molybdenum metal, the hydrated species becomes less significant in the gas than MoO_3 unless the water vapor content is extremely high [106].

2.1.2 Brittle to Ductile Transition in Molybdenum Alloys

The historical development of molybdenum alloys has primarily focused on lowering the brittle-to-ductile transition temperature (BDTT) that arises from sensitivity to oxygen impurities. In line with classical BDTT behavior for body centered cubic (BCC) metals, the brittle transition can often occur at temperatures around 10% of the absolute melting point, which, for molybdenum, is near ambient (17°C). Extensive work on cast, pure molybdenum found that very low concentrations of oxygen, carbon, and nitrogen caused large increases in the BDTT, with oxygen being the most potent [87, 63]. Additionally, these impurities were identified as strongly segregating to, and then weakening, grain boundaries. Associated with the BDTT was a change in fracture behavior as ductile deformation was replaced by transgranular and intergranular cleavage. In comparing the effects of oxygen and carbon, it was noticed that when both were present, carbon lowered the embrittlement due to oxygen by increasing the grain boundary fracture strength compared to oxygen impurities alone. Kumar and Eyre showed that carbon not only reduced the driving force for oxygen segregation, but could form grain boundary carbides [63].

Control of oxygen impurities and carbide formation are fundamental aspects of the molybdenum alloys TZM and MHZ. Both alloys have specific carbon contents and are alloyed with titanium, zirconium, and hafnium. Between carbon reducing segregation of oxygen to grain boundaries and the strong oxide formation of Ti, Zr, and Hf savaging any grain boundary oxygen, the grain boundaries in these alloys have very little embrittlement from oxygen. Additionally, all the metals present form hard and refractory carbides allowing for some precipitation strengthening and locking of grain boundaries [25]. In some

applications nitriding can be used for further precipitation strengthening by forming Ti, Zr, and Hf carbonitrides [83].

Two other less common alloys of molybdenum take a different approach to lowering the BDTT. Alloys containing high amounts of rhenium (10 to 25% Re) are found to be far less sensitive to oxygen embrittlement, even with traditional casting techniques [47]. However, due to the high cost of Re these alloys are prohibitive for most structural applications. The primary exception is as a weld filler in which less material is used and high purity processing is impractical [80]. With the evolution of high purity processing techniques the need for alloying to control oxygen impurities is not as great [23]. Specifically powder metallurgy utilizing oxide dispersion strengthening (ODS) has been used to produce ODS molybdenum based upon lanthanum oxide particles [82, 24].

As all the molybdenum alloys above (TZM, MHZ, Mo-Re, and ODS-Mo) take great care to control the grain boundary chemistry, it is no surprise that they are sensitive to the microstructure and thermo-mechanical processing. In general, these alloys should not be used in either as-cast or recrystallized conditions. Worked microstructures have considerably higher strengths and lower brittle-to-ductile transition temperatures due to impurity distributions, the relationship between grain size and impurity concentration on grain boundaries, and the presence of grain boundary precipitates [83, 82].

2.1.3 Embrittlment in Molybdenum Solid Solutions of Boron and Silicon

With the aim of providing both strength and oxidation resistance at high temperatures (above 1000℃), Mo-Si-B composites rely upon a surface silica layer as one of the few potential oxidation barriers for these temperatures [8]. The details of the multiphase Mo-Si-B system will be expanded upon in the following section, but first the solid solutions of boron and silicon in molybdenum will be reviewed. Of these, the molybdenum-boron system is far more straightforward as the solubility of boron in αMo is extremely low, Figure 2.3 [110]. Additionally, boron does not have the same embrittling behavior as oxygen. Instead, small amounts have been used to improve the mechanical properties of some molybdenum alloys and weld fillers through grain refinement via the formation of grain boundary borides

[127, 80].

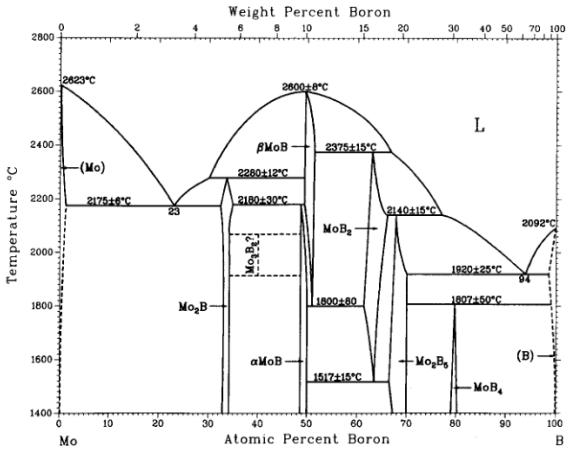

Figure 2.3: The molybdenum - boron equilibrium phase diagram [110].

Work on dilute Mo-Si alloys, which are indicative of the αMo phase in oxidation resistant composites, has shown that low amounts of silicon can dramatically raise the brittle to ductile transition temperature (BDTT). Unlike the low solubility of boron, silicon will dissolve to a few atomic percent in molybdenum even at 1600℃, Figure 2.4 [36]. However, at 1600℃ and below, diffusion is sluggish making equilibrium determination difficult. While the change in BDTT has not been directly measured, the research of Kumar, Sturm, and Saage does provide some data on the effect of Si content on the temperature at which yielding is observed under tension [55, 114, 96]. With 3 at% Si, which is near the 1600℃ solubility limit, molybdenum will yield at and above 1000℃ but not at 538℃. When the Si content is reduced to 1.5 at%, the onset of yielding is between 538 and 816℃ and when it is 0.34 at% yielding is observed at 260℃, but the room temperature fracture toughness is low, measured at 7.8 $^{MPa}/\sqrt{m}$ indicating brittle behavior [114].

The reason for the loss of plasticity in dilute Mo-Si alloys is the combination of both dislocation pinning by silicon in solution and grain boundary embrittlement by the segregation of excess silicon. The solute segregation to and weakening of grain boundaries is similar to the embrittlement of molybdenum by oxygen described above. In the work of both Jain [55] and Saage [96], Auger electron spectroscopy was used to directly measure the silicon segregation. As shown in Figure 2.5, the Si concentration is substantially higher

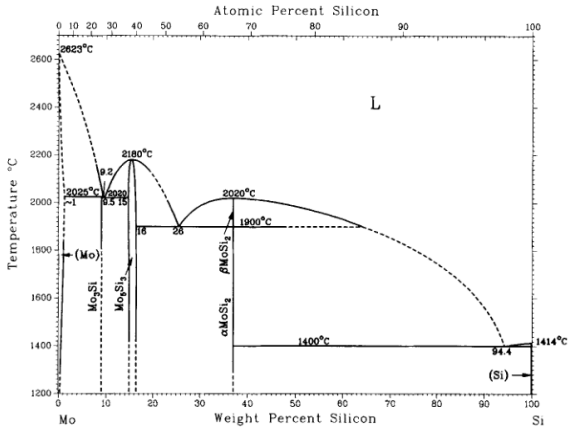

Figure 2.4: The molybdenum - silicon equilibrium phase diagram [36].

on grain boundaries, exposed through intragranular fracture, than within grains that fracture transgranularly. Additionally, in investigating the high temperature creep behavior, Jain utilized atom probe field ion microscopy to further understand the silicon distribution. Silicon was found to segregate to dislocation cores as well as grain boundaries, while the atomic distributions for both boron and carbon did not show any dislocation interactions [55].

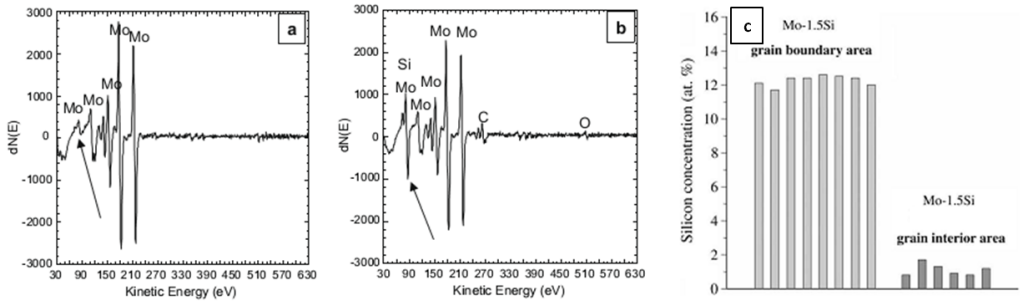

Figure 2.5: Auger electron spectra (AES) of dilute Mo-Si alloys fractured transgranularly (a) and intergranularly (b) [55]. Relative Si concentrations on grain boundaries and grain interiors also calculated from AES (c) [96].

2.2 Molybdenum - Silicon - Boron System in the Molybdenum Rich Corner

The first significant progress towards structural molybdenum composites with oxidation resistance began with the investigation of the Mo-Si-B ternary phase diagram by Nowotny [84]. Later, Berczik [7] developed and patented compositions in the molybdenum rich corner

of the ternary which had both good high temperature mechanical properties and oxidation resistance, Figure 2.6. Primary within the range of compositions is that with a volume fraction of αMo between 50 and 55% and silicon and boron weight percentiles of 3% and 1% respectively. This composition resides within the three phase field including Mo_3Si (A15) and Mo_5SiB_2 (T2) along with αMo. Microstructurally and mechanically these Mo-Si-B composites are intended to behave like a metal matrix reinforced with a hard phase. The αMo matrix promotes toughness by deforming at crack tips as well as bridging any sharp cracks passing through the intermetallic phases [69, 30].

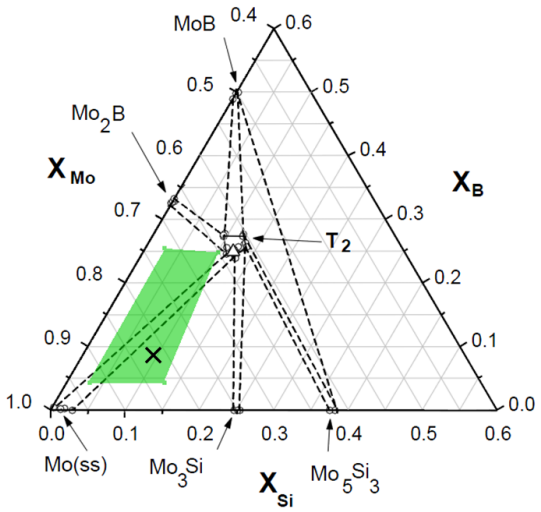

Figure 2.6: Molybdenum rich corner of the Mo-Si-B equilibrium phase diagram at 1600°C in mole fractions. The region highlighted is patented in reference [7]. The marked composition at 8.9% Si and 7.7%B (3% and 1% by weight respectively) has been the most researched to date.

2.2.1 Processing Techniques

Mo-Si-B composites have been produced by a wide range of casting and powder metallurgy techniques. The initial patented materials were produced via rapid solidification followed by heat treatment and consolidation of the supersaturated powders to form a fine microstructure with a continuous αMo matrix [7]. While this processing route yields an excellent microstructure, it is neither cost effective nor scalable, resulting in a search for alternatives.

Many researchers have utilized multiple-remelt arc casting of high purity, elemental Mo, Si, and B, however the nature of the system makes forming an αMo matrix difficult.

Figures 2.7 and 2.8 show the Mo-T2 quasibinary and liquidus projection of the Mo-Si-B ternary [100, 85]. From inspection of these diagrams, solidification of most molybdenum rich compositions will progress with primary αMo solidification followed by borides, T2, and finally A15. The resulting microstructures tend to have coarse and isolated αMo grains and strong composition gradients including non-equilibrium phases (ie. borides for Mo-T2-A15 compositions). Examples of these can be seen in Figure 2.9 [85]. Due to the refractory nature of this system, traditional approaches to modifying the as-cast microstructures, such as hot work and heat treatments, are unable to effectively develop a continuous αMo matrix.

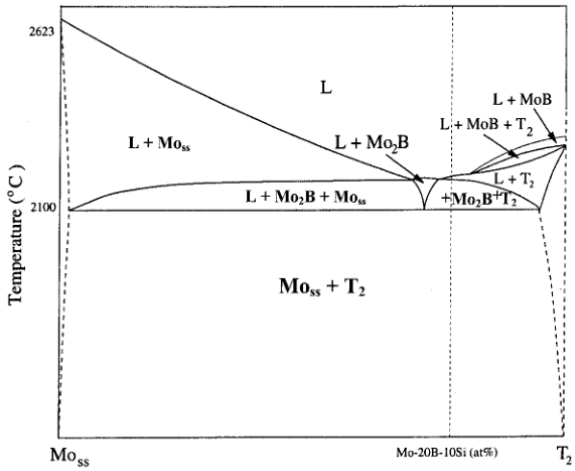

Figure 2.7: The quasibinary Mo-Mo_5SiB_2 (T2) estimated phase diagram [100].

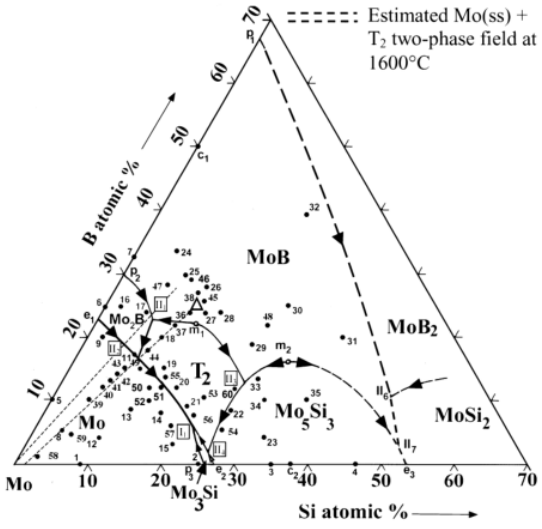

Figure 2.8: Liquidus projection of the Mo-Si-B system [85].

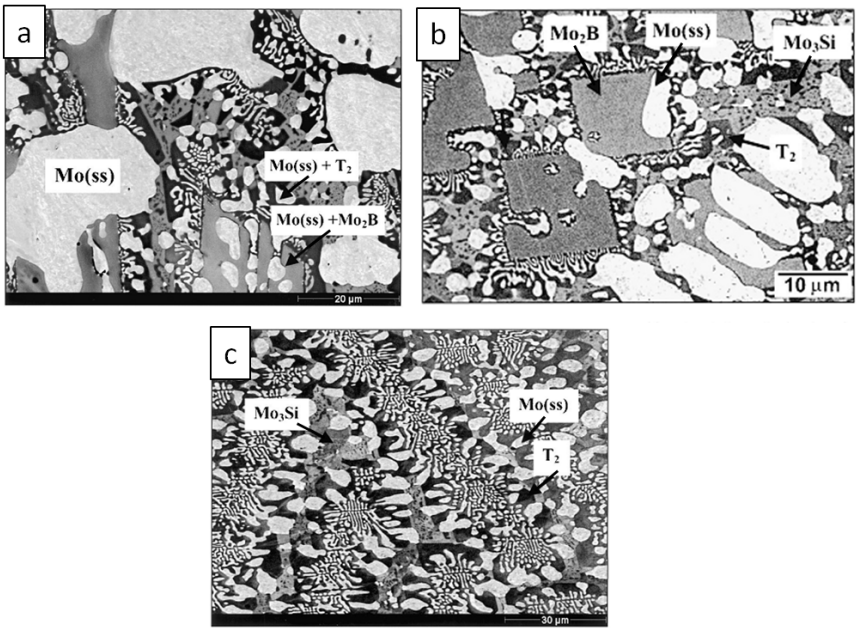

Figure 2.9: Solidification microstructures of arc cast Mo-Si-B imaged using backscatter scanning electron microscopy (SEM). The αMo phase appears brightest. (a) Mo-5Si-10B, (b) Mo-7Si-14B, and (c) Mo-9.6Si-14.2B. Compositions in atomic percentile [85].

All the production routes for Mo-Si-B composites that have resulted in a fine microstructure and αMo matrix, involve powder processing. Two in particular have demonstrated both strength and oxidation resistance and avoid solidification, and its related challenges, entirely. One avenue employs mechanical alloying of elemental Mo, Si, and B powders in an effort to replicate Bercik's original process (precipitation from a single phase) without the cost of rapid solidification [60]. Mechanical alloying forms a super saturated solution of molybdenum and silicon (up to 10 at% Si), although little, if any boron is incorporated. The resulting powder is sufficiently fine, homogeneous, and reactive to allow sintering and heat treatment in the range of 1500 to 1700℃, depending upon the use of hot isostatic pressing (HIP'ing). During the heat treatment, Si leaves solution and reacts to form both A15 and T2. The final material has a homogeneous and fine microstructure and demonstrated properties in line with the best cast and worked alternatives. However, mechanically alloying is still relatively costly and contamination can be difficult to limit. An alternative process which addresses both these issues was developed utilizing silicon and boron nitrides as low oxygen starting materials [78]. Fine powders of molybdenum, silicon nitride (Si_3N_4), and

boron nitride (BN) are dispersed in an organic liquid and then ultrasonically spray dried, yielding a homogeneous powder well suited for traditional powder processing. Pressuresless sintering at 1600℃ resulted in densities greater than 95% of theoretical and a material with mechanical and oxidation properties in line with both mechanically alloyed and cast and worked alternatives. Figure 2.10 shows the microstructures resulting from the mechanically alloying and nitride reaction processing routes.

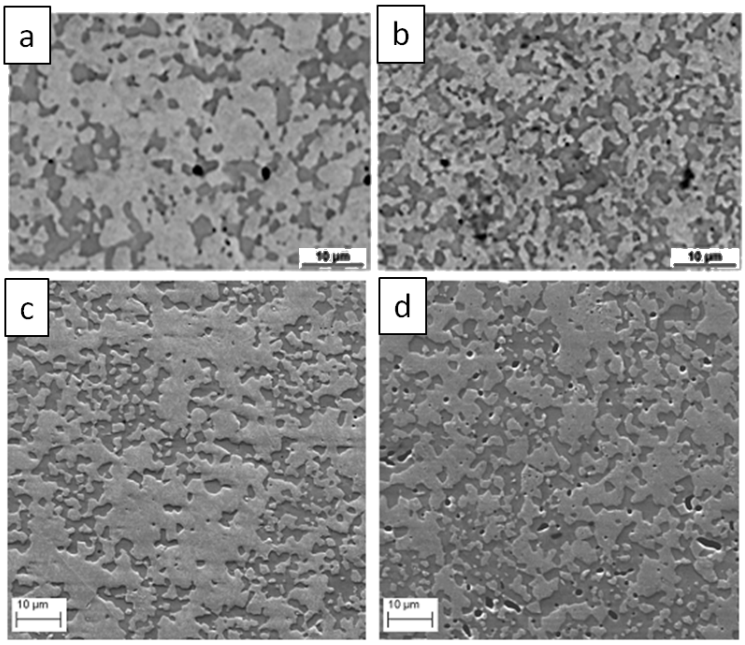

Figure 2.10: Microstructures of powder processed Mo-Si-B imaged in SEM. The αMo matrix is brightest and A15 and T2 are indistinguishable from each other. (a), Mo-6Si-5B, and (b), Mo-9Si-8B, are mechanically alloyed and hot isostatic pressed at 1500℃ [43]. (c), Mo6Si-7.8B, and (d), Mo-8.9Si-7.7B, are reacted from spray dried nitrides and pressurelessly sintered at 1600℃ [79].

2.2.2 Mechanical Properties

Investigations into the mechanical properties of Mo-Si-B composites have typically focused on either the high temperature strength and creep resistance or the brittle-to-ductile transition and toughening mechanisms at relatively "low" temperatures, below the BDTT. The general findings have been twofold; firstly that the microstructure plays a significant role, with a continuous αMo matrix needed for any low temperature toughness, and secondly

that the behavior of the αMo phase itself (with silicon solid solution and any oxygen embrittlement) is the primary factor determining the BDTT [69].

At ambient temperatures Mo-Si-B composites have consistently been found to be completely brittle. Lemberg measured the K_{Ic} fracture toughness of both the mechanically alloyed and nitride reaction processed material to be below 8 $^{MPa}/\sqrt{m}$ [70]. Auger emission spectroscopy of these fracture surfaces showed considerable segregation of both silicon and oxygen, consistent with the findings of pure and traditional molybdenum alloys.

The few investigations into identifying the brittle-to-ductile transition temperature show a dependence upon the material processing and thus the degree of silicon solid solution and segregation. For compositions all near Mo-3wt%Si-1wt%B (in the Mo-A15-T2 phase field), Jain found the BDTT to be between 1100 and 1200℃, Figure 2.11c [55]. This study used powder produced by the plasma rotating electrode process (PREP), consolidated via hot isostatic pressing (HIP), and finally isothermally forged. Kruger found a lower BDTT, around 950℃, for the mechanically alloyed material consolidated by sintering at 1600℃ and HIP'ing at 1500℃, Figure 2.11a and b [62]. Additionally, within this same study, alloying with 0.5 or 1 at% zirconium reduced the BDTT to around 850℃. This is consistent with the results of single phase Mo-1.5at%Si bend bars containing Y_2O_3 and zirconium which were ductile at 816℃ and 538℃ respectively, Figure 2.12 [96].

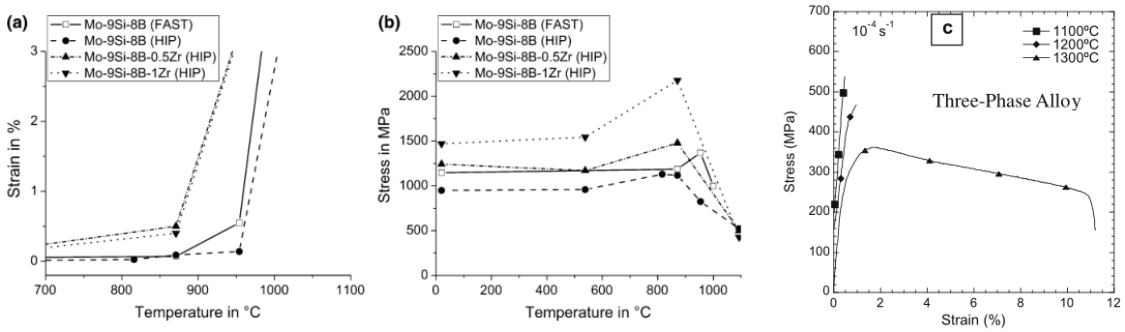

Figure 2.11: Mechanical properties of Mo-A15-T2 material with a continuous αMo matrix. (a) and (b) show the results of bend bars produced by mechanically alloying [62]. (c) are uniaxial tensile tests of material produced by PREP+HIP+forging [55].

At temperatures above the BDTT, Mo-Si-B composites have both high strength and toughness. As shown in Figure 2.11, both Kruger and Jain found yield strengths at 1200

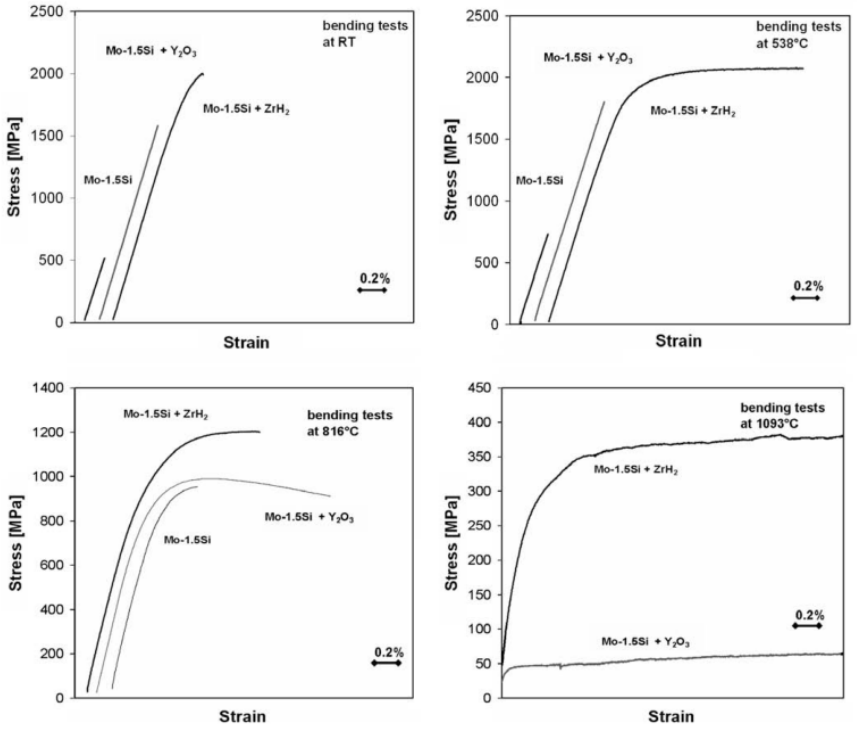

Figure 2.12: Bend test results at various temperatures for molybdenum with 1.5at% silicon in solution and around 1% of either yttria (Y_2O_3) or zirconium [96].

and 1300℃ to be around 350 to 500 MPa [62, 55]. Lemberg also measured the toughness at 1300℃ and found the K_{Ic} of the mechanically alloyed and nitride reaction processed material to be 22 and 26 $^{MPa}/\sqrt{m}$ respectively [70], Figure 2.13.

Along with high strength and toughness, use as a high temperature structural material requires high creep resistance. Schneibel measured high creep resistance at 1400℃ for a material with discontinuous αMo, however the need for lower temperature toughness precludes its use [102]. Kruger and Jain have measured the creep resistance of various cast and powder metallurgical Mo-Si-B materials with continuous αMo at temperatures between 1100 and 1300℃ [62, 55]. In Figure 2.14 the constant stress strain rate for a number of mechanically alloyed Mo-9at%Si-8at%B materials is shown along side the single-crystal, nickel-based superalloy CMSX-4 [62]. While the lower temperature, low stress performance of the superalloy was better, Mo-Si-B had significantly higher resistance at 1200℃. The exception to this was the very fine grained FAST material which was field assisted sintered (FAST) and had a submicron average grain size. Figure 2.15 shows the creep life of another

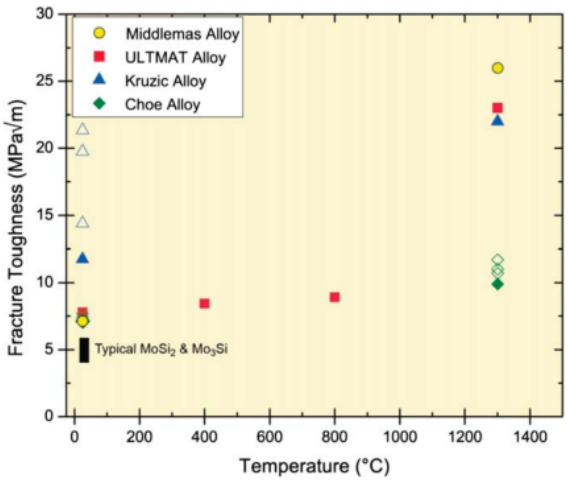

Figure 2.13: Fracture toughness a various temperatures for Mo-A15-T2 materials with continuous αMo matrix. The Middlmas alloy is produced by nitride reaction and the ULTMAT by mechanically alloying. The Kruzic and Choe alloys are considerably coarser and have an αMo matrix produced by vacuum annealing intermetallic powders [70].

Mo-Si-B material as the Larson-Miller parameter calculated from testing between 1100 and 1300°C [55]. Two nickel based superalloys (René80 and 2GSX) are also included and, again, the Mo-Si-B material had greater high temperature creep resistance.

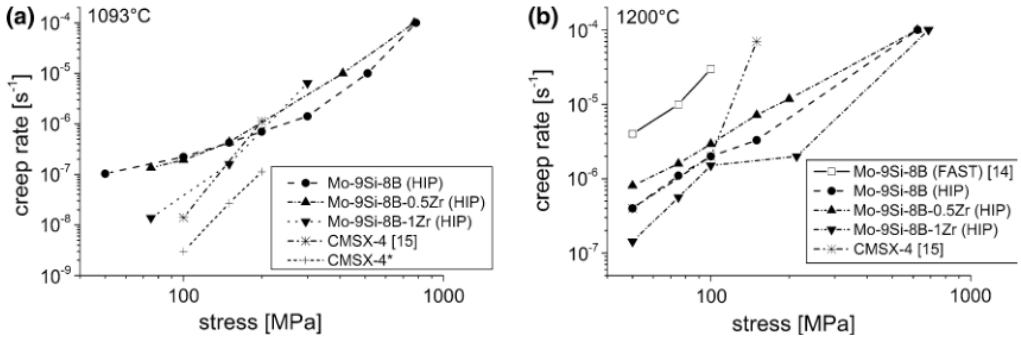

Figure 2.14: Constant load creep resistance of mechanically alloyed Mo-9at%Si-8at%B compared to the single crystal superalloy CMSC-4 at 1093 and 1200°C [62].

2.2.3 Oxidation Results and Models

The high temperature oxidation resistance of Mo-Si-B materials is based upon the high stability and low permeability of silica [8, 65]. Unlike $MoSi_2$ however, the molybdenum rich materials are unable to grow a protective silica surface layer from every location within their microstructure. The inclusion of boron can aid in the development of a continuous surface

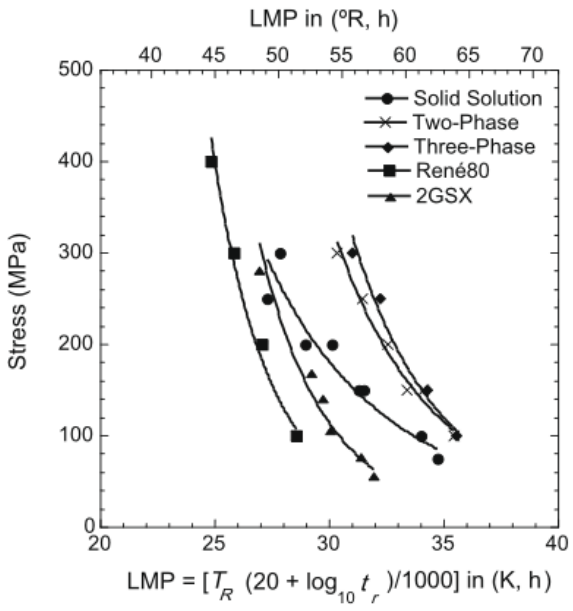

Figure 2.15: Creep resistance of Mo-A15-T2 material and two nickel-based superalloys as a function of the Larson-Miller parameter [55].

layer. The process by which this occurs depends upon the composition, bulk microstructure, and temperature of oxidation. The results of high intermetallic fraction materials will be presented first as they represent the majority of the Mo-Si-B oxidation results. Afterwards the results of αMo matrix materials and then a Mo-Si-B based coating will be given.

2.2.3.1 Discontinuous αMo

The high intermetallic fraction Mo-Si-B materials, aside from the well known $MoSi_2$, are composed of Mo_5Si_3 (T1), A15, T2, and in some cases discontinuous αMo phases. Akinc et al. investigated boron-doped T1 as a more creep resistant alternative to $MoSi_2$ [2]. They found that small boron additions, which moved the composition into the T1-T2-A15 phase field, greatly improved the oxidation resistance at temperatures between 800 and 1500℃. Additionally, samples with a higher B/Si ratio (and thus lower borosilicate viscosity) were found to have the lowest weight loss rate during oxidation. Reducing the viscosity of the borosilicate helped close surface pores left behind as MoO_3 evaporated from the oxidizing T1 grains [2].

While boron-doped T1 has good oxidation resistance over a wide range of temperatures

and high creep strength, it lacks potential toughening from the αMo phase. In order to develop some toughness, other researchers investigated compositions in the T2-A15-αMo phase with discontinuous αMo at a volume fraction around 30 to 40%. However, these materials have a greater difficulty of being oxidation resistant as the oxidation of exposed αMo grains leaves non-protective regions far larger than those from T1, T2, or A15. To compensate, these materials have higher boron contents than the B-doped T1 of Akinc et al., and thus lower borosilicate viscosities. Parthasarathy et al. extensively investigated the oxidation behavior of cast Mo-12at%Si-12at%B at temperatures from 500 to 1300℃ [90]. Figure 2.16 shows the oxidation mechanism over different temperature regimes for pure molybdenum and the Mo-Si-B material of Parthasarathy. It was found that the relative magnitude of MoO_3 volatilization, B_2O_3 evaporation, borosilicate viscosity, and the various species' diffusivities greatly changed the weight gain or loss kinetics. At high temperatures (800 to 1300℃) the material developed oxidation resistance after a period of transient weight loss due to MoO_3 evaporation. However, at temperatures between 650 and 750℃ the borosilicate was too viscous to prevent continuous loss of MoO_3.

The work of Dheeradhada et al. [29] focused on the specifics of 1300℃ oxidation of a cast Mo-13.2at%Si-13.2at%B very similar to that of Parthasarathy et al. At this temperature both authors observed the formation of a two layer oxidation structure composed of an intermediate molybdenum and borosilicate layer between the outer boria (B_2O_3) lean silicate and the base material. The formation of these layers is due to the diffusion of oxygen, silicon, boron, and molybdenum through and underneath the surface silicate [29]. As oxygen diffused into the base material, it oxidized the silicon and boron within the A15 and T2 phases forming a layer of molybdenum with isolated borosilicate regions. This "internal oxidation" zone represents a range of oxygen concentrations greater than the limit for boria and silica stability but below the limit for molybdenum oxide formation.

While the results of Parthasarathy et al. and Dheeradhada et al. reveal much of the steady state oxidation mechanisms, neither focused upon the nature of the initial transient oxidation. This was specifically addressed by Roy et al. [95] and Rioult et al. [94], who in addition evaluated the effect of microstructural size. Both used similar cast compositions,

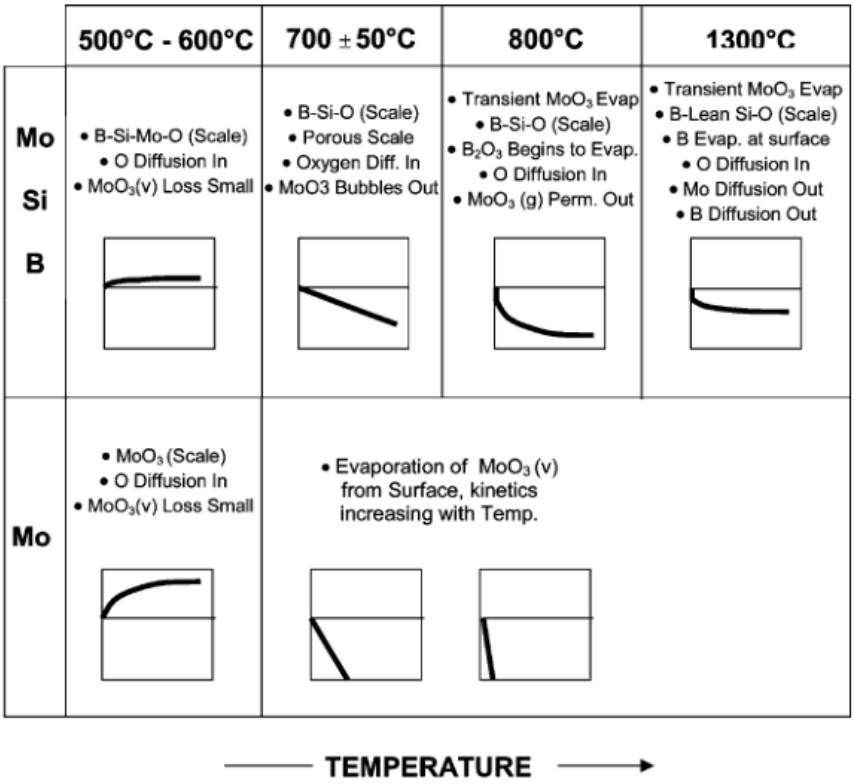

Figure 2.16: Oxidation mechanism of molybdenum and Mo-12at%Si-12at%B over different temperature regimes [90].

approximately Mo-14at%Si-10at%B, and found similar weight losses upon oxidation at 1100 and 1150°C. In studying transient oxidation, both works expose polished samples to air (or 20% oxygen in argon) in a thermogravimetric analyzer (TGA) for periods of 20 seconds to 15 minutes. Figure 2.17 shows the surface appearance after 20 and 60 seconds in which thinly coated cavities over αMo grain and porous silica over A15 grains are evident.

In spite of finding similar oxidation weight losses and transient surface appearances, Roy et al. and Rioult et al. develop fundamentally different theories for the transient oxidation mechanism. Roy observed the size of the surface cavities located over αMo dendrites to decrease during the transient oxidation [95]. The cause was interpreted as viscous flow of the surface borosilicate closing off the cavities. Because the cavities are the location of active oxidation, reducing their size and number lowers the oxidation weight loss rate. As this rate approaches zero, the transient oxidation comes to and end. Roy et al. modeled the competition between borosilicate flow and MoO_3 evaporation as shrinking cavities of

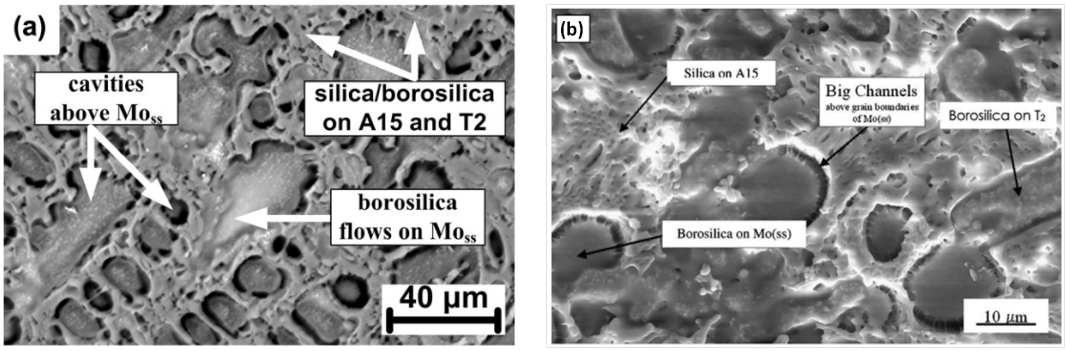

Figure 2.17: Surface appearance of Mo-14at%Si-10at%B after oxidation for 20 seconds at 1150℃ (a) [95] and 60 seconds at 1100℃ (b) [94].

various cross sectional shapes. They found that a conical shape most closely matched the oxidation weight loss results [95].

The oxidation model developed by Rioult et al. is based upon an assumption quite opposite to that of Roy et al. From their observations on the oxidation of the individual phases, and the lack of resistance from αMo and A15, Rioult concludes a greater "importance of consumption of the largest grains of Mo and A15 rather than borosilica glass spreading in determining transient oxidation behavior" [94]. The model they developed considered local oxidation fronts into the material being terminated only upon encountering a T2 grain. Effectively, the surface area participating in oxidation started with the bulk composition and then become depleted of αMo and A15 as they were consumed and ultimately replaced by T2. Based upon their measurements of the oxidation rates of the individual phases, the net weight loss was calculated as a function of the varying area fraction. Additionally, the authors matched their model to the oxidation results of materials with differing microstructural sizes, successfully showing greater transient weight loss for coarser, as larger αMo and A15 grains needed to be consumed before the oxidation front was terminated by T2 [94].

The complexity of the oxidation behavior of Mo-Si-B materials is such that slight compositional changes quickly exceed the capabilities of the previous models. In improving the fracture toughness of cast Mo-11.2at%Si-8.1at%B by aluminum additions, Das et al. found a significant loss of oxidation resistance at 1100℃ due to the formation of surface mullite and cristobalite instead of a proctective borosilicate glass. However, through minor

additions of cerium, some of the oxidation resistance was regained as cerium inhibited the formation of mullite from the borosilicate glass [28]. The complexity of Mo-Si-B oxidation does not only result from composition variations, but also from microstructural changes as shown in Figure 2.18 from the work of Wang et al. on the primarily T2, Mo-12.5at%Si-25at%B [122]. In this cast material, the matrix is T2 dendrites with Mo-A15-T2 eutectic. Upon short term oxidation at 1200℃, the eutectic phases oxidized to a greater depth and with a thicker scale than the large T2 grains. However, this became reversed after 2 hours, with the borosilicate scale over the T2 grains being thicker and much of the eutectic phases being replaced by a complex molybdenum containing oxide. After 100 hours, these regional variations disappeared with the oxide scale being a uniform and thick borosilicate with entrained, blocky MoO_2 grains near the internal oxidation interface.

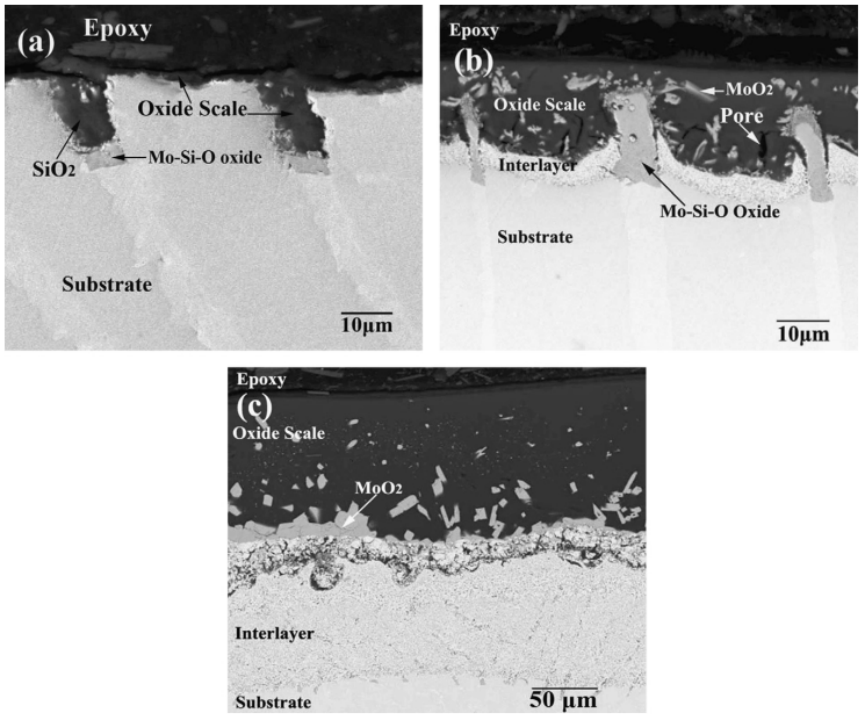

Figure 2.18: Cross section of the oxide scale formed on Mo-12.5at%Si-25at%B at 1200℃ after 10 minutes (a), 2 hours (b), and 100 hours (c) [122].

2.2.3.2 Continuous αMo

Unlike Mo-Si-B materials with discontinuous αMo, those with it as a continuous matrix can not rely upon consumption of αMo grains during oxidation to ever be completely

terminated in a more oxidation resistant phase. Thus spreading of the borosilicate, such as considered by Roy et al., must be the operating oxidation resistance mechanism. Helmick et al. investigated the oxidation resistance of cast Mo-3wt%Si-1wt%B at temperatures from 816 to 1100℃ and under static and flowing air [45, 44]. Figure 2.19 shows the volatile species diagrams they calculated at 1350K for both molybdenum and boron oxides and hydroxides. The authors note that the "evaporation of MoO_3 is a major reason why the borosilicate layer can develop even though the silicon and boron concentrations are low. Evaporation of MoO_3 permits the SiO_2 and B_2O_3 to accumulate on the surface of the MoO_2 layer that covers the alloy surface" [44]. Following this evaporation, the borosilicate viscosity is also noted as being very important in determining the ability of the borosilicate to flow and cover the material surface. However, because of the high partial pressure of boron oxides and hydroxide along with the air flow factors investigated by Helmick, the borosilicate viscosity is neither simple nor constant [44].

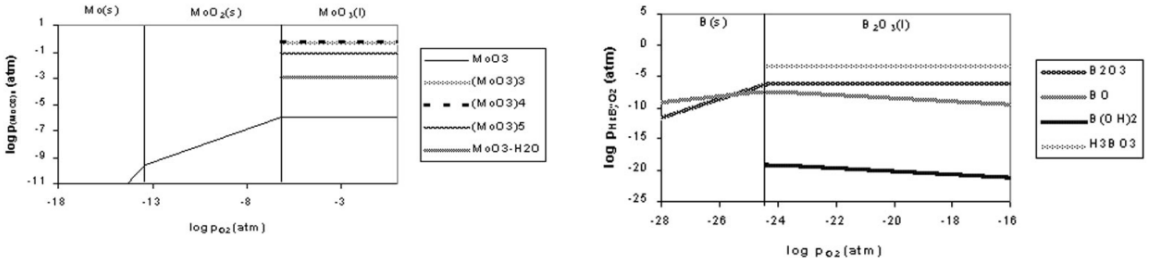

Figure 2.19: Volatile species of molybdenum and boron at 1350K as a function of oxygen partial pressure and with 0.1atm of water vapor [44].

Helmick identified cavity/channel behavior that was far more significant in the high αMo materials than in those discussed previously. While good oxidation resistance occurred at 1000℃ under all the air flow conditions, samples at both 816 and 1100℃ failed to be protected at high air flow rates [44]. Figure 2.20 shows the surfaces of two such samples. At 816℃, the left image in the figure, a protective glass is present at the leading edge, however large bubbles and then open channels persist downstream, indicating that at this temperature the oxidation behavior is sensitive to the gas composition [44]. This variety of behaviors was not seen at the higher temperature, 1100℃, and instead deep, open channels formed throughout.

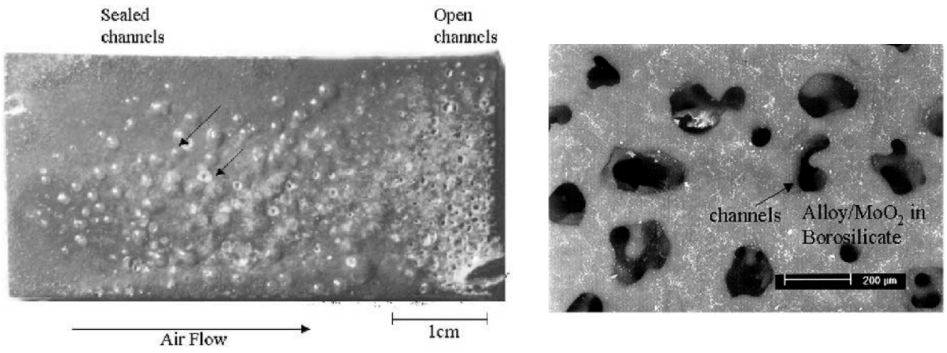

Figure 2.20: Surface appearance of Mo-3wt%Si-1wt%B oxidized at 816℃, left, and 1100℃, right for 1 hour. The air flow at 816℃ was 1 cm/s while at 1100℃ it was 10 cm/s [44].

In contrast to the limited conditions for oxidation resistance found by Helmick et al., the research on mechanically alloyed Mo-9at%Si-8at%B (approximately Mo-3wt%Si-1wt%B) by Burk et al. found excellent oxidation resistance up to 1200 and 1300℃ [11, 12, 13]. Unfortunately, no reason by any author had been given for the differing results between these studies. Figure 2.21 shows the oxidation weight loss at temperatures from 900 to 1300℃ measured in a TGA [13]. With the exception of 900℃, these samples quickly developed thin and continuous borosilicate coatings such as that shown in Figure 2.22 on the right.

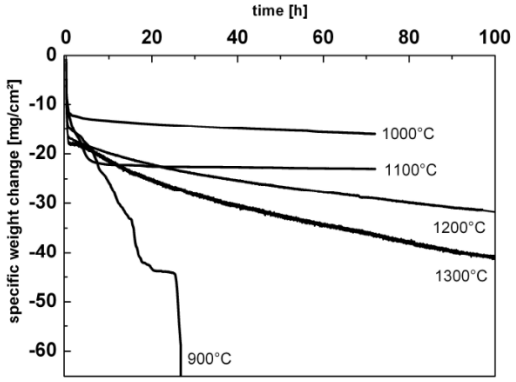

Figure 2.21: Weight loss of mechanically alloyed Mo-9at%Si-8at%B during oxidation at various temperatures [13].

In addition to a base Mo-9at%Si-8at%B composition, Burk looked at the effect of various additives upon oxidation resistance [12, 13, 11]. Chromium was added to improve the oxidation behavior at 700-900℃ by forming a chromia scale. However, improvements were only realized for high chromium contents, 20-25at%, which resulted in a loss of oxidation resistance at higher temperatures. Minor additions of lanthana and zirconium, who's

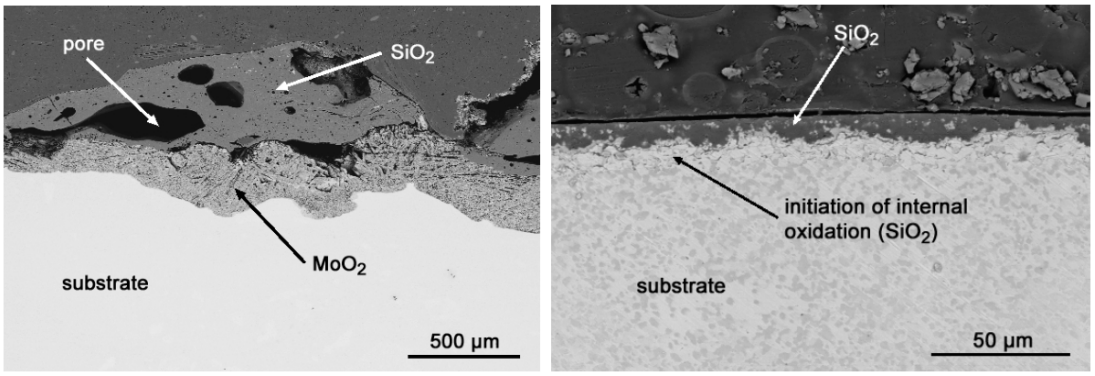

Figure 2.22: Cross sections of mechanically alloyed Mo-9at%Si-8at%B oxidized at 820℃ for 7 hours (left) and at 1100℃ for 72 hours (right) [13].

primary function was to improve mechanical properties, were found to slightly aid in the lower temperature oxidation (down to 820℃ for lanthana) without serious detriment to the oxidation at 1000 and 1100℃[13].

Due to the increased toughness from zirconium alloying in Mo-Si solid solutions, Burk et al. further investigated its effect upon oxidation. Added at 0.5 and 1 at% to the mechanically alloyed Mo-9at%Si-8at%B, zirconium was found to have little effect upon oxidation at 750 and 820℃, improved resistance at 1100℃, and considerable loss of resistance at 1300℃ [11]. Figure 2.23 shows these results and can be compared to Figure 2.21. At 1200 and 1300℃, the zirconium containing material was observed to have protrusions and "microcraters" on the surface of the borosilicate glass. The authors suggest that the protrusions and microcraters, which may form during bubbling of MoO_3 in the borosilicate, persist and cause the loss of oxidation resistance due to damage within the borosilicate layer from the zirconia (ZrO_2) phase transformation [11]. Figure 2.24 on the right shows the process schematically. Because the monoclinic-tetragonal phase transformation occurs above 1100℃ and with a large volume decrease, it was believed to create voids within the borosilicate [11].

More extensive investigations into modified, mechanically alloyed Mo-9at%Si-8at%B was performed by Majumdar et al. using two levels of yttria (Y_2O_3) additions [71, 72]. At oxidation temperatures of 1000℃ and below, a relatively high addition of yttria was found to improve the oxidation resistance. However, at temperatures of 1100℃ and above,

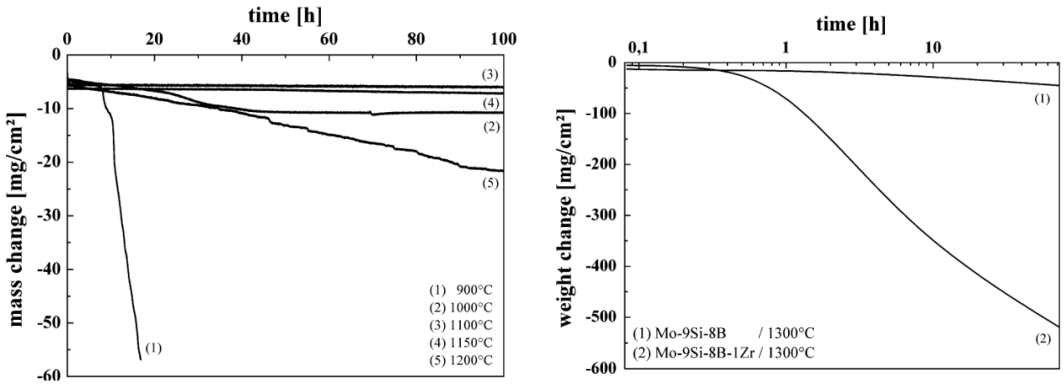

Figure 2.23: Weight loss of mechanically alloyed Mo-9at%Si-8at%B with zirconium during oxidation at various temperatures. The values shown on the left can be compared to the base composition in Figure 2.21. On right, the behavior at 1300℃ of both the base and zirconium modified material is shown [11].

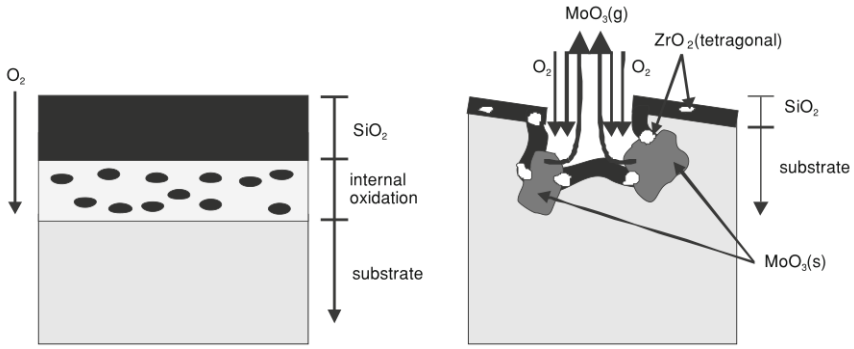

Figure 2.24: Schematic of oxidation at 1300℃ for both the base mechanically alloyed Mo-9at%Si-8at%B and it modified with zirconium. Damage from the zirconia particles prevents oxidation resistance [11].

a lower concentration of yttria gave greater improvements. This performance was even extend to 1400℃ at which temperature the formation of a yttrium-silicate surface on the borosilicate appeared to be the source of the greater oxidation resistance, Figure 2.25 [71]. At lower temperatures, the cause of the improved oxidation resistance was not entirely clear however the authors identified two potential aspects. Yttrium was observed to segregate to the interface between the glass and the MoO_2 and then reduce the inward oxygen diffusion, lowering the growth rate of the MoO_2 layer. Additionally, the authors identified the presence of yttrium-molybdate phases, which are significantly more stable than MoO_3, and thus both lower MoO_3 evaporation and aid in the formation of a protective borosilicate [72].

Just as some minor additions were found to improve the high temperature oxidation

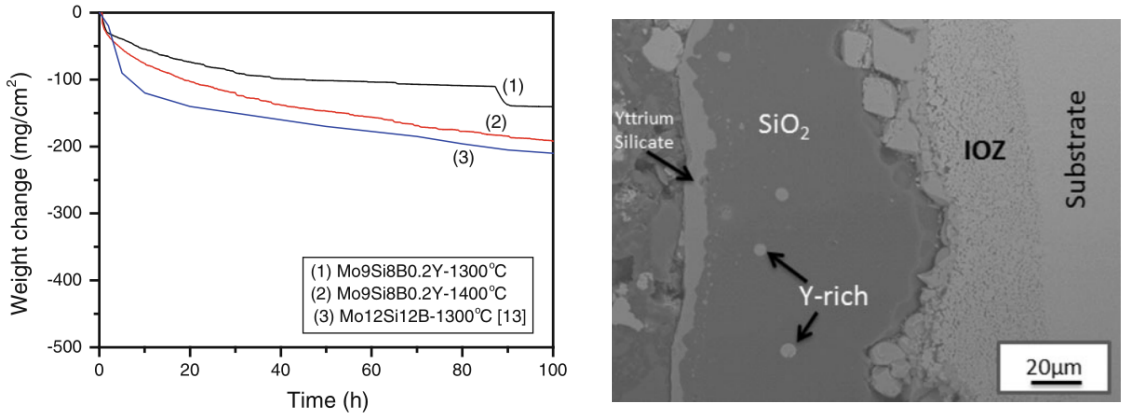

Figure 2.25: High temperature oxidation of yttria modified, mechanically alloyed Mo-9at%Si-8at%B with yttrium at 0.2at%. Shown at left is the weight loss at 1300 and 1400°C compared to the non-modified material at 1300°C. The cross section, on right, is the yttria modified sample after 2 hours at 1400°C [71].

resistance of mechanically alloyed Mo-Si-B, Sossaman et al. identified substantial improvements of cast Mo-2wt%Si-1wt%B and Mo-3wt%Si-1wt%B with minor iron additions [107]. Figure 2.26 shows the reduced weight loss and thinner and more uniform scale formed on the Mo-2Si-1B material due to iron. The authors hypothesize that during the solidification process, iron segregated into the A15 grains as it is the last phase to solidify. Upon oxidation iron fluxed the pure silica formed by the local oxidation of the A15 grains, reducing the time for that porous silica to become protective [107]. Additionally, they identify iron-molybdate phases, similar to the results of Majumdar et al., however they do not speculate as to any effects on the material behavior [107]. These results are likely very similar to the claims in a patent of Woodard et al., however few details are giving there within [124].

2.2.3.3 Mo-Si-B Based Coatings

While not in the molybdenum rich corner of the phase diagram, coatings based upon Mo-Si-B compositions are relevant due to certain similarities during oxidation and their compatibility with structural Mo-Si-B materials, raising the possibility of use as environmental barrier coatings (EBC). Two works, those of Lange et al. [67] and Downs et al. [32], both utilize a pack-cementation technique to apply a Mo-Si-B coating composed primarily of T1, T2, and $MoSi_2$. Applied to a Mo-Si-B material more optimized for strength, creep, and toughness (such as Mo-3wt%Si-1wt%B), these coating provide excellent oxidation resistance

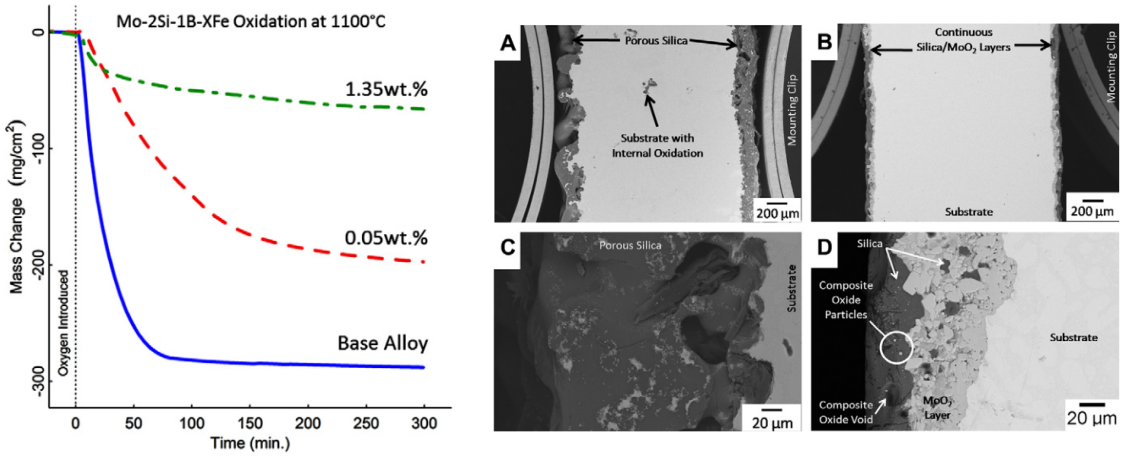

Figure 2.26: Improved oxidation of cast Mo-2wt%Si-1wt%B from minor additions of iron. On the left is the weight loss during oxidation at 1100℃. The sample cross sections on the right are for the non-modified composition (A and C) and the high iron addition (B and D) all after 1 minute at 1100℃ [107]

along with being chemically compatible and having a similar thermal expansion coefficient [67]. Lange et al. show this during 500 hours of oxidation at 1300℃ including a number of thermal cycles to room temperature [67]. Figure 2.27 shows the low weight change they measured as well as the sample cross section. Although some cracks did develop from the thermal cycles, the self healing ability of both the coating and underlying Mo-Si-B material prevented catastrophic oxidation [67].

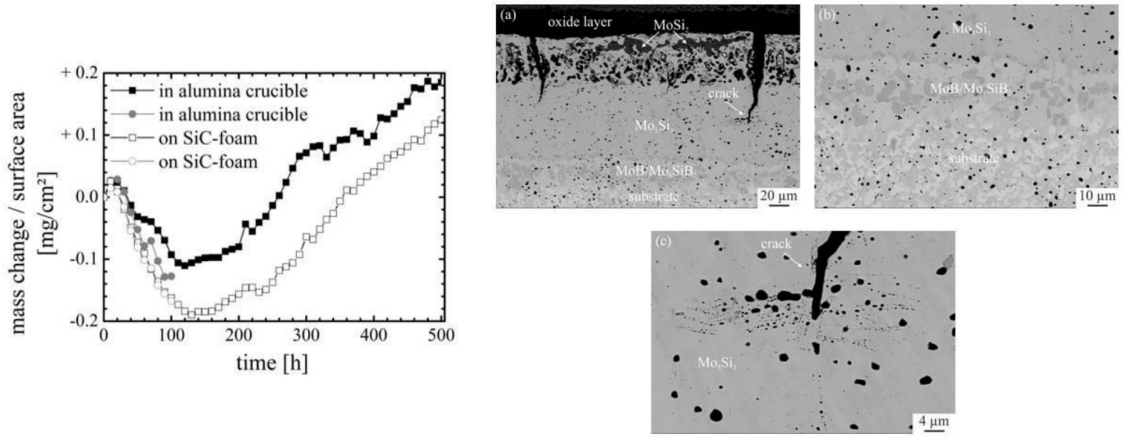

Figure 2.27: Oxidation of a pack-cemented Mo-Si-B coating on Mo-9at%Si-at%B. Two different sample supports were used for oxidation, both with very low weight change over 500 hours. The cross sections shown are after 500 hours at 1300℃ [67].

The ingestion of sand or volcanic ash is a significant challenge to modern jet engines

as these substances, primary calcium-magnesium aluminosilicates (CMAS), aggressively attack the coatings used on nickel based superalloys [32]. Any replacement material must therefore have some resistance to this CMAS attack. Downs et al. investigated the reactions between Mo-Si-B coatings and representative CMAS at temperatures from 1200 to 1500℃ [32]. Figure 2.28 shows cross sections through the CMAS and Mo-Si-B coatings after 25 hours at 1200, 1300, and 1400℃. The reaction layers do not show signs of degradation at any of these temperatures. Interestingly, the authors note significant formation of calcium-molybdate, $CaMoO_4$, and speculate that this may even improve CMAS resistance by both reducing molybdenum losses and preventing calcium from fluxing the surrounding silicate glass [32].

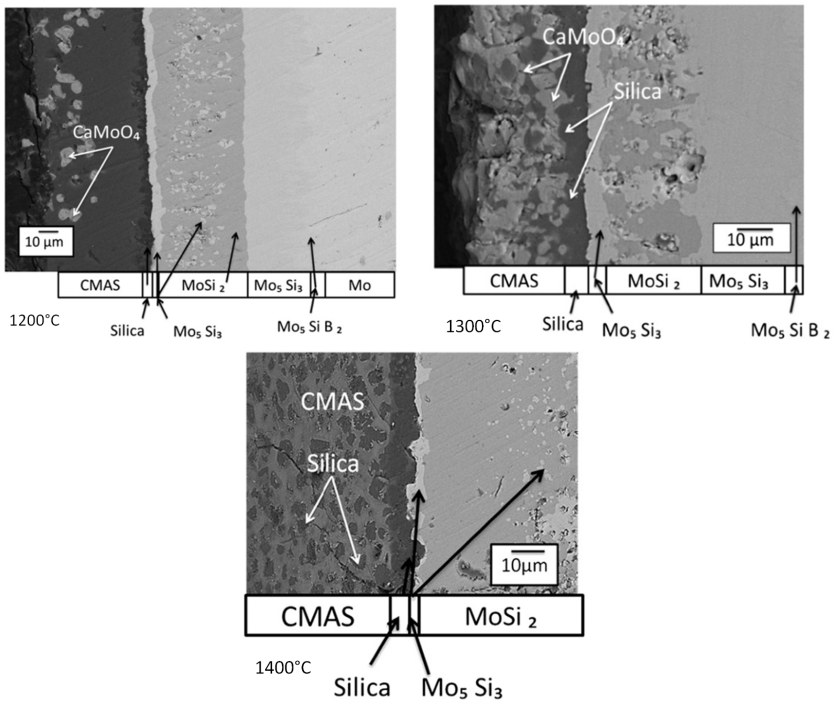

Figure 2.28: Sample cross sections showning interaction between CMAS and Mo-Si-B coatings at 1200 (left), 1300 (right), and 1400℃(bottom). All are after 25 hours of exposure. [32].

2.3 Silica, Borosilicate, and other Glasses

The application of glass science, specifically borosilicates, to Mo-Si-B materials has received little attention even though the borosilicate behavior is critical to the oxidation resistance.

Based upon the studies of Mo-Si-B oxidation, the role of the borosilicate can be generalized into two aspects: formation of initial surface layer and subsequent degree of oxidation protection. The controlling properties of the borosilicate include viscosity, permeability, diffusion, solubility of various species, and any tendency for crystallization/devitrification. All these properties are highly dependent upon the glass (or melt) structure which, for borosilicates, is not as well understood as the pure silica and boria end members.

2.3.1 Structure of Silicates, Borates, and Borosilicates

The atomic structure of amorphous silica is composed of highly polymerized, corner shared SiO_4^{2-} tetrahedra. The high Si-O bond strength and atomic density of this structure results in a very high viscosity with a glass transformation temperature (T_g) of pure, amorphous silica found to be around 1200℃ though viscosity measurements at these temperates are challenging [31]. In contrast, pure boria has a low T_g and a structure based upon trigonal-planar BO_3^{3-} [121]. The BO_3 units link into hexagonal boroxyl rings that are joined through B-O-B linkages on every boron atom [59]. This structure has low packing efficiency, giving free volume for easy rotation of the boroxyl rings and thus relatively low viscosity.

The fundamentally different atomic structures of the silica and boria liquids would suggest liquid-liquid immiscibility in their binary system. Indirectly, the results of Riebling [93] on the compositional dependence of density and viscosity and Boike et al. [9] on the thermodynamic activities of boria and silica support the conclusion of two separate liquids. However, this has not consistently been observed directly [50]. These authors do note the potential difficulties in obtaining and observing the equilibrium structure of pure borosilica due to both the sensitivity to impurities and the very high viscosity of pure silica acting as a kinetic hindrance [9].

One borosilicate system that has received considerable study is that of the Pyrex/Duran type commercial glasses. These glasses, which contain approximately 12% B_2O_3, 4%Na_2O, and 1.5%Al_2O_3 balanced with silica, can be understood as being composed of two dissimilar liquids, the fractions of which depend upon the degree of boria charge compensation [126, 105]. The coordination and bonding of boron can convert from the trigonal BO_3 to

tetrahedral BO_4 when charge compensated by a glass modifier such as sodium. This is the same as the integration of aluminum into a silica structure (charge compensation allowing for AlO_4 tetrahedra). The tetrahedral BO_4, and AlO_4, are more compatible with the silicate type structure and are instrumental in common, well behaved glasses. In the Pyrex/Duran boroaluminosilicates, sodium first compensates the AlO_4 and then the boron, resulting in around one quarter of it converting to BO_4 [105].

While typically considered stable, the Pyrex/Duran glasses can slowly devitrify with cristobalite precipitation at temperatures between 700 and 1000℃ [56]. Gupta and Jean investigated this process using a mixture of borosilicate and high silica glass powders [41]. They found the cristobalite to first form at the interface between the two glass compositions and then grow into the high silica glass particles at a rate controlled by the transport of sodium in the borosilicate glass [56]. The presence of the glass modifier (sodium or potassium) at the interface between the two glasses allowed for local formation of cristobalite, a reconstructive process that is typically rate limited by the breaking of O-Si-O linkages. Additionally, due to the low solubility of these ions in cristobalite, the borosilicate allowed for their transport to the continuously moving devitrification front by a complex dissolution and precipitation mechanism between the borosilicate and high silica glasses. The authors also identify Al_2O_3 and Ga_2O_3 additions as a way to kinetically bias the system away from devitrification as these species diffuse into and stabilize the interfacial reaction layer more quickly than that layer can devitrify [56].

As previously mentioned, the structure of borosilicates is sensitive to impurities and additives. With regard to the Mo-Si-B materials here, the effect of transition metals is most relevant. In general, the transition metal oxides have limited solubility in silica type liquids and tend to have large composition ranges of phase separation [50]. In borosilicates, the results of Chanmuang et al. are informative. Inspired by the similarly low thermal expansions of Kovar (Fe-Ni-Co alloy) and boroaluminosilicates of the Pyrex/Duran type, the authors investigated the structure and strength of joints between the two [19]. After a short oxidation of the Kovar to develop an oxide surface, bonding of the glass was done either in air or vacuum. The interfaces are shown in Figure 2.29 with the left image corresponding

to the join made in air while the right image is for the vacuum bonded. Although an iron oxide surface was present in both approaches prior to bonding, a FeO interlayer remained only in the air bonded case, along with phase separation of the borosilicate and dendritic fayalite (iron silicate), all features missing in the vacuum bonded material [19]. During bonding in air, a significant amount of iron dissolved into the glass inducing both phase separation into iron rich and poor region and further crystallization of fayalite within the iron rich glass phase. Although the preexisting iron oxide also dissolved during vacuum bonding, its concentration in the borosilicate never exceeded the single phase solubility limit and thus no phase separation or devitrification was observed. The dramatic difference between these two cases indicates the sensitivity of borosilicates to transition metal oxides.

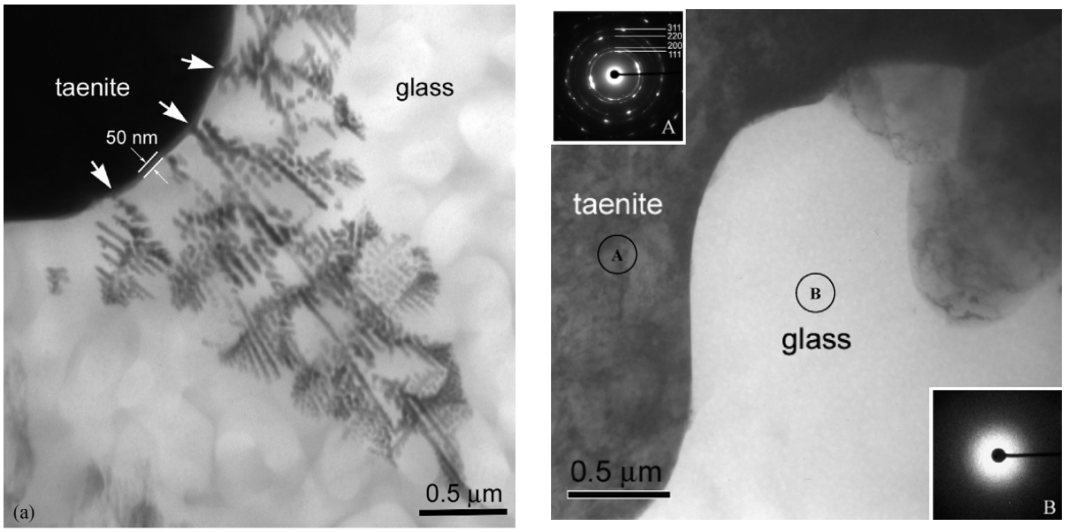

Figure 2.29: Transmission electron microscopy images of air bonded (left) and vacuum bonded (right) Kovar to borosilicate joints. Taenite is the Fe-Ni phase of Kovar. The FeO interlayer, dendritic fayalite, and phase separation in the glass on the left are not present in the vacuum bonded case [19].

2.3.2 Silicate Viscosities

High temperature viscosities have been measured on many silicate liquids and glasses by researchers with interests varying from glass science and traditional glass making to geology and vulcanology. Between the experimental difficulty of these high temperature measurements and the structural variations within the liquids, as described above, significant variations exist between the results of different researchers. Comparative results can be drawn

that are relevant to Mo-Si-B materials.

The Mo-Si-B materials which have shown oxidation resistance at temperates above 1100℃, reviewed in Section 2.2.3, form borosilicates with silica fractions above 60%. This differs from most common glasses which have silica contents below that value. As shown in Figure 2.30 the silica fraction has a profound influence upon the high temperature viscosity [117]. Thus the majority of investigations into silicates at similar temperatures to Mo-Si-B oxidation are on liquids with viscosities that are orders of magnitude different.

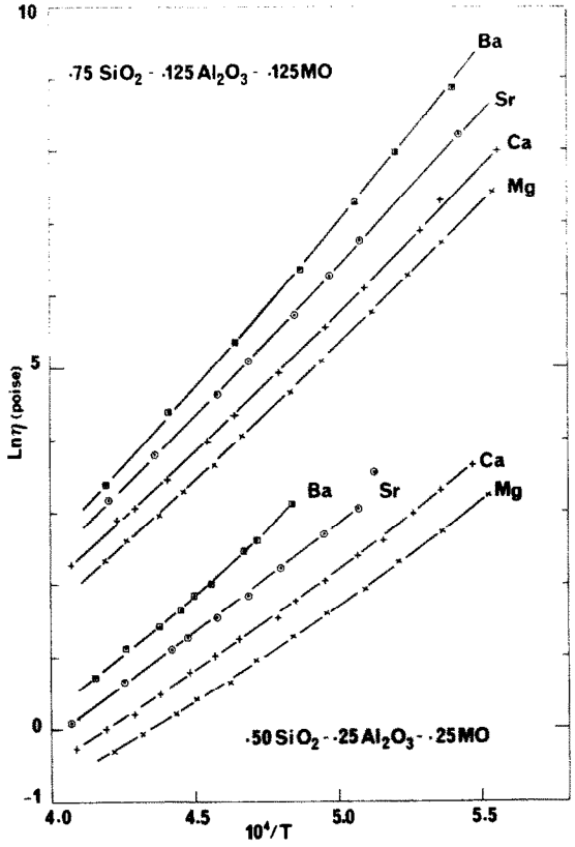

Figure 2.30: Temperature dependence of viscosities for various ternary silica-alumina systems grouped by total silica fraction.[117].

The Pyrex/Duran type commercial glasses are the closest in both silica and boria content to the borosilicate generated during Mo-Si-B oxidation, however, the charge compensation by sodium, and therefore network forming behavior of alumina and boria make this system significantly different. The most directly comparable viscosity measurements are shown in Figure 2.31 and were drawn from a number of sources [118, 31, 117] by Middlemas who

also fit the trends [77]. Given the structural uncertainties of borosilicates and the volatility of boria, discussed in Section 2.3.5, application of these results to Mo-Si-B oxidation is challenging. However two important conclusions can be drawn. First, the high temperature viscosities are very high, within two orders of magnitude to that of the multi-decade pitch-drop experiment ($2.3 \times 10^8\ Pa \cdot s$) [34], itself considered "enormous" when compared to common fluids. Second, as any boria evaporates, the surface borosilicate viscosity can change dramatically, nearly three orders of magnitude at 1300℃ as the composition changes from 30% to 10% boria.

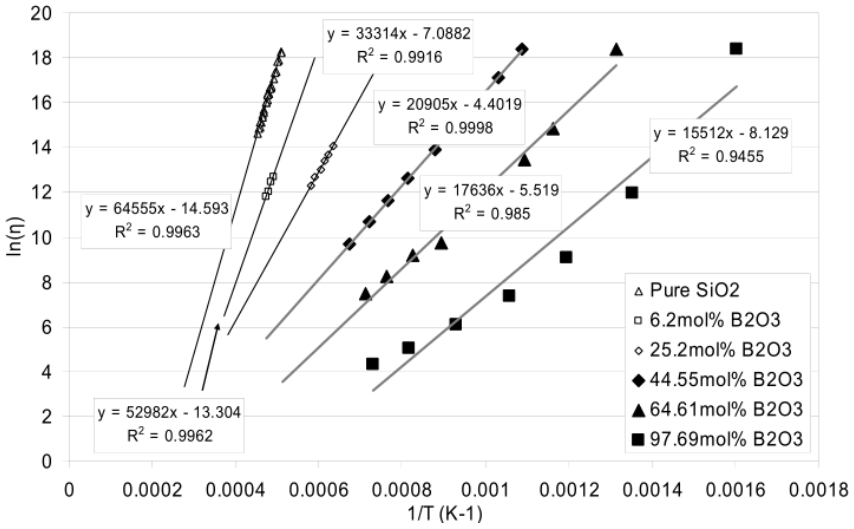

Figure 2.31: Borosilicate viscosities at varying temperatures and for different compositions from [77] with data compiled from [118, 31, 117].

2.3.3 Oxygen Permeability and Diffusion

Formation of a borosilicate coating is not sufficient to guarantee oxidation resistance of Mo-Si-B materials. The coating must also be a barrier to oxygen transport between air and the substrate. Lamkin and Riley [65] reviewed the oxygen transport through a wide variety of silicate liquids, glasses, and crystalline polymorphs. On the left of Figure 2.32 is shown the temperature-diffusion regimes for these different silicates and includes both atomic/ionic diffusion (D_O) and molecular permeation (D_{O_2}). Schlichting [101] measured the oxidation of silicon coated with various binary silicates, including silica rich borosilicates, and calculated the oxygen diffusion of those coatings as at different temperatures, Figure 2.32 on the right.

It can be seen in both of these works that high silica systems have low oxygen transport at elevated temperatures allowing them to behave as oxygen barriers, consistent with the conclusions of Birks and Opila [8, 89].

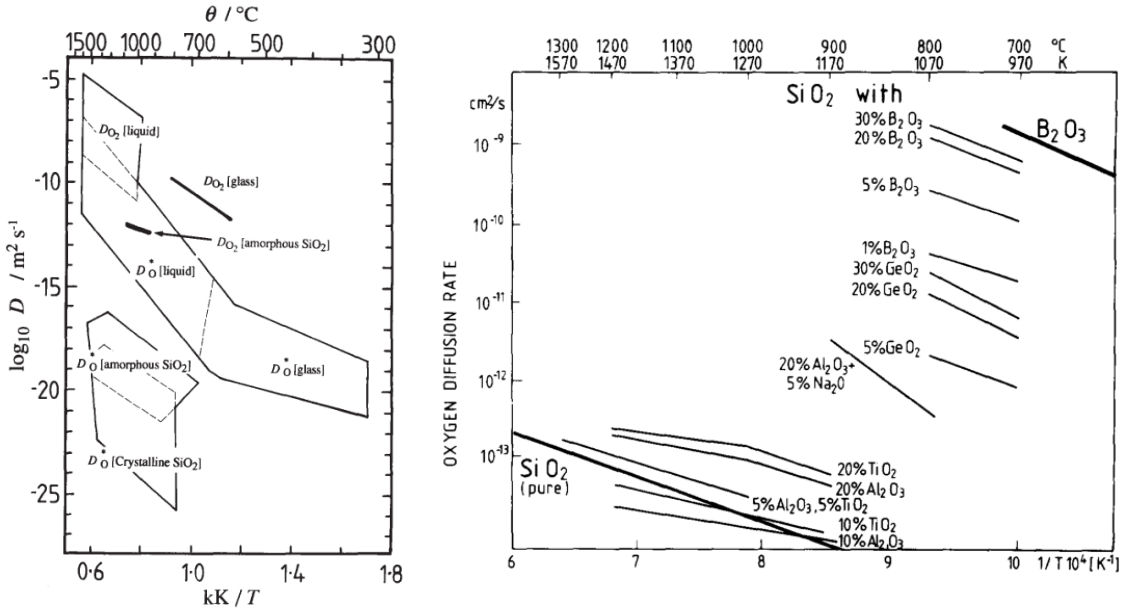

Figure 2.32: Oxygen diffusion and permeation through liquid, glass, and crystalline silicates from Lamkin and Riley [65] on the left and Schlichting [101] on the right.

2.3.4 Molybdenum in Glasses

The only extensive investigations of molybdenum species within borosilicate glasses were done in the interest of vitrification of nuclear waste. The solubility of molybdenum, as the MoO_4^{2-} molybdate species, in silicate glasses is very low, less than 1wt% in alkali boroaluminosilicates [16]. This has been explained by Pauling's stability rules in which the sum of bond valencies for a Mo-O-Si linkage (required for integration of molybdenum into the silicate network) would overbond the oxygen atom [17]. Spent nuclear fuel has a significant molybdenum content leading its solubility and precipitation behavior during vitrification to limit the waste loading [18]. Specifically, the formation of water soluble, mixed alkali molybdates/chromates restricts the viability of vitrification for long term waste storage [16].

The works of Martineau et al. and Caurant et al. have identified molybdenum segregating to depolymerized regions in liquid-liquid phase separated borosilicates [73]. Competition for alkali and alkaline earth ions results in sodium and calcium also segregating to the molybdate liquid at the expense of charge compensating BO_4 network units [18]. Figure 2.33 shows this structure schematically [17]. These researchers found that increasing the boria content shifted the distribution of sodium ions and changed the composition of the molybdenum regions away from Na-molybdate and towards Ca-molybdate which is a preferred phase due to its lower water solubility [17]. Chouard et al. identified a reduction in liquid-liquid phase separation and devitrification in molybdenum containing borosilicates with high neodymium contents. This was due to the neodymium ions segregating to the depolymerized regions (or regions high in non-bonding oxygen) along with the molybdates. The presence of both species within these regions increased the local chemical disorder and thus confused the devitrification process upon cooling [20].

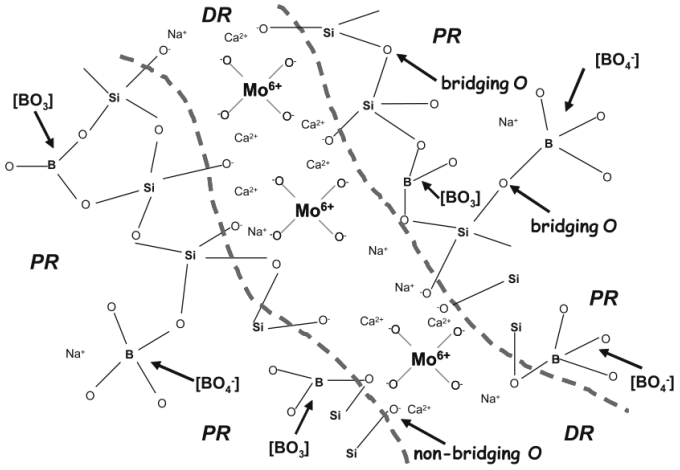

Figure 2.33: Schematic of molybdenum location within a soda-lime borosilicate glass. PR are polymerized regions of bridging SiO_4 and BO_4 units while DR are depolymerized regions of a Na/Ca molybdate liquid [17].

2.3.5 Volatile Losses from Glass Melts

Considering the dependence of both viscosity and oxygen transport of borosilicates on the boria content, the boron volatility during oxidation of Mo-Si-B materials can have a

profound effect, however it has received little more then mention during research into Mo-Si-B. This is due to the challenges inherent in measuring such a light element from a thin surface layer in a refractory application. The behavior of pure boria and the results of studies into tradition glass melt processes can give insight into the impact of boron evaporation on Mo-Si-B oxidation resistance.

Many species can participate in the volatilization of boria including: BO, BO_2, B_2O, B_2O_2, and B_2O_3 itself. The temperature and oxygen partial pressure dependence of these have been studied by a number of researchers [111, 108, 66]. At the temperatures and environments relevant to Mo-Si-B materials, hydrated species also become important. In fact the HBO_2 species has the highest equilibrium partial pressure under many such conditions [75, 54]. Figure 2.34 shows the vapor pressures of the three most significant species over boria in 1 bar oxygen with 20 ppm water vapor.

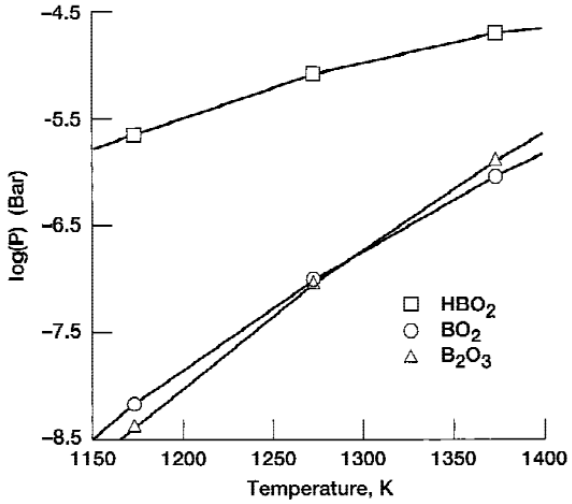

Figure 2.34: Equilibrium vapor pressure of the three primary species over boria in 1 bar oxygen and 20 ppm water vapor [54].

The volatile loss of species such as boron is dependent upon many factors beyond the equilibrium partial pressure including the composition, temperature, and diffusivity of both the source and gas as well as the gas velocity and turbulence [119]. Many of these factors are captured in Figure 2.35 which is a schematic of evaporation from a glass melting process. In both that situation and protective oxides in combustion environments, the kinetics of the volatile loss is related to the driving force of the evaporation reactions (including the

product and reactant pressures) and the gas velocity raised to a power between 0.5 and 0.8 for laminar and turbulent flows respectively [88].

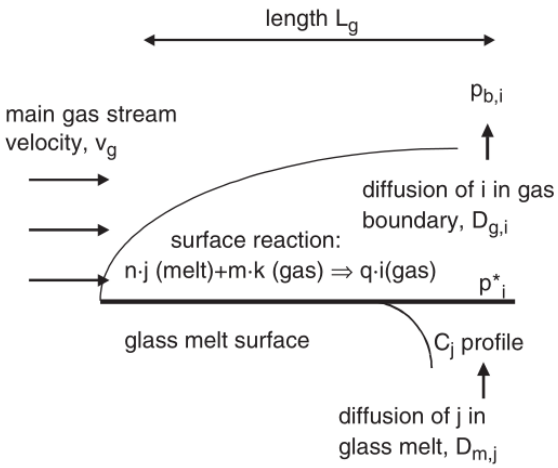

Figure 2.35: Schematic of the volatile loss from a gas flow over a glass melt. The melt species j, such as boria, reacts with a gas species i, such as water vapor, to form a volatile produce, such as HBO_2 [119].

In measurements of boron and sodium evaporation from glass melts, an additional factor can often become dominant. Depletion of these species from the silicate greatly raises the viscosity and lowers the diffusivity resulting in a high silica skin that acts as a barrier between the air and melt bulk. After the initial evaporation to form this skin, diffusional transport through it becomes rate limiting [5] This has been observed in a number of commercial and model glass melts [120, 86, 26].

2.4 Additional Relevant Systems

2.4.1 Crystalline Molybdates

The potential improvement in Mo-Si-B oxidation by minor transition metal additions [107, 124] and the identification of molybdates within those samples raises questions as to the structure of the molybdate compounds. Strobel and Le Page identified hexagonal molybdates of manganese, iron, cobalt, and nickel of the $M_2Mo_3O_8$ type as well as some crystals of $MMoO_4$ and M_2MoO_8 [113]. Others have further studied the $MMoO_4$ type compounds for a variety of applications. Figure 2.36 shows the high temperature stability ranges for cobalt, manganese, and nickel molybdates as a function of oxygen pressure [53, 97, 52]. During

the oxidation of Mo-Si-B materials, most of these oxygen concentrations would likely exist within the oxidation layers.

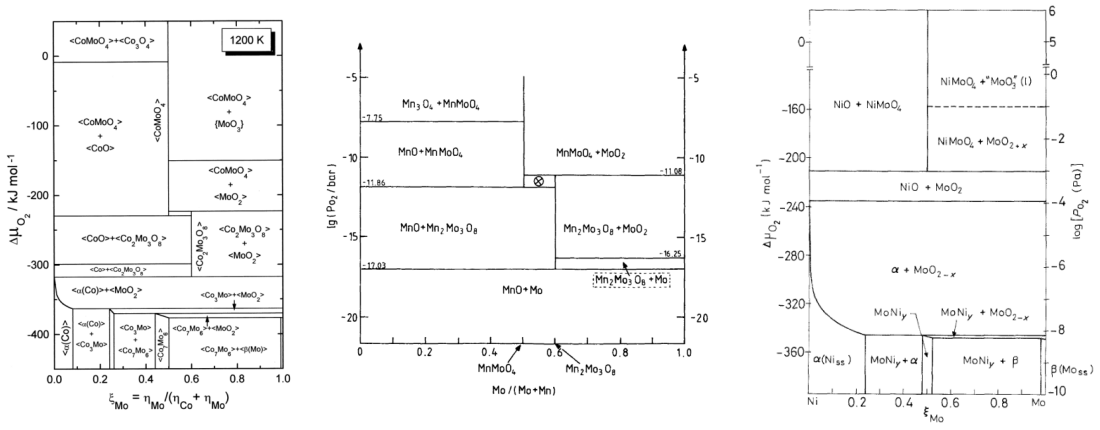

Figure 2.36: Stability diagrams for cobalt, manganese, and nickel molybdates as a function of oxygen potential. Cobalt and manganese are shown for 1200K while nickel is at 1373K [53, 97, 52].

Most of the molybdates, including ones not listed above, have melting points considerably higher than MoO_3, some even higher than the boiling point of MoO_3 (such as $CaMoO_4$, MP of 1445℃). The effect of these compounds upon the equilibrium MoO_3 vapor pressure has received little attention due to limited applications. One application however, is in the addition of molybdenum to tool steels. Chychko et al. investigated magnesium and calcium molybdates as potential additives to electric arc furnace production of steel which would not have as high a loss as pure MoO_3 [21]. Figure 2.37 shows their thermogravimetric results for $CaMoO_4$, line 1, and $MgMoO_4$, line 2, during heating to 1300℃ in argon. They found that calcium molybdate has a far lower evaporation rate than either magnesium molybdate or pure MoO_3.

2.4.2 Alkaline-Earth Aluminosilicates

Reactions between silica and water vapor at temperatures around 1500℃ and above is a serious challenge for many materials including SiC ceramic matrix composites [33]. Investigations into protective, environmental barrier coatings (EBC's) for these materials has potential application to αMo matrix Mo-Si-B due to similar thermal expansion coefficients of SiC and molybdenum, both around 5×10^{-6}/℃.

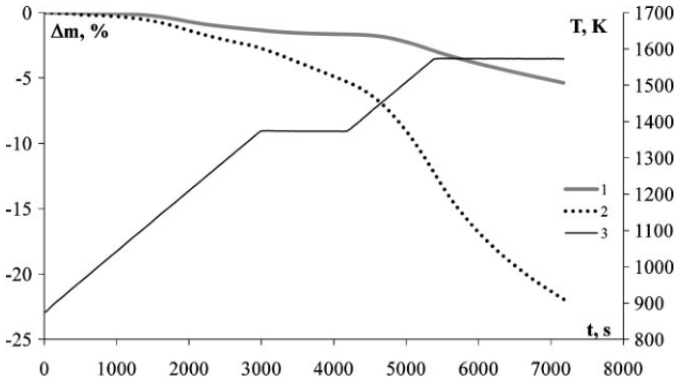

Figure 2.37: Thermogravimetric analysis of $CaMoO_4$, line 1, and $MgMoO_4$, line 2, in argon. Line 3 indicates the temperature [21].

Eaton et al. and Lee et al. investigated the use of strontium-barium aluminosilicate (BSAS), yttrium silicate, and various rare earth silicates as coating on SiC [33, 68]. While some of the rare earth silicates were found to have the greatest protection, their high cost limits their application. The BSAS coatings, though not as resistant to water vapor, did show good protections. This material is both easier to produce using traditional powder processing (fully react by 1200℃) and is air stable to at least 1500℃ [4]. BSAS is a solid solution between strontium aluminosilicate, $SrAl_2Si_2O_8$, and barium aluminosilicate, $BaAl_2Si_2O_8$, and in the monoclinic polymorph. An interesting advantage to this system is that the thermal expansion can be adjust by varying the strontium to barium fraction [4].

CHAPTER 3

EXPERIMENTAL METHODS

The experimental methods described below are divided into two sections, processing of the Mo-Si-B composites and characterization. Samples were produced utilizing the powder processing techniques developed by Middlemas [77] with the exception of modifications to the firing and sintering procedure, which is covered in detail in Chapter 5. Development of compositions for oxidation resistance involved both varying the silicon and boron fractions in the base Mo-Si-B composite as well as minor additions of other elements. Standard metallographic and scanning electron microscopy (SEM) techniques were employed for microstructural characterization and analysis of oxidized samples.

3.1 Composite Production

3.1.1 Raw Materials

The base Mo-Si-B composites were produced from the same raw materials used by Middlemas and detailed particle size distributions and surface area measurements can be found within his work [77]. Table 3.1 lists the raw powders with their purity, size, and oxygen content specifications. The molybdenum powder grade, LTS, is intended for powder processing and has greater sinterability than standard molybdenum powders. However, the high surface area to drive sintering also increases the oxygen content. The specifications reported are for the as-received powder which, it is believed, accumulated additional oxygen during subsequent processing. Improvements in the hydrogen de-oxidation portion of the firing and sintering process are able to mitigate the increased oxygen content, see Chapter 5.

Numerous modifications were made to the base Mo-Si-B compositions through various minor additions. These included the transition metals iron, nickel, cobalt, yttrium, and manganese and an oxide compound $SrAl_2Si_2O_8$ (SAS). With the exception of manganese, these were introduced into the powder batch as fine oxides. Other than yttria and SAS, the oxide was reduced during firing. Table 3.2 shows the particle sizes and purities of these

Table 3.1: Powder specifications for base Mo-Si-B composite formulation

Material	Supplier - Grade	Purity [wt%]	Particle Size [μm]	Surface Area [m^2/g]	Oxygen Content
Mo	Climax - LTS	>99.9%	0.5-1.7 FSS	1.5 - 4 BET	<1.5wt%
Si_3N_4	UBE - SN-E03	99%	0.5 d_{50}	4.0	0.82wt%
cBN	Advanced Abrasives - #0.5	-	0.54 d_{50}	11.8	0.92wt%

additions except for SAS. The strontium aluminosilicate (SAS) was produced separately, ground, and then added to the Mo-Si-B slurry. Table 3.3 lists the powders used in producing SAS. These were spray dried in an acetone slurry with 3wt% PMMA as a dispersant in the same manner as the Mo-Si-B composites described in the next section. Spray dried granules were fired in air with holds of 4 hours at 400℃ for burnout, 12 hours at 925℃ for calcining, and 12 hours at 1200℃ for reaction [4]. The furnace heating and cooling rates were $4^{\circ C}/_{min}$. The resulting powder was fully reacted to $SrAl_2Si_2O_8$ with little sintering allowing for easy grinding and introduction into the Mo-Si-B slurry.

Table 3.2: Powders for composition modifications

Material	Supplier	Grade	Purity	Particle Size
Fe_2O_3	AEE	FE-601	99.9%	1-5μm
NiO	AEE	NI-601	99.8%	-325 mesh
Co_3O_4	AEE	CO-601	99.9%	-400 mesh
Y_2O_3	Inframat Advanced Materials	39N-0802	99.95%	30-50nm APS
Mn	AEE	MN-101	99.5%	$< 10\mu m$

Table 3.3: Powders for $SrAl_2Si_2O_8$ production

Material	Supplier	Grade	Purity	Particle Size
$SrCO_3$	Alfa Aesar	14343	99%, 1% Ba	-325 mesh, typical 1μm
Al_2O_3	Sumitomo	AKP-20	99.99%	0.57μm d_{50}
SiO_2, Fumed	Alfa Aesar	89709	99.5%	-325 mesh, 5 m^2/g S.A.

3.1.2 Slurry Formulation

A single slurry formulation was used for all the compositions produced and is based upon the work of Middlemas [77]. The acetone slurry was batched to 10% by volume solids excluding

the organics polymethylmethacrylate (PMMA) and stearic acid. These organics were added at 3% PMMA and 0.3% stearic acid by weight of the solids. The PMMA acted as both a dispersant in the slurry and a binder for the spray dried powder. The stearic acid was used as a lubricant to reduce pressure gradients during green body formation. After batching, slurries were mixed and deagglomerated on a roller mill in high density polyethylene jars with 3mm diameter, 99.8% alumina balls. Milling was done overnight, 16 to 18 hours, up to the moment they were spray dried so as to limit any powder settling.

Where possible, fresh ACS grade acetone was used to minimize potential water contamination. The PMMA was Elvacite 2008 produced by Lucite International. It is a low molecular weight (approximately 37,000 $^{g}/_{mol}$) methyl-methacrylate primarily used in low viscosity lacquers and inks. For the application here, it is an effective stearic dispersant in acetone and a binder for the powders produced during spray drying. Additionally, as determined by Middlemas [77], it decomposes into volatile species between 350 and 400°C in inert or reducing atmospheres thus giving a clean "burnout" of the green body during firing. The stearic acid was 98% purity supplied by Alfa Aesar (product number A12244). It is a well known dry lubricant and is soluble in acetone.

3.1.3 Spray Drying

Homogenous granules of the Mo-Si-B composite precursor material were produced from the acetone slurry by spray drying with ultrasonic atomization. For the wide range of compositions studied in this work, relatively small slurry batches, typically 20ml, were used. A single syringe pump (New Era Pump Systems, Wantagh, NY) delivered the slurry to the spray dryer at a constant $700^{ml}/_{hr}$. Atomization of the slurry was done with an ultrasonic nozzle (Sono-Tek, Milton, NY) operating at 48kHz. The ultrasonic vibration of the nozzle creates a standing wave in the slurry on the nozzle tip. At a high enough amplitude, the wave peaks pinch off due to capillarity and droplets fall away from the nozzle as a low velocity spray. For spray drying, the ultrasonic nozzle was placed at the top of a heated chamber wherein the droplets dried as they fell due to the evaporation of the acetone. The chamber was held just below the slurry boiling point for rapid, and

uniform, acetone evaporation, and had a constant nitrogen purge flowing at 2 SCFM to prevent acetone vapor accumulation.

During spray drying, the atomized droplets dried before falling to the bottom of the chamber, where the granules were collected. These granules were screened through 100 mesh to give a homogeneous and flowable powder well suited for dry pressing. For the small (20ml) batches, the typical yield was 60 to 70% of the batched solids with around 8% being >100 mesh and the remainder as line losses in the tubing, syringe, and mill jar. A few larger batches were produced and had a similar fraction of greate than 100 mesh but higher yield (80+ %) due to similar absolute line losses. Figure 3.1 shows typical spray dried granules. The granules were between 10 and 100μm in diameter with an average of around 30μm, which is in good agreement with the measurements of Middlemas [77].

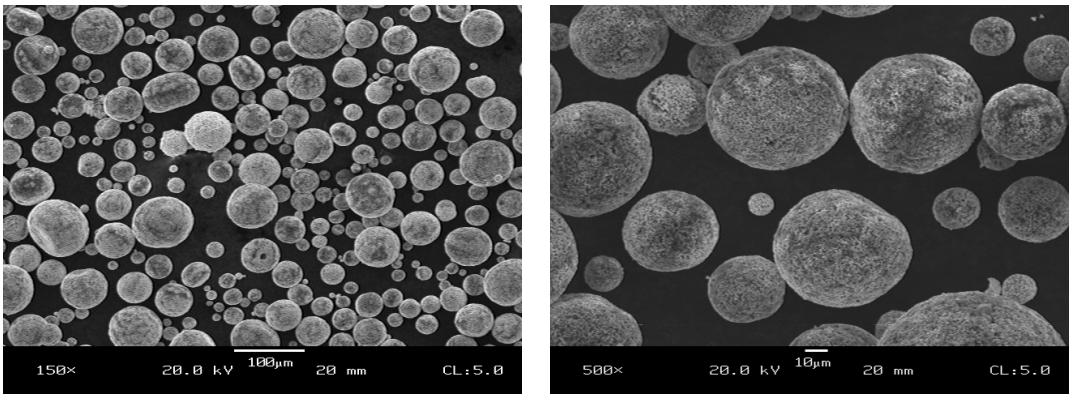

Figure 3.1: Typical ultrasonically atomized and spray dried powder of Mo, Si_3N_4, and BN with PMMA binder.

3.1.4 Consolidation and Firing

Standard powder processing techniques for green body formation, such as pellet pressing and cold isostatic pressing, were employed effectively due to the spray dried granules' relatively coarse size and spherical shape. The majority of samples were produced by axially pressing round pellets of 13mm diameter and 2-3mm thickness using a floating vacuum die lubricated with an acetone - stearic acid solution. Pressing to 450 MPa resulted in green densities around 55% of the theoretical Mo-Si-B density.

Firing of the Mo-Si-B composites, as either a green body or loose powder, encompassed

six different reaction stages: dehydration, de-binding, de-oxidation, nitride decomposition, intermetallic reactions, and sintering. Initial firings were done with a two step cycle having holds of 4 hours at 400℃ and 6 hours at 1600℃ for binder removal and sintering respectively. Heating and cooling rates were 3 and 5 $^{\circ C}/_{min}$ respectively and the entire cycle was done under titanium-gettered Ar-10%H_2 flowing at $150^{cc}/_{min}$. However, this procedure was found to be insufficient for Mo-Si-B composite due to not fully completing some of the six stages. Improvements in the firing process addressed many of these as individual steps and are covered in Chapter 5.

Due to the various changes made to the firing process, a number of furnaces were used. Two $MoSi_2$ tube furnaces (Micropyretics Heaters International, Cincinnati, Ohio and MTI Corporation, Richmond, California) fitted with alumina tubes of diameters between 1in and 60mm were used for the high temperature firings. Additionally, an FeCrAl wire wound tube furnace (MTI Corporation, Richmond California) was used for some separate de-binding. All firings were done in titanium gettered atmosphere using a Centorr getter (Centorr Vacuum Industries, Nashua New Hampshire). The atmospheres were either pure Argon or Ar-10%H_2, both supplied by AirGas Products, and metered by a rotameter or a mass flow controller (GFC17, Aalborg, Orangeburg, New York). The firings were done at 1 atmosphere and used an oil double bubbler to prevent air entering from the exhaust. Additionally, a hygrometer (Cermet II, Kahn Instruments, Wethersfield, Connecticut) was placed in the effluent gas stream to measure the water vapor generated during sample de-oxidation.

The final firing process involved separate de-binding (2 hours at 400℃ under dry argon) before firing in the setup shown schematically in Figure 3.2. The furnace temperature, gas flow rate, and dew point were logged during the entire run (typically 18 hours) with a DI-145 analog-to-USB converter (DataQ Instruments). Hypothetical time, temperature, and dew point traces are shown in Figure 3.3 for an idealized two step firing with hydrogen reduction and sintering holds. The peak in the dew point is associated with the water vapor generated during hydrogen de-oxidation of a metal oxide. Equation 3.1 allows for conversion of the measured dew point into the water vapor partial pressure [1]. Combined with the mass flow controller data, and assuming ideal gas behavior, the water vapor flow rate was calculated.

This was then numerically integrated over the furnace run to give the total water generated. During the firing process development, reported in Chapter 5, another representation of this data was useful. Plotting the cumulative, normalized water generation against the furnace temperature clearly showed during which furnace steps de-oxidation occurred. Firings in which >90% of the total water was generated by the end of the de-oxidation step were considered well optimized.

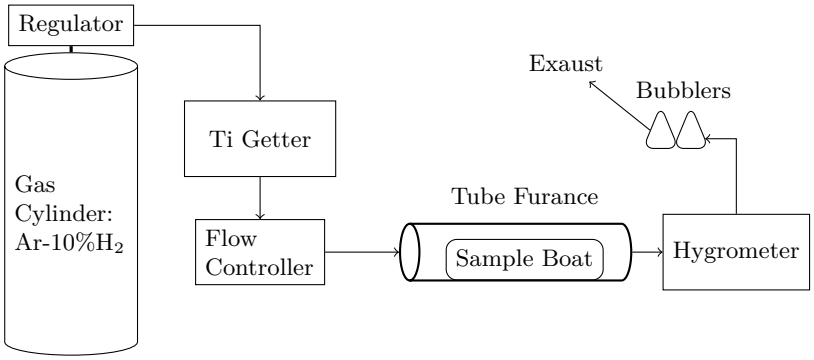

Figure 3.2: Schematic of the final furnace setup used for pressureless sintering of Mo-Si-B composite pellets.

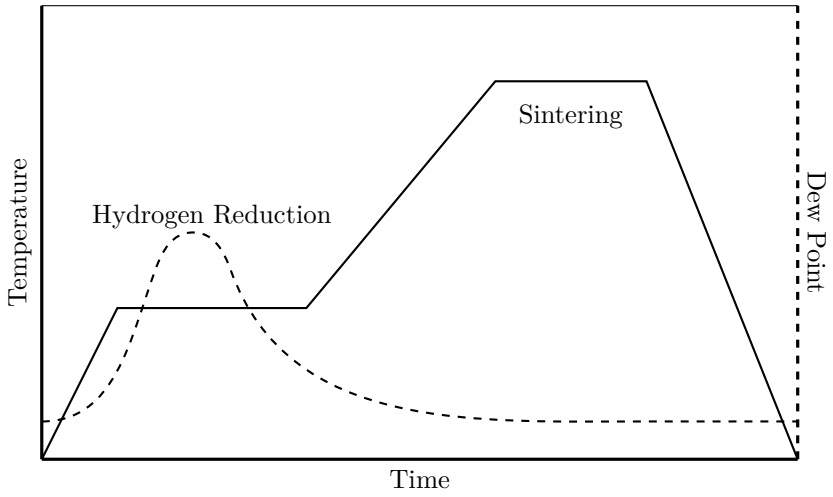

Figure 3.3: Idealized temperature and dew point profiles for a two step firing of Mo-Si-B composite pellets.

$$T_{dew}[^{\circ}\mathrm{C}] = -273.15 - \frac{6151.9}{\ln(P_{H_2O}[atm]) + 3.6245} \tag{3.1}$$

A few samples were consolidated by hot isostatic pressing (HIP) after a prefiring to 1300℃ following the above de-binding and de-oxidizing procedure. The HIP runs were

done by American Isostatic Presses (Columbus, Ohio). A cycle of 6 hours at 1300℃ under 45ksi argon was used. Both steel and titanium cans were used with a variety of can filling procedures, the details of which are the subject of Section 5.3.

The density of the consolidated samples was calculated by Archimedes method using water. Dimensional shrinkages and weight losses were also tracked for run-to-run consistency and back verifying weight losses from nitride decompositions and de-oxidation. Sample surface appearance was found to be a useful indicator of the furnace tube condition. Small cracks in the alumina tubes could not always be identified at room temperature but still opened during the firing, introduction atmospheric oxygen. Although not enough to form MoO_3, the surface MoO_2 would color the samples yellow.

3.2 Characterization and Oxidation Testing

3.2.1 Microstructural Characterization

The microstructures of Mo-Si-B composites were studied by standard metallographic techniques and scanning electron microscopy (SEM). Both as-fired and post-oxidation pellets were sectioned in half using a high speed diamond saw to reveal both the internal microstructure and any near surface variations. Prior to sectioning, the oxidized samples were encased in two part epoxy to preserved the surface structures. The sectioned samples were then hot mounted in phenolic epoxy for grinding and polishing. A standard series of SiC grinding papers and diamond polishing suspensions were used before final polishing with colloidal silica for 3 minutes.

Imaging of the polished samples was done in an Amray 1810 scanning electron microscope (SEM) using both secondary and backscatter modes and fitted with a PGT energy dispersive spectrometer. The oxidation samples were first sputter coated with gold to ensure a conductive surface. In the oxidized sample cross sections, the phase contrast between the bulk and borosilicate was sufficiently large for imaging in secondary mode, however differentiating the bulk phases (αMo, A15, and T2) needed to be done in backscatter mode. Comfirmation of the constituent phases for select samples was done by x-ray diffraction (XRD) performed by Will Daloz (Georgia Institute of Technology).

3.2.2 Oxidation Resistance

The oxidation of Mo-Si-B composite samples was done in laboratory air in one of three resistive furnaces. Two $MoSi_2$ furnaces were used for temperatures above 1000℃ while a single Kanthal wire furnace (Paragon Industries, Mesquite, Texas) was used at 800℃. One of the high temperature furnaces (Keith Company, Pico Rives, California) was a bottom loading box furnace with limited air circulation which prompted additional testing in a large tube furnace (GSL-1600-80, MTI Corporation, Richmond, California). For oxidation under forced air, a 3" diameter bilge fan was placed at one end of the tube furnace.

For all the oxidation testing, the furnace was preheated to the target temperature before introducing the sample. Sectioned pellets were supported on platinum wire and placed upon refractory trays. The trays were inserted directly into the hot furnace to limit transient heating effects. The oxidation was interrupted at various points to weight and image the samples. At these points the sample trays were quickly removed from the furnace, placed upon refractory brick, and the samples transfered to a cool refractory tray. Total sample heating and cooling times are estimated at 30-45 seconds and 2 minutes respectively based upon when the samples appeared to glow the same as the surrounding furnace for heating and could be touched upon cooling. With respect to the total oxidation time, the interruptions were done at 10, 30, and 90 minutes followed by a final 18.5 hour portion giving a total oxidation time of 20 hours.

CHAPTER 4

FRAMEWORK FOR COMPOSITE DEVELOPMENT

The development of Mo-Si-B composites is a balance between strongly competing material optimizations. The best performing compositions and microstructures are very different when designed for oxidation resistance verses mechanical properties, both of which differ considerably at high and low temperatures. Identifying, understanding, and optimizing all these factors is well beyond the scope of this dissertation. The research here is focused on developing improved powder processing, the role of composition in the oxidation resistance at 1300℃, and the mechanisms by which oxidation resistance develops.

Due to the strongly opposed structure-property optimization of Mo-Si-B composites for mechanical verses oxidation performance [69], a framework is necessary to guide development of one set of properties without loosing sight of the others. To that end, this chapter will lay out the competing material optimizations and provide the framework within which the powder processing and oxidation resistance was developed. Key to this are assumptions made about the necessary conditions for toughness and high temperature strength of Mo-Si-B composites and their application to gas turbines, specifically the operating temperature and use of coatings. With these assumptions, the development framework allows separation between the oxidation and mechanical aspects of the Mo-Si-B material, generally divided between the metallic, αMo matrix and remaining intermetallics respectively. Because of this separation, these materials are referred to here as metal matrix composites.

First and foremost of the competing Mo-Si-B optimizations are the opposing material design directions for oxidation resistance and toughness, considering, for example, the question of optimal silicon content. Regardless of the temperature, higher silicon contents will both improve oxidation resistance and lower fracture toughness. In fact, the extremes of this trade off are well known engineering materials. $MoSi_2$ heating elements are exceedingly brittle but oxidation resistance up to 1600℃ while the structural Mo alloys (low-carbon

arc cast, oxide dispersion strengthened, and TZM/MHZ) have high toughnesses at high temperatures but a complete lack of oxidation resistance above 400℃.

Furthermore, considering different temperature ranges only reveals additional material trade-offs. The Si/B ratio is the primary controlling factor for oxidation resistance at differing temperatures. For example, pure T2 (Mo_5SiB_2) is oxidation resistant in the temperature range of 900 to 1000℃ but generates a borosilicate too fluid to limit the oxidation processes at higher temperatures. By raising the Si/B ratio to that of Mo-3wt%Si-1wt%B, the window of oxidation resistance can be raised by around 200℃. No single composition has oxidation resistance all the way from the upper limit of MoO_2 protection, 400℃, to potential use temperatures in the 1200 to 1300℃ range.

The differing material demands over the wide range of temperatures considered exists for the mechanical properties as well. The well established trade-off between yield strength and strain to failure does exist in Mo-Si-B composites, and is exacerbated by the wide range of temperatures. High deformability at the low end is strongly related to low strengths at the upper temperatures. Perhaps the most diametrically opposed mechanical properties are toughness and creep resistance. The high temperature creep resistance has been attributed to both the high intermetallic volume fraction and silicon solid solution restricting dislocation motion [55, 114]. However, these two factors have also been specifically identified as the cause of brittle behavior below 1000℃ [70]. Development of Mo-Si-B composites with high toughness by reducing constraint from the intermetallic grains and lowering solid solution strengthening from silicon runs the risk of loosing the creep resistance also necessary for use in gas turbines.

The following approach has been taken for Mo-Si-B material design. All composites were at least 55% by volume αMo in order to maintain the continuous matrix phase needed for any potential bulk ductility. This was extended up to 60 or 65% when improved mechanical properties were deemed more significant than a higher initial weight loss on oxidation. Note that the long term oxidation resistance is believed to be far more sensitive to the silica melt composition than the molybdenum fraction of the base material. The remaining 45 volume % was split between the various phases which partake in forming an oxidation resistant

layer (these phases are all considered hard and thus are interchangeable from a mechanical behavior standpoint). The relative fractions of these phases was determined by the optimal borosilicate composition formed upon oxidation at the use temperature.

All the oxidation resistance factors were designed specifically for the peak use temperature for two reasons. First, it has been shown that once a protective layer is formed, it is still protective at lower temperatures, see section 6.2.6.3. Second, the primary need of the composite's oxidation resistance is damage tolerance during use and it is assumed that an environmental barrier coating (EBC) system will provide all the oxidation resistance under nominal operation. The primary implication of the use temperature is to specify the Si/B ratio and thus the A15/T2 ratio. Minor oxide additions, such as SAS, were a small portion of the 45 volume %, as per their content in the borosilicate. With the design for oxidation resistance contained within the composition of this 45%, subsequent material design steps for mechanical properties can be focused on the remainder. In this way the design for oxidation resistance and strength/toughness can be mostly separated along the lines of the different phases within the composite.

4.1 Composition of the Borosilicate Melt

Comparison of the silicon to boron ratios in Mo-Si-B composites (both those studies here and most published works) to the silicate viscosities given in Sections 2.3.2 shows that borosilicates involved in the oxidation resistance of Mo-Si-B are above their glass transformation temperature (T_g). Even upon loss of boria (through its evaporation), oxidation at 1300℃ will still be above the T_g of pure, amorphous silica (around 1200℃ [31]). Based upon this, the borosilicate surface layer formed during oxidation of Mo-Si-B composites is more aptly called a melt rather than a glass. Although silica rich liquids have high viscosities, they still have more kinetic mobility than a true glass and thus can suffer from phenomenon such as phase separation, devitrification, and precipitation.

Despite the complexities of the structure of borosilicate liquids (see Section 2.3.1), this research will tend to assume that those formed on Mo-Si-B composites are single phase melts. This can be justified as no borate-silicate phase separation was observed in oxidized

samples and because the size scale of most structural variations is far smaller than the mechanisms associated with Mo-Si-B oxidation. This single phase assumption, along with neglecting boria evaporation, greatly simplifies the specification of Mo-Si-B compositions. With regard to oxidation resistance, Mo-Si-B composite samples will be referred to by either their Si/B atomic ratio or a "equivalent" borosilicate. The equivalent borosilicate composition is calculated from the bulk Mo-Si-B composite assuming (1) total evaporation of molybdenum, (2) no loss of boron, (3) oxidation of remaining elements to their dominate oxide in glasses (ie. B_2O_3 or MnO), and (4) complete dissolution of these oxides into a single phase melt.

4.2 Selection of Oxidation Temperature and Conditions

The oxidation mechanism investigations and composition development for oxidation resistance in this work focused on performance at 1300℃. Selection of this temperature is somewhat arbitrary and mainly based upon a convenient overlap of the favorable mechanical properties and the upper limit for oxidation results of published Mo-Si-B composites. Additionally, 1300℃ is at least 150℃ higher than the maximum for single crystal, nickel base superalloys and thus would yield significant increases in gas turbine efficiency.

The temperature is not the only factor to consider for oxidation resistance in gas turbines. Real combustion environments contain significantly higher water vapor and somewhat reduced oxygen content depending upon how lean the combustion runs. Additionally, the gas flow velocity is very high and, for aircraft use, the duty cycles included numerous thermal cycles between the operating temperature and ambient. These last factors are not captured well by traditional TGA equipment which has limited gas flow and temperature ramping capabilities. The testing utilized in this work approximated these factors better, at the expense of accuracy and true isothermal conditions. The preferred approach for interrupted oxidation testing was done in a large tube furnace with forced air flow from a fan placed at one end. The furnace was held at temperature and the sample quickly inserted and removed after set times to both minimize transient temperature effects and capture the thermal shock behavior. Samples which were found to perform well in this oxidation testing

can be considered "robust" with respect to thermal cycling and gas flow. Finally, oxidation in laboratory air is more relevant to combustion than oxygen-argon/nitrogen mixes due to the presence of water vapor albeit less than many combustion environments.

In developing oxidation resistant Mo-Si-B composites, the framework used here is more concerned with "graceful failure" type oxidation resistance rather than the best possible resistance over thousands of hours. This is drawn from the beliefs that (1) Mo-Si-B composites will have to compromise between oxidation resistance and strength/toughness and (2) the oxidation resistance for the majority of a Mo-Si-B component's life will come from a coating system. Similar to the damage tolerance design of structural components, graceful failure during oxidation is concerned with the continued performance and predictability after damage occurs. While a coating on pure molybdenum can provide oxidation protection under ideal conditions, the presence of any damage would rapidly result in catastrophic failure from uninhibited local oxidation. Coatings on Mo-Si-B components however, can withstand damage due to the composite growing its own borosilicate to resist further oxidation. Testing is therefore focused upon exposing clean Mo-Si-B surfaces to the operating temperature, 1300℃, for moderate times. Aircraft engine components may only need to maintain performance for 100's of hours after any damage occurs, a window allowing for identification and repair.

4.3 Interaction with Coatings

The primary oxidation resistance for any Mo-Si-B composite part will come from a coating system as the coating will not have to compromise oxidation resistance in favor of mechanical properties. Therefore, a relevant question for the Mo-Si-B development framework is what the interaction might be with potential coating systems. These systems often have multiple layers filling one of three roles: environmental protection, thermal protection, or bonding between the layers. Environmental barrier coatings (EBC) must be non-reactive and have low transport of oxygen and other species. Thermal barrier coatings (TBC) are often highly porous to maintain a large thermal gradient between the substrate and hotter combustion gases. Because of limitations in compatibility (often thermal expansion) bond coats are

used between these layers and the substrate.

For Mo-Si-B composites there are two primary options for EBC's; either T1 based, pack cemented coatings [32, 67] or mullite, BSAS, rare-earth silicate systems developed for SiC-SiC composites [33, 68]. Both of these systems have shown excellent stability at high temperatures and resistance to water vapor and Ca-Mg-aluminosilicate (CMAS) attack. However, which is better suited to Mo-Si-B composes is unknown as each have different advantages. The T1 based coatings are chemically compatible with Mo-Si-B as both are primarily molybdenum and can form the T2 phase as a bond layer and interdiffusion barrier. The thermal expansion of T1, and the other phases within these coatings, do not necessarily match Mo-Si-B well and cracks have been seen to slowly develop during thermal cycling [67]. The potential to adjust the thermal expansion of BSAS, through varying the Sr/Ba ratio can likely minimize cracking and thermal shock damage. Although SAS coatings have been found to provide local oxidation protection [22], the chemical difference between the metal matrix substrate and oxide coating may limit the strength of the interface.

Although the Mo-Si-B composites development here is aimed at 1300℃ as a use temperature, the combustion gases in current gas turbines exceed this by 100's of degrees. This is made possible with current superalloys by the use of TBC's and cooling, however, if similar systems are not comparable with Mo-Si-B components, then combustions temperatures would have to be lowered. Current TBC's are composed of porous, stabilized zirconia which is very sensitive to attack by fluid CMAS [32]. It is unknown if the higher viscosity borosilicates that develop on Mo-Si-B composites would have the same detrimental reactions with a TBC. If so, a bond coat might be needed to prevent contact.

CHAPTER 5

PROCESSING - MICROSTRUCTURE DEVELOPMENT

Careful control of oxygen has been a critical factor throughout this dissertation's investigation of the processing, microstructure, and properties of Mo-Si-B composites. Not only do molybdenum, silicon, and boron have very different properties when oxidized verses reduced, it is exactly these differences which allow for both mechanical properties and oxidation resistance at high temperatures. On one hand, the metallic molybdenum and the two intermetallics are needed for high temperature strength and creep resistance. For oxidation resistance, on the other hand, the volatility of MoO_3 is necessary to create a surface enriched in borosilciate. Additionally, the boria is required to flux the borosilicate for rapid initial coverage but then must also leave by its own volatilization. The low oxygen permeation of a high silica surface layer is exactly what imparts oxidation resistance in the long term. The challenge during processing to obtaining these various behaviors. First, the thermodynamic favorability of silicon and boron oxides makes preventing their formation difficult. Second, the refractoriness of molybdenum necessitates a fine particle size for sintering, which in turn introduces a high green-body oxygen content. Two steps initially developed by Middlemas allow for these challenges to be overcome [77]. Utilizing nitrides as the silicon and boron sources greatly reduces their initial oxygen content and kinetically limits their oxidation up to around 1000℃. Additionally, firing in a reducing atmosphere (gettered Ar-10%H_2 in this case) allows for removal of the oxygen present on the molybdenum power at temperatures below the rapid oxidation of the nitrides. Maintaining this dry and reducing atmosphere through the reaction and sintering portions of the firing cycle is critical to successful production of Mo-Si-B composites.

The composite production techniques used here were modified iteratively to improve composition control. The first two sections of this chapter address the issues associated

with oxygen control during firing of green compacts and the steps taken to quantitatively improve the firing process. The final section covers the limited application hot isostatic pressing built upon the prior developments. For all the samples produced via pressureless sintering, little change in microstructure was observed. It is believed that the lack of variability is due to the highly refractory nature of the silicon and boron intermetallics controlling the densification behavior. A change in the initial powders would likely have an influence on the microstructure, however this was beyond the current scope.

While little microstructural variation was observed, material properties, such as the oxidation resistance, are far more sensitive to subtle changes in composition. For example a loss of 10% boron (from Mo-3Si-1B to Mo-3Si-0.9B in wt%) would change the equivalent borosilicate composition from 30 to 28 at% boria which, at 1300℃, is a 50% increase in viscosity. The corresponding changes in phase volume fraction would only be a 10% decrease in T2 which is similar to the increase in the molybdenum phase due to solid solution effects and half the associated decrease in A15 fraction. In the other direction, a 10% loss of silicon (from Mo-3Si-1B to Mo-2.7Si-1B) results in a phase volume fraction change on the same order as the 1600℃ solid solution effect and a borosilicate viscosity decrease of 40%. Variability in processing with effects of this scale are challenging to directly measure, but can have a significant impact upon material properties.

5.1 Pressureless Sintering without In-Line Hygrometer

At the start of this work, Mo-Si-B composites were produced by the process developed by Middlemas [77]. Typically 13mm diameter pellets with a hight of 3 to 5mm were pressed from the spray dried powder using a floating cylindrical die at a pressure of 60ksi. The pellets were then fired in a single run that included debinding, reacting, and sintering. A tube furnace was used with an Ar-10%H_2 atmosphere flowing at around 150 $^{cc}/_{min}$. To limit oxygen contamination, the Ar-H_2 was purified in a titanium getter prior to entering the furnace. Debinding was done by a four hour hold at 400℃ during which the PMMA decomposed into shorter chains which are volatile. The PMMA volatiles were carried downstream to the cool end of the tube where they deposited.

At progressively higher temperatures, three important reactions occurred. First, the oxygen present on the fine molybdenum powder was reduced by the hydrogen atmosphere forming water vapor which was carried out of the hot zone by the flowing gas. It is significant that this step happens early in the firing as the amount of oxygen contained in the molybdenum powder is around 40% of the total silicon and boron and can cause substantial oxidation. At temperatures above 1100℃, the decomposition and reaction of the silicon and boron nitrides with the molybdenum occurred, as Middlemas verified with TGA, DSC, and XRD [77]. The decomposition reaction happen very quickly making a furnace hold unnecessary. At temperatures of 1300℃ and above, the LTS molybdenum is known to sinter. However, because of retardation by Si and B, these composites need a sinter step of at least six hours at 1600℃ in order to reach >95% density. Due to the high sintering temperature, an alumina tube and $MoSi_2$ heating elements were used, necessitating slow heating and cooling rates, typically between 3 and $5^{\circ C}/_{min}$.

5.1.1 Densification and Typical Microstructures

The process of spray drying and reaction synthesis with silicon and boron nitrides is quite flexible with respect to the starting powders and has been used to produce compositions between pure molybdenum and high intermetallic composites such as Mo-3wt%Si-1wt%B, as well as the inclusion of refractory oxides and other transition metals. The sintering behavior and densified microstructures of these various composites has been observed to be very similar to the results of Middlemas [77] and is primary controlled by the slow sintering kinetics of the silicon and boron intermetallic phases. Figure 5.1 shows the microstructure of pure molybdenum produced in the same manner for reference. Because of the high silicon and boron content, typical Mo-Si-B microstructures are considerably finer, but still equiaxed and have uniformly distributed phases, Figure 5.2. The similarity of the phases present in Mo-Si-B composites results in low imaging contrast. In a scanning electron microscopy (SEM) the intermetallics appear darker than the molybdenum matrix in backscatter mode, however there is too little contrast between T2 and A15 to distinguish them from each other.

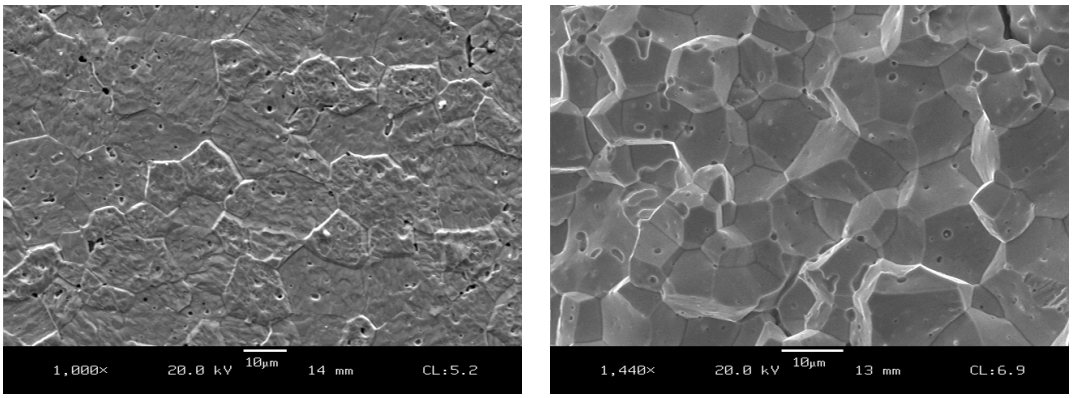

Figure 5.1: Microstructure of sintered molybdenum etched with Murakami's reagent (100g water, 15g potassium ferricyanide, 2g sodium hydroxie), left, and fracture surface, right.

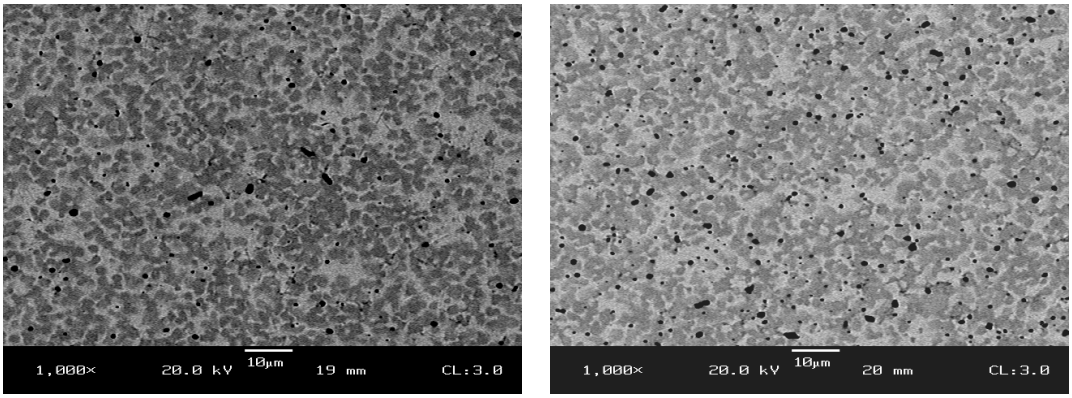

Figure 5.2: Backscatter SEM images from two separate Mo-3wt%Si-1wt%B spray dried batches. The silicon and boron intermetallics both appear dark grey. Pores and entrained silica are black.

The densification behavior of Mo-Si-B composites is believed to be controlled primarily by the amount of sluggish silicon and boron intermetallics and the behavior of surface oxides on the molybdenum powder. The combined effects of these two mechanisms are shown in the theoretical densities of various samples in Figures 5.3 and 5.4. In general, densities beyond 95% require sintering at or above 1600℃ for 6 hours for compositions with around 45 percent by volume intermetallics. However, among the compositions investigate here, two types were identified as having greater sinterability. While these results, discussed in the following paragraphs, are technically interesting, they only operate for compositions that are not suitable for the oxidation resistance or mechanical properties needed here and were thus abandoned in subsequent work.

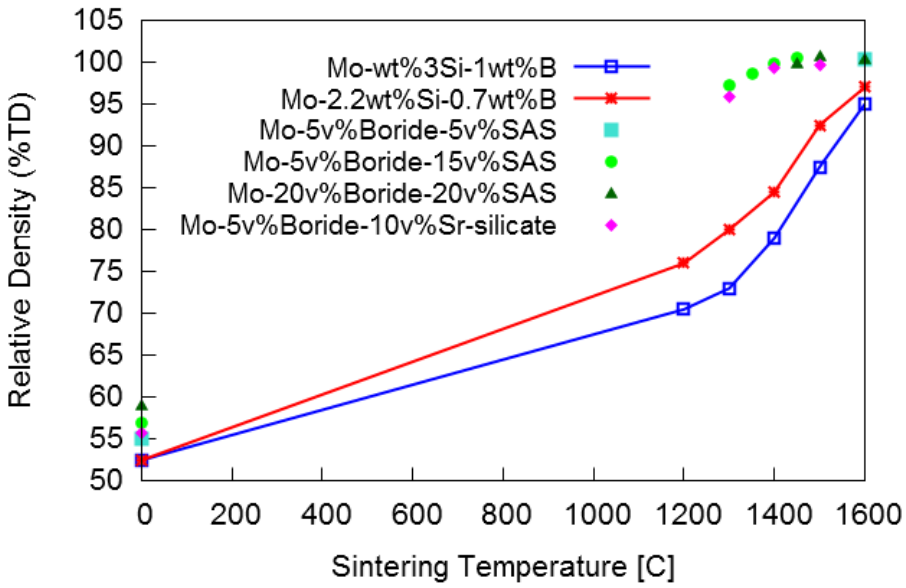

Figure 5.3: Sintering curves comparing the result of Middlemas [77] and various molybdenum boride (Mo_2B) - SAS compositions.

Experimental batches with refractory oxides instead of A15 showed some sizable increases in sinterability. Two refractory oxides in particular were successful, mullite and the 1:1:2 strontium aluminosilicate ($SrO : Al_2O_3 : 2SiO_2$) referred to here as SAS. It was found that composites containing either of these oxides in addition to either Mo_2B or T2 would reach full density at 100 to 200℃ less than composites containing only the T2 and A15 intermetallics. However, the degree of increased sinterability appeared to be related to the volume fraction of the oxide and only occurred when the intermetallic's volume fraction is comparable to the oxide's. For densitification at 200℃ lower, around 20 volume % of both the oxide and intermetallic were needed. The need for both the refractory oxide and some boron containing intermetallic suggests that a small amount of boron oxides form and cover the solid-gas surfaces inhibiting sintering. When the refractory oxides are present however, they become a more favorable location for the boron oxides, which then acted to "clean" the molybdenum surfaces and allows for increased densification. Because mullite and SAS are quite refractory, they are able to absorb the boron oxide(s) without forming their own liquid oxide which would in turn limit sintering. However, these composites high in boron and refracotry oxides are not oxidation resistant; the silicate melt which would form is very

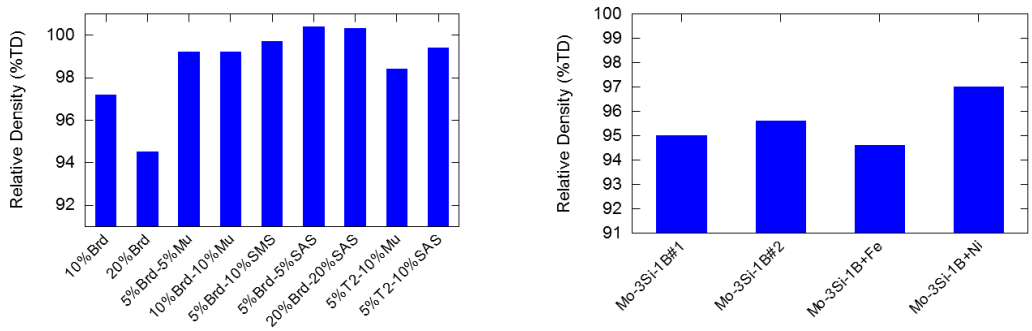

Figure 5.4: Densities of various composites sintered at 1600℃. At left the compositions are given as volume percentiles while at right the base composition is 3wt% Si and 1wt% B. Brd referes to Mo_2B, Mu to mullite, and SMS to strontium metasilicate.

rich in glass modifiers and thus has a viscosity too low to be protective.

The second observed increase in sinterability is more typical of liquid-phase sintering aids. Within the transition metals added to improve oxidation resistance, nickel has a very unusual behavior with respect to both sintering and mechanical properties. Compared to both the base Mo-3wt%Si-1wt%B and the same with minor iron additions, the nickel containing composite had increased sinterability, reaching 97%TD at 1550℃. Reviewing the literature, this effect is not surprising; there are a few reports of Ni as a sintering aid in molybdenum [51]. Specifically the δNiMo intermetallic has a low melting temperature, which is possibly depressed even more as a grain boundary phase. TEM imaging of Ni alloyed molybdenum greatly supports this view by showing a very thing δNiMo phase covering the grain boundaries [51]. This grain boundary phase is also responsible for the other significant effect of nickel, substantially reduced ductility. As an intermetallic, δNiMo is brittle and because it can cover much if not all of the grain boundaries, it controls the mechanical properties by promoting brittle, intergranular fracture.

5.1.2 Detrimental Oxygen and Water Vapor Reactions

As demonstrated by the estimate at the start of this section, relatively small changes in silicon or boron content can have a large effect upon the material properties, such as 10% composition changes resulting in 40-50% changes in borosilicate viscosity. It is useful then to consider what detrimental reactions might occur during processing which could cause

composition changes of such a magnitude. Because variations in phase fraction of only a few percent are difficult to identify by either XRD refinement or area fractions from backscatter SEM imaging, there is little explicit evidence. Some results will be presented which hint at certain oxygen control issues.

The control of oxygen in Mo-Si-B processing can be broken down into three topics: sources of oxygen, potential reactions, and loss of oxides. There are two primary sources of oxygen, water vapor contamination in the furnace atmosphere and the initial oxygen content of the molybdenum powder. Due to the high surface area of this sinterable powder, it is by far the most significant source, with oxygen contents between 1wt%, typically reported by the manufacture, and upwards of 3wt%, back calculated from sample weight losses. For composites which are 80 to 85 at% molybdenum, the total oxygen content is in excess of 6.5 at%. Compared to the boron and silicon content of the green body, this oxygen content is around 80% of the total boron and 70% of the silicon. The second primary oxygen source, water vapor within the furnace atmosphere, is initially low due to the use of a titanium getter to purify the Ar-H_2, however as the oxygen on the molybdenum powder is reduced, the local dew point can increase faster than the water vapor is swept away.

The thermodynamically most favorable oxide in the Mo-Si-B system is SiO_2, followed closely by B_2O_3. Under all reasonable experimental condition, hydrogen is able to reduce molybdenum oxides, however silicon and boron can reduce any water vapor. Due to their mobility, a number of reduced oxide, hydroxide, and hydrated species are also significant. These are gaseous or high partial pressure compounds including: SiO, H_3BO_3, and H_2MoO_4 [35, 54, 6]. These compounds are of specific concern as they allow for mechanisms by which silicon and boron may be lost from the composite, changing the composition and thus the properties of the boroslicate needed for oxidation resistance. A two step process in which silicon or boron are oxidized to SiO_2 or B_2O_3 and then react with either hydrogen or the water vapor present from simultaneous reduction of molybdenum, can form the volatilite SiO and H_3BO_3 as in equations (5.1) and (5.2). Transport of these species out of the powder compact would results in a partial loss of silicon and boron prior to sintering.

$$SiO_2 + H_{2(g)} \rightarrow SiO_{(g)} + H_2O_{(g)} \tag{5.1}$$

$$B_2O_3 + 3H_2O_{(g)} \rightarrow 2H_3BO_{3(g)} \tag{5.2}$$

Depending upon the extent to which the silicon and boron loss mechanisms above occur, the compositional change could be very difficult to observe in the final phase fractions. However, if the reactions are localized then regions strongly depleted in the intermetallic phases would exist even if the overall effect is small. Figure 5.5 shows the cross section at the surface of a sintered Mo-Si-B composite in which depletion of A15 and T2 is evident. A similar surface depletion of 10 to 20 μm was observed on all samples. Because this depletion is present only on the sample surface, the reactions which cause it must involve the atmosphere around the samples. Due to the hydrogen content, the oxygen source is water vapor. Based the silicon and boron concentration within a 20 μm surface layer, the estimated total water vapor needed is 1.5×10^{-4}mol. During a typical firing, a sample would spend around eight hours at high temperatures, including a six hour hold and the time for both heating and cooling. At a flow rate of 150 $^{cc}/_{min}$ and assuming a water vapor concentration of 50ppm, a total of 1.46×10^{-4} mol of water vapor would flow through the furnace tube. While this is only a rough estimate, and could easily vary by a factor of five, the good agreement supports this mechanism. For the gas used here, 10% H_2 in argon, a water vapor content of 50 ppm is a dew point of approximately -48℃, which is a very dry system but theoretically attainable with a titanium getter.

Concern with potential oxidation of silicon and boron nitrides prompted thermogravimeteric evaluation to aid in revealing the tempeature at which reactions were occurring. Because processing these materials relies upon the slow kinetics of the nitride's reactions, the time and temperature by which the hydrogen de-oxidation completes is significant. If the furnace run ramps to temperatures at which the nitrides oxidize rapidly before the hydrogen de-oxidation has finished, then oxidation and potential loss of silicon and boron is likely. Thermogravimeteric analysis (TGA) is a convenient and precise method to identify the temperatures at which the relevant gas species evolve during a given time-temperature cycle,

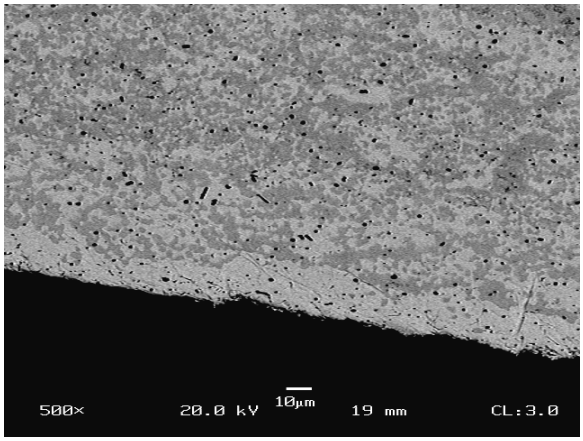

Figure 5.5: Cross section of a sintered Mo-3wt%Si-1wt%B sample showing the surface (bottom) depleted of the A15 and T2 phases.

however it does not specifically identify the species involved. Figure 5.6 shows the percentage weight losses of a variety of samples during a furnace ramp $5^{\circ C}/_{min}$ in an atmosphere of flowing Ar-2%H_2. Four different compositions were evaluated to separate the effects of added organics and nitrides: as received molybdenum powder, spray dried molybdenum powder, spray dried molybdenum and boron nitride, and spray dried powder of the Mo-3wt%Si-1wt%B type composition. Additionally, the as received molybdenum, spray dried molybdenum, and molybdenum-boron nitride compositions were run as both loose powder and as small pressed pellets.

All the thermogravimeteric traces in Figure 5.6 have the expected major weight loss steps. These include an initial 0.5% loss due to absorbed water, decomposition of the PMMA between 350 and 400℃, hydrogen reduction of the molybdenum powder over a mid range of temperatures, and finally decomposition of the nitrides at approximately 1300℃. While all the loose powder runs show these reactions occurring as expected and with little weight loss in between, the pressed pellets continue to slowly loose weight above 1000℃. Because this is too high a temperature for PMMA reactions and too low for the A15 and T2 forming reactions, the continued weight loss was a result of the hydrogen de-oxidation lagging behind the temperature ramp. This behavior in pressed pellets occurred across all the compositions and thus was associated with reduced transport of the de-oxidation reactants and products within a compact of 40 to 50 percent open porosity. These results

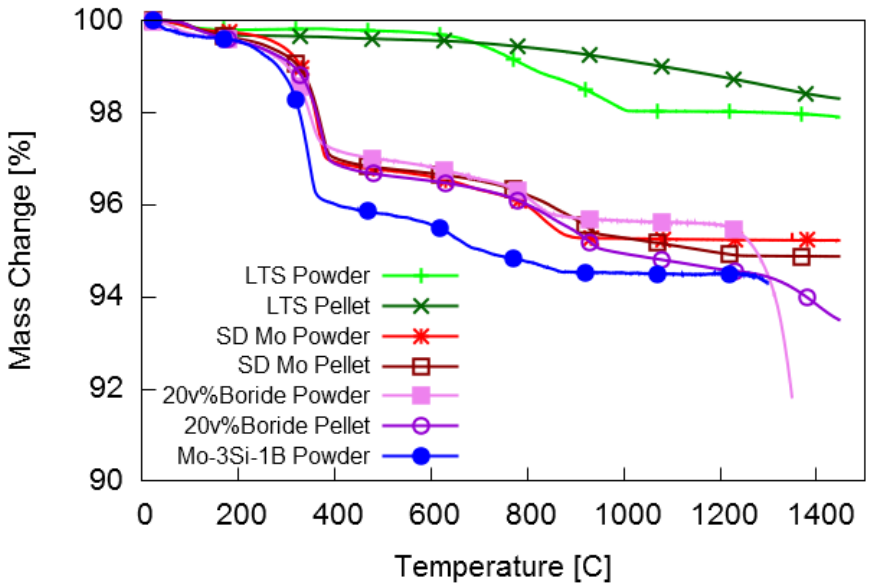

Figure 5.6: Thermogravimeteric weight losses of various pure molybdenum and Mo-Si-B samples in Ar-2%H_2. LTS is the as-received molybdenum powder and SD refers to spray dried molybdenum.

highlighted the need to modify the firing cycle during the de-oxidation step to account for the form and number of samples. Because of sample size limitations in TGA furnace setups, an alternative approach using a hygrometer to monitor the effluent dew point was developed.

5.2 Pressureless Sintering with Hygrometer Analysis

While much of the work done utilizing silicon and boron nitrides and firing in a argon-hydrogen atmosphere was done by Middlemas [77], a quantitative measure of the de-oxidation was never implemented. As discussed at the start of the previous section, slight oxidation of silicon or boron could easily go unnoticed and become an unexpected and serious issue if processing parameters where changed (such as a lager number of samples or a different firing furnace). In fact, it was the sensitivity of silica containing samples (part of the analogous project of Daloz [27]) that revealed the slight oxidation issue. In these samples the oxidation of only 10% of the boron nitride was enough to fully "melt" any silica and form a very fluid borosilicate, which was evident in the microstructure. Because of the difficulties in quantitatively measuring boron contents, the difference between a Mo-3Si-1B

and Mo-3Si-0.9B could easily be missed. In order to tackle the various issues described above, a hygrometer was attached to the effluent line of the firing furnace to measure water generation. Because of the very low dew point attainable by a Ti-getter and the large amounts of water vapor released by de-oxidation of the molybdenum powder, changes in the effluent gas's dew point clearly indicate both the onset and completion of molybdenum de-oxidation. With this capability in place the firing cycle was optimized for complete de-oxidation at as low a temperature as possible so as to minimize potential oxidation of the silicon and boron nitride.

The hygrometer used (Kahn Cerimet II) measures the water vapor concentration around a metallized ceramic probe which, when the temperature and pressure are known, can be converted into dew point. Additionally, because the system used here has a known argon partial and that hydrogen and water vapor are the only other significant species, the $^{H_2}/_{H_2O}$ ratio can be determined. By placing the hygrometer probe into the furnace effluent stream and metering the total gas flow rate with a mass flow controller, the water vapor flow rate out of the furnace tube can be calculated. Because the inlet stream is purified by a titanium getter, it is reasonable to assume the measured effluent water is the same as the water generated by the sample and, for low dew points and high flow rates, that the water vapor flow rate is the same as its generation rate by the sample de-oxidation. Integration of the water flow throughout the firing cycle gives the total water generated by the de-oxidation. It should also be noted that the Kahn hygrometer is designed for measuring relatively rapid changes and so the slow heating rates and long furnace times used here minimized the potential for measurement lag.

While the hygrometer is very effective at measuring clean gas streams, care needed to be taken to prevent damage by particulates or clogging by other contaminates, and thus a coalescing filter was placed upstream. It was realized after a few furnace runs that the PMMA vapor condensates from debinding were a problem for the effluent gas monitoring setup as they were clogging the fine filter protecting the hygrometer. Even though a bypass line around the hygrometer was used during debinding, sufficient PMMA remained in the cool end of the tube so as to clog the filter later in the firing, often at a hot zone temperature

around 800℃. As a work-around, the debinding was performed in a separate furnace with a specific debinding run of two hours at 400℃ under dried Ar.

5.2.1 Iterative Firing Improvements

Commensurate with the production of samples for composition development, the effects of a number of process variations during firing were observed utilizing the hygrometer traces for the entire furnace run. The results were used to identify improvements to the firing procedure, primarily with regard to low temperature de-oxidation. The typical hydrogen reduction of molybdenum oxide occurs in two primary steps associated with the reactions 5.3 through 5.5 [57, 58, 104]. The reactions generating Mo_4O_{11} and MoO_2 begin as low as 400 to 700℃ and often overlap. The complete reduction of MoO_2 to the metal occurs as a single step starting at 600 to 800℃. For the production of powder metallurgical molybdenum, de-oxidation is often done around 1100℃ in moist hydrogen in order to expedite the process. However, this process can't be translated to Mo-Si-B composites due to the oxidation of silicon and boron which would rapidly occur at 1100℃. Thus new processing parameters were developed. Optimization of the sample de-oxidation was done by identifying the temperatures at which the onset and double dew point peaks occurred and then varying process parameters for rapid and low temperature completion of de-oxidation to minimize potential nitride oxidation. The available firing parameters included furnace ramp rates and isothermal holds, intermittent vacuum cycles, and increased gas flow rates.

$$4MoO_3 + H_2 \rightarrow Mo_4O_{11} + H_2O \tag{5.3}$$

$$Mo_4O_{11} + 3H_2 \rightarrow 4MoO_2 + 3H_2O \tag{5.4}$$

$$MoO_2 + 2H_2 \rightarrow Mo + 2H_2O \tag{5.5}$$

Initial de-oxidation tests were done on pure molybdenum powder run at $5^{\circ C}/_{min}$ up to 1200℃ and at a flow rate of $150^{cc}/_{min}$. The hygrometer traces for two of these runs are shown in Figures 5.7 and 5.8. In addition to the dew point behavior during de-oxidation, the initial portion of these traces show the furnace drying steps. In the first run, 5.7,

four vacuum and backfill cycles were used to dry the system from ambient conditions to a dew point of -27℃ while the furnace was holding at 75℃. After the final backfill, the gas flow rate was set to $150^{cc}/_{min}$ and the furnace ramp, of $5^{\circ C}/_{min}$, was started. The dew point increased quickly during this ramp with a series of overlapping peaks between 100 and 600℃ which are associated with both removal of adsorbed water and the initial reduction of molybdenum oxides. Between 600 and 800℃ the dew point is level as the water generation and flush rates are equal. Around 840℃, the dew point again increases as the rate of reduction of molybdenum oxides increases. The de-oxidation rate for a number of runs has been observed to increase significantly in the temperature range of 850 to 900℃. This is believed to be associated with an increase in the mobility of molybdenum oxides, either MoO_3 which melts at 813℃ or the hydrated H_2MoO_4. Due to the sample size, low flow rate, and high heating rate, the dew point in the first run did not reduce again till after the 1200℃ hold. Two major conclusions were drawn from this initial result of the hygrometer; first all previous sample firings would have maintained a high dew point above 1200℃ raising the possibility of oxidation of the nitrides. Second, a hold or reduced ramp rate was needed for de-oxidation to be completed at lower temperatures.

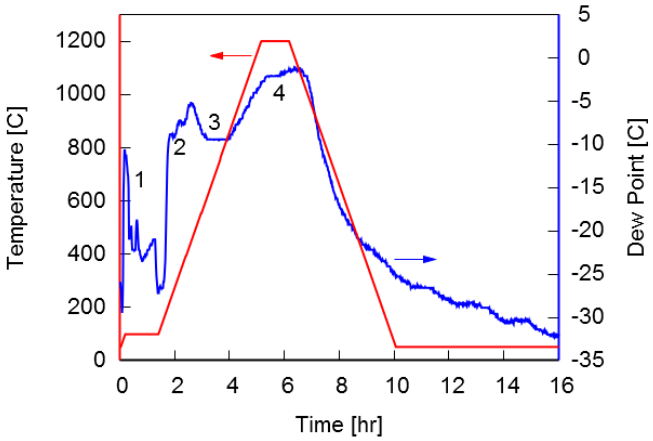

Figure 5.7: Hygrometer traces showing dewpoint (in blue) of gas (right Y-axis) from two molybdenum powder de-oxidation runs plotted against time. The red line shows temperature at the left Y-axis. Regions are indicated: (1) vacuum and back fill cycles, (2) overlapping surface desorption and de-oxidation, (3) steady state water generation and removal, and (4) remaining de-oxidation peak.

A second de-oxidation run of pure molybdenum powder, Figure 5.8 was done with the

inclusion of two holds to aid in the completion of de-oxidation. The holds were placed at temperatures before the apparent increase in molybdenum oxide mobility in order to minimize the number of volatile oxides. One hold was placed just before this point, at 800℃, while the other was early in the reduction process at 500℃. The isothermal dew point change was used to evaluate the efficiently of holding at these temperatures for de-oxidation. A rapid rise *and* fall in the dew point is an indication of efficient reduction by hydrogen. Additionally, in order to remove any potential accumulated water vapor, a vacuum was pulled at the end of each hold and mid way through the 800℃ hold. The rapid rise in dew point after the first two vacuum cycles shows that water vapor accumulation is minor with respect to the flow rate. The third vacuum cycle does appear to have aided in water removal as the dew point does not return to the same level. While the hold at 500℃ only had a small effect upon the initial rising dew point, it peaked and began to fall halfway through the 800℃ hold. Although a small increase in dew point did occur during the high temperature hold, the peak is far less than in the first run, indicating that the majority of the de-oxidation was completed during the 800℃ hold.

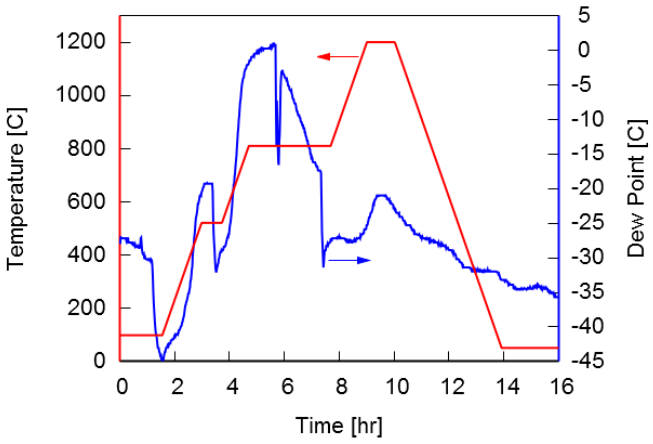

Figure 5.8: Hygrometer traces showing dewpoint (in blue) of gas (right Y-axis) from two molybdenum powder de-oxidation runs plotted against time. The red line shows temperature at the left Y-axis. Holds are at 500 and 800℃ and evacuation cycles at 3.4, 5.7, and 7.3 hours.

The impact of a hold at 800℃ upon the firing of Mo-Si-B composite samples, as pressed pellets, is shown in Figure 5.9. This run was early in the processing developed and had a lower gas flow rate, $150^{cc}/_{min}$, and higher ramp rate, $5^{\circ C}/_{min}$, than later runs. However,

the double peak associated with the two step reduction of molybdenum oxides is apparent. The 2 hour and 20 minute hold at 800℃ also contained the entire de-oxidation process, starting with the second reduction peak (dew point of -1℃) and ending with a dew point of -33℃. The cumulative water generated verse time, normalized to the total water generated, Figure 5.9 right, shows that the majority of de-oxidation occurred during ramping to 800℃ and during part of the hold.

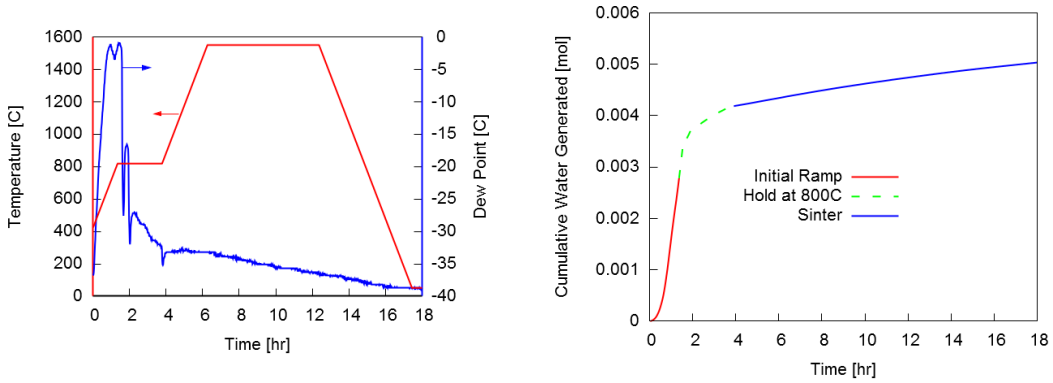

Figure 5.9: Temperature profile and hyrgometer trace of a de-oxidation and sintering run with a hold at 800℃ (left). The cumulative water generation, from integrated flow and dew point values, is shown on the right with colors indicating the portions of the firing cycle: initial ramp, hold at 800℃, and sinter.

While de-oxidation at 800℃ has been identified as effective, oxidation of silicon and boron nitrides by water vapor is still a concern at that temperature. Based upon the observation that the dew point increased very quickly during the ramp to 800℃, this ramp rate was reduced from $5^{\circ}C/min$ to $3^{\circ}C/min$ to allow time for more complete de-oxidation at those intermediate temperatures. Figure 5.10 compares the normalized, cumulative water generation verses furnace temperature of runs ramping at $5^{\circ}C/min$ and $3^{\circ}C/min$ between 600 and 800℃. It can be seen that a larger portion of the total de-oxidation is occurring at lower temperatures with the slower ramp rate. Three additional features deserve mentioning. First, the run at $3^{\circ}C/min$ includes a short hold at 1200℃ which was added to allow for dissolution of minor manganese alloying bellow its melting point. Second, both runs attain the same percentage of total de-oxidation at the end of the 800℃ hold. While it is possible that this has physical meaning, it is believed that it occurred simply by chance as the dew points are different and this did not occur in all runs. Finally, the slope of the cumulative

water generation for the $3^{\circ}C/min$ run is higher going up to the sintering hold and flatter on cool down which is indicative of improved furnace conditions as the dew point on cooling should be low with little water vapor in the effluent.

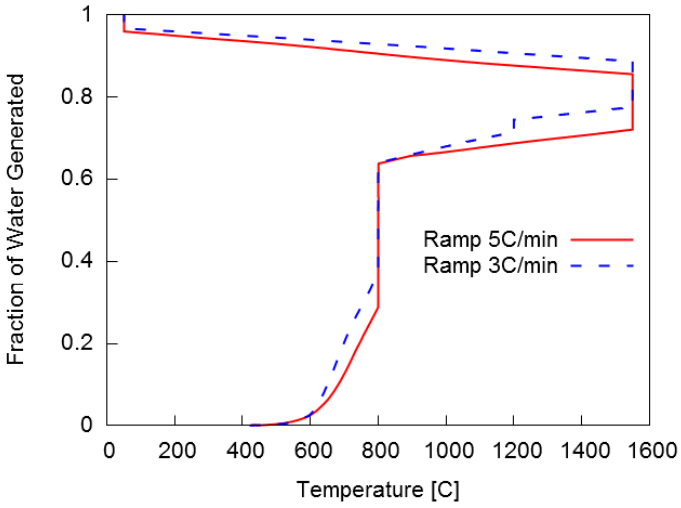

Figure 5.10: Comparison of cumulative water generation verse furnace temperature for two runs each normalized by their total calculated water generation. The furnace ramp rate between 600 and 800℃ was slowed from $5^{\circ}C/min$ to $3^{\circ}C/min$ with a corresponding increase in the water generation during this range.

Modifying the time - temperature profiles lead to the improved de-oxidation shown above, however, this is only one of the many process variables. The gas flow rate and number of samples in a furnace run are critical parameters determining both the hydrogen supply and demand as well as the water vapor removal rate. Figure 5.11 shows the dew point and water vapor flow rate traces of runs with differing sample size and gas flow rates during the critical de-oxidation temperatures. The run shown on the left, MoSiB-3-150, had a gas flow rate of $150^{cc}/min$ while the one on the right, MoSiB-3-300, contained twice the number of samples and had twice the flow rate, $300^{cc}/min$. Additionally, though not as evident in these traces, the $3^{\circ}C/min$ ramp started 100℃ earlier in the MoSiB-3-300, at 500 instead of 600℃. Comparing the traces in Figure 5.11 it can be seen that doubling both the sample size and flow rate maintained very similar dew points throughout de-oxidation by approximately doubling the water vapor flow rate.

While the similar dew point traces for runs MoSiB-3-150 and MoSiB-3-300 would suggest

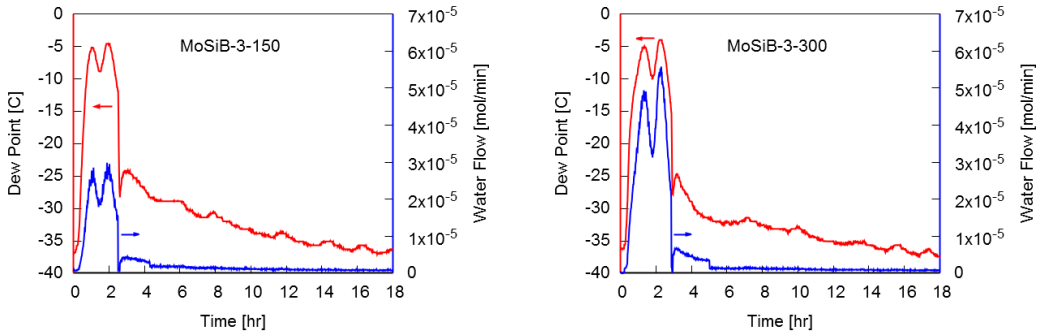

Figure 5.11: Dew point and molar water flow rate traces for runs with differing flow rates and ramp rates during de-oxidation portion. At left a slowed ramp of $3^{\circ}C/min$ started at 600℃ while the same rate started at 500℃ on right. The left and right gas flow rates during de-oxidation are 150 and 300 cc/min respectively. Although the dew points are similar, the high gas flow rate results in a higher water generation rate.

similar de-oxidation efficiency, the cumulative water generated as a function of furnace temperature was actually significantly different, Figure 5.12. The first difference is the initial increase in de-oxidation rate which occurs with the slowed ramp and higher flow rate step. For the MoSiB-3-300 run, this firing step was done at 500℃ instead of 600℃ for MoSiB-3-150. The net effect of this is that the MoSiB-3-300 run has generated an addition 7% of its total water vapor by 600℃. Interestingly, just between 600℃ and the end of the hold at 800℃, the MoSiB-3-300 run continued to outperform the MoSiB-3-150 with and additional 8% of the total water vapor being generated. Even though the sample size and gas flow rate were increased proportionally, the higher flow rate appears to additionally improve de-oxidation. The overall effect on these two runs was a higher fraction of the total water vapor generation occurring below and during the 800℃ hold with MoSiB-3-300 having generated 79% verses 64% for MoSiB-3-150. The increased "dryness" of the high temperature portion caused by a lower temperature ramp start and increased gas flow rate was a significant step and expanded upon by the subsequent processing trials.

Further increases in the gas flow rate were found to give additional improvements to the de-oxidation. Figure 5.13 compares the cumulative water generation of nearly identical furnace runs with gas flow rates of $300^{cc}/_{min}$, MoSiB-3-300, and $500^{cc}/_{min}$, MoSiB-3-500. While the peak dew points during these two runs are relatively close, -5.8℃ for MoSiB-3-300 verses -3.8℃, de-oxidation started earlier and remained at a higher fraction of completion

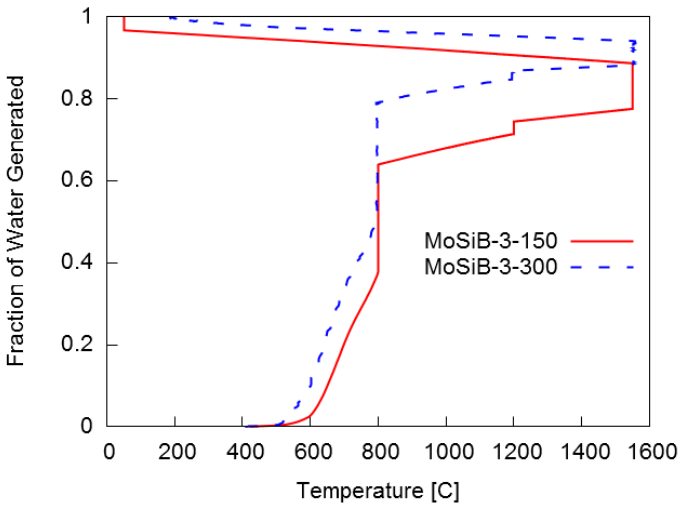

Figure 5.12: Comparison of cumulative water generation verse furnace temperature for the two runs shown in Figure 5.11 each normalized by their total calculated water generation. The gas flow rate was doubled to $300^{cc}/_{min}$ in MoSiB-3-300.

throughout the de-oxidation step of MoSiB-3-500. By the end of the hold at 800℃ the higher flow rate run had generated nearly 90% of the total measured water vapor. It should be noted that the de-binding step was done in a separate furnace run for MoSiB-3-500. This allowed for use of the hygrometer at temperatures below 400℃ but is not believed to have a significant impact upon the molybdenum de-oxidation measurements.

Even with the improvements from raising the gas flow rate to $500^{cc}/_{min}$, a considerable portion of the de-oxidation still occurred during the 800℃ hold, a temperature at which the oxidation resistance of boron and silicon nitride is questionable. In an effort to extend the gains of a slowed ramp rate during heating to 800℃, the heating rate from 450 to 800℃ was reduced to $2^{\circ C}/_{min}$ from $3^{\circ C}/_{min}$. Figure 5.14 compares the cumulative water generation as a function of furnace temperature for runs with these two heating rates. Ramping at $2^{\circ C}/_{min}$ results in significantly more water vapor being generated between 600 and 800℃. For the slower ramp (MoSiB-2-500) only 10.8% of the measured water is generated during the 800℃ hold compared to 29.8% for MoSiB-3-500, in spite of MoSiB-2-500 having five pellets instead of four and its hold being shorter, 30 minutes instead of one hour. Of final note is that the hold at 1200℃ was abandoned for MoSiB-2-500 due to it being considered ineffective because of the slow interdiffusion in molybdenum.

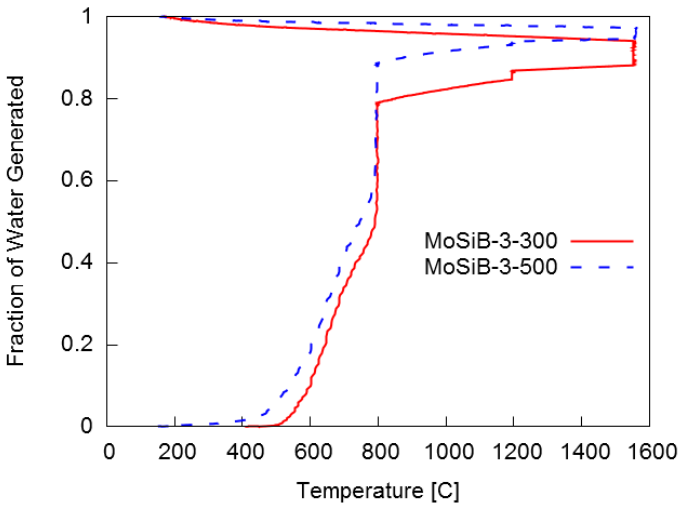

Figure 5.13: Comparison of cumulative water generation verse furnace temperature for two runs each normalized by their total calculated water generation. The gas flow rate was increased from 300 to 500$^{cc}/_{min}$.

The final change made to the de-oxidation and pressureless sintering process for the production of Mo-Si-B composite samples was the elimination of the vacuum cycle at the end of the 800℃ hold. Nearly identical runs, differing in the inclusion of this vacuum cycle, are shown in Figure 5.15. It can be seen that the vacuum cycle at the end of the 800℃ hold had little effect upon the dew point trace. Due to the detrimental effect of high temperature evacuations on the life of refractory furnace tubes, slight improvements are not considered worthwhile. This result also indicates that it is the local equilibrium and reactions of the sample, and not the gas transport, which control the de-oxidation under these conditions.

5.3 Hot Isostatic Pressing

Hot isostatic pressing (HIP'ing) has previously been used as a final processing step to close porosity left after pressureless sintering [77, 60]. The lower process temperatures and times for consolidation by HIP'ing do create certain additional advantages for using it as the only consolidation techniques for Mo-Si-B composites. By eliminating exposure to temperatures of 1500 or 1600℃, the grain size, silicon solubility, and manganese evaporation can all be greatly reduced.

The first of the advantages, reduced grain size, benefits both strength and oxidation

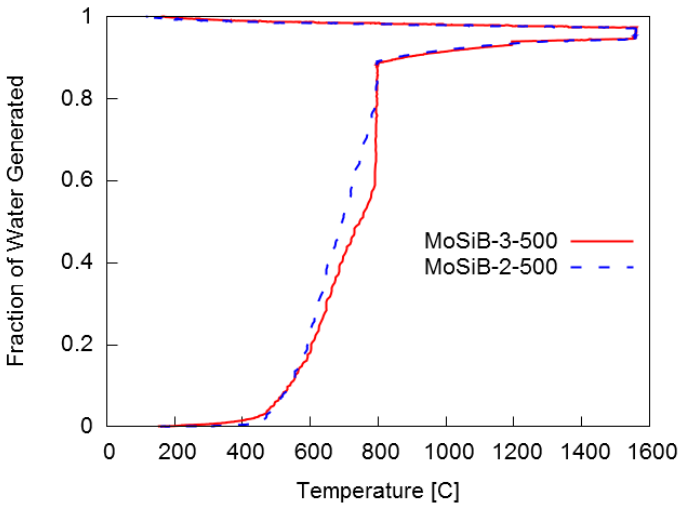

Figure 5.14: Comparison of cumulative water generation verse furnace temperature for two runs each normalized by their total calculated water generation. Run MoSiB-2-500 ramped at $2^{\circ}C/min$ from 450 to 800℃ and was held at 800℃ for 30 minutes while MoSiB-3-500 ramped at $3^{\circ}C/min$ and had a hold for 1 hour at 800℃.

resistance with a slight decrease in creep resistance, depending upon the amount of grain refinement. Any additional effect upon toughness is unknown as both beneficial and detrimental aspects can occur; a higher grain boundary area will reduce the concentration of grain boundary segregants, strengthening them, while Hall-Petch effects will raise the critical resolved shear stress of the grains. The balance between the two determines whether yielding or grain boundary fracture occur first.

A substantial weakness of the Mo-Si-B system has always been the high brittle-to-ductile transition temperature (BDTT) arising from the combined solid solution strengthening and grain boundary weakening effects of silicon solution within a molybdenum matrix. However, the degree to which these effects cause an elevated BDTT has been shown to depend upon the equilibrium silicon solid solution in the αMo phase. This solid solution is temperature dependent. By lowering the process temperature to 1300℃, the silicon solid solution can be significantly lowered which will in turn lower the BDTT. The degree to which the beneficial effects will happen is yet to be determined and is difficult to predict due to the lack of experimental data on the Mo-Si system at relatively low process temperatures.

The third, and final, advantage to using HIP as the primary consolidation of Mo-Si-B

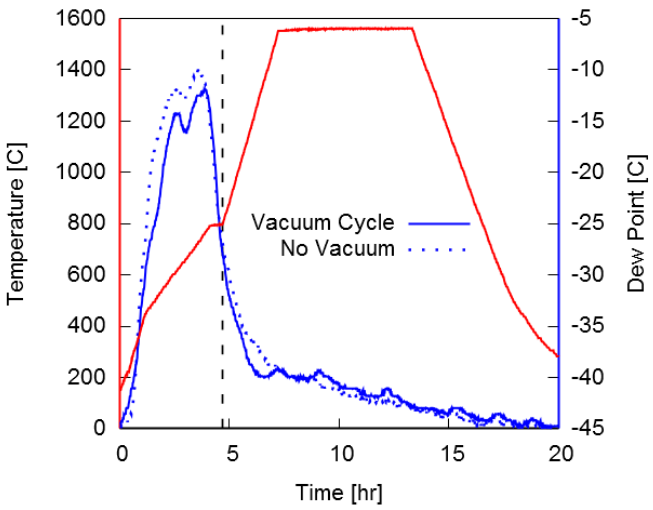

Figure 5.15: Temperature and dew point profiles of two runs differing only in the use of a evacuation cycle at the end of the 800℃ hold (vertical dashed line). Very little, if any, effect on the overall dew point behavior is seen from the inclusion of this vacuum cycle.

composites is the ability to use manganese as a minor addition. As will be shown in the next chapter, the oxidation resistance of manganese modified samples was found to be superior to all other compositions. However, production of these samples was severely limited by the volatility of manganese metal. Metallic manganese has a high vapor pressure which increases dramatically above 900℃ [48]. However, its oxide (MnO) is relatively refractory and has a high energy of formation. In powder metallurgical steels containing manganese the evaporation, oxide formation, and subsequent oxide precipitation can be controlled by the oxygen partial pressure [48]. Because the processing of Mo-Si-B composites aims for a very low oxygen partial pressure, manganese tends to be reduced and then lost from the powder compact due to its volatility at temperatures where dissolution into the Mo-Si-B material is very slow. In the processing developed here, furnace atmospheres only became reducing enough for the reduction of MnO at temperatures above 1300℃, see Figure 6.38. The use of HIP'ing however, allows for avoiding those temperatures in an "open" condition, preventing manganese loss and allowing time for it to dissolve into the Mo-Si-B phases.

Although it has the aforementioned advantages, hot isostatic pressing of Mo-Si-B composites has a number of challenges due to the necessary de-oxidation and nitride decomposition steps prior to the HIP run itself. Traditional HIP processes focus on filling evacuated

HIP cans and then welding the can shut as a hermetic gas barrier for HIP'ing. The processing of Mo-Si-B composites however, involves significant gas transport. Over the temperatures critical to de-oxidation, a relatively high hydrogen flow rate is needed to complete the step efficiently. Then, at temperatures around 1200℃, nitrogen gas is generated by the decomposition and reactions to form A15 and T2 [77]. Sealing of the HIP can must therefore occur after the Mo-Si-B material has progressed through these steps. Exposing any reacted (but not sintered) Mo-Si-B powder to an oxygen containing atmosphere, such as during filling of a HIP can in air, risks re-oxidizing the material and squandering the advantages of using the nitrides. A method was developed which maintained atmosphere throughout processing by firing the Mo-Si-B powder contained in a tube which became the HIP can. A significant difficulty for this process was the sensitivity of the HIP can material to hydrogen embrittlement. Although this was mitigated for low carbon steel, by running in vacuum after completion of the de-oxidation, titanium tubing fractured easily due to its far greater hydriding sensitivity.

The method developed to deoxidize, decompose, react, and evacuate the Mo-Si-B material all within the HIP can and in one furnace run differed from traditional HIP'ing where cans typically have just one opening for both filling and evacuation. The cans used here had both gas inlet and outlet tubes welded onto opposite ends of the can. Because HIP'ing at 1300℃ can be done with low carbon steel or titanium cans, the production of cans with inlet and outlet tubes is relatively simple. The filled can is placed inside an alumina tube within a standard high temperature tube furnace with tube fittings allowing for a constantly flowing argon blanket gas to protect the outside of the HIP can from oxidation. By extending the gas tubing approximately 10in from the hot zone and passing through refractory inserts at the furnace wall, the cool end of the tubing was maintained below 50℃ allowing for typical tube fittings to be used. The inlet and outlet tubes are thus attached to the same gettering Ar-H_2 gas supply and hygrometer as was used for pressureless sintering. By including ball valves on both the inlet and outlet, the HIP can can be evacuated and then temporarily sealed before permanently welding off the tubing.

5.3.1 Encapsulated in Low-Carbon Steel

Initial consolidation of Mo-Si-B composites in steel cans was done with pressed powder compacts. Directly following the de-oxidation procedure developed for the previous pressureless sintering was not completely successful; incomplete de-oxidation at the end of the 800℃ hold caused an additional dew point peak at around 1000℃(during the ramp portion) due to increased reactivity of Mo-oxide vapor. Even increasing the gas flow rate to $1000^{cc}/_{min}$ and the 800℃ hold time to 2 hours did not eliminate this higher temperature dew point peak, as shown in Figure 5.16. Two factors could restrict the rate of de-oxidation in these runs, the greater amount of Mo-Si-B powder requiring even more gas flow and the pressed compact and can geometry limiting gas transport.

A subsequent set of samples were produced to address the de-oxidation issues by filling the low carbon steel cans with Mo-Si-B powder, held in place by steel wool. Unfortunately, due to the relatively high gas velocities and small particle sizes, the bed of powder moved under the gas flow, jamming against the steel wool on the outlet. Although only a small amount of the powder escaped, the jammed powder created a significant pressure gradient against the gas flow, up to 25 psi. In one sample, this back pressure was constant throughout the de-oxidation cycle and the de-oxidation was in fact completed by the end of the 800℃ hold. However, the other samples experienced pressure drops at differing points during their de-oxidation, and also incomplete de-oxidation by the end of the same 800℃ hold, with additional dew point peaks during the subsequent ramp. The implication of this set of results is that when the gas flow bypasses the Mo-Si-B powder bed, even within the steel can, the de-oxidation became very inefficient. In the one successfully de-oxidized sample, which did not have a pressure drop, the gas flow never created or found a way to bypass the powder, resulting in both a high pressure gradient and effective de-oxidation. Given a de-oxidation furnace geometry with greater control of the gas-powder interaction, consistent and effective de-oxidation would be feasible.

Regardless of the varying de-oxidation results, those samples which were successfully HIP'ed had densities between 93 and 98% of theoretical. The HIP cycle was 6 hours at 1300℃ under 45ksi argon. Figure 5.17 shows the resulting microstructure compared to

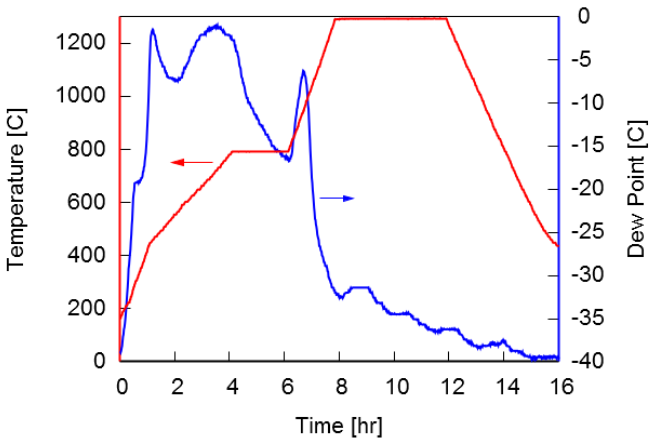

Figure 5.16: Temperature and dew point traces for a Mo-Si-B compact in a low-carbon steel can prior to HIP'ing. The dew point peak after the 800°C hold is indicative of incomplete prior de-oxidation.

a pressurelessly sintered sample. Although the grain size is clearly reduced, a reasonable amount of inclusions are also present. These are most likely silica formed during either the incomplete de-oxidation or evacuation of the HIP can prior to being welded hermetic.

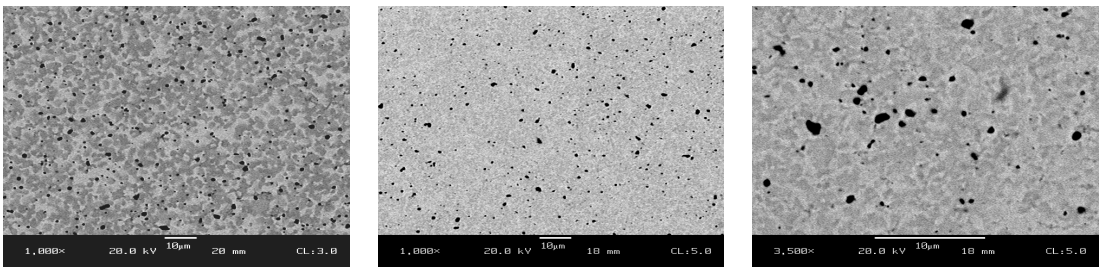

Figure 5.17: SEM-BS microstructures of pressurelessly sintered (left) and HIP'ed (middle and right) Mo-Si-B composites showing the reduced grain size and consolidation from HIP'ing.

Although the firing and HIP'ing in the low-carbon steel cans was mostly successful, a serious issue was identified during oxidation testing of the densified Mo-Si-B composite. Figure 5.18 shows a surface and cross section typical of these samples. Extensive surface devitrification followed by spallation resulted in poor oxidation resistance. In cross section, these samples were found to have iron and manganese oxides and silicates. The manganese was intentionally added to aid oxidation resistance, however the presence of iron was due to contamination from the HIP can. Based upon the results of other, pressurelessly sintered samples with intentionally added iron (the results of which are shown in the next chapter)

the total iron contamination is estimated to be on the order of 1 at%. Although this is a low value, it has been found to cause extensive devitrification and spallation during oxidation at 1300℃. The existence of this contamination is surprising as the diffusion of iron in molybdenum is low at 1300℃ and the cans were lined with molybdenum foil to prevent contact with the samples. It is believed that a minor vapor species of iron, potentially a hydroxide formed during de-oxidation, was responsible for the low level but relatively uniform contamination. Additionally, the powder fired material qualitatively appeared to have most extensive devitrification, which would agree with the higher surface area of the steel wool in the tube ends providing a greater amount of a vapor species.

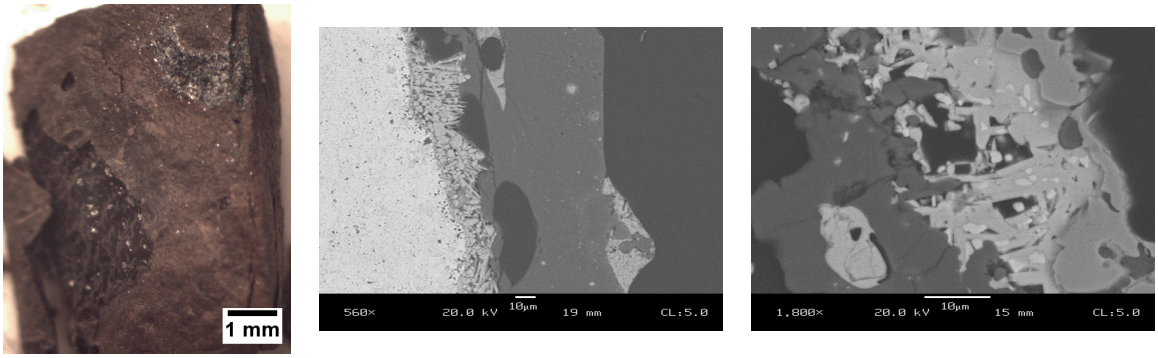

Figure 5.18: Appearance of Mo-Si-B composited HIP'ed in a low-carbon steel can after oxidation at 1300℃ for 90 minutes. Devitrification and spallation can be clearly seen in the surface apprearance (left). The SEM-BS images of the cross section show a more needle shape to the MoO_2 interlayer and extensive iron and manganese oxides on the surface.

5.3.2 Encapsulated in Titanium

As an alternative to using low-carbon steel cans, a couple Mo-Si-B samples were encapsulated in grade 2 (un-alloyed) titanium. Because of the far higher oxide stability and lower vapor pressures than iron, titanium did not contaminate the Mo-Si-B material. However, the sensitivity of titanium to hydrogen is greater due to the formation of hydrides. Hydrogen embrittlement of the low-carbon steel occurred by dissolution of hydrogen into the iron which reduced its plasticity during HIP'ing, but could be removed by evacuation at high temperatures during the firing cycle. In addition to solid solution hydrogen, titanium forms hydrides at temperatures up to around 800℃. These hydrides are very brittle and their formation causes a volume expansion, both factors which resulted in cracking of the

gas lines within the de-oxidation furnace during the initial portion of the firing.

Instead of entirely firing and HIP'ing within the same tube, the titanium encapsulated Mo-Si-B material was de-oxidized as powder in alumina boats. Figure 5.19 shows the dew point traces for this powder de-oxidation compared to the material previous run in low-carbon steel cans. Although the peak dew point and gas flow rates were similar (due mainly to the total amount of molybdenum), the more efficient gas transport without the steel can resulted in completion of the de-oxidation prior to ramping beyond 800℃.

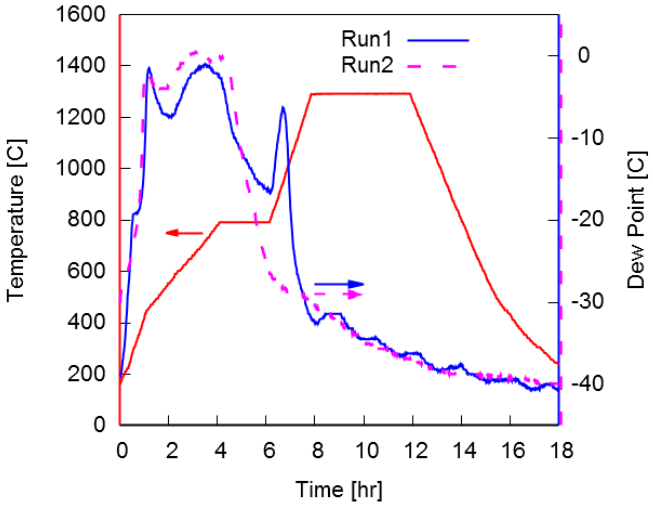

Figure 5.19: Temperature and dew point traces for both the Mo-Si-B compact in a low-carbon steel can (run1) and powder in alumina boats (run2) prior to HIP'ing.

After the de-oxidation and nitride decomposition cycle, the Mo-Si-B powder was poured into the prepared titanium can which was quickly evacuated and sealed. Although the powder transfer between the boats and HIP can was done under a blanket of argon, some oxidation likely occurred. In spite of these issues, a sample did consolidate successfully with a density measured at 98% of theoretical. The microstructure is shown in Figure 5.20 with another, pressurelessly sintered Mo-Si-B sample for comparison. Just as for HIP'ing in the steel can, the titanium encapsulated composite has a finer grain size.

Arguably more significant than the microstructural results was the oxidation performance of the titanium can'ed material, which had intentional manganese additions. The results are shown in detail in Section 6.2.7 however the good resistance and, more importantly, the lack of devitrification is evidence of (1) that manganese loss did not occur and

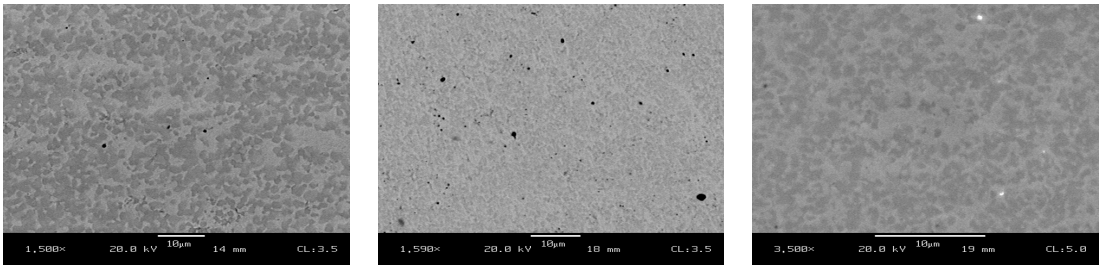

Figure 5.20: SEM-BS microstructures of pressurelessly sintered (left) and HIP'ed (middle and right) Mo-Si-B composites showing the reduced grain size and consolidation from HIP'ing. A titanium can was used to prevent sample contamination.

(2) that there was no contamination from the titanium can as titanium oxide would cause extensive crystallization [12]. The conclusion from this sample is that HIP'ing in titanium cans is a viable process for consolidating Mo-Si-B composites having minor manganese additions to improve their oxidation resistance. However, there is need for substantial improvements upon the present implementation. Because of the need for a high gas flow rate (during de-oxidation and nitride reaction/decomposition) and atmosphere control to prevent re-oxidation, specialized and dedicated equipment is needed. This could take the form of a vertical, fluidized-bed type reaction tube that could be tilted to pour powder into a prepared can or a separate glove box to manually transfer the powder from a standard furnace into the can. Neither approach is prohibitively difficult, especially considering the savings from processing at temperatures at and below 1300℃ compared to sintering at 1600℃.

CHAPTER 6

COMPOSITION TAILORING FOR OXIDATION RESISTANCE

6.1 Understanding Oxidation Behavior

The oxidation of Mo-Si-B composites is arguably the most complex behavior of the material system due, in large part, to the number of reactions and interactions. Chemical reaction and transport occurs at and across solid, liquid, and gas phases with properties changing significantly both over time and at different temperatures. In order to simplify this problem, this work has focused on oxidation at 1300°C and in laboratory air, as described in Section 4.2. However, even for just these conditions, the critical material aspects for oxidation resistance needed to be investigated. The published literature contains little compositional variation, few results over consistent times and temperatures, and certain inconsistencies which are likely due to differing experimental conditions. Given the wide compositional flexibility afforded by the processing techniques developed in this work, a sizable effort on understanding the oxidation behavior has been done to establish the role of composition on developing oxidation resistance, as well as a general understanding of the oxidation mechanisms. Based upon this work, an oxidation model has been developed with the intent of both understanding Mo-Si-B composite oxidation and to aid in optimization of compositions for oxidation resistance.

Many published oxidation results of the Mo-Si-B system are not particularly applicable to the composite development here due to having a discontinuous αMo phase. Often researchers have evaluated Mo-Si-B materials that are cast (resulting in primary αMo solidification), are father away from the molybdenum rich portion (such as systems with approximately 1/3 αMo), or are in the T1-T2-A15 field [2, 74, 90, 91, 94, 115, 125]. The critical difference between these systems and one with a continuous αMo phase is whether or not the oxidation "front" proceeding normal to the surface can be completely terminated by silicon and boron containing phases. If this is true, then the need for the borosilicate

to spread is far less. As an extreme example, the boron-doped T1 type materials do not rely upon flow of the borosilicate melt. They are instead optimized with a far lower boron content which only acts to speed up the densification, though viscous sintering, of the highly porous silica that forms during oxidation of T1 [2]. However, in the interest of mechanical properties (such as toughness from crack trapping), a continuous αMo matrix is desired. The presence of a continuous, αMo matrix during oxidation makes the formation of an oxidation resistant scale more difficult. As this matrix lacks any oxidation resistance, it can instead form a continuous network of internal channels, if the borosilicate does not coat the surface. Obtaining both mechanical toughness and oxidation resistance puts greater demands upon the behavior of the protective borosilicate layer; both its ability to cover the material's surface and its role as a barrier to further transport.

The body of published works investigating Mo-Si-B materials with continuous αMo microstructures does not cover a wide range of compositions. Nearly all are based upon 3wt% silicon and 1wt% boron (9 and 8 at% respectively) and either substantial macro-alloying of chromium or titanium or a few minor additions including iron, nickel, and lanthanum [13, 12, 28, 72, 107]. While the minor additions are relevant to the work here at 1300℃, the Si/B ratio is of more concern as it primarily dictates the borosilicate's properties.

Additionally, most proposed theories of the oxidation process have a two stage process which generally reflects the overall weight loss behavior. These stages are, first, a transient during which the borosilicate layer is developed, and then a steady state stage once the surface layer is protective. While these two stages are important, they are not a sufficiently complete description and do little to inform material development. Observations of numerous samples without oxidation resistance implies that the critical step in the overall process is the development of a *sufficiently thick* and continuous borosilicate coating. Many samples within a wide variety of compositions have shown persistent holes, channels, or bubbles within and throughout the borosilicate layer. The question of how to eliminate these features is one of controlling the transition from the initial, transient stage to the protective steady state. The results presented in this section have lead to the development

of a three stage theory for oxidation focused upon the transitions between: exposed molybdenum with limited borosilicate formation, a thin *but not* protective coating, and finally a sufficiently thick and thus protective layer. The details of this three stage theory are given in Chapter 7.

6.2 Results of 1300℃ Oxidation Testing

The reported oxidation resistances of Mo-Si-B materials has considerable variability, particularly at the upper most temperatures evaluated. In the work of Helmick and Middlemas, Mo-3wt%Si-1wt%B is found to have good resistance at 1100℃, inconsistent at 1200℃, but then consistently poor performance at 1300℃[45, 77]. On the other hand, Burk and Berczik show very good oxidation resistance at all these temperatures [11, 7]. Unfortunately none of these authors offer an explanation for the differing results. At the inception of the research reported here, the behavior of Mo-3wt%Si-1wt%B was found to be consistent with the results of Middlemas, which is to be expected as the processing and evaluation techniques he developed were the staring point for this work.

Three different batches of compositions near Mo-3wt%Si-1wt%B have been produced at separate times for various performance and processing evaluations. Regardless of any processing differences, the three batches have shown a consistent oxidation behavior and are in agreement with the results of Middlemas [77]. While reasonably resistant to oxidation at 1000 and 1100℃, the samples have little protection at the critical temperature of 1300℃. After a typical period of rapid initial weight loss, during which the expose molybdenum oxidizes and evaporates, the weight loss behavior slows to a still relatively high, relatively linear rate as shown in Figure 6.1. This behavior is indicative of a borosilicate surface layer which only slightly restricts oxidation.

The morphology of the oxidation layer on Mo-3wt%Si-1wt%B samples after a few hours at 1300℃ was consistently found to be a thick surface borosilicate layer with many large openings and some entrained bubbles. This morphology was similar to Helmick's observations of some samples tested at 1100℃ [45] but is quite different from the results of Burk and the data presented in the patents of Berczik [11, 7]. Based upon the results given

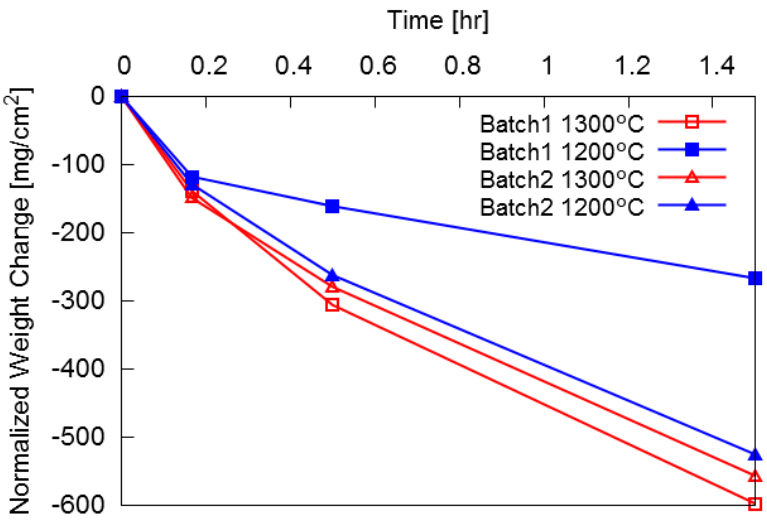

Figure 6.1: Surface area normalized weight loss for two hours of oxidation at 1300°C of Mo-3wt%Si-1%B.

throughout this chapter it is believed that both slight material contamination and the experimental setups used for oxidation testing could be the source of the discrepancies over Mo-3wt%Si-1wt%B.

The pursuit of understanding why some Mo-3wt%Si-1wt%B samples are reported to have dramatically better oxidation resistance at 1300°C than others lead to exploring the mechanisms involved in the oxidation of Mo-Si-B materials. Of particular interest was the evolution of the surface borosilicate and why open holes or channels would persist instead of forming a smooth and dense layer. The porous glass was consistently observed here however, it was unclear if its origin was from a very fluid borosilicate being pushed aside by evaporating molybdenum oxide or if the borosilicate itself was too viscous to spread and inhibit molybdenum oxidation in the first place. Because only limited observations are possible from interrupted oxidation testing, samples of varying compositions were produced in order to change the borosilicate's viscosity and observe the effect upon oxidation. Three compositions were made with slightly different silicon and boron amounts; a higher viscosity at 3.2wt%Si-1wt%B, a lower at 3wt%Si-1.2wt%B, and an intermediate at 3.1wt%Si-1.1wt%B. The silicon to boron atomic ratios of these three are 1.2, 0.96, and 1.1 respectively. Additionally a composition of 3.9wt%Si-1.5wt%B (Si/B atomic ratio of 1) was produced for

comparison to another published work that found oxidation resistance at 1300℃ [90].

Of the samples with compositions slightly adjusted from Mo-3wt%Si-1wt%B, none showed oxidation resistance at 1300℃. Their behavior was in fact very consistent and in line with the Mo-3wt%Si-1wt%B samples. Figure 6.2 shows the surface appearance after 3 hours at 1300℃ for the 3.1wt%Si-1.1wt%B sample on the left. The 3.9wt%Si-1.5wt%B, shown on the right of Figure 6.2, had a better appearance than the samples with higher molybdenum contents however, it too had some holes in the glass and a relatively high, linear oxidation rate. Unfortunately, as this sample was also only 87% dense, it can't be reliably compared to the published results [90].

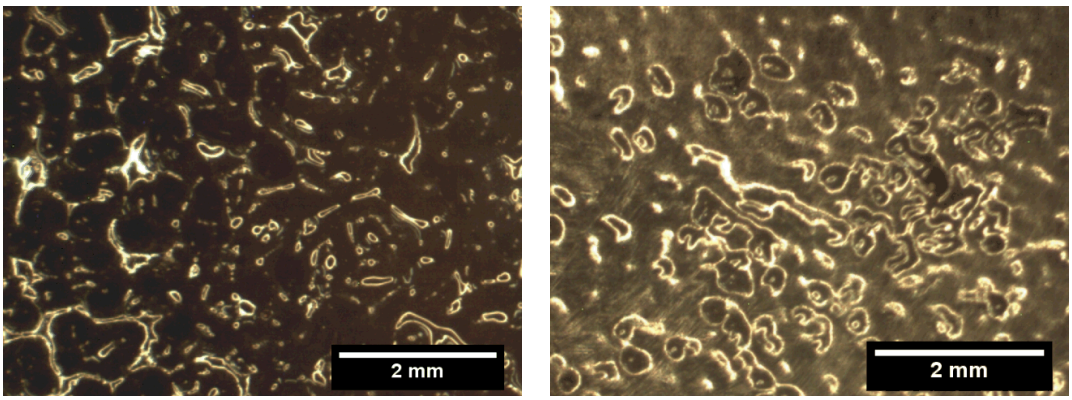

Figure 6.2: Surfaces of Mo-3.1wt%Si-1.1wt%B (left) and Mo-3.9wt%Si-1.5wt%B (right) after 3 hours of oxidation at 1300℃. Both show open holes which are associated with a high oxidation rate.

6.2.1 Mo - 3wt%Si - 1wt%B with Iron and Nickel Minor Additions

With no change in 1300℃ oxidation found for slight variations in Si/B ratio, and alternative approach of improving Mo-Si-B composites was needed. Two pieces of literature, Sossaman's and Woodard's [107, 124], specifically claim improved high temperature oxidation resistance of nominally Mo-3wt%Si-1wt%B through the minor additions of iron and nickel. Additionally, some other publications show interesting and sizable effects from other minor additions, though not necessarily improvements at high temperatures. Two batches were produced with separate additions of either iron or nickel in Mo-3wt%Si-1wt%B to determine if the improvements at 1300℃ could be reproduced. The concentration of iron and nickel in the composites, 0.5wt%, was between those used by Sossaman and Woodard.

At this point onward, modifications to base Mo-Si-B compositions will be referred to based upon their theoretical concentration in the borosilicate glass upon oxidation. This will be called the equivalent glass and is calculated as if all the molybdenum was removed and the remaining constituents fully oxidized. For these two iron and nickel modified compositions, the equivalent glass would contain 5.3mol% FeO or NiO. The oxidation testing at 1300°C of these sample showed significantly improved behavior at short times for both compositions, Figure 6.3.

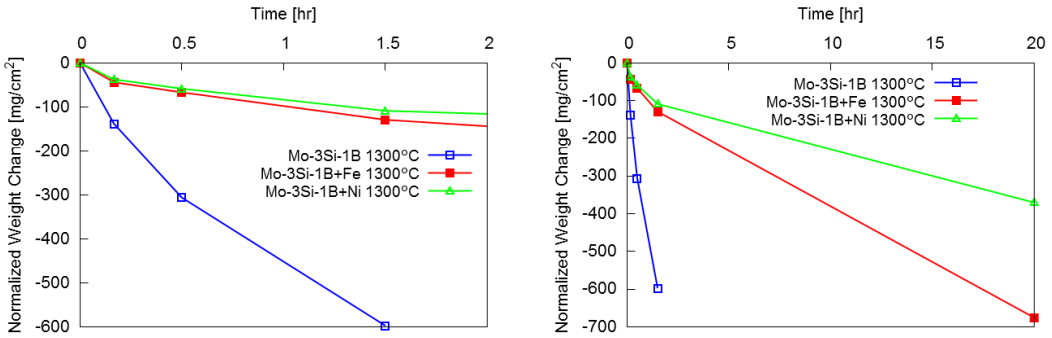

Figure 6.3: Oxidation of Mo-3wt%Si-1wt%B at 1300°C compared with additions of Fe and Ni. First 2 hours at left.

Although the initial oxidation behavior of samples modified with iron and nickel was promising, the relatively thin surface borosilicate broke down over moderate times, leading to a moderate weight loss rate and, in the case of Fe, nearly compete consumption of the sample within 20 hours. The mechanisms by which these two compositions failed are different, not just from each other but from the base Mo-3wt%Si-1wt%B. Cross sections of Ni containing samples after 45 minutes and 20 hours of oxidation show a nearly continuous layer of nickel oxide or Ni-silicate on all surfaces between the borosilicate melt and air or other gases, Figure 6.4. While some regions on the samples appeared protected by the borosilicate others, after 20 hours, suffered from "internal/channel oxidation" similar to that seen by Middlemas and Helmick [77, 44]. The considerably higher weight loss of the iron modified composition is reflected in the structure of its oxidation layer. Like the Ni containing sample, some iron oxide or silicate particles are seen on the gas surface of the borosilicate however, both phase separation and devitrification of the borosilicate occurred between 45 minutes and 20 hours of oxidation, Figure 6.5. The presence of phase separation,

devitrification, and surface silicates is indicative of an unstable and mobile borosilicate melt which would likely not be and effective barrier to oxidation and resulted in the high oxidation rate measured here.

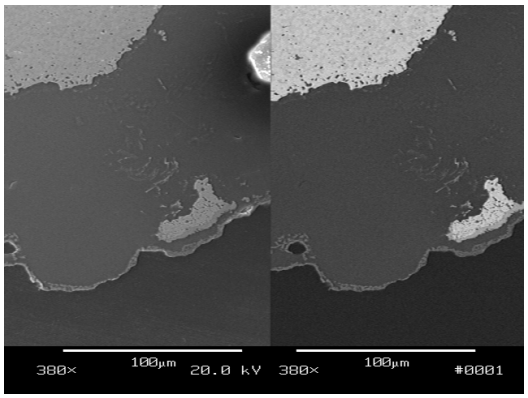

Figure 6.4: Cross section of oxidized Mo-3wt%Si-1wt%B with Ni addition at 1300℃ after 20 hours.

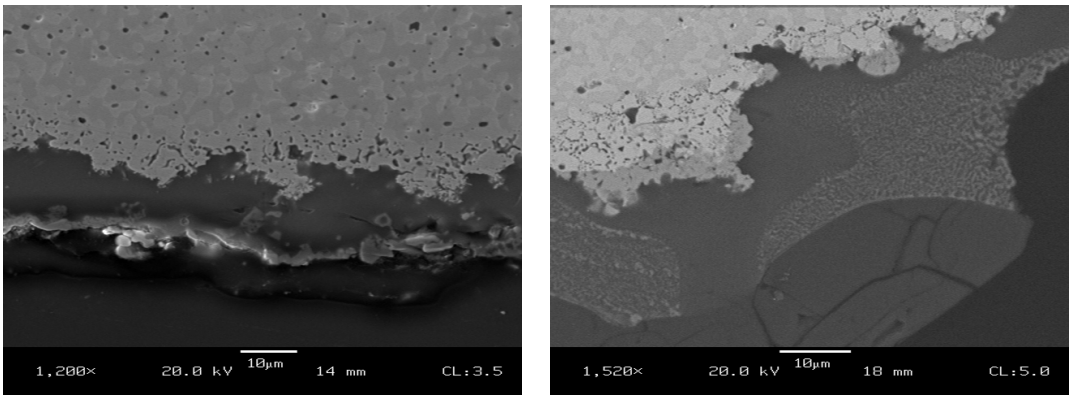

Figure 6.5: Cross section of oxidized Mo-3wt%Si-1wt%B with Fe addition at 1300℃ after 40 minutes (left) and 20 hours (right).

The presence of rapid oxidation pathways arising from either cracking of crystalline silicates or the more fluid member of any phase separation are believed to cause the moderately high oxidation rate of iron and nickel modified samples. Both of these issues with the borosilicate are familiar problems in traditional silicate glasses and suggest that an improved borosilicate composition is needed. As the borosilicate behavior is primarily dictated by the Si to B ratio, subsequent compositions were produced and evaluated with varying Si/B ratios. Iron and other additives were still included, generally at lower levels, as their beneficial effect upon the initial oxidation at 1300℃ is quite significant. However, nickel

was abandoned due to the formation of the NiMo intermetallic phase on grain boundaries. While this phase does aid in sintering, it profoundly reduces the material fracture toughness [51].

6.2.2 Variation in Si-to-B ratio with Cobalt, Iron, Manganese, and Yttria Additions

The initial oxidation results of Mo-3wt%Si-1wt%B with either iron or nickel additions showed that relatively minor levels of transition metals can significantly improve oxidation resistance at 1300℃. However, this is only one factor in the development of truly oxidation resistant composites. In the development work here, three factors are considered most significant: the silicon to boron ratio, type of transition metal additive, and the addition amount. Based upon processing compatibility and known glass or glaze behavior, a number of transition metals were evaluated. The results of cobalt, iron, manganese, and yttrium were positive enough to warrant further study.

While down selection of these additives is an important factor to the composite development, it is considered second to the silicon to boron ratio in dictating the properties of the borosilicate melt. The results in this section have been selected specifically to show the effect of the Si/B ratio for four different additives with the additive amount held roughly constant. This was of particular interest due to the observed holes and open channels during 1300℃ oxidation of the base Mo-3wt%Si-1wt%B without additives. The underlying mechanism forming these features, and why they persisted during oxidation, was not clear. If the borosilicate was of too high a viscosity then its viscous flow would be too sluggish to "close" holes and thus lead to channel formation. If, on the other hand, the viscosity was too low then the partial pressure of molybdenum trioxide could oppose the melt flow and again lead to persistent channels. This mechanistic uncertainty motivated the evaluation of compositions covering a wide range of Si/B ratios with viscosities over nearly three orders of magnitude at 1300℃.

Although the following results allow for reasonably direct comparisons between compositions, some sample to sample differences should first be mentioned. In addition to the

composition development, simultaneous work was being done on both processing development and understanding of the oxidation mechanisms. Over the time frame in which these samples were produced, three changes were made to processing and the oxidation procedure. First, processing improvements in effectively deoxidizing samples prior to sintering resulted in a furnace atmosphere that reduced manganese oxide, allowing for evaporation of metallic manganese. This limited the manganese results to only those performed early on and without subsequent improvements to the testing methodology. The second change related to this oxidation furnace atmosphere. Most of the early testing was done in a bottom loading box furnace, while a tube furnace was used for later testing. In both cases the atmosphere was static, laboratory air but some differences were seen and will be expanded upon in later sections. Finally, the sample surface preparation varied among some of the results presented here. Most samples were taken as-fired and simply cut in half, exposing both the as-fired and internal surfaces to oxidation, and revealing any processing effects. However this does not yield the true, material oxidation rate and so some samples had their as-fired surfaces ground off. The overall effect though, was observed to be far less significant that the composition. The effects of these three changes are most significant during the first 10 minutes of oxidation so, to aid in making sample to sample comparisons, the oxidation rates between 10 and 30 and between 30 and 90 minutes will be used instead. The weight loss magnitudes and borosilicate thicknesses will be expanded upon in the subsequent sections dealing with individual compositional series.

Samples containing silicon to boron ratios between 1 and 4.77 at% were subjected to interrupted oxidation at 1300℃ and their weight losses measured at 10, 30, and 90 minutes. All samples had a αMo fraction between 50 and 55 volume % and additives of either manganese, coblat, yttria, or iron. The addition amount was approximately 0.25 at% of the bulk or 1.7 at% of the equivalent glass.

The weight change between 10 and 30 minutes of oxidation is shown in Figure 6.6, expressed at the weight loss per hour normalized by the initial surface area. Because the majority of the borosilicate surface layer forms before 10 minutes, the weight loss rate immediately thereafter represents the ability of the borosilicate to become protective. This

degree of protection can also be seen in Figure 6.7 which shows the oxidation rate between 30 and 90 minutes however, additional mechanisms can become significant at the longer time spent at 1300℃. Particularly the evaporation of boron oxide and silicate devitrification manifest themselves in this later time frame. A decrease in the oxidation rate between 10 to 30 and 30 to 90 minutes represents a borosilicate layer with decreasing gas transport due to an increase in viscosity via boria loss. In some samples however, an increase in the oxidation rate at the longer times is seen, which corresponded to devitrification of the borosilicate.

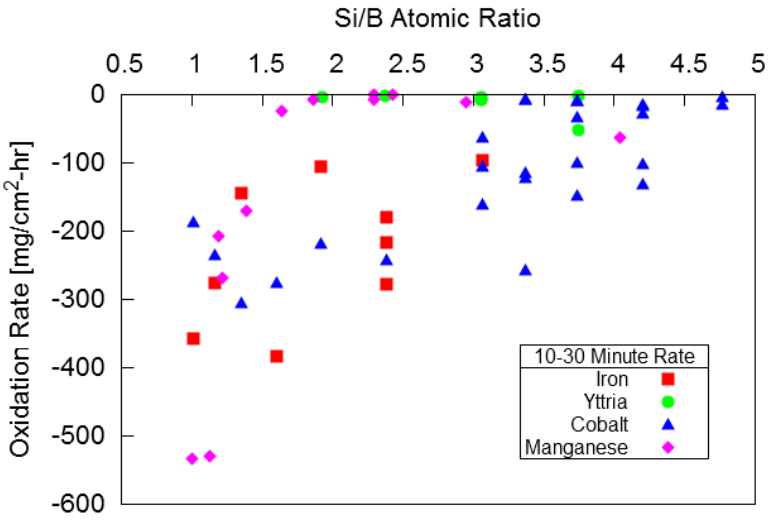

Figure 6.6: Weight loss rate between 10 and 30 minutes of oxidation at 1300℃ in $^{mg}/_{cm^2 \cdot hr}$ for samples of various Si/B ratios and additions of manganese, cobalt, ytrria, and iron.

In Figure 6.6, higher Si/B ratios have greater oxidation resistance. From a material development standpoint this is a significant conclusion and it explains the poor oxidation behavior seen for Mo-3wt%Si-1wt%B samples for which the Si/B atomic ratio is too low at 1.13. The optimal Si/B ratio across all sample sets here is located in the range of 2 to 3 which corresponds to a borosilicate of 80 to 85 at% SiO_2. The morphology of the surface borosilicate at the high and low Si/B extremes is also informative for understanding the observed behaviors. The persistent holes and channels existed for low Si/B compositions while at high Si/B, flakes of borosilicate spalled off during sample cooling.

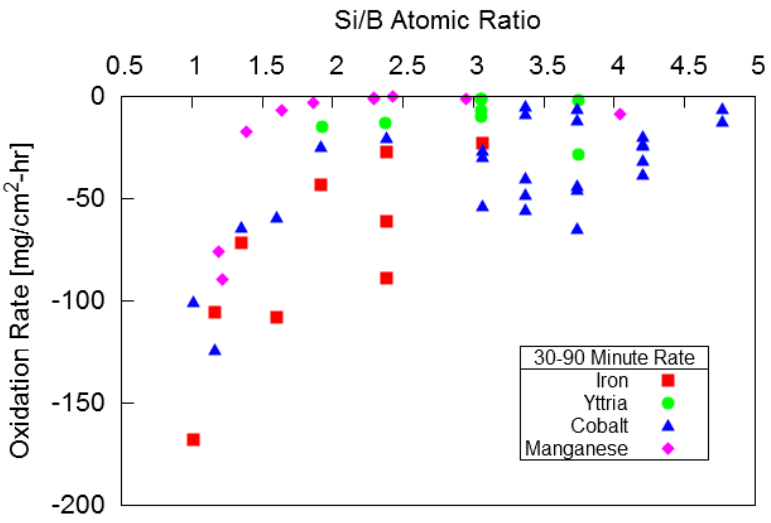

Figure 6.7: Weight loss rate between 30 and 90 minutes of oxidation at 1300℃ in $^{mg}/_{cm^2 \cdot hr}$ for samples of various Si/B ratios and additions of manganese, cobalt, ytrria, and iron.

6.2.3 Results of Iron Additions

The effect of iron additions, across many iron concentrations and Si/B ratios, was generally found to be beneficial during initial oxidation but then become detrimental, often with complete surface devitrification after only 90 minutes at 1300℃. The morphology of the initial borosilicate layer tended to have smaller and fewer of the holes which are associated with the poor oxidation of the base Mo-Si-B materials. This improvement is reflected in the reduced weight loss measured at 10 and 30 minutes of oxidation. The degree to which the initial surface morphology improved was found to be a function of both iron content and the Si/B ratio. At longer times however, a combination of phase separation, iron-species crystallization, and large scale devitrification of the borosilicate melt were observed and had a pronounced negative effect upon the oxidation resistance. Again, these processes were a function of the iron content and Si/B ratio, resulting in samples displaying complex, mixed behaviors.

As phase separation and crystallization are know to occur in glasses of high iron content [19, 50, 121], a variety of compositions were produced with reduced iron additions as well as higher Si/B ratios. The results of oxidizing these compositions at 1300℃ in a bottom loading box furnace will be compared at high, medium, and low iron content and across

Si/B ratios based upon morphological appearance.

The surface area normalized weight loss after 10 minutes of oxidation and the linear weight loss rates from 10 to 30 and 30 to 90 minutes are shown in Figure 6.8 for different iron additions as a function of the Si/B ratio. At only 10 minutes of oxidation, there is no clear trend with the Si/B ratio but the higher iron additions do perform best, having the lowest weight loss. However, the oxidation rates after the initial period have a clear trend with the Si/B ratio showing improved resistance at higher viscosities. Considering the 30 to 90 minutes rate as the best indication of long term oxidation resistance, the results indicate and optimum Si/B ratio between 2.5 and 3 with a moderate iron addition; 0.5 at% of the metallic phase or approximately 1.9 at% FeO in the equivalent glass. Higher oxidation rates were measured for the compositions both higher and lower in Si/B and iron content and this behavior is reflected in the sample's morphology, specifically open surface holes and/or devitrification.

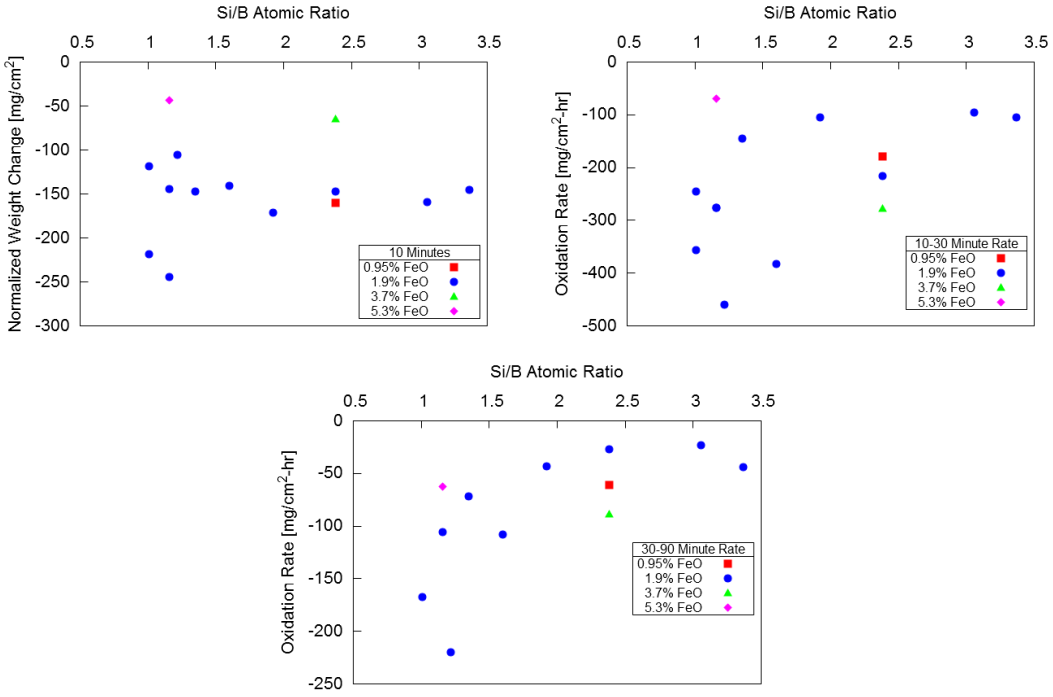

Figure 6.8: Surface area normalized weight losses of iron modified Mo-Si-B compositions oxidized at 1300℃ for 10 minutes, top left, and the linear rates between 10 and 30 minutes, top right, and 30 and 90 minutes, bottom

Considering the lowest iron addition first, the borosilicate oxidation layer resembled that

of the base Mo-Si-B composites with only a slightly improved appearance. This composition was batched at 0.25 at% Fe in the metallic phase which corresponded to a borosilicate melt of 0.95 at%FeO and a Si/B ratio of 2.4. Figures 6.9 and 6.10 show the surface appearance, optically, and cross section in backscattered-SEM. In the first image, Figure 6.9 left, taken after 10 minutes of oxidation, the many open holes in the borosilicate glass can be seen. However, after 90 minutes, the surface is mostly free of holes and nearly completely devitrified, Figure 6.9 right. The SEM images in Figure 6.10 give more insight into the structure at 90 minutes of oxidation. While the surface crystallization is too thin to be seen in cross-section, the many open holes have been replaced by a network of pores and channels within the borosilicate and beneath a mostly dense and continuous glass layer. Additionally a significant amount of molybdenum and MoO_2 is entrained within the thick regions of borosilicate glass, even very near the original sample surface. This is an indication of how the borosilicate can be protective, however, the pore and channel forming mechanism results in oxidation pathways circumventing these regions of local protection.

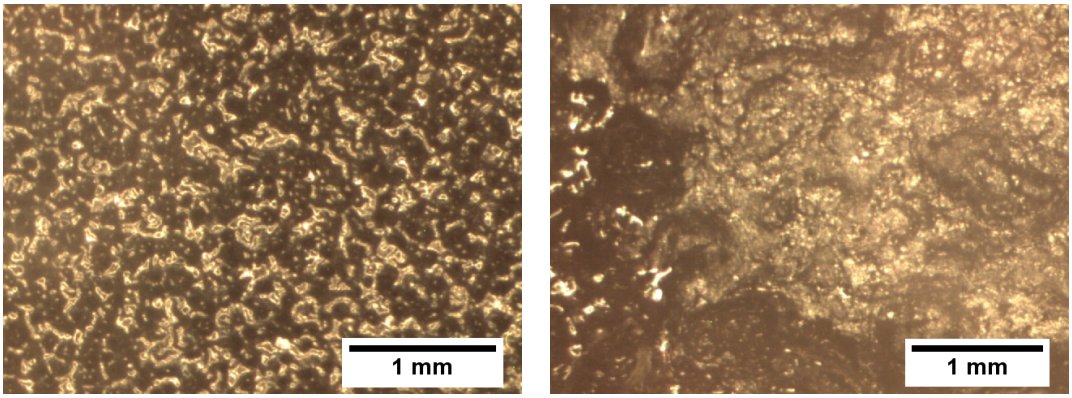

Figure 6.9: Surface of low iron addition Mo-Si-B composite oxidized at 1300℃ for 10 minutes, left, and 90 minutes, right. Open holes are apparent at 10 minutes while nearly complete surface devitrification has occurred by 90. The scale is approximate.

In contrast to the lowest iron additions, the samples with the most iron had the smallest weight loss at 10 minutes of oxidation and did not show the open holes characteristic of the base Mo-Si-B. However, these compositions also showed the most severe devitrification and phase separation longer times. Cross sections of this behavior have already been shown for the highest iron content in Figure 6.5. The surface of this sample at 10 minutes of oxidation,

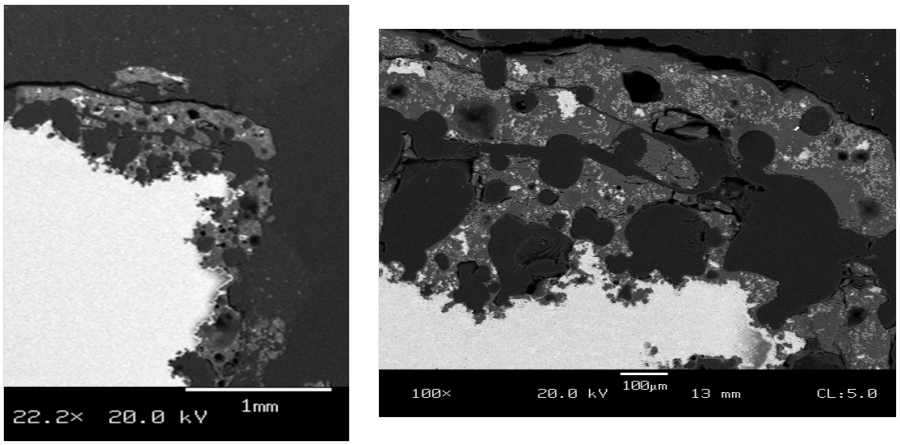

Figure 6.10: Cross section of low iron addition Mo-Si-B composite oxidized at 1300℃ for 90 minutes showing pores/ channels through the glass with entrained molybdenum oxide. The image on the right is a higher magnification of the same area. Both are SEM images in backscatter mode and the glass fractures are from sectioning and mounting.

shown in Figure 6.11, does not have any open holes but is also completely crystalline, with a reddish tint, unlike the typical glossy, black glass seen on the base Mo-Si-B samples. The weight loss up to 20 hours at 1300℃ was significantly improved over the base Mo-3wt%Si-1wt%B. However, extensive phase separation and devitrification were observed at 20 hours. Interestingly, a sample oxidized for just 40 minutes at 1300℃ had a dense and continuous surface borosilicate with limited surface crystallization and no indication of phase separation, Figure 6.5 left. The loss of protection arose from a change in the borosilicate behavior after 40 minutes. Comparing the two highest iron content samples, the higher iron one performed better both in terms of 10 minute weight loss and the two linear rates, Figure 6.8, but developed a red, crystalline surface much faster. In addition to differing iron contents (5.3 at% FeO verses 3.7% in the equivalent glass) the lower iron sample had a higher Si/B ratio. Its believed that the higher boron content allows the high iron concentration to improve the initial oxidation behavior by delaying the onset of devitrification associated with dropping below a critical boria concentration. Because of the high evaporation of boron species at 1300℃, any critical concentration of boria will be reached eventually, making high boron, high iron compositions not advantageous for long term oxidation resistance.

The need to balance the beneficial effect of iron addition on the initial oxidation resistance against the extensive devitrification observed for high concentrations lead to an

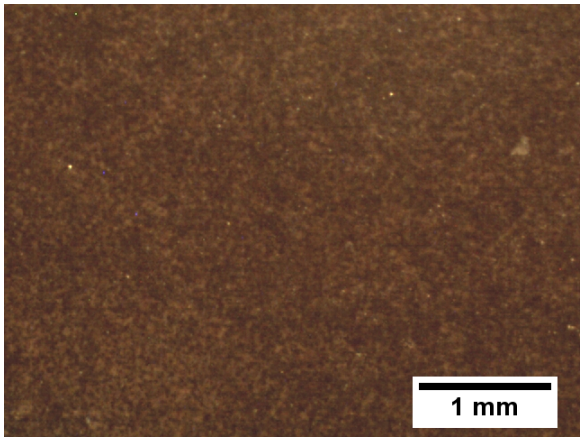

Figure 6.11: Surface of Mo-Si-B sample with the highest iron addition after 10 minutes of oxidation at 1300℃. Neither open holes nor any vitreous material is evident. The crystalline surface does have a red tint.

investigation of compositions with a moderate iron content across many Si/B ratios. For all these samples, the equivalent glass composition had 1.9 at% FeO. As seen in Figure 6.8, the best 30 to 90 minute oxidation rate was measured with a Si/B ratio just over 3. Below this value the weight loss rate increased with reducing Si/B. The surface morphology also changed significantly with the Si/B ratio and at different oxidation times. Figure 6.12 shows the surfaces after 10 and 90 minutes of oxidation for samples with three different Si/B ratios, 1.6, 2.4, and 3.1. At the shortest period of oxidation, 10 minutes, increasing the Si/B ratio reduced the appearance of open holes in the borosilicate resulting in, qualitatively, improved surface coverage. At the later oxidation times, 30 and 90 minutes, these three samples had differing behaviors. The lowest Si/B sample showed both coarsening of surface holes and growth of devitrified regions, Figure 6.12b.

Of particular note in Figure 6.12b is the structure of the devitrifying regions. Due to the low iron content, and verified in some samples by x-ray diffraction, the large crystalline regions are not fayalite (Fe_2SiO_4) or pure iron oxide but rather silica, either quartz or cristobalite. These crystals appear to be growing radially along the borosilicate surface and to have a red region at their growth front. This structure is believed to arise from an iron rich devitrification front in which the iron acts as a glass modifier allowing for the re-constructive transformation of amorphous to crystalline silica. However, due to the low

solubility of iron in either quartz or cristobalite, the iron is rejected from the devitrified region and thus accumulates in the growth front.

Unlike the mixed behavior of the low Si/B sample in Figure 6.12, the one with a Si/B ratio of 2.4 showed rapid surface devitrification and few holes at the later oxidation times. Figure 6.12d shows the complete devitrification at 90 minutes. Interestingly, the sample with an even higher Si/B ratio, 3.1, had less devitrification with the extent of surface crystallization in between the 1.6 and 2.4 samples at 30 and 90 minutes, Figure 6.12f. However, and crucially, there was little evidence of open holes on the surface, and this is credited with the lower weight loss rate for higher Si/B. The cross sections of these three samples after 90 minutes of oxidation are shown in Figure 6.13. All have pores and channels below a mostly dense borosilicate, considerable amounts of molybdenum entrained in the glass, and cracks parallel to the sample surface. However, these structures are at different size scales being smaller and thinner at the higher Si/B ratio.

Extension of the trends of reduced weight losses and thinner surface layers with higher Si/B would theoretically lead to a material considered oxidation resistant, however, the tendency for devitrification and spallation was observed to increase at even higher Si/B ratios. The majority of the iron modified samples were not oxidized beyond 90 minutes due to observed cracking and spallation of the borosilicate during the interrupted oxidation testing. This issue was most severe for the highest Si/B ratio tested, 3.4, which also had extensive devitrification. In all these samples, cracking occurred parallel to the substrate and is attributed to the thermal expansion mismatch between the base composite (CTE appoximatly 5ppm/°C) and low expansion devitrified regions (quartz or cristobalite). It was concluded that high viscosity, iron modified Mo-Si-B composites would not obtain oxidation resistance due to their high devitrification tendency.

6.2.4 Results of Cobalt Additions

Modification of Mo-Si-B composites with minor additions of cobalt showed improvements in oxidation resistance beyond those of iron additions as well as revealed more aspects of the various mechanisms occurring during oxidation. Compositions were evaluated to higher

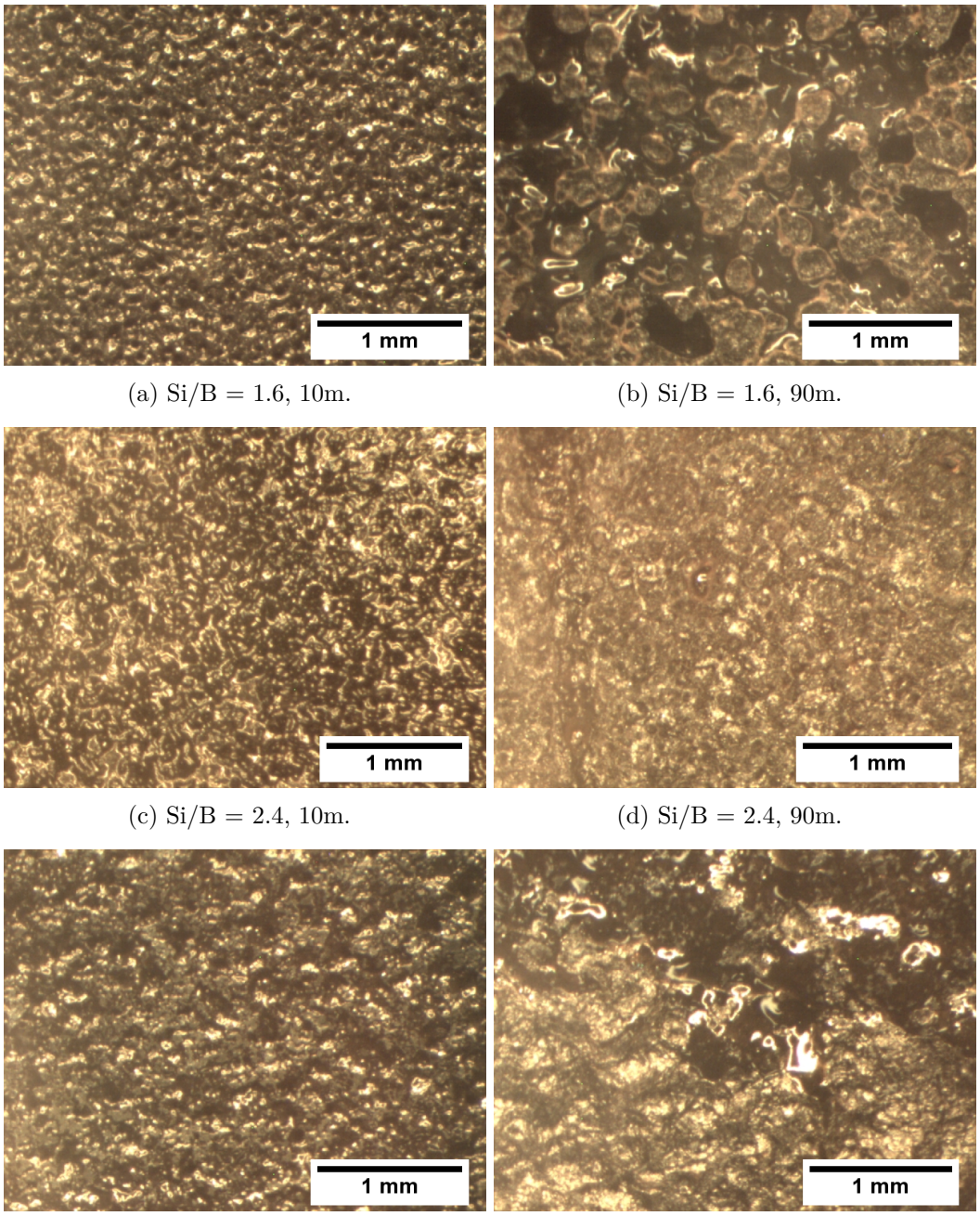

(a) Si/B = 1.6, 10m. (b) Si/B = 1.6, 90m.

(c) Si/B = 2.4, 10m. (d) Si/B = 2.4, 90m.

(e) Si/B = 3.1, 10m. (f) Si/B = 3.1, 90m.

Figure 6.12: Surface of Mo-Si-B samples with a moderate iron addition and various Si/B ratios after 10 and 90 minutes of oxidation at 1300℃.

Si/B ratios and to lower, but not higher, transition metal contents. Importantly, a change in the furnace used for oxidation was made during the evaluation of cobalt containing samples. The initial oxidation testing was done in a bottom loading box furnace, the same as used

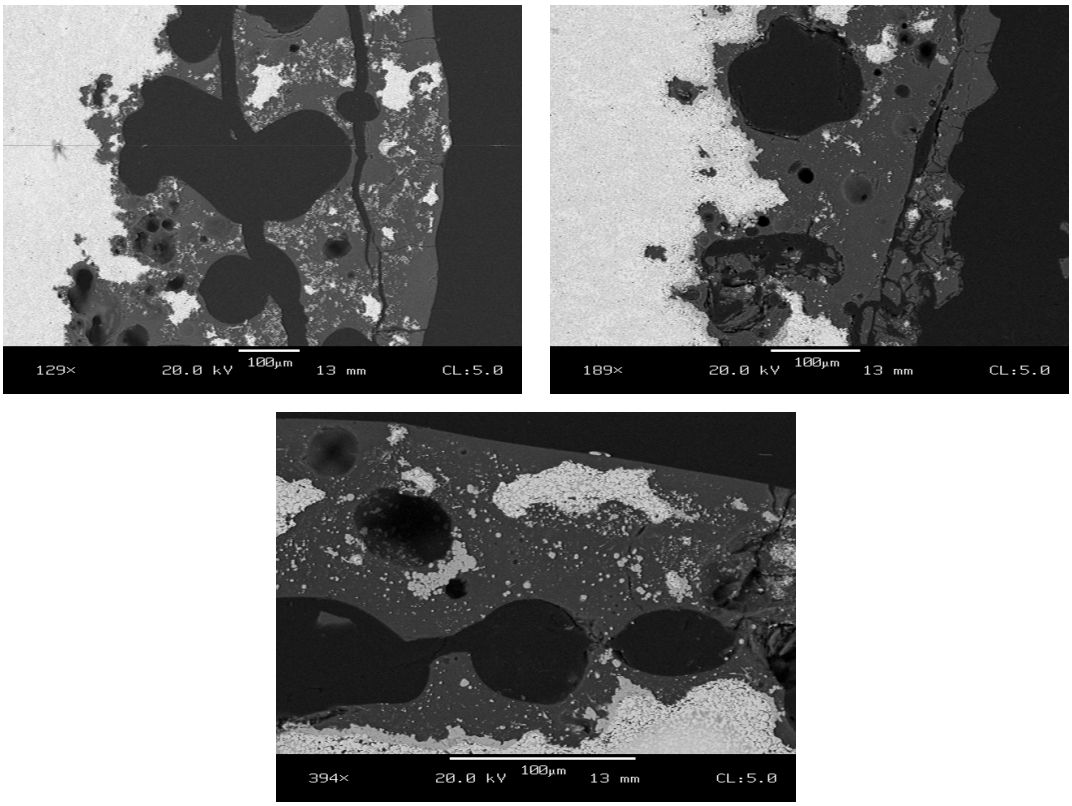

Figure 6.13: Cross sections of 1.6 (top left), 2.4 (top right), and 3.1 (bottom) Si/B ratio samples with a moderate iron addition after 90 minutes of oxidation at 1300℃.

for the iron containing samples. However, due to concerns with molybdenum oxide build-up and stagnant atmosphere effects upon oxidation, the later samples were oxidized in a horizontal tube furnace. While the furnace change did result in better oxidation resistance, the impact on oxidation performance is less than that of the range of compositions studied. This compositional effect will be discussed first followed by comparisons between samples of the same composition oxidized in the two furnaces.

The surface area normalized weight loss and weight loss rates are shown in Figure 6.14 as a function of Si/B ratio for samples with 50-55% by volume αMo and a CoO content of 1.9 at% in the equivalent glass. At 10 minutes of oxidation, two pronounced groups are seen in which the weight loss decreases with increasing Si/B. These two groups are split across a Si/B ratio of 3 with those samples of a larger Si/B having smaller weight losses than any of the samples of Si/B between 1 and 3. The significant jump between these two trends does not correspond to changes in experimental techniques nor the order in which the samples

were produced, and seems to be a result of the material behavior. Interestingly, the linear weight loss rates at longer oxidation times, taken to 30 and 90 minutes, show the opposite dependence upon the Si/B ratio, with the weight loss rates decreasing as the Si/B increases. The oxidation rate is more significant to the long term behavior than the 10 minute loss as can be seen in Figure 6.15 where the two groupings are still evident however the general trend is of lower total weight loss at 90 minutes for higher Si/B.

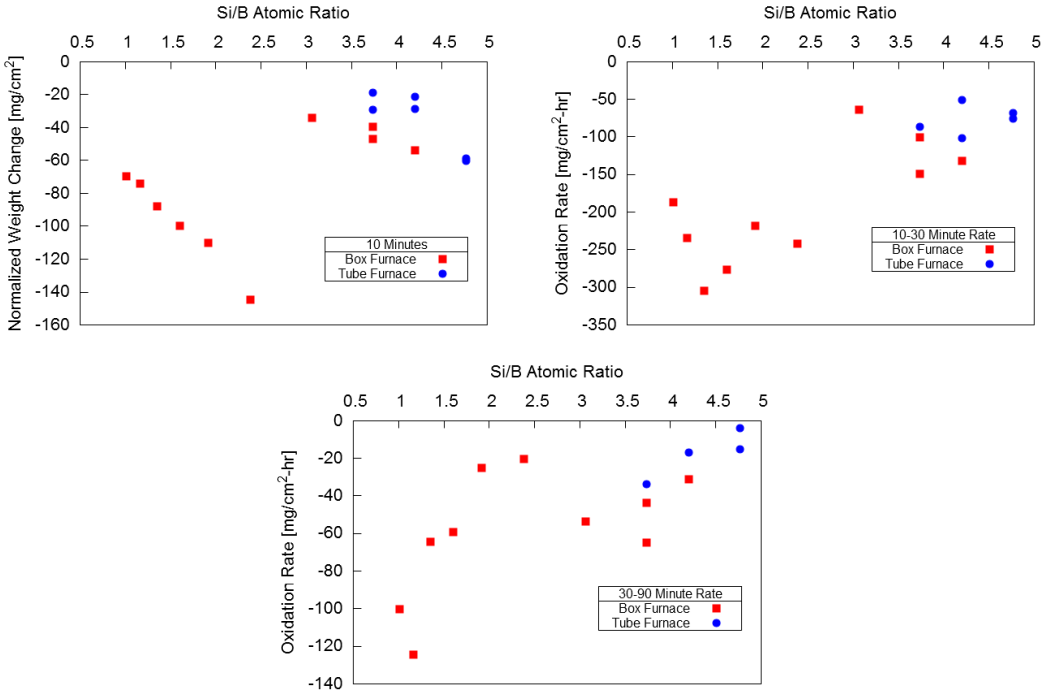

Figure 6.14: Surface area normalized weight losses of Cobalt modified Mo-Si-B compositions oxidized at 1300℃ for 10 minutes, top left, and the linear rates between 10 and 30 minutes, top right, and 30 and 90 minutes, bottom

While the measured weight loss indicate a dramatic change in oxidation resistance around a Si/B of 3, the surface morphologies suggest a continuous change in behavior. After 10 minutes of oxidation the open holes in the surface borosilicate of low Si/B samples were progressively replaced by regions of a flat-glassy surface with increasing Si/B, Figure 6.16. The flat-glassy regions appeared to be in the process of breaking down by lateral oxidation underneath them occurring in shallow depressions in the surface. The extent to which this processes had occurred at 10 minutes increased with the Si/B ratio, as shown in Figures 6.16c and 6.16d. The differentiating factors between open holes and the depressions

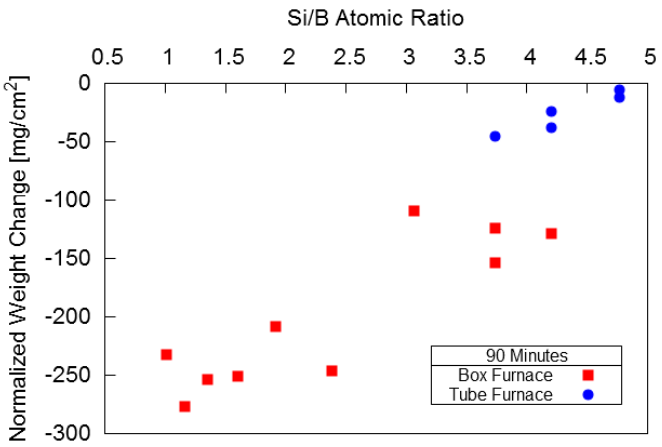

Figure 6.15: Surface area normalized weight losses of Cobalt modified Mo-Si-B compositions oxidized at 1300℃ for 90 minutes.

seen at higher Si/B are the more clearly defined edges to the flat-glassy regions around the depressions and the visible borosilicate at the bottom of the depressions. The appearance of the flat-glassy regions is the only surface morphology difference observed in samples above and below a Si/B ratio of 3.

As the oxidation progressed beyond 10 minutes, the initial surface of all samples became heavily devitrified. As in the iron modified compositions, the lowest Si/B samples showed less extensive devitrification than the mid range and the highest Si/B samples had delayed devitrification with some vitreous regions still present at 30 minutes. Figure 6.17 shows this devitrificaiton for cobalt modified samples after 90 minutes of oxidation as well as some spallation. Due to this spallation, the oxidation testing was terminated after 90 minutes. Surface layer cracking parallel to the base material was observed and attributed to the lower thermal expansion of the quartz or cristobalite surface than the bulk composite. In the mid range of Si/B ratios, this cracking resulted in spallation of large portions of the top and sides of the samples. The high Si/B ratio samples tended to suffer from spallation of smaller flakes revealing a pot-marked structure beneath the borosilicate layer with a reddish tint, Figure 6.17 on right.

Figure 6.18 shows cross sections of samples with Si/B ratios just below and above 3 after 90 minutes of oxidation. While similar at first glance, two aspects are significantly different. First, the oxidation layer (the borosilicate, pores or channels, and any MoO_2) is

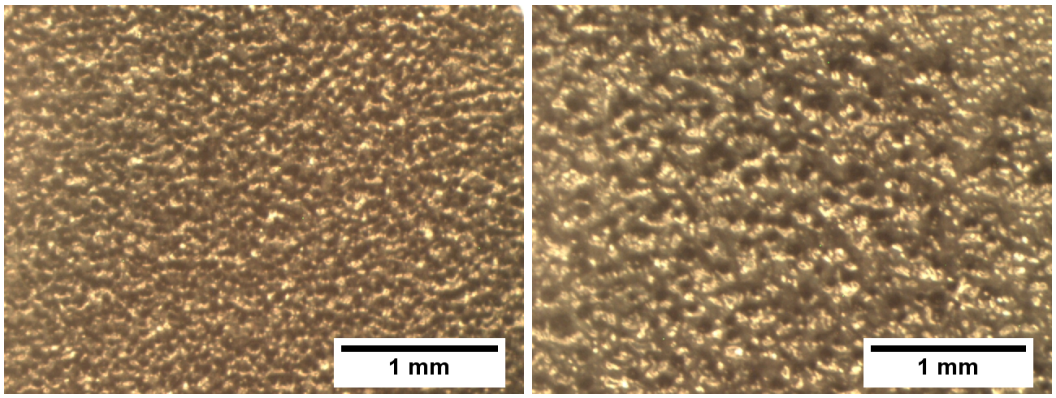

(a) Si/B = 1.0 (b) Si/B = 2.4

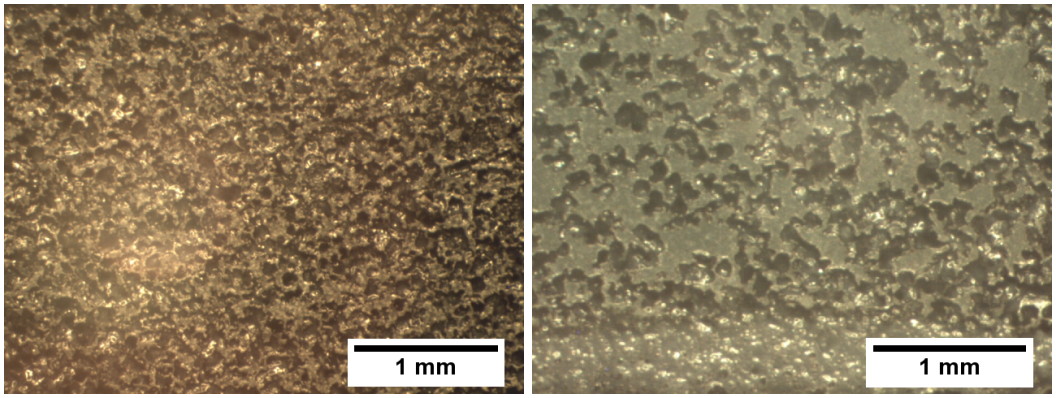

(c) Si/B = 3.1 (d) Si/B = 4.2

Figure 6.16: Surface of cobalt modified Mo-Si-B samples after 10 minutes of oxidation at 1300℃. Open holes in the borosilicate are present in (a) and (b) while (c) and (d) show a partially broken down flat surface with borosilicate visible at the bottom of the depressions.

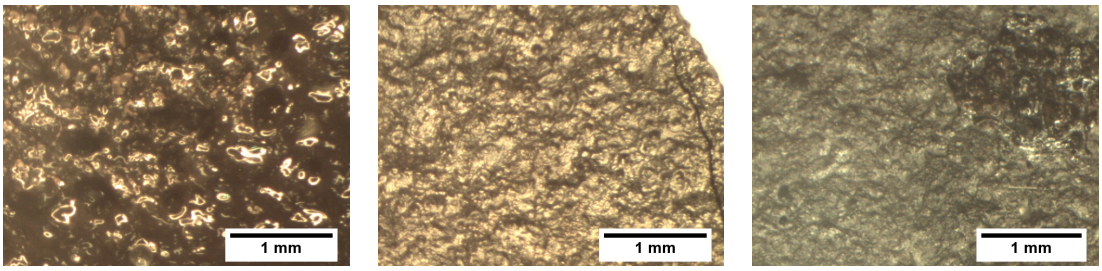

Figure 6.17: Surface of cobalt modified Mo-Si-B samples after 90 minutes of oxidation at 1300℃. Left to right the Si/B ratio is 1, 1.9, and 4.2.

considerably thinner for the Si/B ratio of 3.1. Second, the lower Si/B ratio sample has far more molybdenum and/or MoO_2 entrained within the borosilicate. These features, along with the existence of flat-glassy regions at 10 minutes, are the only morphological differences observed between samples below and above a Si/B ratio of 3. The behavior of the initial

flat-glassy regions and whatever mechanisms lead to the thinner oxidation layer with less entrained molybdenum are related to the improved oxidation resistance for higher Si/B compositions and therefore warranted further investigation.

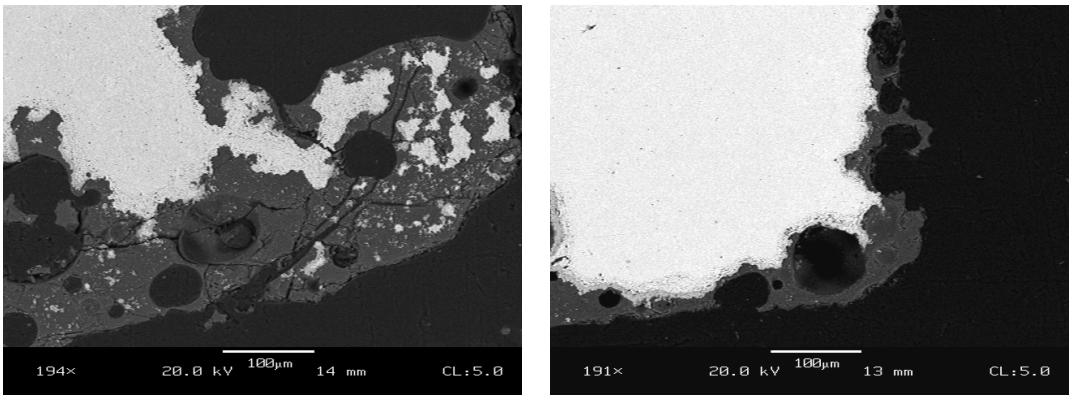

Figure 6.18: Cross sections (SEM-backscatter) of cobalt modified Mo-Si-B composites after 90 minutes of oxidation at 1300℃. The Si/B ratio is 1.9 on left and 3.1 on right. The higher Si/B ratio results in a thinner borosilicate layer with less entrained molybdenum. The borosilicate appears gray, in between the brighter molybdenum composite and black epoxy mount.

6.2.4.1 Short Time Oxidation

The presence, and subsequent breakdown, of the flat-glassy regions had not been observed prior to the cobalt modified compositions and prompted an investigation into oxidation at shorter times. Four quarters of a sample pellet with a Si/B ratio of 3.7 were polished on top and bottom and then oxidized in the tube furnace for periods of 1, 2, 6, and 10 minutes. While heating and cooling was minimized by quickly pushing the samples into or out of the 1300℃ furnace, it was still a significant portion of the 1 and 2 minute durations. Qualitatively, the samples would appear to have the same brightness of the surrounding furnace walls approximately 20 seconds after being inserted into the hot zone. Figure 6.19 shows the surfaces of these samples in both optical and SEM-secondary imaging. At and beyond 2 minutes the surface borosilicate is smooth and continuous with some indication of collapsed bubbles. At 1 minute however, both a flat borosilicate and undercutting depressions are present. Comparing the surface area normalized weight losses of these four samples with

the results of a separate sample of the same composition but subjected to interrupted oxidation of 10, 30, and 90 minutes reveals that the initial oxidation occurs very quickly and that there is little weight loss between 1 and 10 minutes, Figure 6.20. Beyond 10 minutes however, additional oxidation mechanisms dominate causing an increase in the oxidation rate.

6.2.4.2 Interpretation of Weight Loss Behavior

A theory was developed specifically to explain the varying short, mid, and long term oxidation behavior and will be briefly summarized here for the cobalt modified results. Excluding devitrification, the progression to oxidation resistance follows three stages, each characterized by different dominating phenomenon. In the first stage, areas of αMo are exposed to air and oxidize simultaneously with the T2 and A15 grains. The high oxidation and evaporation rate of pure molybdenum dominates the overall behavior, however the contribution of the αMo oxidation to the total weight loss becomes progressively smaller as the exposed area fraction of pure molybdenum decreases. In its place, a thin and dense borosilicate melt layer will form with a thickness and morphology dependent upon the surface wetting and borosilicate fluidity. Surface coverage by this borosilicate defines the start of the second phase of oxidation. The borosilicate melt layer is, however, very thin, as was seen in the sample oxidized for only one minute. By a rough estimation, the oxidation needed to form a borosilicate layer just $5\mu m$ thick corresponds to around $10^{mg}/_{cm^2}$ and would consume around $12\mu m$ of bulk material. A borosilicate layer of this thickness is not considered to be protective when newly formed due to its high boria content. Not only does boria increase the permeability of silica glasses but it can easily lower the viscosity to the point where it is unable to suppress growth of MoO_3 bubbles. Because of this high oxygen transport and bubble growth, the second stage of oxidation is dominated by the nucleation, growth, and popping of MoO_3 bubbles within a thin and relatively fluid borosilicate.

Ideally, the second stage oxidation would progressively thicken the borosilicate layer through permeation controlled oxidation and molybdenum removal via bubbling. Increasing the borosilicate thickness lowers the underlying oxygen activity at the molybdenum

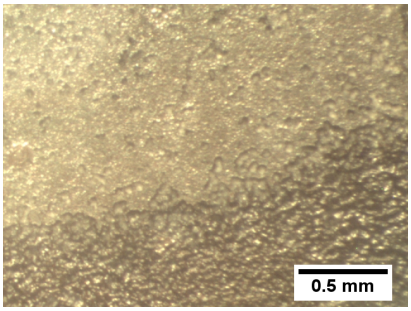

(a) 1 minute.

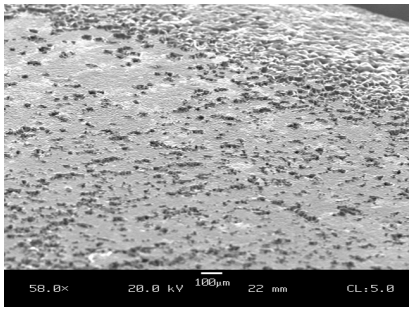

(b) 1 minute, SEM.

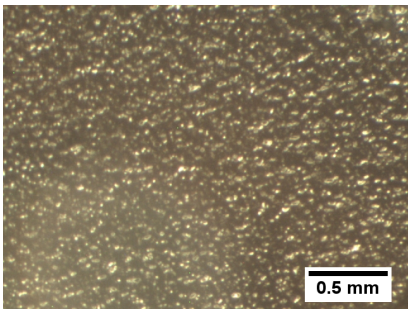

(c) 2 minutes.

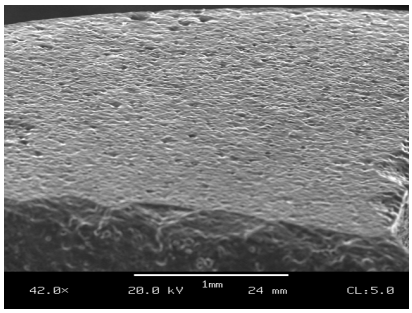

(d) 2 minutes SEM.

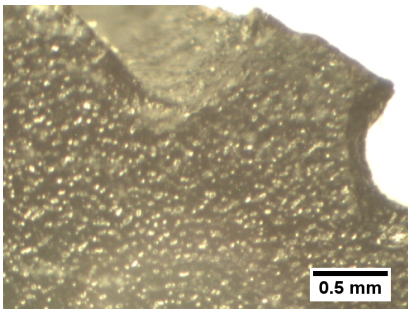

(e) 6 minutes.

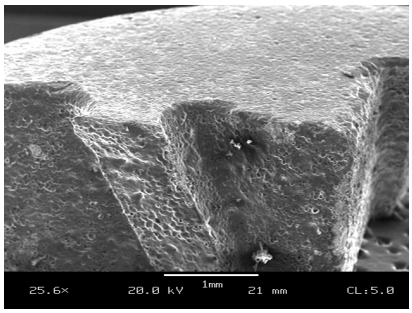

(f) 6 minutes, SEM.

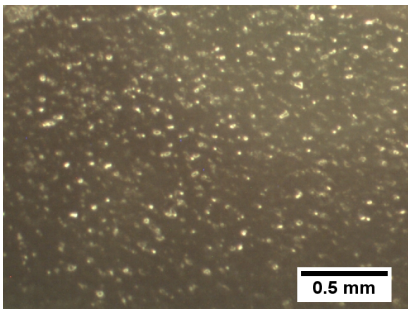

(g) 10 minutes.

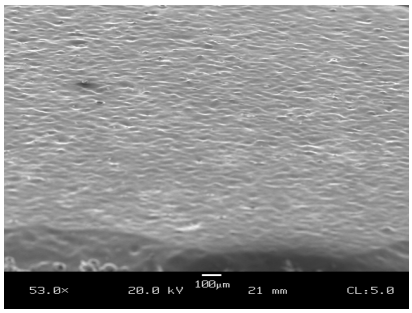

(h) 10 minutes, SEM.

Figure 6.19: Optical and SEM-secondary images of cobalt modified sample surfaces after 1, 2, 6, and 10 minutes of oxidation at 1300℃. The optical scale bar is approximate. Si/B = 3.7. The SEM images are of tilted samples to highlight topology.

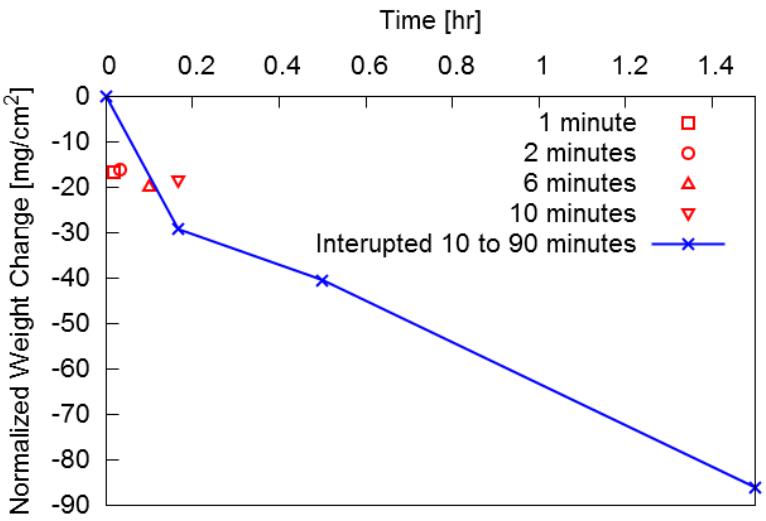

Figure 6.20: Surface area normalized weight loss of cobalt modified Mo-Si-B with Si/B = 3.7. Both the standard 10, 30, and 90 minute interrupted oxidation testing and single samples exposed for 1, 2, 6, and 10 minutes are shown.

containing phases. The transition to slow, parabolic oxidation occurs when the oxygen activity becomes too low for MoO_3 formation. However, the cobalt modified samples evaluated here deviated from this progression due to two additional phenomena: the borosilicate melt not fully leveling after bubble popping and thermal expansion related cracking followed by spallation. Both of these phenomena are strongly related to the boria content in the borosilicate melt. Because of boria evaporation at high temperatures, the melt composition depends upon both the bulk silicon and boron concentrations as well as the boria evaporation rate. Assuming that the boria evaporation is roughly constant between the samples of different compositions, the time to reach any specific boria concentration is inversely related to the initial sample composition. As the interrupted oxidation testing was performed at consistent durations of oxidation, 10, 30, and 90 minutes, the surface borosilicate composition at those times scaled with the bulk silicon to boron ratio.

Considering first the 10 minutes weight loss shown in Figure 6.14, the trend of increasing weight loss with increasing Si/B ratio is due to the occurrence of a high weight loss regime below a critical boria content in the borosilicate. Because all the samples experience boria evaporation, their weight loss is a combination of the time spent before and after reaching this critical boria content. The higher initial viscosity samples more quickly progressed

through the stages of oxidation, entering into the higher weight loss rate regime. This rapid oxidation was then a greater fraction of the total 10 minutes for these higher Si/B ratio samples, thus resulting in greater total weight loss.

Also evident in Figure 6.14 are two groups of samples having the same general trend but shifted in weight loss. The origin of the two groups of samples, above and below a Si/B ratio of 3, is because of differing rapid oxidation mechanisms. Below a Si/B ratio of 3 the borosilicate melt formed within the MoO_3 bubbles during stage two is sufficiently fluid that it does not coat the bottom of a bubble but rather accumulates on the sides of the bubble. This may be driven by either rapid and continuous bubbling forcing the melt away from the bottom or surface tension pulling the melt to the bubble walls. In either case an open channel forms which removes molybdenum from the bottom while entraining molybdenum or MoO_2 in its side walls.

Observation of the samples' surfaces showed that the open channel diameter increased with increasing Si/B ratio, such as in the top images of Figure 6.16. In general the coarser open holes can be associated with: lower viscosity, higher surface tension, or greater time for coarsening. The first two possibilities can be disregarded as (1) the opposite trend with Si/B was observed and (2) the surface tension is not expected to vary significantly between these compositions. The greater time for coarsening agrees with the argument that the higher Si/B ratio samples progressed to, and stayed in, this stage more quickly and longer.

The second group of compositions in Figure 6.14, those with a Si/B ratio greater than 3, also had an increasing weight loss at 10 minutes with increasing Si/B ratio, however they tended to follow the ideal stages of oxidation much closer. Figure 6.19 shows the transition out of initial (stage one) oxidation, 6.19b, and that the borosilicate was leveling during the subsequent stage two. Cross sections of the samples shown in 6.19d and 6.19h indicate a thickening of the borosilicate layer, from approximately $10\mu m$ at 2 minutes to $25\mu m$ after 10 minutes. The lack of open holes in these samples means that borosilicate leveling was occurring concurrently with borosilicate thickening. The increase in 10 minutes weight loss with higher Si/B ratio is again due to the less viscous compositions progressing more quickly through the oxidation stages. At 10 minutes, the sample with a Si/B ratio of 3.1,

shown in Figure 6.16c, was just transitioning from first to second stage oxidation with a high areal density, and thus small scale, of depressions in the initial flat-glassy regions. The samples of higher Si/B were, after the same period of oxidation, farther into the second stage; with increasing amounts of the surface having the smooth borosilicate which had replaced the flat-glassy regions of stage one. Figure 6.16d captures the transition between the smooth, second stage borosilicate, at the bottom of the image, as well as the flat-glassy region breakdown in the upper portion of the image. The 10 minute appearance of the even higher Si/B sample showed no flat-glassy regions remaining, indicating full transition into stage two oxidation. However, this sample also showed the deviation from ideal oxidation resistance at 10 minutes which caused it, and the lower Si/B ratio samples, to ultimately lack oxidation resistance. Figure 6.21 shows part of the sample surface in which the borosilicate had too high a viscosity for the MoO_3 to either pop or level upon cooling. The thin but high viscosity borosilicate layer which existed on these samples at longer times still allowed enough oxygen permeation for MoO_3 formation but prevented the growth, popping, and subsequent leveling of bubbles due to its low fluidity. A slow separation between the borosilicate and base material became catastrophic once the fragile bubbles were fractured mechanically or from devitrification followed by thermal shock cracking and spallation.

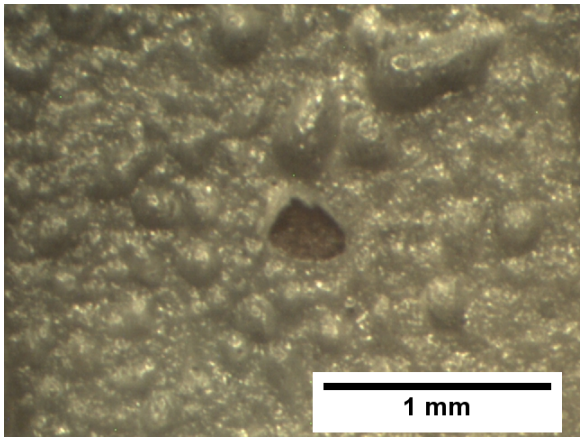

Figure 6.21: Surface of cobalt modified Mo-Si-B composite with a Si/B ratio of 4.8 after 10 minutes of oxidation at 1300℃ showing large and fragile MoO_3 bubbles in a high viscosity borosilicate.

The oxidation rates calculated to 30 and then 90 minutes, shown in Figure 6.14, are a

combination of the 10 minute weight loss, a general trend of slowed oxidation with higher Si/B ratios, and the sensitivity to thermal shock damage. The linear rate between 10 and 30 minutes most strongly shows slower oxidation with higher Si/B as the behavior of all samples during this period is dominated by MoO_3 bubble growth and popping. As the bubbles are restricted by the borosilicate melt's viscosity, the rate of MoO_3 removal slows with higher Si/B ratios. For the samples of a Si/B ratio less than 3, the melt viscosity continued to dominate the oxidation rate in the 30 to 90 minute period with a further slowdown as the boria evaporated. The samples of a Si/B ratio above 3, on the other hand, began to have considerable devitrification during this time period, showed numerous cracks and spallation, and had an increase in the weight loss rate. It is unclear if the accelerated oxidation was due to cracking during devitrification at temperature or from prior cracks formed upon quenching for the previous time step's weighting. In either case the presence of spallation and cracking parallel to the substrate is an indication of thermal shock resistance too low for these materials to be of use.

6.2.4.3 Oxidation Furnace

The above discussion has neglected two additional results from the cobalt modified samples: the use of two different oxidation furnaces and variations in the cobalt concentration. As was mentioned at the beginning of this section and is shown in Figure 6.14, two furnaces were used in the oxidation testing of the cobalt modified samples. Due to concern with a stagnant atmosphere in the bottom of the box furnace having a negative, and non-representative, effect upon oxidation, separate halves of a few samples were oxidized in both the box furnace and a horizontal tube furnaces. For all these compositions and at all oxidation times, the weight losses were less for the samples tested in the tube furnace. The surface appearance suggested a lower tendency for open holes and channel-type behavior in the tube furnace. This could have been caused by the more stagnant atmosphere of the box furnace either slowing the loss of boria, leading samples to behave as if they had a lower Si/B ratio, or stabilizing MoO_3 gas or liquid inside bubbles, preventing the borosilicate from leveling. Because the development of these composites is for gas turbine applications, a stagnant

atmosphere is unrealistic and all the subsequent oxidation testing was conducted in the tube furnace. For even later work, a fan was added to the tube furnace to both blow fresh air over and remove MoO_3 from the samples during oxidation. The results of this are shown in Section 6.2.8.

6.2.4.4 Effect of Cobalt Amount

All the above results for cobalt additions only pertain to a single cobalt concentration. This amount was selected based upon the results of iron additions in which a metal oxide, MO, concentrations of 1.9 mol% in the equivalent glass was found to be best. However, a few lower concentrations of cobalt were produced and, similar to the iron results, there was a reduction in the devitrification tendency. Samples with Si/B ratios 3.7 and 4.2 were produced with cobalt concentrations in the equivalent glass of both 1.2 and 1.9 mol% as well as a Si/B of 3.2 with cobalt at 0.78 and 1.2 mol%. In Figure 6.22 the percentage increase in oxidation weight loss for reducing the cobalt amount is shown for 10, 30, and 90 minutes as well as the 30 to 90 linear rate. In this representation, a positive value is a loss of oxidation resistance from a lowered cobalt concentration. After 10 minutes of oxidation, all cobalt rich compositions had less weight loss than the cobalt lean ones. This remained the case at later times for the comparison between 0.78 and 1.2 mol% CoO. However, comparing 1.2 to 1.9 mo% CoO showed the opposite at longer times with higher weight losses for the samples richer in cobalt. These results are in agreement with the oxidation resistance theory developed here; the initial oxidation, which dominates the 10 minute weight loss values, is strongly improved by the addition of transition metals. At longer times however, these ternary additions to the borosilicate cause devitrification which ultimately leads to catastrophic oxidation. The optimal composition is one in which enough cobalt is added to aid the initial oxidation but not enough for large scale surface devitrification. The results in Figure 6.22 suggest a cobalt addition near 1.2 mol% as CoO. However, in this and all cobalt samples, devitrification still ultimately occurred leading to a loss of oxidation resistance. It was concluded that no simple Mo-Si-B composite with cobalt additions could posses long term oxidation resistance at 1300℃.

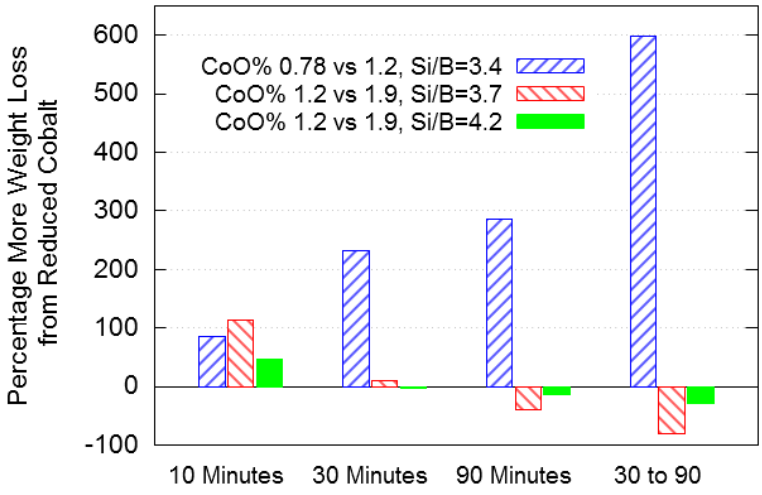

Figure 6.22: Variation in measured oxidation weight loss with differing levels of cobalt additions to Mo-Si-B composites oxidized at 1300°C.

6.2.5 Results of Yttria Additions

Similar to the cobalt additions, minor amounts of yttria (Y_2O_3) resulted in considerably improved initial oxidation followed by devitrification and spallation after moderate times at 1300°C. This similarity is curious as these two transition metals have significantly different free energies of oxidation, ionic radii, and coordinations in silicate glasses [50, 121]. Like the results of iron and cobalt modifications, an optimum concentration of yttria exists where there is a beneficial effect on the initial oxidation resistance with minimal devitrification and spallation later. However, as in those other series of samples, no composition was found in which devitrification was completely eliminated and it was ultimately concluded that no simple yttria modified Mo-Si-B composite would develop long term oxidation resistance.

While serious issues were found for long term oxidation, the initial resistance of yttria modified Mo-Si-B samples was superior to all other compositions evaluated. Figure 6.23 shows the normalized weight loss after 10 minutes of oxidation as well as the linear rates to 30 minutes and between 30 and 90 minutes. Although fewer compositions were evaluated, it can be seen that the initial weight losses were on par or better than the best cobalt modified samples. Additionally these yttria containing samples only showed a single trend of increasing weight loss at 10 minute with increasing Si/B ratio. However the range of

Si/B ratios evaluated was small enough to not capture any potential changes in oxidation mechanism. The Si/B ratios and yttria contents were selected based upon the best performing iron and cobalt analogs and thus the low Si/B and very high yttria compositions were ignored. Instead more emphasis was placed upon yttria concentrations in the equivalent glass between 0.31 and 1.5 mol% Y_2O_3. All these samples were effective in eliminating the open hole borosilicate structure seen in non-modified Mo-Si-B samples, although the lowest yttria content appeared to be borderline based upon similar cobalt modified surfaces. Figure 6.24 shows representative borosilicate surfaces after 10 minutes of oxidation. The trend of increasing coarseness of the borosilicate structure with increasing Si/B ratio agrees with the interpretation of the cobalt results, although the yttria content is not constant here and may have also played a role.

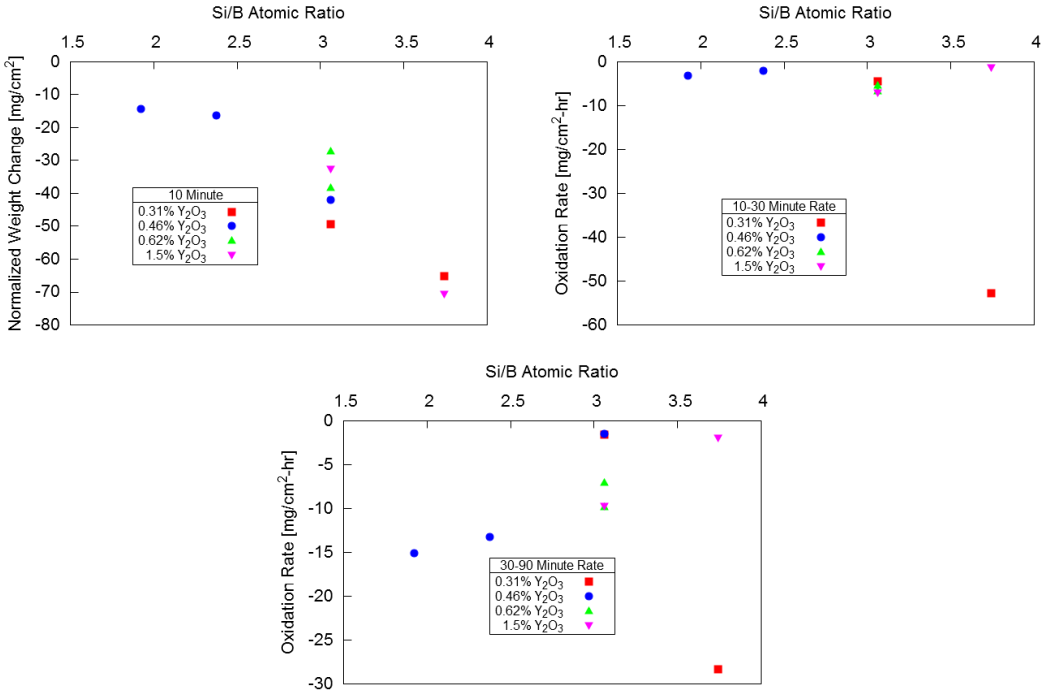

Figure 6.23: Surface area normalized weight losses of Yttria modified Mo-Si-B compositions oxidized at 1300℃ for 10 minutes, top left, and the linear rates between 10 and 30 minutes, top right, and 30 and 90 minutes, bottom

With the exception of one composition, the linear oxidation rates show a changing behavior with initially slow weight loss accelerating between 30 and 90 minutes. The exception to this was the composition with the highest Si/B, 3.7, and lowest yttria content, 0.31, which

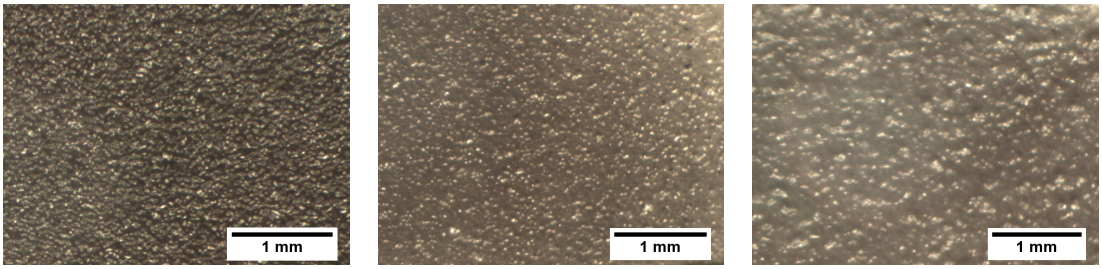

Figure 6.24: Surface of Yttria modified Mo-Si-B samples after 10 minutes of oxidation at 1300℃. Left to right the Si/B ratios are 2.4, 3.1, and 3.7 with Y_2O_3 mol% in the equivalent glass of 0.46, 1.5, and 0.31.

had mixed devitrification and a few open channels during the entire oxidation testing. All the other samples had an increase in the oxidation rate between the 10 to 30 and 30 to 90 minutes periods, indicating a deviation from the ideal oxidation reaction pathway. This deviation was commensurate with observed devitrification and cracking of bubbles or spallation of large surface flakes, as seen in Figure 6.25. The degree of accelerated oxidation rate as well as the severity of devitrification and spallation were observed to increase with both the Si/B ratio and yttria content. For a constant Si/B ratio this can be seen in Figure 6.26 where, although the 10 minute weight loss was less, the high yttria samples have a greater increase in linear oxidation rate. This may, however, not be due to a change in mechanism as much as these samples progressing more quickly through the stages of oxidation and, due to their deviation, spending more time in a higher weight loss rate regime.

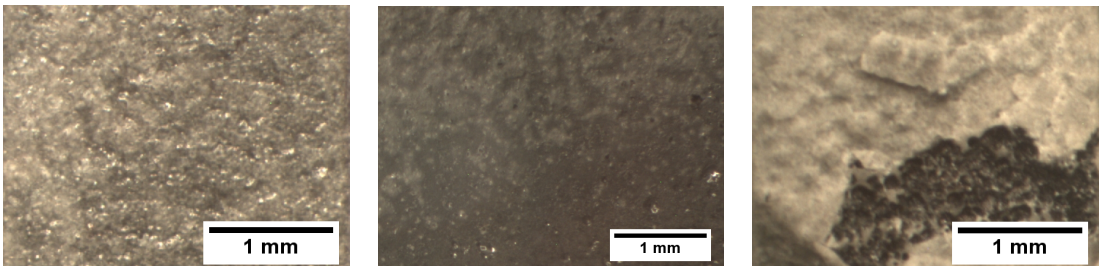

Figure 6.25: Surface of Yttria modified Mo-Si-B samples after 90 minutes of oxidation at 1300℃. Left to right the Si/B ratios are 1.9, 3.1, and 3.7 with Y_2O_3 mol% in the equivalent glass of 0.46, 0.31, and 1.5.

Encouraged by the excellent initial oxidation results, the composition with the least acceleration in weight loss rate during the 30 to 90 minute period was further oxidized to 20 hours total. Samples with three surface treatments, as-fired, coarse ground, and ground

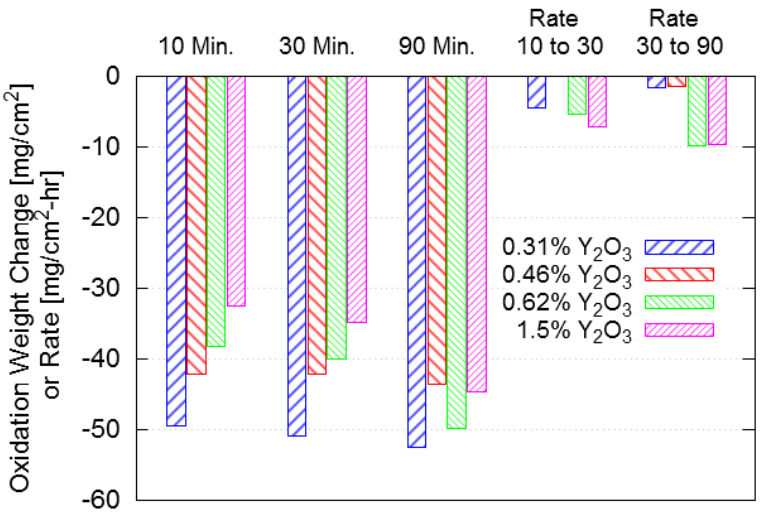

Figure 6.26: Dependence of surface area normalized weight loss and linear loss rate on yttria content during oxidation at 1300℃. The Si/B ratio for these samples was 3.1.

and polished, were used. While no effect of polishing was seen, the two ground samples did have a lower initial weight loss due to removal of the as-fired, silicon and boron depleted layer. The oxidized surface morphologies between the three did not have any differences as removal of surface molybdenum by either oxidation or mechanical means does not effect the borosilicate structure which forms subsequently. Figure 6.27 shows the weight loss with oxidation time including previous non-modified Mo-Si-B samples as well as the initial iron and nickel compositions. While the improvement in the weight loss is dramatic, the surface of this yttria modified sample still showed extensive devitrification and thus a sensitivity to thermal shock. The surfaces at 90 minutes and 20 hours of oxidation are shown in Figure 6.28 in which both dull, devitrified regions, and fragile bubbles can be seen. The roughness of the borosilicate surface after 18.5 hours of isothermal oxidation (the step between weighting at 90 minutes and 20 hours) does suggest that the long term oxidation behavior is controlled by slow popping and incomplete leveling of MoO_3 bubbles rather than the interfacial cracking and spallation seen in various samples at 90 minutes such as Figures 6.25 and 6.17.

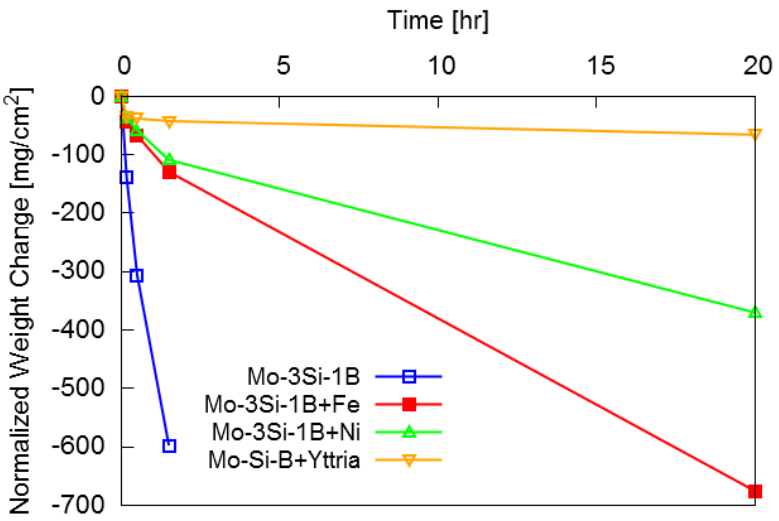

Figure 6.27: Surface area normalized weight loss during interrupted oxidation testing to 20 hours at 1300℃ for a yttria sample with a Si/B = 3.1 and Y_2O_3 of 0.46 mol%. Results of iron and nickel modified as well as base Mo-Si-B from Figure 6.3 are included for comparison.

6.2.5.1 Effect of αMo Volume Fraction

Before concluding the results on yttria additions, one last compositional variation, of a different sort, deserves mention. In the interest of balancing oxidation and mechanical properties, a sample of elevated αMo content was produced. In theory, if the oxidation resistance is not degraded too extensively, a higher αMo volume fraction would reduce the constraint on matrix deformation, improving toughness. The composition evaluated had an αMo volume fraction of 60% and a Si/B ratio (2.4) and yttria content (0.46) to match the equivalent glass of the sample shown in Figure 6.24 on the left. The surface area normalized weight loss for up to 90 minutes of oxidation at 1300℃ is shown in Figure 6.29 for both compositions. After roughly twice the initial weight loss, the weight loss curve of the high molybdenum sample is parallel to the one containing more total silicon and boron. The implication of this is that after the initial weight loss, the oxidation behavior is dictated nearly entirely by the borosilicate composition and not the overall molybdenum content. This increases the material design freedom to include higher αMo volume fractions, particularly in conjunction with approaches to mitigate initial oxidation issues, such as coatings or pre-oxidation.

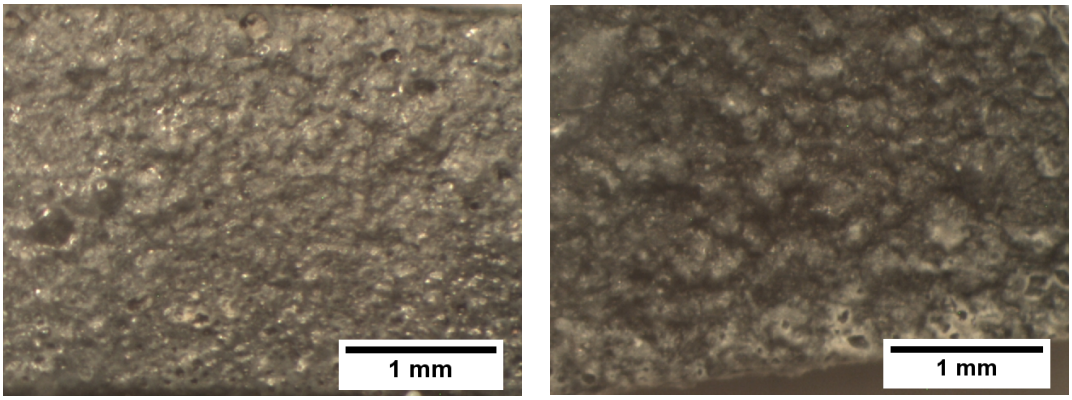

Figure 6.28: Surface of Yttria modified Mo-Si-B samples after 90 minutes, left, and 20 hours, right, of oxidation at 1300℃. The sample Si/B ratio was 3.1 and Y_2O_3 concentration in the equivalent glass was 0.46 mol%.

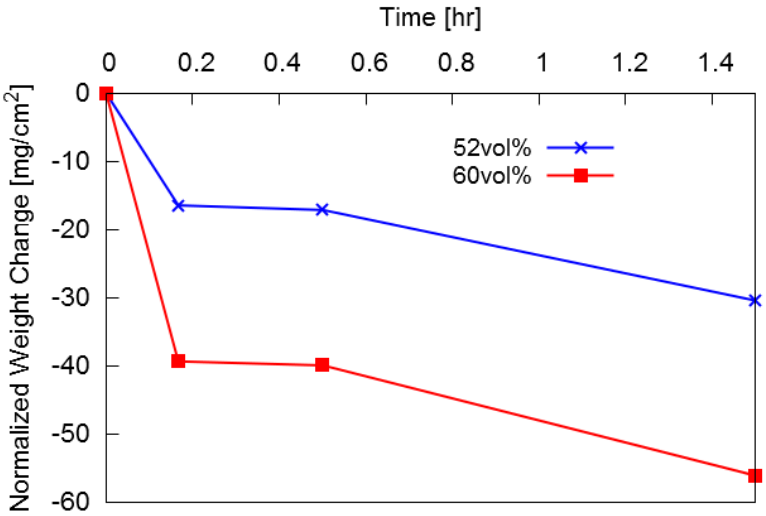

Figure 6.29: Surface normalized weight loss over 90 minutes at 1300℃ for samples of equivalent Si/B ratios and yttria contents in the borosilicate but differing αMo volume fractions. The higher, 60 verse 52 vol%, molybdenum sample was similar after a greater initial weight loss.

6.2.6 Results of Manganese Additions

The modification of Mo-Si-B composites with minor manganese additions resulted in a series of compositions that possessed oxidation resistance over 20 hours at 1300℃. The best of these samples was also used to demonstrate protection from oxidation at moderate temperatures after pre-oxidation at 1300℃ with less than $0.5^{mg}/_{cm^2}$ of weight lost after 24 hours at 800℃. Although manganese is being presented last in the results of transition metal additions, due to its superior oxidation resistance, these samples were produced and

evaluated before the iron, cobalt, and yttria samples.

The simultaneous development of both material processing and composition tailoring for oxidation resistance had a significant effect upon the manganese modified compositions. The primary aim of the processing development was to fully complete the de-oxidation of molybdenum powder at low temperatures so that the high temperature intermetallic forming reactions and sintering would occur in a very low oxygen environment. This limited the potential of forming volatile silicon and/or boron oxides prior to sintering of the composite. However, metallic manganese has both a low melting point and high vapor pressure at the temperatures needed for pressureless sintering. During the production of the initial manganese modified samples, the sintering furnace atmosphere had a dew point high enough to stabilize MnO. This both limited any loss of manganese and could have formed volatile silicon and boron oxides resulting in an uncontrolled change in the Si/B ratio. Subsequent improvements to the firing process resulted in lower dew point at the elevated temperatures which, in turn, caused better retention of silicon and boron at the expense of significant manganese loss. The investigations into iron, cobalt, and yttria modifications were instigated due to this loss of processablility of manganese containing samples by pressureless sintering.

The samples for which results are shown below are from a series of manganese modified Mo-Si-B batches fired back-to-back with consistent processing procedures and a moderately low dew point. Most likely these had limited manganese losses and somewhat less control over the silicon and boron contents than the iron, cobalt, and yttria containing samples produced later. Interestingly, the oxidation resistance of the manganese containing Mo-Si-B composites was found to be quite different from the iron, cobalt, and yttria samples. Instead of an initial flat-glassy borosilicate which subsequent devitrified, the manganese samples tended to remain vitreous and have an extended but slow second stage oxidation. The 10 minute weight loss had a relatively weak dependence upon the Si/B ratio, as shown in Figure 6.30. The linear oxidation rates however, do show a strong composition dependence with a minimum weight loss rate for the Si/B ratio between 2 and 3. Because of the lack of devitrification, the oxidation rate between 30 and 90 minutes tended to be less than that

between 10 and 30 minutes, and allowed for these samples to be evaluated up to 20 hours, Figure 6.30.

Before specifically addressing the results of these samples, two factors need to be mentioned. First, the compositions in this series fall into three categories: a constant manganese fraction with only the Si/B ratio varying, the same manganese fraction with an addition of strontium aluminosilicate (SAS), and a Mo-Si-B composition with twice the previous manganese addition. It can be seen in the long terms rates of Figure 6.30 that these two modifications to the Mo-Si-B+Mn series had the best oxidation resistance. The second factor is that all the testing was done with as-fired pellets simply cut in half and oxidized in the bottom loading box furnace. As was previously discussed, these two experimental conditions lead to higher initial weight losses due to as-fired surfaces depleted of glass formers and potentially detrimental local atmosphere effects. This makes comparison to the cobalt and yttria modified samples difficult, however the results here are self consistent and would be expected to be better with the improved experimental techniques.

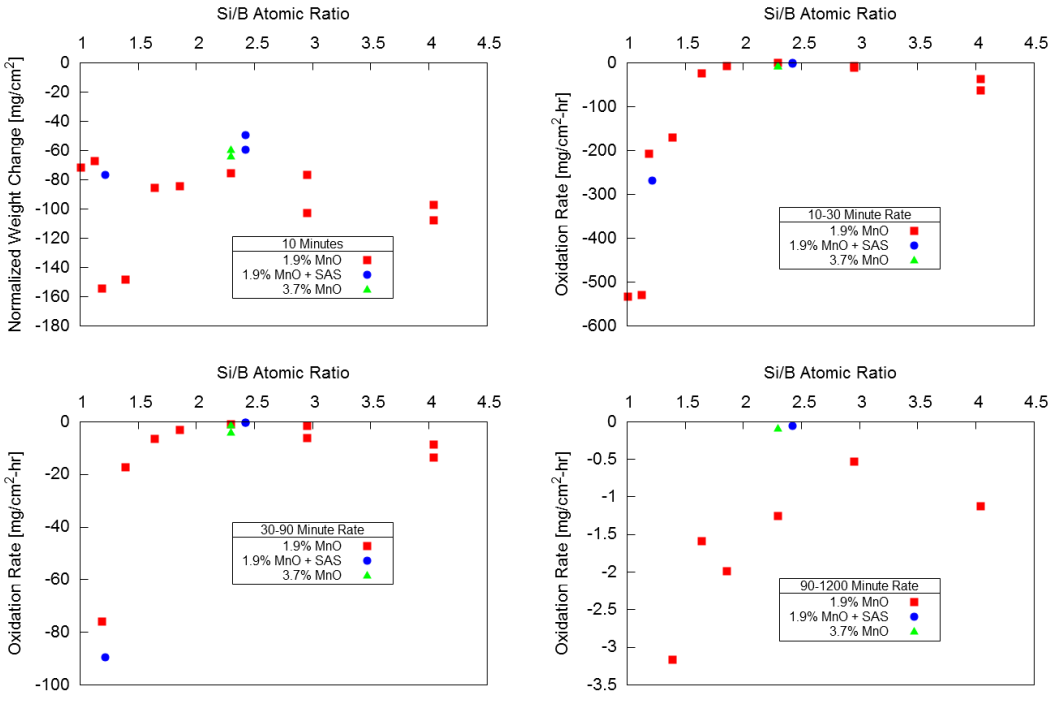

Figure 6.30: Surface area normalized weight losses of Manganese modified Mo-Si-B compositions oxidized at 1300℃ for 10 minutes, top left, and the linear rates between 10 and 30 minutes, top right, 30 and 90 minutes, bottom left, and 90 minutes to 20 hours, bottom right.

Considering first the samples with constant Mn fraction and varying Si/B ratio, the open hole borosilicate structure after 10 minutes of oxidation was again observed to disappear at a sufficiently high Si/B ratio, above 1.5. The samples with a Si/B ratio above this value showed extended second stage oxidation with bubbles, or their remains, evident at 30 minutes, Figure 6.31. In fact the sample with the most optimum Si/B ratio, 2.4, continued to display second stage behavior after 90 minutes, Figure 6.32, a point at which all the iron, cobalt, and yttria samples were devitrified and showing substantial spallation. It appeared that although the second stage oxidation mechanism was slow, the borosilicate leveling slightly lagged behind the bubble generation leading to an increase in the borosilicate topology with many, moderately sized bubbles entrained in the borosilicate, Figure 6.32.

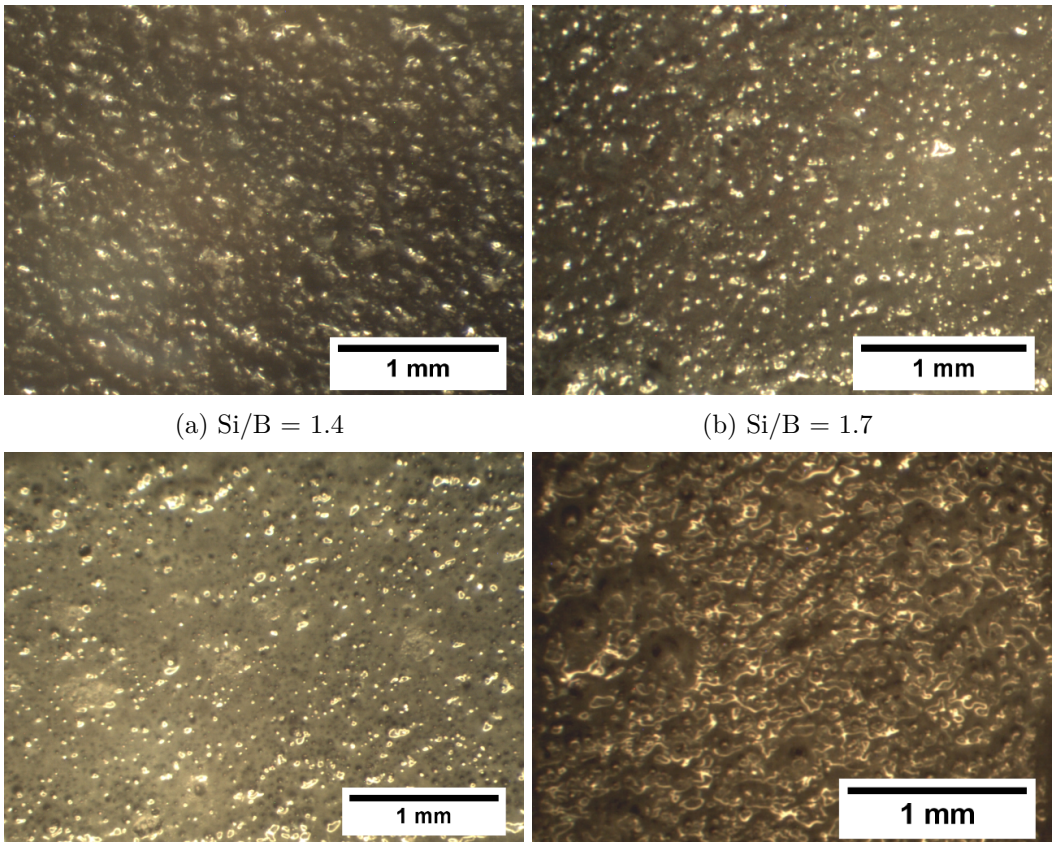

(a) Si/B = 1.4 (b) Si/B = 1.7

(c) Si/B = 2.4 (d) Si/B = 3.1

Figure 6.31: Surface of manganese modified Mo-Si-B samples after 30 minutes of oxidation at 1300℃. A lumpy surface borosilicate is progressively replaced by entrained bubbles and then a coarser, cratered surface. All contain manganese at 1.9 at% in the equivalent glass.

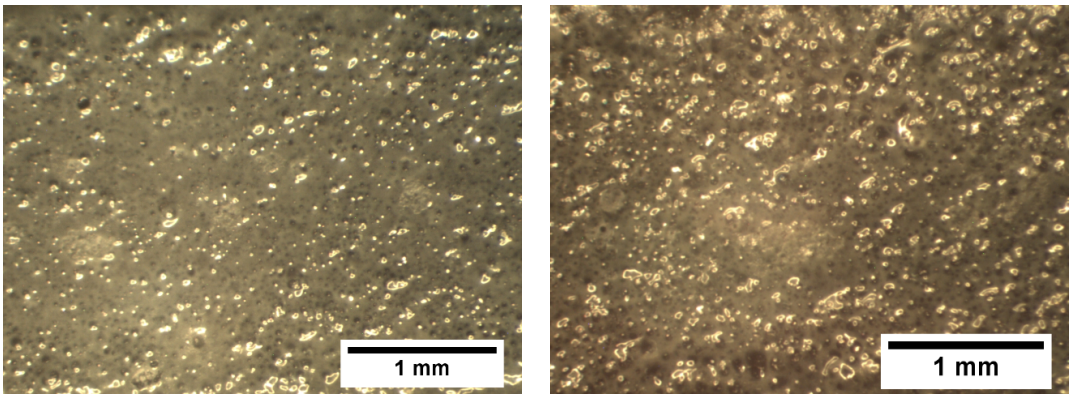

Figure 6.32: Surface of a manganese modified Mo-Si-B sample with a Si/B ratio of 2.4 and MnO at 1.9at% in the equivalent glass after 30 minutes, left, and 90 minutes, right of oxidation at 1300℃.

The extended second stage oxidation continued to dominate the behavior between 90 minutes and 20 hours for all except the highest Si/B ratio sample. Figure 6.33 shows the large bubbles that covered the surfaces of these samples after a total of 20 hours of oxidation. Two significant observations can be made. First, the persistence of these large bubbles suggests that these compositions would not continue to have oxidation resistance if the bubbles continued to grow and/or were damaged. Second, the lack of crack or spallation from the bubble growth means that the borosilicate remained vitreous, even with the long term boria loss. These observations suggest that if the composition could be modified to successfully exit second stage oxidation (forming a sufficiently thick borosilicate layer) then long term oxidation resistance would occur. Samples having simply a higher Si/B ratio were not superior as the borosilicate appeared to have too high a viscosity and seemed to have formed a very thin devitrified surface, which resisted borosilicate leveling after bubble popping even at 30 minutes of oxidation.

6.2.6.1 Adjusted Compositions

Two adjustments to the manganese modified Mo-Si-B compositions were made. In one, the strontinum aluminosilicate $SrAl_2Si_2O_8$ (SAS) was added at 1% by volume of the bulk, while in the other the manganese content was doubled. The first will be referred to as "Mn+SAS" while the second as "Double-Mn." The Si/B ratio for both these samples was between 2.4 and 2.5 and the equivalent glass compositions are given in Table 6.1. The oxidation resistance

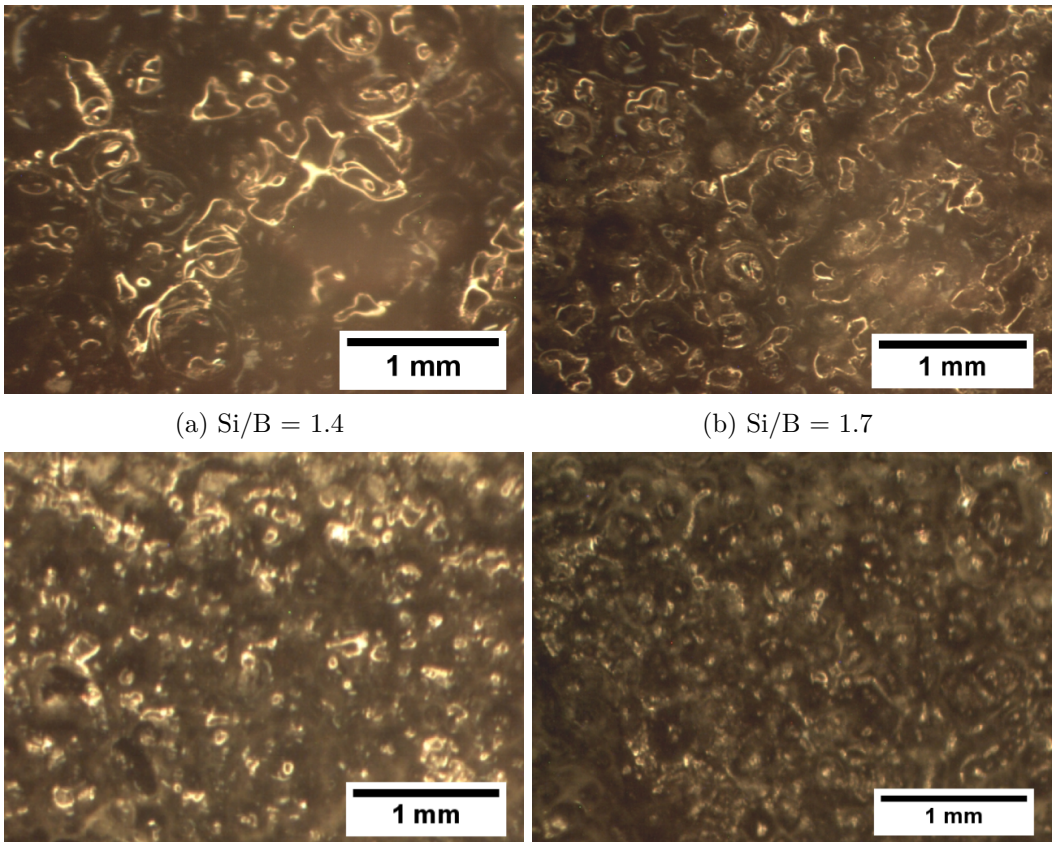

(a) Si/B = 1.4 (b) Si/B = 1.7

(c) Si/B = 2.4 (d) Si/B = 3.1

Figure 6.33: Surface of manganese modified Mo-Si-B samples after 20 hours of oxidation at 1300℃. Slow MoO_3 bubble growth occurred during the long isothermal hold after weighting at 90 minutes. All contain manganese at 1.9 at% in the equivalent glass.

for both was found to be substantially better than the other manganese modified samples, particularly in lacking large bubbles after 20 hours at 1300℃. In fact, these two samples appeared to very quickly exit stage two oxidation and had very little change in surface topology during the entire testing period. Figures 6.34 and 6.36 show consistent locations on the surfaces of these samples throughout the oxidation testing and many of the same topological features persist with little change over 20 hours. These features likely arose from either microstructural inhomogeneities or the last bubbles to pop during the second stage of oxidation. What is most significant is that no entrained bubbles, growing or static, are observed meaning that these samples very quickly entered stage three oxidation in which the oxygen flux is too low and the borosilicate viscosity too high for either MoO_3 bubble growth or melt separation form the base material.

Figures 6.35 and 6.37 show the borosilicate formed on sectioned pellets (away from any fired surface effects) after 20 hours of oxidation at 1300℃ of the Mn+SAS and Double-Mn samples. In both the borosilicate was relatively thin and well adhered, as would be expected from the excellent oxidation resistance. However, differences between the two compositions are apparent. The surface of the high manganese sample had some crystallization along side a vitreous borosilicate melt, Figure 6.37, while the SAS modified sample remained fully glassy in appearance, 6.35. While the degree of crystallization must not have been too detrimental for this oxidation testing, it could, under different conditions or at lower temperatures lead to failure.

In cross section of the Mn+SAS and Double-Mn samples, Figures 6.35 and 6.37, the presence of internal oxidation beneath the borosilicate layer and some small particles of MoO_2 within the borosilicate are not unusual, however the high manganese sample does have some additional, interesting features. First, the depth of the internal oxidation is significantly larger in the high manganese sample. This resulted from greater total oxygen transport through the borosilicate and into the base material. Second, a number of the MoO_2 particles within the borosilicate are more acicular in shape and are reminiscent of needles seen in other high manganese samples and believed to be a Mn-molybdate. Third, a dense and relatively thick layer of MoO_2 exists underneath the borosilicate. The existence of this MoO_2 layer establishes specific of oxygen activities through the sample thickness. The mechanism by which this layer forms is unknown, but is intriguing, as its structure does not reflect the microstructure of the bulk composite. Due to the lack of secondary phases within the MoO_2 layer, and its often coarse grain appearance, formation by reduction of a liquid MoO_3 layer is considered a possibility, though no direct evidence for this exists. The fourth and final interesting feature of the high manganese sample is the presence of a complex structure between the dense MoO_2 layer and the internal oxidation, Figure 6.37. In this complex, multi-layered structure the MoO_2 and internal oxidation layers are separated by a thin silica layer. Additionally, full reduction of the MoO_2 to metallic Mo is seen on the internal side of the MoO_2 grains. This is believed to form by outward diffusion of silicon and/or boron through the internal oxidation layer. Upon reaching the MoO_2 layer, the

silicon and/or boron reduces it, forming a new, immobile borosilicate layer and metallic molybdenum. This variety of features is indicative of the complexity of the third stage of oxidation, in which the behavior is dominated by diffusional transport. At different points during oxidation and locations within the Mo-Si-B composite, the relative diffusivities of Si, B, and Mo must be considered alongside that of oxygen to fully explain the material behavior.

Table 6.1: Equivalent glass composition of samples modified from manganese modified Mo-Si-B series in mol%.

Sample	B_2O_3	SiO_2	Al_2O_3	SrO	MnO
Mn+SAS	16	81	0.6	0.6	1.9
Double-Mn	17	80	0	0	3.7

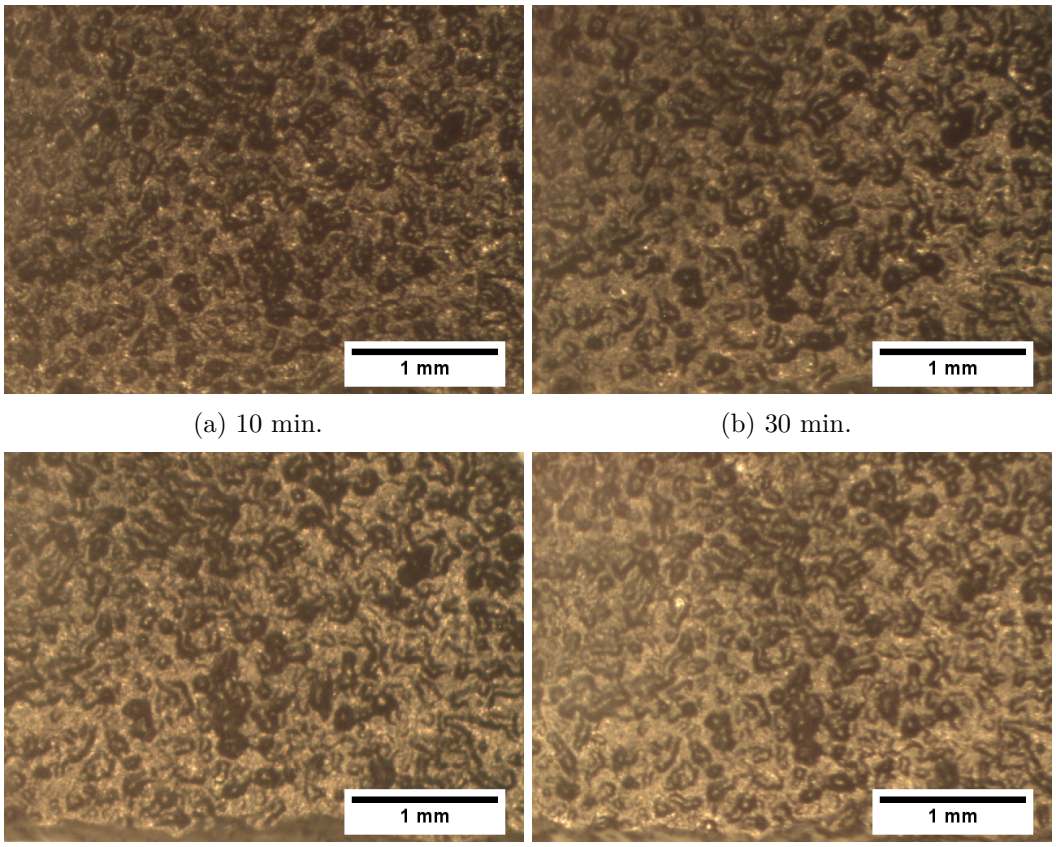

(a) 10 min. (b) 30 min.

(c) 90 min. (d) 20 hr.

Figure 6.34: Surface of a manganese modified Mo-Si-B sample "Mn+SAS" with the composition given in Table 6.1. Many of the same surface features can be identified throughout the oxidation testing indicating very little change in the sample over the 20 hours at 1300℃.

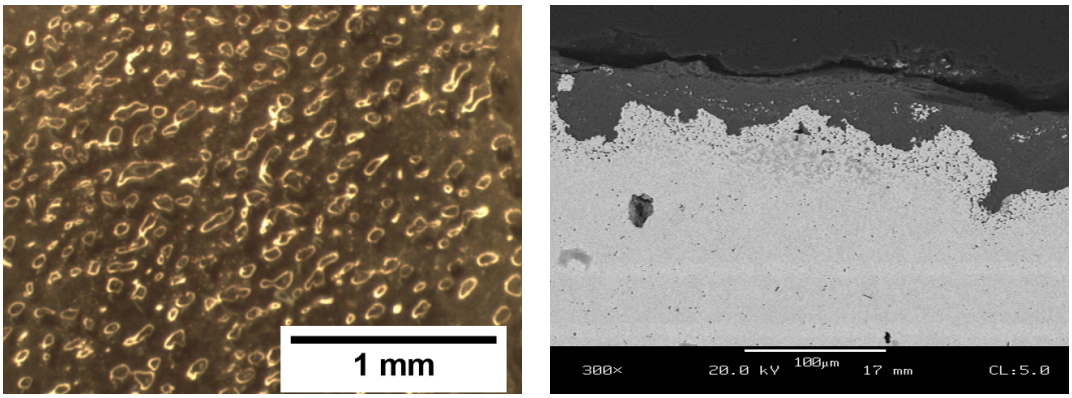

Figure 6.35: Surface, left, and cross section, right in SEM-BS, of a manganese modified Mo-Si-B sample "Mn+SAS" with the composition given in Table 6.1 after 20 hours of oxidation. The highly vitreous appearance without bubbles indicates a stable and protective borosilicate melt.

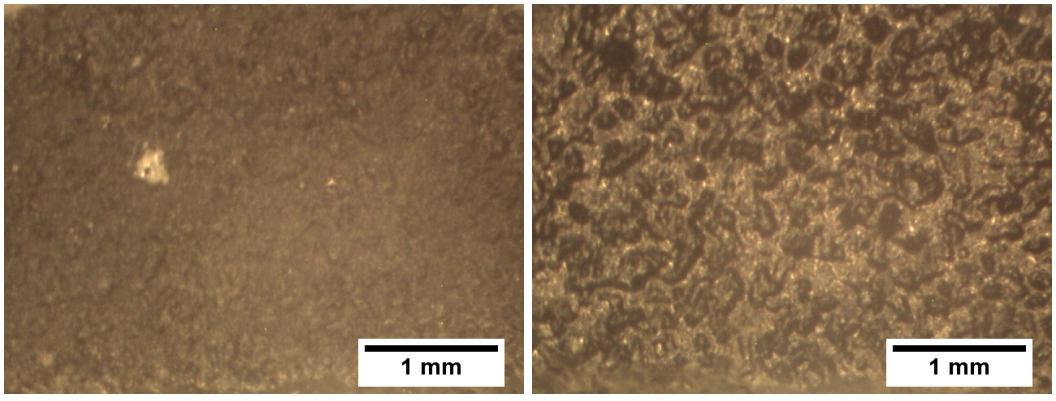

(a) 10 min.

(b) 30 min.

(c) 90 min.

(d) 20 hr.

Figure 6.36: Surface of a manganese modified Mo-Si-B sample "Double-Mn" with the composition given in Table 6.1. Some of the same surface features can be identified at both 30 and 90 minutes. Image (d) is of the opposite side.

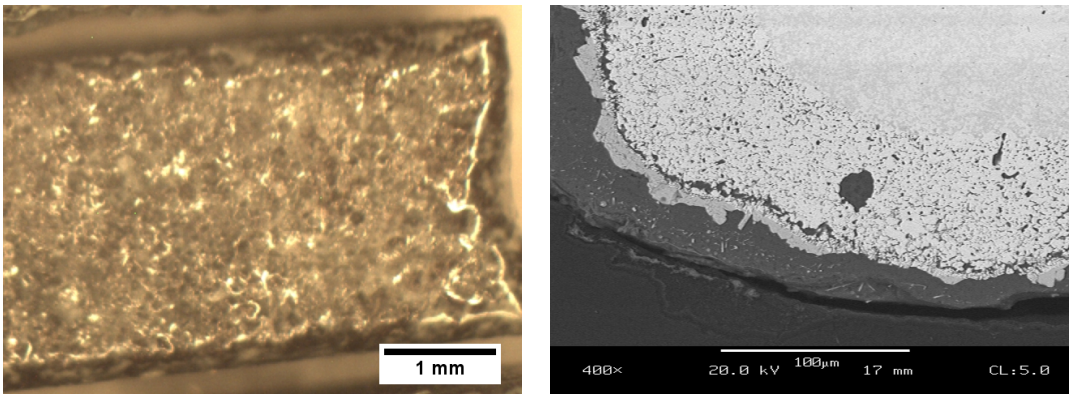

Figure 6.37: Surface, left, and cross section, right in SEM-BS, of a manganese modified Mo-Si-B sample "Double-Mn" with the composition given in Table 6.1 after 20 hours of oxidation showing both vitreous and crystalline regions.

6.2.6.2 Manganese Loss During Sintering

Three sets of compositions were produced in an attempt to expand upon and possibly improve the Mn+SAS composition above. These sets focused on slight composition changes, doubling of the manganese content, and increasing the Si/B ratio to 3.1. Unfortunately, all attempts to fire (nitride reactions and sintering) these compositions, as well as to reproduce the original, failed to yield samples possessing oxidation resistance near that found initially. This was due to one of two sequential issues within the firing process. First, the furnace tube developed a small crack within the hot zone that only opened at high temperatures. Figure 6.38 shows the dew point trace during the high temperature sintering stage for a firing with the cracked tube, firing #2. Comparison to the firing #1 (which was for the run that yielded the best oxidation resistance) shows an increase in the dew point during the later half of the sintering hold for firing #2 which was due to oxygen leaking in. While the leak would occur throughout the high temperature portion, it would only register on the hygrometer once enough sintering of the molybdenum had occurred to separate silicon and boron from the furnace atmosphere. Thus the dew point only increased after a few hours of sintering, however, the damage was already done. Replacing the furnace tube did eliminate the high temperature dew point increase which, along with other improvements to the firing-sintering procedure, allowed for a drier furnace atmosphere to limit silicon and boron oxidation. However, this lower dew point, shown in Figure 6.38 firing #3, resulted

in the reduction of any MnO which had previously prevented the evaporation of metallic manganese. All the firings after the furnace tube replacement suffered from evaporation of manganese, the second issue, and thus loss of oxidation resistance. Upon oxidation these samples tended to show either open holes from too low a manganese content, surface devitrification from too high a SAS to MnO ratio, or a mixed behavior along with excessive internal oxidation.

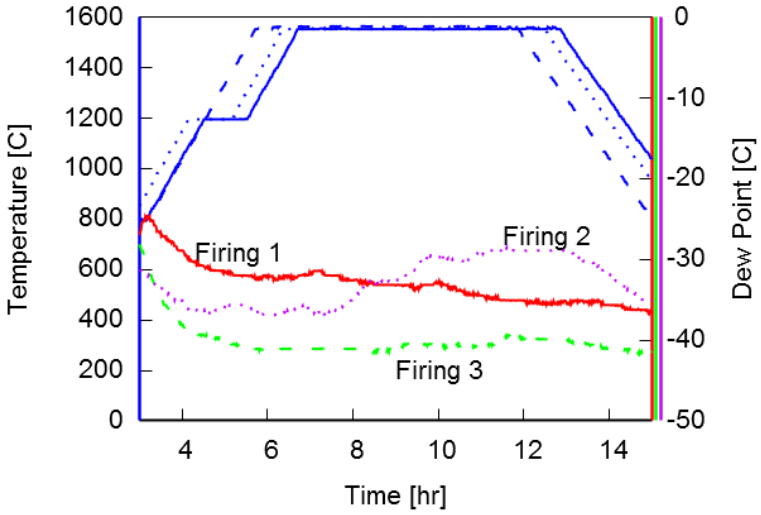

Figure 6.38: Comparison of dew point traces during three firings of manganese and SAS modified Mo-Si-B composites highlighting the high temperature portion. Firing 1 resulted in the samples with excellent oxidation resistance. The later firing 2 suffered from a cracked furnace tube. Firing 3 utilized a new tube and better firing practices which resulted in a dew point below the MnO stability.

6.2.6.3 Pre-Oxidation for Lower Temperature Protection

The oxidation resistance mechanism of Mo-Si-B composites is known to be successful only over a range of temperatures with both an upper and lower limit [13, 44]. The critical factor is the removal of molybdenum via MoO_3 evaporation which is necessary for the formation of a dense and continuous borosilicate layer. At lower temperatures the partial pressure of MoO_3 becomes to low for sufficiently rapid removal. Additionally, the native oxides of molybdenum are known to become non-protective above 600-700℃ due to high oxygen diffusion and eventually melting of the equilibrium oxide, MoO_3 [38]. The sum effect is that between approximately 700 and 1000℃, Mo-Si-B composites experience rapid

oxidation as solid or liquid MoO_3 forms more quickly than it evaporates and the borosilicate is unable to spread into a continuous surface layer. While compositional modifications could potentially improve oxidation resistance in this range, it would be at a loss of high temperatures resistance. The approach taken by the material development scheme used here is to tailor the composition for the high (and use) temperatures and rely upon the protective borosilicate grown at the elevated temperatures to provide oxidation resistance during excursions to lower temperatures.

To demonstrate this approach for oxidation resistance at low and moderate temperatures, a pre-oxidation treatment was done to the best performing manganese modified samples. The "Double-Mn" and "Mn+SAS" samples, as described in Table 6.1, were initially oxidized at 1300℃ for 90 minutes in order to develop a protective borosilicate surface. This pre-oxidation was then followed by interrupted oxidation testing at 800℃, a temperature at which molybdenum composites show very poor oxidation resistance due to the rapid growth and expansion of MoO_3. Due to the lower evaporation rate of MoO_3 at 800℃, molybdenum can experience considerable weight gain instead of loss. Figure 6.39 shows the surface normalized weight change of these two samples, both during the pre-oxidation and the subsequent 24 hours at 800℃. Both had a period of slight weight gain during the first 20 hours at 800℃ followed by weight loss during the subsequent four interruptions at one hour intervals. However, the measured weight gain or loss rates were very slow; the "Double-Mn" sample peaked around $1^{mg}/_{cm^2 hr}$ and the "Mn+SAS" sample stayed below $0.5^{mg}/_{cm^2 hr}$.

The surfaces of the pre-oxidized "Double-Mn" and "Mn+SAS" samples after 24 hours at 800℃ are shown in Figure 6.40. The majority of the surfaces of both samples were protective, showing little change over the testing, however certain locations, particularly on the face where the sample pellet was originally sectioned, did oxidize with the sizable volume expansion expected at this temperature. It is believed that small flaws in the pre-oxidation layer (local devitrification, a MoO_3 bubble, or chipped borosilicate) created a pathway for oxidation that then grew over 24 hours into the features observed. In these locations the growing MoO_3 grains pushed away the surface borosilicate layer, stretching and fracturing it. The MoO_3 formation under the borosilicate resulted in the measured weight gains as

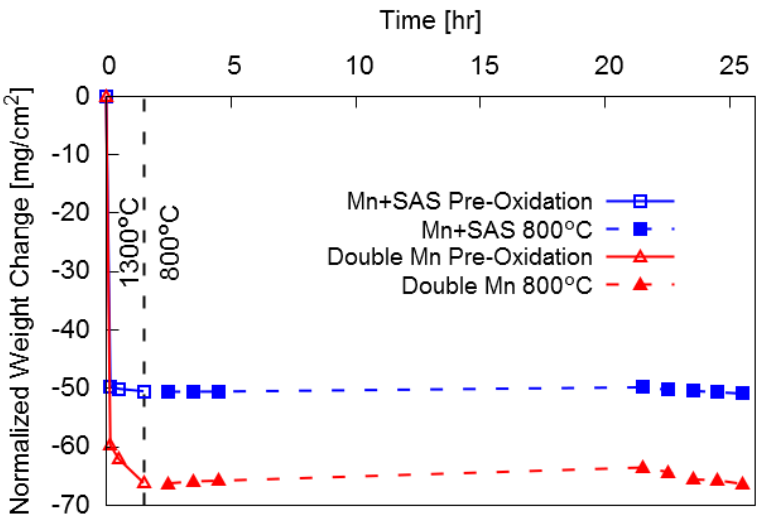

Figure 6.39: Surface area normalized weight loss of samples "Double-Mn" and "Mn+SAS" during both 90 minutes of pre-oxidation at 1300℃ and 24 hours at 800℃.

the evaporation of MoO_3 was restricted. The change to a measured weight loss during the last four interruptions is believed to be caused by thermal shock fracturing the stretched borosilicate and allowing MoO_3 evaporation to occur more rapidly than its formation.

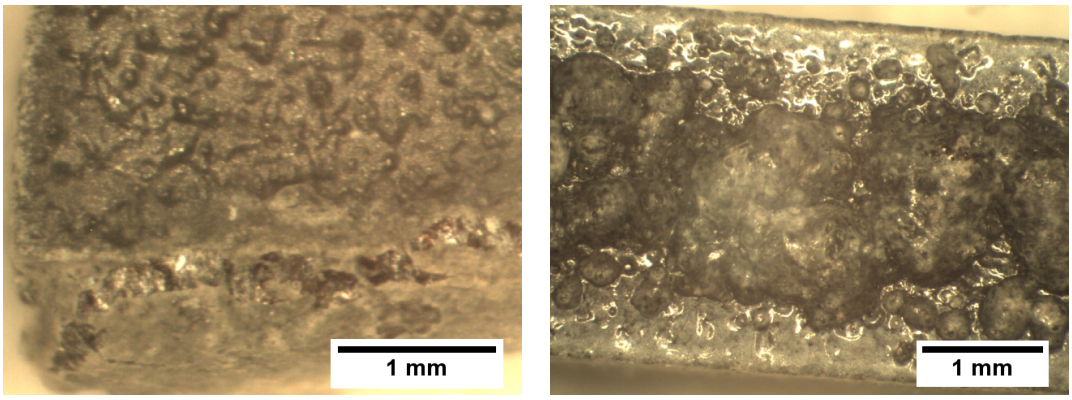

Figure 6.40: Surfaces of pre-oxidized manganese modified Mo-Si-B composites after 24 hours of oxidation at 800℃. The pre-oxidation was 90 minutes at 1300℃. At left is the "Double-Mn" sample showing the well protected region at the top and oxidizing region at the bottom. At right is the less extensive oxidation of the only non-protected surface of the "Mn+SAS" sample.

Cross sections of the pre-oxidized then oxidized at 800℃ samples highlight the strikingly different behavior of different locations on the same samples. Figure 6.41 shows backscattered SEM images of the "Double-Mn" sample and Figure 6.42 shows the same for the "Mn+SAS". In both, the left image is a low magnification view of the non-protected region,

though neighboring areas which did not oxidize are also present. The right images show the protected surfaces at a higher magnification. These protected locations appear very similar to those after 20 hours at 1300℃, Figures 6.37 and 6.35, as would be expected because the same initial borosilicate was grown in the first 90 minutes at 1300℃. Perhaps the only noticeable difference is the disappearance of the MoO_2 layer present in the high temperature "Double-Mn" sample, Figure 6.37, but not at 800℃, Figure 6.41. The inward diffusion of oxygen from the layer into the bulk may still be rapid enough at the lower temperature to eliminate any MoO_2.

The structure of the regions actively oxidizing at 800℃, Figures 6.41 and 6.42 on right, is complex and was not investigated in depth. Both MoO_3 grains and borosilicate pockets formed simultaneously and appear to have a strongly aligned portion on the air side and a more homogeneous and equiaxed portion near the base composite. Given how close to the MoO_3 melting point this test was, a wide variety of growth mechanisms could be operating. However, the successfully protected areas on these samples are considered more significant as they demonstrate the ability for a borosilicate layer formed at 1300℃ to continue to be protective at lower temperatures. The few, local flaws which lead to the observed oxidation could be prevented by better material handling or a longer pre-oxidation treatment. Additionally, the dwell at 800℃ for 24 hours is considered an extreme for the material being developed here. Rather, extended periods at 1300℃ with only short excursions to lower temperatures are expected. Under this cycle, the extent of any low temperature oxidation is limited by the exposure time and the return to 1300℃ allows for healing or reformation of a protective layer.

6.2.7 Results of HIP'ed Samples

As discussed in Section 5.3, a few samples were consolidated by hot isostatic pressing (HIP) at 1300℃. These samples were never fired to temperatures above 1300℃, preventing the loss of manganese that occurred in pressurelessly sintered samples after effective de-oxidation was developed. Two materials were used for the HIP cans, low carbon steel and titanium. As will be shown below, the steel cans contaminated the Mo-Si-B composite to the detriment

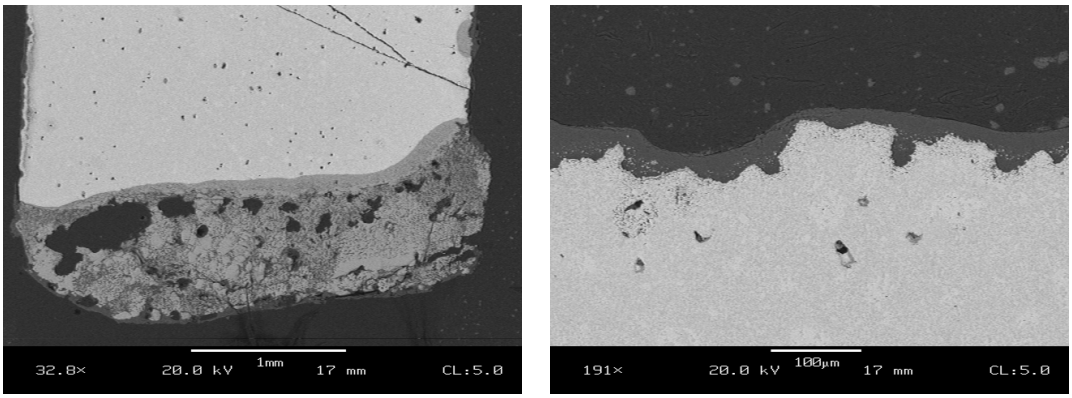

Figure 6.41: Cross sections of sample "Double-Mn" after a pre-oxidation of 90 minutes at 1300℃ and the oxidation for 24 hours at 800℃. The face with limited protection is shown on the left while the other, protected, surfaces appear as on the right.

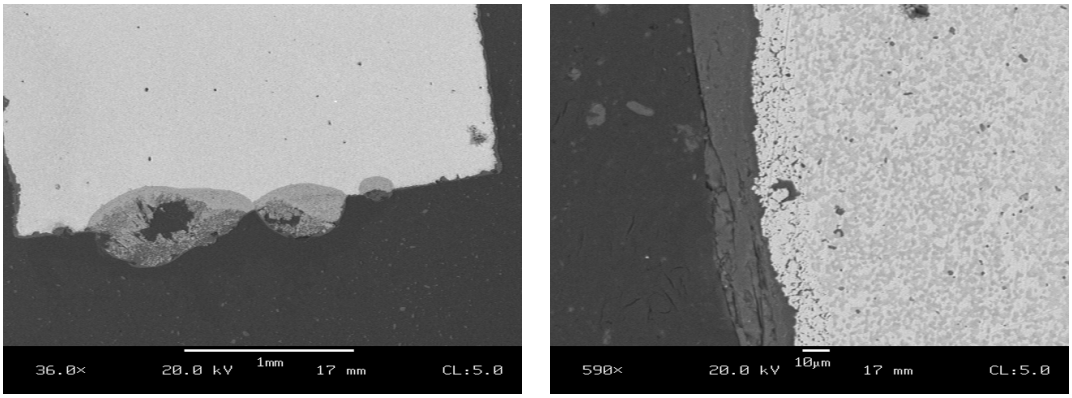

Figure 6.42: Cross sections of sample "Mn+SAS" after a pre-oxidation of 90 minutes at 1300℃ and the oxidation for 24 hours at 800℃. The face with limited protection is shown on the left while the other, protected, surfaces appear as on the right.

of the oxidation resistance. Titanium cans did not react with the Mo-Si-B material and showed the improved oxidation resistance due to retention of manganese during processing.

6.2.7.1 Encapsulated in Low-Carbon Steel Cans

The appearance during oxidation of the Mo-Si-B composites HIP'ed in steel cans was very similar to the previous, iron modified samples with relatively high iron contents. The Mo-Si-B powder placed into the cans was intentionally modified with manganese, but not iron, with compositions based upon the oxidation resistant samples from the prior manganese modified series. During oxidation testing of the HIP'ed samples, extensive devitrification

and spallation occurred and iron was identified throughout the samples along with manganese. Although the presence of iron contamination was detrimental to the oxidation resistance, see left image in Figure 5.18, analysis of the cross sections revealed surprising phases and morphologies.

Cross sections of samples oxidized for 90 minutes at 1300℃ are shown in Figure 6.43 and 6.44. The first set of images, in 6.43, are of locations at the borosilicate-air interface and show extensive crystallization which caused spallation during heating and cooling. Interestingly, the phase in contact with air is often just iron oxide, likely hematite (Fe_2O_3). In contact with this, but on the borosilicate side, is a significant amount of a Fe-Mn mixed phase believed to be of a spinel type. Additionally, within this, and within the borosilicate, are various molybdenum rich phases containing Fe and Mn. These could be the molybdates (Fe,Mn)MoO_4 or (Fe,Mn)$_2Mo_3O_8$ [113, 97], though further analysis would be needed to identify the exact composition and structure.

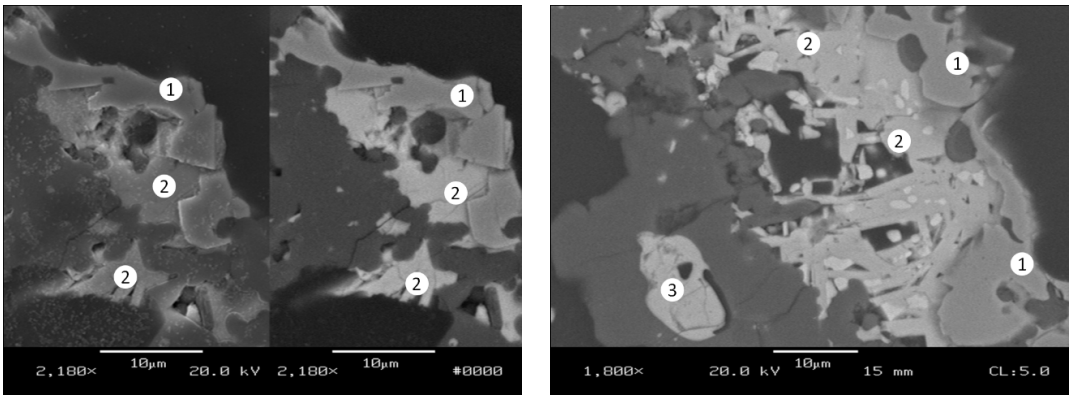

Figure 6.43: Cross section views near the air interface of oxidized, Mo-Si-B composite HIP'ed in steel cans. On the left, side-by-side secondary and backscatter images of the same location are shown. The indicated locations are believed to be the following phases: (1) hematite-Fe_2O_3, (2) Mn-Fe spinel, and (3) Fe/Mn containing molybdate.

The images in Figures 6.44 and 6.45 are of locations closer to the bulk material and include the MoO_2 interlayer. While some Fe/Mn molybdates are present, the coarse and blocky grained MoO_2 in Figure 6.44 are similar to the non-HIP'ed material. However, the images in Figure 6.45 show an additional morphology. At these locations some of the molybdenum oxide takes on an acicular morphology with significant Fe and Mn contents identified by EDS (on the order of 5 to 10 at%, excluding oxygen and boron). The morphology of

this molybdenum-oxide interfacial layer is unusual and raises questions as to its formation mechanisms. Its effect upon the overall oxidation resistance is also unclear though it may be associated with a stabilization of the molybdenum-oxide, potentially reducing its volatility. However, the lack of this morphology in the most oxidation resistance, non-HIP'ed samples implies that any advantage is likely small and the growth of needles may simply be an outcome of the relatively high iron and manganese contents.

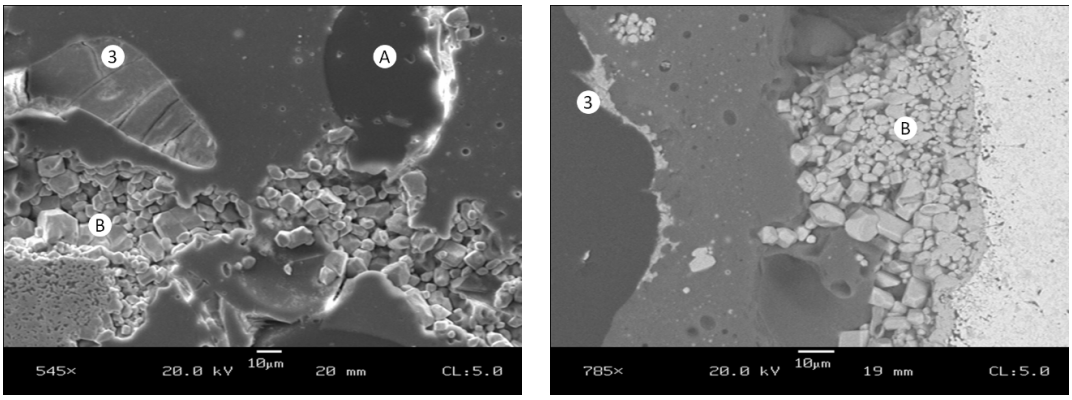

Figure 6.44: Cross section views including the MoO_2 interlayer of oxidized, Mo-Si-B composite HIP'ed in steel cans. Portions of the base material can be seen in both. The indicated locations are the following: (A) epoxy filled pore within borosilicate, (B) MoO_2, and (3) Fe/Mn containing molybdate with atomic ratios for Mn-Fe-Mo of approximately 2-2-6.

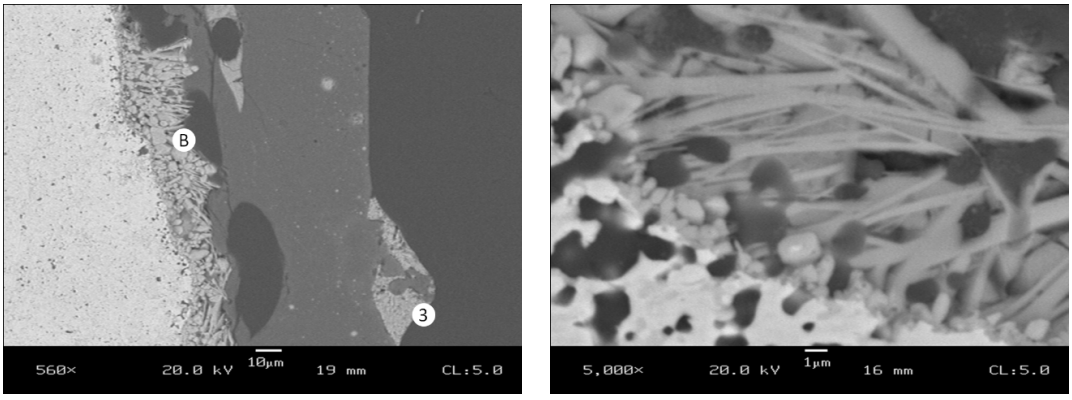

Figure 6.45: Cross section views including the MoO_2 interlayer of oxidized, Mo-Si-B composite HIP'ed in steel cans. These regions have acicular molybdenum oxide within the nominally MoO_2 layer containing Fe and Mn. The indicated locations are the following: (B) acicular and blockly MoO_2 and (3) Fe/Mn containing molybdate

6.2.7.2 Encapsulated in Titanium Cans

Unlike the Mo-Si-B material HIP'ed in low-carbon steel cans, the one encapsulated in titanium did not have any signs of contamination. During oxidation testing, spallation did not occur and very little crystallization was seen. As shown in Figure 6.46 this sample appeared very similar to a previous, pressurelessly sintered composition with an identical manganese addition. The surface area normalized weight loss during oxidation is shown in Figure 6.47 along with the three previous manganese samples having the closest Si/B ratios. The differences in initial weight loss are partially due to different sample geometries affecting calculation of the surface area. However, the oxidation rates for the HIP'ed material, both to 90 minutes and then to 20 hours, are in between the high and low Si/B samples that were not HIP'ed. Using titanium as a HIP can therefore produces Mo-Si-B composites consistent with the previous oxidation results, but with the added benefits of HIP'ing.

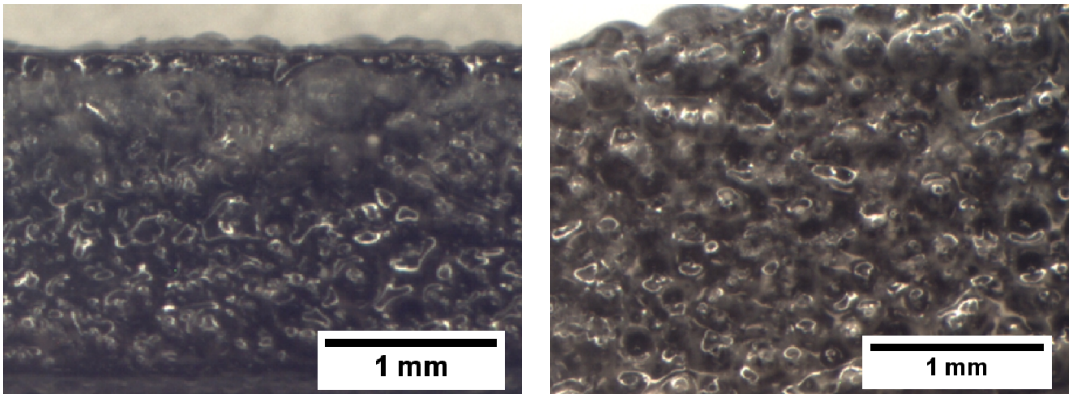

Figure 6.46: Surface appearance of Mo-Si-B composite HIP in a Ti can after oxidation at 1300℃ for 20 hours (left) compared to a pressurlessly sintered sample (right), both modified with manganese. The Si/B of the HIP sample was 2.5 while the sintered was 2.4 however both have a similar appearance indicating successful processing with manganese.

While the oxidation resistance of the HIP'ed Mo-Si-B sample is not as good as the previous Si/B=2.4 material, their behavior is quite similar with both forming some bubbles during the 20 hours of oxidation. Previous adjustments to this composition (by adding 1 volume % SAS) resulted in the best 1300℃ oxidation resistance found at any point in this work. Because SAS is compatible with the HIP'ing process, it is expected that using a titanium can to consolidate manganese and SAS modified Mo-Si-B with a Si/B ratio of 2.4

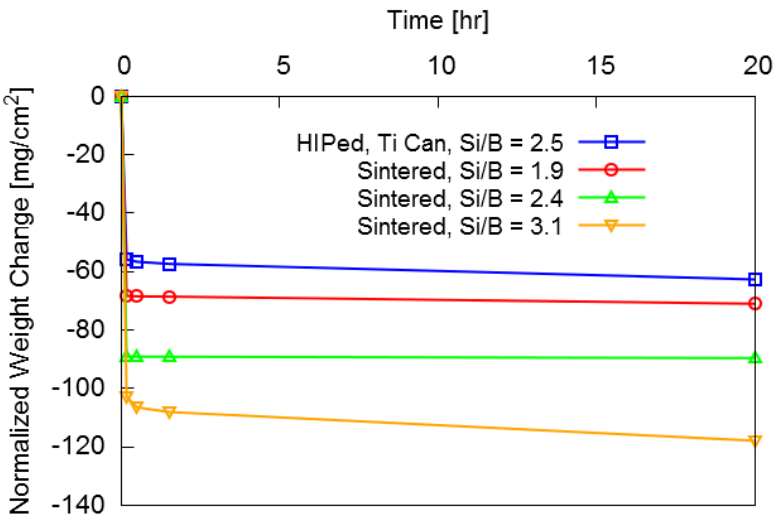

Figure 6.47: Surface area normalized weight loss during oxidation at 1300℃ in flowing air for both the HIP'ed Mo-Si-B can'ed in Ti and three pressurelessly sintered samples. All have minor manganese additions and the Si/B ratios are as indicated. The first data point for the HIP'ed material is after just 3 minutes of oxidation.

would not only produce an oxidation resistance material but be a scalable and cost effective processing technique.

6.2.8 Effect of Air Flow During Oxidation

Oxidation resistance in Mo-Si-B composites involves a fine balance wherein a critical amount of molybdenum oxidation must occur in order to generate a borosilicate layer, which in turn must, by definition, prevent further molybdenum oxidation to achieve oxidation resistance. The composition, as explored previously, has a major effect upon this balance. However, it was found that the oxidation environment plays a substantial role. It had been shown before that Mo-Si-B oxidation performance changes dramatically at different temperatures with generally poor resistance below 900℃ and above 1300℃. Typically the experimental work showing this is only done in static laboratory air or, occasionally, in synthetic air (20% oxygen in argon or nitrogen) with a slow flow rate.

During the interrupted oxidation testing described previously, two observations were made which raised the question of the significance the local sample atmosphere on developing oxidation resistance. First, MoO_3 crystal deposition in the space between the furnace tube and refractory inserts within the tube occurred away from the hot zone where the

temperatures were presumably 600-800℃. It many cases the deposited network of MoO_3 crystals appeared thick and extensive enough to encompass the entire space around the inserts. When disrupted for sample removal these crystals would release a small "puff" of MoO_3 smoke. Second, for a small number of samples which had the poorest oxidation resistance, a similar "puff" of MoO_3 smoke would occur at the moment when the sample was pulled from the hot zone into cool, and fresh, air. While the MoO_3 "smoke" is only visible when the vapor temperature is low enough for it to precipitate, the intensity at which it occurred suggested the samples may have accumulated excess MoO_3 during the previous time step due to a local atmosphere significantly different than air. Additionally, the buildup of MoO_3 crystals around the furnace inserts could easily impede mixing of internal and external air, allowing for a local atmosphere change.

For application in a combustion environment, static air performance is an unrealistic analog, especially for any molybdenum matrix material where displacement of the sizable volume of MoO_3 gas is critical to developing a borosilicate layer. In order to remove any local MoO_3 accumulation away from the sample, a modification to the oxidation testing setup was implemented wherein a fan was placed at one end of the horizontal tube furnace to constantly supply fresh air and displace oxidation products in the hot zone during testing. This approach is more similar to a turbine combustion environment albeit at a flow rates far less than gas turbines. The first challenge for this implementation was the sample cooling due to the air flow. To compensate, the furnace setpoint temperature was raised until the desired equilibrium temperature was measured at a second thermocouple inserted into the hot zone. A thermocouple temperature between 1250 and 1300℃ was selected due to the high variability in the setup and as sample self heating has been observed during the initial, rapid oxidation. This corresponded to a furnace setpoint of 1375℃ for the furnace, furnace tube, and fan used. It should also be noted that the flowing atmosphere was only used for the first 90 minutes of oxidation. Samples which displayed minimal oxidation at 90 minutes were oxidized for a further 18.5 hours in the same furnace set to 1300℃ and without forced air flow.

Of the compositions for which oxidation results under static air are described previously,

12 nearly identical samples, often the second half of the same pellet, were subsequently oxidized in the forced air setup. This set of samples included cobalt, yttria, and manganese as modifiers and covered a Si/B range of 1.4 to 3.7, all with 50 to 55 volume % αMo. While the number of samples was too few to give clear trends with individual compositional parameters, comparison between static and flowing tests of the same compositions showed the air flow effects to be sizable and consistent across the wide range of compositions.

Only two of the previous cobalt modified pellets were available for the oxidation testing under flowing air. The Si/B atomic ratios were 3.4 and 3.7 with cobalt amounts of 1.2 and 1.9 at% in the equivalent glass respectively. As was consistently seen for oxidation in flowing air, the initial weight losses were higher *and* subsequent weight loss rates lower in the flowing air. The higher initial weight loss was due to more aggressive oxidation during the first few minutes, however differing surface preparations prevented a quantitative comparison. Most significantly though, the linear weight loss rate between 30 and 90 minutes of oxidation was reduced by 82 and 64% for the two samples. This improvement allowed oxidation testing to continue to 20 hours total, giving an estimate of long term resistance. Figure 6.48 shows the normalized weight loss for the two compositions in static air up to 90 minutes and in flowing air up to 20 hours at 1300°C.

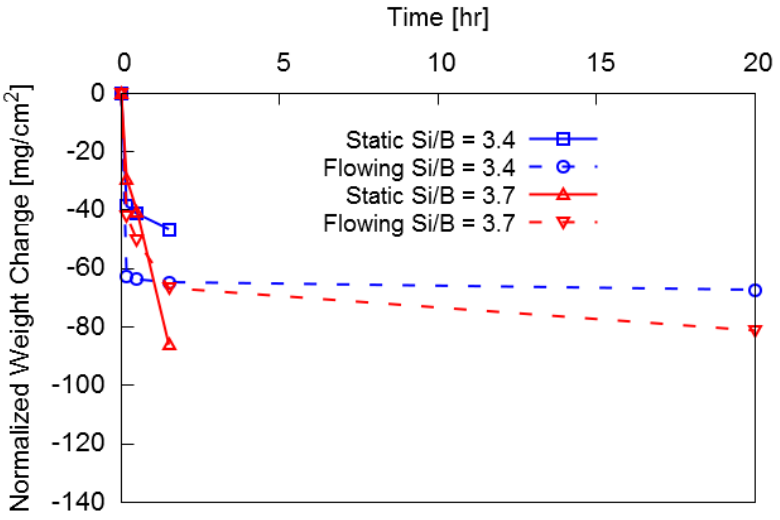

Figure 6.48: Surface area normalized weight loss of two cobalt modified Mo-Si-B composites under both static and flowing air with the sample temperature approximately 1300°C. Higher initial loss but lower long term oxidation rates are seen in during flowing air testing.

While the higher initial weight loss seen in the flowing air testing was only a qualitative assessment for the two cobalt modified samples, a set of four yttria modified pellets had identical surface preparations (coarse grinding to remove any as-fired surface effects) for both static and flowing air testing. These four samples had compositions with Si/B ratios of 3.1 and 3.7 and yttria contents of both 0.3 and 1.5 mol% in the equivalent glass. The resulting normalized weight losses after 10 minutes of oxidation were all higher under flowing air, by 38 to 160%, with lower Si/B and higher yttria contents being correlated with a larger percentage increase in weight loss. However, after the initial 10 minutes of oxidation, all these samples showed improved oxidation resistance in the flowing air with weight loss rates between 30 and 90 minutes reduced by 13 to 99%. As with the cobalt samples, the improved performance allowed these samples to be oxidized for an additional 18.5 hours. Two further yttria modified samples with lower Si/B ratios, 2.4 and 1.9, and an intermediate yttria content, 0.5 mol% in the equivalent glass, were also oxidized in flowing air. The higher Si/B composition had a similarly improved performance however the lower Si/B, 1.9, did not. While this was only observed for one sample, it is possible that the Si/B ratio and air flow rate for improved oxidation resistance are inversely related. Figure 6.49 shows the surface area normalized weight losses for these six samples during oxidation up to 20 hours compared to the previous static air testing done to 90 minutes. One aspect of these weight losses that deserved particular mention is the lack of a downturn at 30 minutes under flowing air conditions. When this was observed during static air oxidation, it occurred along with extensive devitrification and spallation. While some fine grained devitrification may have still occurred during flowing air testing, no spallation was seen.

The final four samples used for comparing oxidation in flowing and static air were modified with manganese, at 1.9mol% MnO in the equivalent glass, and had Si/B ratios of 1.4, 1.7, 1.9, and 2.4. While the forced air testing was done using the developed procedure, the prior static air testing was done early in the Mo-Si-B composition evaluations and utilized the bottom loading box furnace and samples with as-fired surfaces. The resulting improvements seen in flowing air testing are thus due to multiple compounding factors including surface preparation, furnace, and air flow. However, the prior static testing was

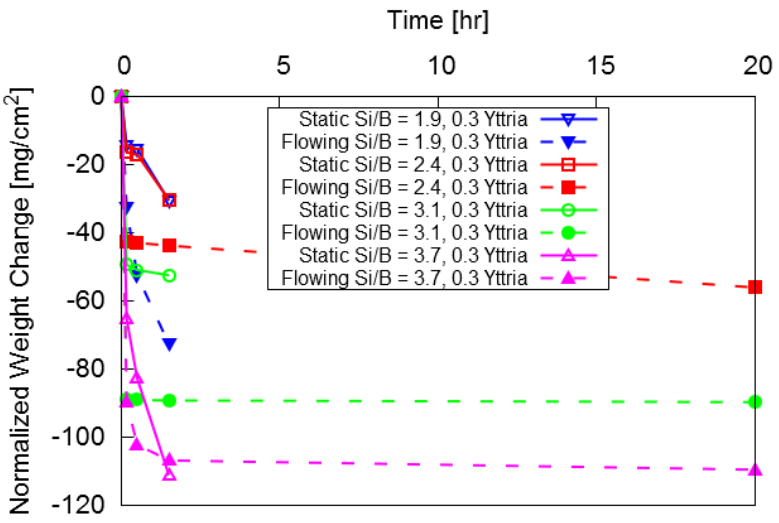

Figure 6.49: Surface area normalized weight losses of six yttria modified Mo-Si-B composites under both static and flowing air with the sample temperature approximately 1300°C.

done up to 20 hours, allowing for comparison of long term oxidation rates. In fact, the oxidation rates for all four samples and at all time steps were dramatically improved with flowing air. The lowest Si/B sample showed rate reductions of 50 to 70% while the other three were 80 to 98%. The largest improvements were for the highest Si/B sample with a long term oxidation rate improving from -1.25$^{mg}/_{cm^2 \cdot hr}$ in static air to -0.026$^{mg}/_{cm^2 \cdot hr}$ under flowing air. The surface area normalized weight losses over 20 hours of oxidation are shown in Figure 6.50.

Although continuous and rapid evolution of MoO_3 gas is, by definition, not oxidation resistance, a certain portion must be removed quickly during the initial stage of oxidation in order to gain long term resistance for Mo-Si-B materials. This initial oxidation allows a sufficient amount of boron and silicon to be freed from the bulk microstructure and form a thick borosilicate glass coating. Both the removal of MoO_3 and the delivery of atmospheric oxygen are critical to this process. If however, the local atmosphere of the material becomes saturated with MoO_3 vapor and/or depleted of oxygen, the borosilicate melt may be impeded by condensed MoO_3 or be too thin to offer longer term protection. While these local atmosphere features were not directly observed during oxidation testing, they can explain the somewhat unusual results of oxidation in flowing air.

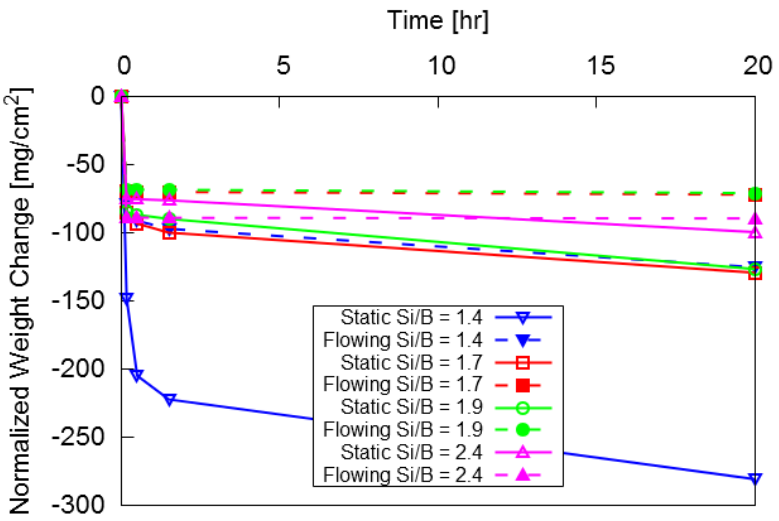

Figure 6.50: Surface area normalized weight losses of four manganese modified Mo-Si-B composites under both static and flowing air with the sample temperature approximately 1300°C.

While the improved long term oxidation rate under flowing air is very encouraging, the disappearance of catastrophic spallation is a more surprising and informative result. Previously spallation had always occurred with extensive devitrification of the borosilicate. However, the immiscibility between the borosilicate and MoO_3 suggests that simply removing MoO_3 more quickly should not affect the borosilicate behavior. Two theories on the relationship between flowing air oxidation and sample spallation are proposed here. The difference between these two theories centers around if the extent of devitrification is less for oxidation in flowing air. Unfortunately the devitrified fraction of the borosilicate after 90 minutes of oxidation is difficult to quantify, particularly post-testing to 20 hours.

In static air oxidation testing, spallation was observed to occur by cracking through bubbles entrained in the borosilicate beneath a devitrified surface, for example in Figures 6.13 on left and 6.25 on right. The thermal expansion mismatch between the bulk and devitrified surface is believed to fracture the glass, which itself is already weakened by numerous internal bubbles. Thus, elimination of spallation can be caused by either suppressing devitrification or strengthening the glass coating. In the first proposed theory, devitrification may be suppressed by rapid removal of boria from the borosilicate melt. Raising the silica fraction increases the melt viscosity, which is analogous to quenching of traditional glasses,

and can slow or eliminate the reconstructive transformation required to form quartz or cristobalite. Because HBO_2 and H_3BO_3 are substantially more volatile than pure boria, a constant supply of water vapor, such as with flowing atmospheric air, would accelerate boron loss. The second proposed theory revolves around strengthening of the borosilicate coating so that spallation does not occur even with equivalent surface devitrification. A denser and more continuous borosilicate layer would be more resistant to thermal stresses. As previously stated, the rapid removal of MoO_3 results in a higher initial weight loss and more surface silica and boria available to form a thicker glass. Additionally, lowering the MoO_3 partial pressure will reduce the number and size of bubbles entrained within the borosilicate. These factors can result in a glass coating more resistant to thermal stress and spallation, even with surface devitrification.

CHAPTER 7

THEORY OF OXIDATION RESISTANCE

7.1 Mechanisms of Oxidation Resistance

The oxidation results presented in the first portion of this chapter show that many mechanisms participate in the oxidation of Mo-Si-B composites. The variations, both between samples and during oxidation for the same sample, indicate that some of these mechanisms occur sequentially while others depend upon specific compositions or oxidation conditions. A theory has been devised to describe the behaviors seen and, more importantly, to inform material development for improved oxidation resistance.

The starting point for the current theory was those theories proposed elsewhere in the literature. In general, other descriptions of the oxidation process focus on an initial stage of approximately linear weight loss followed by a long term parabolic stage. These two stages are defined by an initially porous borosilicate, allowing for MoO_3 evaporation, which, through spreading, becomes dense and continuous for the later stage. This description however, does not explain many of the observed results. Specifically the formation of either bubbles in or channels through the borosilicate are not incorporated. Understanding the origin of these structures is critical in developing Mo-Si-B composites as their presence is associated with a lack of oxidation resistance.

An alternative approach to developing a theory of oxidation behavior is to consider the reverse of the oxidation process, starting with the ideal structure for long term protection. The lowest oxidation rates for Mo-Si-B composites will occur when a dense and high silica layer completely coats the base material. Additionally this layer must be thick enough for the oxygen activity underneath it to be lower than that for the formation of MoO_3. The necessary thickness is thus dependent upon the borosilicate's permeability and, therefore, the higher the silica fraction the thinner the layer can be. In a steady state condition, the low oxygen flux through a high silica layer will be balanced by oxygen diffusion into the base

material where it will form internal silica and boria and potentially a layer of MoO_2. If the silica fraction is sufficiently high, this structure will show very slow parabolic oxidation due to a low permeability [101]. The pertinent question is how to form this structure instead of large bubbles or persistent open channels.

Helpful in understanding the formation of a borosilicate layer on a Mo-Si-B composite are estimations of its thickness and viscosity as well as the partial pressures of the various species involved. It is relatively straightforward to estimate the volume of borosilicate that can be generated by a volume of bulk Mo-Si-B material. Assuming complete evaporation of molybdenum and no loss of boria (the so-call equivalent glass), the change in volume can calculated from approximate molar densities for constant moles of silicon and boron. Additionally, the volume change can be interpreted as a thickness per unit area of planar oxidation and the weight loss and gas change (generated MoO_3, as molecular trimers, and oxygen consumed) can be calculated.

Cross sections of samples oxidized here, as well as in literature results, suggest that a borosilicate thickness of $20\mu m$ is a reasonable target value for long term protection. Applying the above estimations, this $20\mu m$ of borosilicate is formed from between 45 and $50\mu m$ of bulk material, which is around 10x the microstructural size scale of the powder processed composites. A sample with a surface area of 1 cm^2 will experience a net weight loss of approximately $0.04g$ ($40^{mg}/_{cm^2}$). For this small sample $0.02g$ of oxygen will be consumed, which, treated as an ideal gas at 1300℃ and 1 atmosphere, occupies nearly $100cc$. At 20% oxygen, the sample will completely consume all the oxygen from $470cc$ of air around it. Simultaneously, $0.06g$ of $(MoO_3)_3$ will be formed, itself taking up $19cc$. Depending upon the time scale over which this process occurs, the gas transport and local composition would have a significant effect.

A hypothetical oxidation front consuming bulk material to a depth of 10 times the grain size seems unlikely to occur without considerable competition between the borosilicate and MoO_3 vapors. A more reasonable approximation of initial oxidation is the consumption of $10\mu m$ of bulk material (2 or 3 grains deep) which will generate just over $4\mu m$ of borosilicate. For the same small sample of $1cm^2$ surface area, the weight loss is $8.7^{mg}/_{cm^2}$, $100cc$ of air

will be needed, and $4cc$ of $(MoO_3)_3$ will be generated. The value of this hypothetical borosilicate thickness, approximated at $4\mu m$, is important; the threshold between distinct droplets and a continuous layer is associated with a dramatic change in oxidation behavior. A borosilicate melt which could form a $4\mu m$ thick layer may instead form droplets if its surface energies are high enough. However, droplets of this size would be easily observable and, they have not been seen. Rather, very thin layers (on the order of a few microns) can be seen in Figure 6.19b and in published literature[12, 94].

The two estimations above show the disconnect between initial and long term oxidation which necessitated an expanded theory for oxidation behavior. It has been shown that very thin and continuous borosilicate layers form initially, however, they are only around 1/5 as thick as seen in samples with long term oxidation resistance. A mechanism must then exist by which the borosilicate layer can thicken, a process which necessarily requires the removal of molybdenum. This is distinguished from the process which formed the first few microns of borosilicate in that the molybdenum is prevented from freely oxidizing by this very same borosilicate layer. Thus the new thickening process must involve transport of molybdenum oxide through the borosilicate layer.

The thickening of a thin borosilicate melt layer involves four distinct steps. First, oxygen from the air permeates through the borosilicate to the substrate. Next, at the substrate, new silicon, boron, and molybdenum oxides form. If able, newly formed silica and boria will join the overlaying melt, thus thickening it. However, due to the high molybdenum fraction and the mutual lack of solubility between borosilicates and molybdenum oxides, the third step is primarily the transport of MoO_3 as a vapor bubble in the borosilicate. As the bubble grows it stretches the overlying borosilicate, increasing the inward oxygen flux (the permeability is constant but the concentration gradient is over a shorter distance) and thus accelerating its continued growth. Ultimately this causes the outward most bubble wall to become so thin thats its unstable and the bubble pops. Popping leads to the fourth step in which the borosilicate layer flows to fill in the cavity from the bubble and level on the surface. Any new borosilicate generated within the growing bubble will aid in this fourth step. Overall thickening of the borosilicate layer is accomplished by cycling through

these four steps until the oxygen activity at the base of the borosilicate is too low for MoO_3 formation.

The expanded theory of Mo-Si-B oxidation behavior is based upon the above process for borosilicate melt layer thickening as an intermediate stage between initial, roughly linear oxidation and the long term, parabolic behavior. Additional insight can be gained from considering the key factors which cause the transitions between these stages and the various ways in which the process fails and leads to the non-protective structures seen in oxidation testing. In the following paragraphs the aspects of the three individual stages and their transitions will be discussed.

7.1.1 Stage One Oxidation

The very first stage of high temperature oxidation of Mo-Si-B composites occurs when molybdenum is exposed to air resulting in uninhibited formation of MoO_3 vapor and a correspondingly high weight loss rate. This primarily occurs at αMo grains but also on exposed A15 and T2 after the oxidation of surface silicon and boron. Because of a continuous αMo matrix, this stage can continue indefinitely if the borosilicate were immobile. However, the borosilicate formed from T2 is very fluid (50 at% boria) and the porous silica formed from A15 is very fine [94] both of which favor the consolidation of surface borosilicate droplets. This consolidation will occur first where prior T2 grains have been oxidized but will extend over more of the surface as a greater depth of bulk material is consumed. Underneath areas where the borosilicate has consolidated the oxygen activity will still be high enough to form molybdenum oxides due to transport either through the thin borosilicate or circumventing it via locations which are not covered. As stage one progresses, the area fraction of exposed molybdenum will reduce along with the associated high weight loss. Ultimately the overall behavior will no longer be dominated by this free evaporation of MoO_3 and the material will transition out of stage one.

7.1.2 Stage One Transition

The characteristic difference between stages one and two is the unimpeded volatilization of MoO_3. In stage one molybdenum is directly exposed to air while in stage two a thin

layer of borosilicate melt separates the two. Because the formation of MoO_3 from Mo-Si-B composites necessarily generates surface boria and silica, the transition between these two stages of oxidation is dictated by (1) the total accumulation of borosilicate, (2) the surface energy driven consolidation and spreading of the borosilicate, and (3) continued volatilization of MoO_3. The details of this process are not well understood due to the difficulty in experimentally capturing a sample in the midst of transitioning. The short term oxidation results in Figures 6.19 and 6.20 show that samples progress into stage two oxidation very quickly, in less than a few minutes. A new experimental set-up would be needed to increase the heating and cooling rates as well as to quench with minimal effect upon the surface structure.

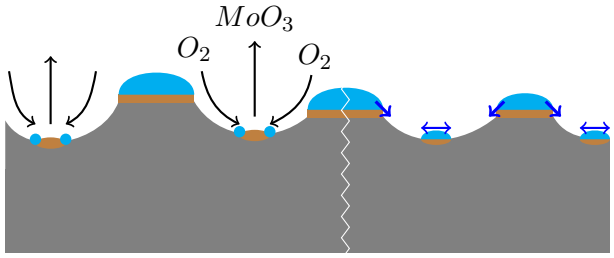

Figure 7.1: Schematic of the transition out of stage one oxidation. The localized gas transport and reactions are highlighted on the left and the spread of the borosilicate is indicated on the right. The bulk composite is shown as a uniform gray across the bottom, brown is condensed molybdenum oxide, and blue is the borosilicate.

Although lacking direct experimental evidence, a number of factors affecting the stage one transition can be hypothesized based upon indirect results and analogous systems. The accumulating borosilicate droplets formed during stage one will attempt to maintain the geometry which minimizes the total surface energy, having interfaces with both vapor (MoO_3 and air) and condensed molybdenum oxide. Given that the stage one to two transition occurs at all, it is reasonable to assume the borosilicate-vapor surface tension is larger than that of the borosilicate-condensed molybdenum oxide. The droplet geometry will thus appear as a hemispherical section with some degree of surface wetting (wetting angle less than 90°). As stage one oxidation progresses, the size and number of borosilicate droplets will increase until, on average, they all overlap and become a single, continuous layer with

minimum surface energy.

While the borosilicate viscosity will dictate the rate at which the droplets change shape (either for minimizing the surface or in response to MoO_3 vapor pressure), it is the surface energies which control the droplet shape and thus the total accumulation needed before forming a continuous layer. On the borosilicate-vapor side the surface tension is expected, for a gas-liquid interface, to be relatively low and insensitive to bulk composition. MoO_3 is know to be extremely effective at lowering the surface tension of glasses and glazes [3] and, during this early oxidation, the atmosphere will be very rich in it. The wetting is, therefore, primarily dependent upon the borosilicate-condensed molybdenum oxides surface energy, which can be highly variable depending upon composition. Exactly which phase the borosilicate is in contact with is unknown but the possibilities include bulk phases (αMo, T2, A15), MoO_2, liquid MoO_3, or liquid transition metal molybdate (TM-molybdate). The later possibility does offer an explanation for the improved initial oxidation seen when modified by minor additions of transition metals or their oxides. All the transition metals evaluated form molybdates with the air stable MoO_4^{-2} species and have melting points considerably higher than MoO_3, e.g. $MnMoO_4$ melting point of 1130℃, [113, 40, 52, 97]. Presumably the equilibrium vapor pressure over the TM-molybdate liquid is also considerably lowered [21]. If this liquid is stabilized (by reducing the vaporization of MoO_3) than the borosilicate may be effectively "floating" on the liquid oxide. The surface energy between these two liquids could be considerably lower than that between the borosilicate and either metallic molybdenum or the MoO_2 phase.

In addition to bulk molybdate effects, two other potential mechanisms in the borosilicate may be at play to lower the apparent surface energy. The transition metal addition oxides might be partitioning into the borosilicate instead of the molybdate. Modifying the borosilicate with transition metal oxides would effect the surface energy, potentially with a reactive wetting structure at the triple line, improving wetting with the underlying molybdenum oxide. Alternatively, although much of the previous theory treats the borosilicate as a single phase, analogous glass systems are well know to phase separate under similar conditions [50, 73]. With the occasional observation of structures similar to Figure 7.2,

the possibility of a dual borosilicate layer should be considered. If borate - silicate phase separation were to occur on a micrometer scale, then its structure during stage one and the transition to stage two might be separate high silica and high boria layers. While the solubility of molybdenum oxide in silicate glasses is know to be very low, little is known about MoO_3-boria melts. The modifying transition metal oxides may again play a role by partitioning to the borate layer, improving miscibility and/or stability of MoO_3. The overall behavior could be due to a complex, triple layer structure of molybdenum oxide, high boria, and high silica which aid in the transition to stage two oxidation.

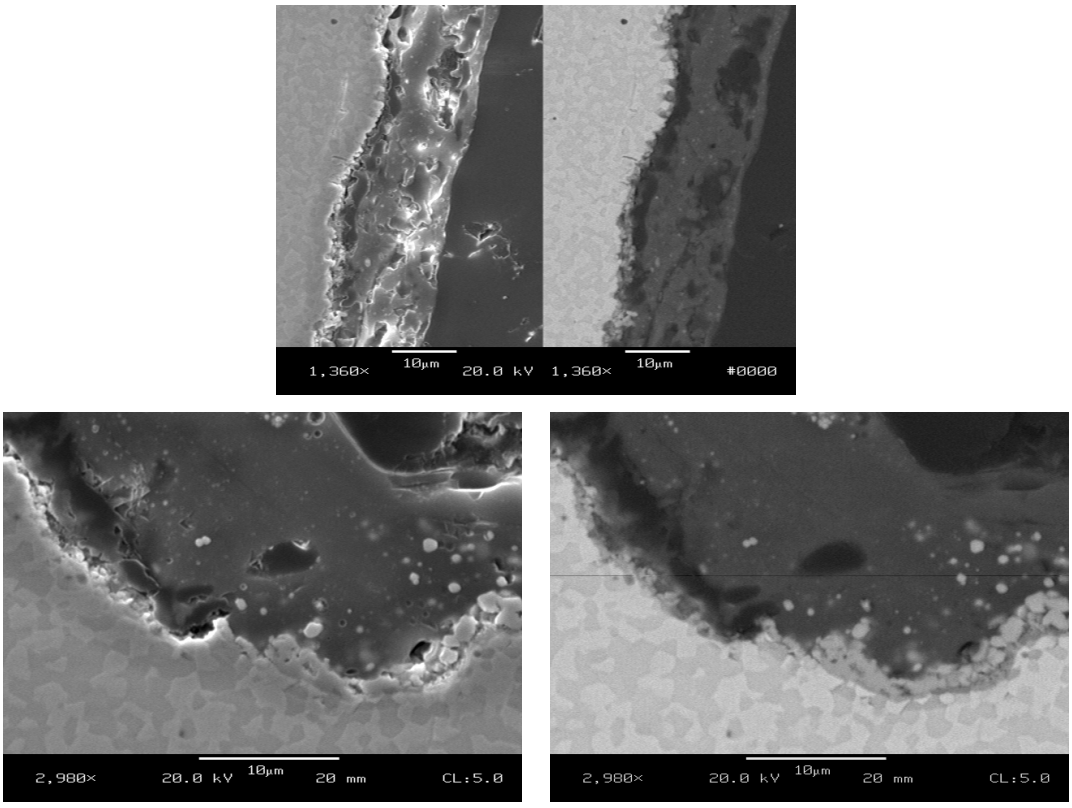

Figure 7.2: Cross section of cobalt modified Mo-Si-B oxidized at 1300℃ for 1 minute. The sample surface is shown in Figure 6.19. Two liquids appear in the borosilicate layer with the darker, presumably borate rich, closer to the underlying material.

7.1.3 Stage Two Oxidation

In the second stage of oxidation a thin layer of borosilicate covers the surface and prevents direct contact between the air and molybdenum. However, crucially, this layer is too thin and too permeable for the underlying oxygen activity to drop below the MoO_3 formation

limit. This results in two important aspects of stage two oxidation: MoO_3 vapor bubbles form in or under the borosilicate layer and, if oxidation resistance is to be achieved, a mechanism must operate to thicken the borosilicate layer. It is specifically these two aspects which necessitated including an oxidation stage before parabolic behavior in the oxidation behavior paradigm. From an experimental perspective it seems unlikely that 50 μm or more of bulk could oxidize and then the formed borosilicate collapse in a single step to give a sufficiently thick layer, of $20\mu m$. Additionally the various potential outcomes of this oxidation stage can explain the failures and unusual surface structured observed.

In describing the stage two oxidation, the ideal behavior (that which leads to oxidation resistance) will be covered before the variations which instead lead to non-protective structures similar to those observed. However, a few ancillary factors will be presented first to contextualize the general behaviors. First, Mo-Si-B oxidation samples did not show any signs of significant gravity effects unless the borosilicate viscosity was exceedingly low. Samples with Si/B ratios approaching oxidation resistant compositions had borosilicate and molybdenum oxide structures that were virtually the same on the top and bottom of the pellets. Due to the temperature of interest, 1300℃, exceeding the MoO_3 boiling point, a distinction needs to be made between boiling and bubbling. In the practical sense, boiling is both vapor bubble formation and buoyancy driven transport. While vapor bubble formation occurs in the oxidation of Mo-Si-B composites, the lack of top to bottom variation indicates that buoyancy is not significant and the bubbling behavior described in this section is driven by other forces. Likely most important of these other forces is the MoO_3 gas-liquid equilibrium vapor pressure, which is the second ancillary factor. At 1300℃, the equilibrium vapor pressure of MoO_3 gas is approximately 3 atm [39]. This gives a sizable driving force to both nucleation of vapor bubbles and their growth. The final ancillary factor is that the solubility of molybdenum oxides in borosilicate melts is very low, particularly when no glass modifier is present to charge compensate the MoO_4^{-2} species [16, 17, 20]. On balance of the above factors, the permeation of MoO_3 or diffusion of MoO_4^{-2} in the borosilicate melt will be insignificant compared to the oxygen permeation and MoO_3 vapor generation.

The importance of stage two oxidation in developing long term oxidation resistance is

thickening the continuous borosilicate layer until the underlying oxygen activity is lowered below the critical value for MoO_3 stability. At the beginning of this stage, the borosilicate layer, although continuous, is relatively thin and fluid. Atmospheric oxygen will thus permeate through the borosilicate to the underlying condensed molybdenum oxide. This oxygen flux will result in continuous nucleation and growth of MoO_3 bubbles. Due to the low solubility of MoO_3 in borosilicates, the small bubbles will be trapped under the borosilicate layer. However, continued oxygen permeation and MoO_3 formation will result in growth of the bubbles via rapid interfacial transport or diffusion within the condensed molybdenum oxide, Figure 7.3 on left. As a bubble grows it will both consume adjacent condensed molybdenum oxides and push upon the overlying borosilicate melt. In turn, these two will respectively free new boron and silicon oxides from the bulk and deform the borosilicate layer. The latter, deformation of the borosilicate layer by the growing bubble, will thin the bubble walls and increase its surface area, causing an acceleration in the oxygen transport, MoO_3 formation, and continued bubble growth. Ultimately the bubble's walls will thin to the point of being unstable, at which point it will pop, releasing MoO_3 vapor into the atmosphere. Additionally, the popping will create a rimmed crater on the borosilicate layer. Due to the higher surface area of the rim and crater, the borosilicate will attempt to level by viscous flow, returning again to a smooth and continuous coating.

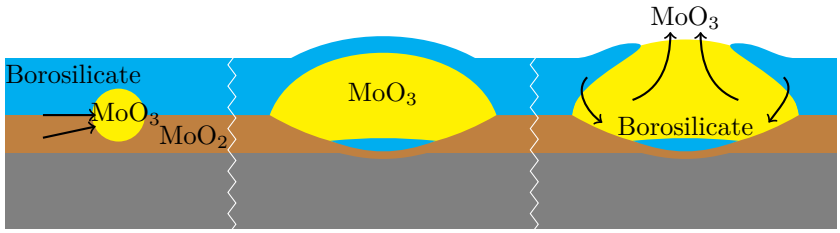

Figure 7.3: Schematic of stage two oxidation showing, at left, the transport of MoO_3 through and along the MoO_2 interfaces. This grows the MoO_3 vapor bubble, shown in the middle, which stretches the borosilicate. When thin enough, the borosilicate "pops" releasing the MoO_3 vapor and flowing to fill the cavity, as shown on the right

Beneath the bubbling surface structure is a layer of MoO_2, αMo, and entrained boria and silica formed by diffusion of oxygen into the bulk material. When adjacent to a growing

MoO_3 bubble, the molybdenum will oxidize and vaporize, freeing the entrained boria and silica. This allows new borosilicate droplets to coalesce in the bottom of the bubble. This new borosilicate performs three roles. (1) it retards continued MoO_3 formation by acting as an additional transport barrier. (2) upon popping of the bubble, this new borosilicate located in the crater bottom will aid in the general borosilicate leveling. Finally, (3), the merging of the new borosilicate with the existing surface layer will increase the total layer thickness and lead towards long term oxidation resistance. Depending upon the size scale of the bubble, it may or may not have a bulk microstructural dependence. If it is relatively small, then growth over prior T2 and A15 grains will generate more new borosilicate. Due to the three roles outlined above, continued MoO_3 bubbling will tend to follow the tortuous path of the prior αMo matrix. Popping of bubbles following this path will create undercutting caverns, instead of simple craters. However, regional borosilicate leveling will still tend to eliminate these structures.

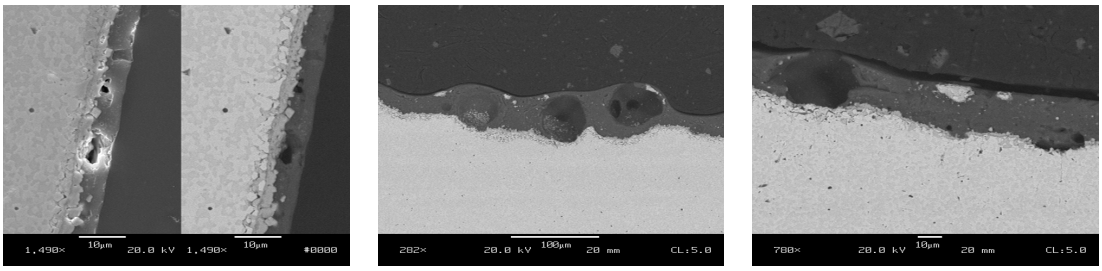

Figure 7.4: Images of MoO_3 bubbles at various points during stage two oxidation. Left, small bubbles forming at MoO_2-borosilicate interface. Middle, bubbles growing and thinning the borosilicate. Right, a bubble right at the point of popping. The left image is after 1 minutes while the other two are after 6 minutes, all at 1300°C.

While the above borosilicate thickening mechanism will lead to a transition out of stage two oxidation and towards long term resistance, it is worth noting some other possible behaviors that may explain the various structures observed. In samples which did not have long term oxidation resistance three specific types of structures were seen and, significantly, the lack of resistance is attributed to the formation of these structures. The first type of structure was only seen in the cross sections of samples and consisted of round vapor pockets completely contained in the oxidation layer. Typically these were quite large and fully within the borosilicate, however there was a wide range of sizes and some located at

the interface between the borosilicate and MoO_2, Figure 7.5. The second type were large bubbles evident on the surface. These were often seen at the 90 minute oxidation step and persisted upon sample cooling, Figure 7.6. The size of these bubbles caused them to be very fragile and suffer from large scale thermal spallation. The third type of structure was an open channel that on the surface appeared as a relatively large hole in an otherwise smooth glass. In cross section however, these surface holes were deep, open channels in a very thick glassy surface, Figure 7.7. The glass around the channel often contained a significant amount of entrained molybdenum oxide, or even bulk Mo-Si-B composite. Occasionally, these channels coarsened in diameter from the interior to the surface. Describing the origin of these three structures is difficult without considering a period of active MoO_3 bubbling, the stage two oxidation presented here.

The observation of large surface bubbles is surprising due to the typical assumption of a relatively fluid borosilicate. Upon cooling MoO_3 vapors inside any bubbles would condense, causing the borosilicate bubble to collapse under atmospheric pressure. The persistence of the large bubbles upon cooling to room temperature suggests a stiff borosilicate. During stage two bubbling, a bubble of limited deformability may never pop and instead grow to the sizes observed. The increased stiffness of the borosilicate can be caused by either boron loss or devitrification. With the bubble walls no longer deforming, and thus not thinning, popping from capillary instability will not occur. Continued MoO_3 generation will grow the bubble both inward, deeper into the bulk, or along the borosilicate and molybdenum oxide interface. Inward growth will tend to be restricted by generation of new borosilicate while growth along the interface requires some deformation of the neighboring borosilicate. Due to the observation of very large surface bubbles, growth along the interface tends to dominate. The ultimate behavior of these large bubbles is unclear as they are very fragile and tended to fracture from thermal shock or mechanical damage during handling for measurement. Additionally, the formation of fine cracks or pin-holes would prevent the buildup of internal MoO_3 pressure, allowing the bubble to continue inward or interfacial growth without catastrophic failure. In the most extreme case of interfacial growth an onion type structure could form wherein large bubbles grow under and parallel to subsequent layers

of borosilicate.

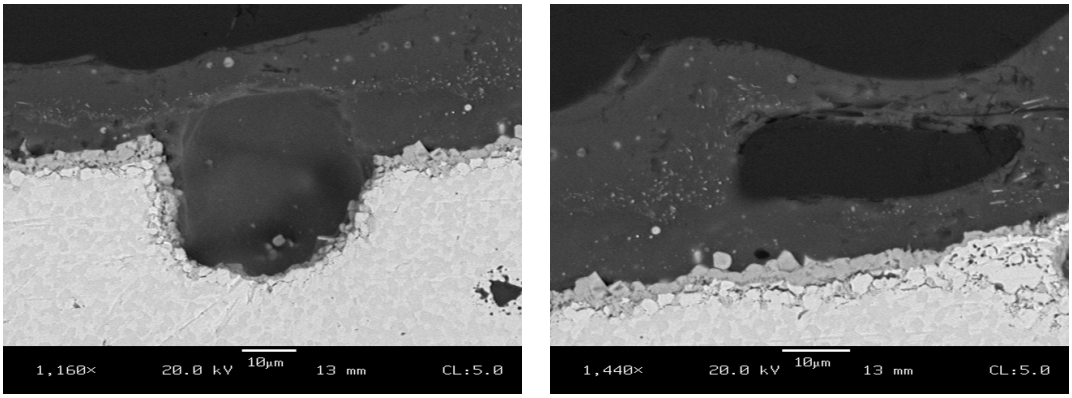

Figure 7.5: SEM-backscatter images of MoO_3 bubbles within the borosilicate in the same cobalt modified samples having a Si/B ratio of 3.1 and oxidized for 90 minutes at 1300℃. The bubble shown on the left formed at the MoO_2-borosilicate interface and has primarily grown into the substrate. The bubble shown on the right however, has had a different and more complex history. On the surface appears to be the remnants of a popped bubble rim which did not level. Additionally, a reasonably thick, new borosilicate layer has formed underneath the bubble.

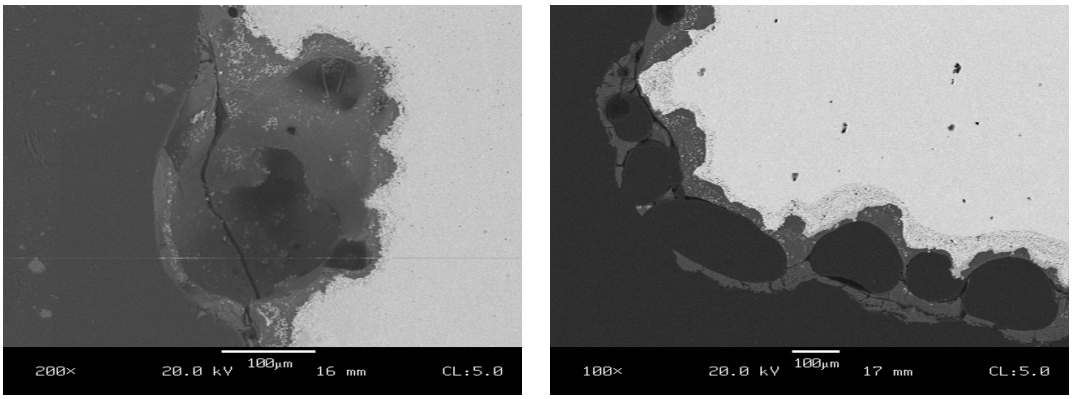

Figure 7.6: SEM images of large surface bubbles formed during stage two oxidation. On left the sample was stopped after 90 minutes at 1200℃ while at right the sample was at 1300℃ for 20 hours. Both have a Si/B ratio of 3.1 however the sample shown on the left had no additions while the one on the right had a minor manganese addition.

While the large surface bubbles are associated with a loss of borosilicate deformability during stage two bubbling, the open channels are believed to arise from the opposite, a new borosilicate layer thats too fluid. After initial bubble popping, the newly exposed borosilicate in the bottom of the crater can continue bubble formation and growth. If the viscosity of the new bubble is too low then its growth may occur more rapidly than the leveling of adjacent borosilicate from the prior bubble popping. This leads to a channel

being formed with (1) new borosilicate being pushed to the sides of the channel and (2) consumption of Mo-Si-B material being highest at the bottom of the crater. Repeated rapid bubbling in the same surface location will starve neighboring bubbles of MoO_3 causing both a deep channel and entrained Mo-Si-B adjacent to the channel.

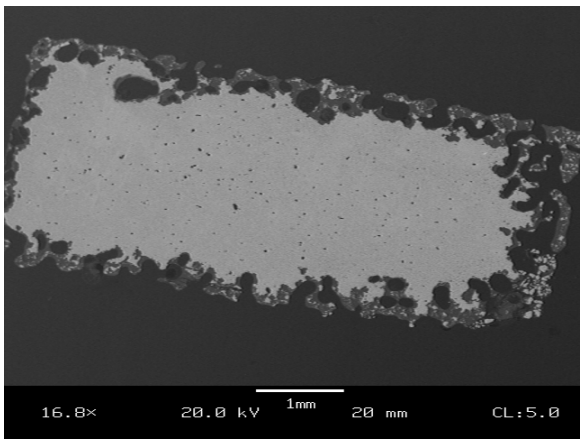

Figure 7.7: SEM image of a full sample cross section in which serious open channel type oxidation occurred after 90 minutes at 1300℃. The sample was modified with a minor iron addition and had a Si/B ratio of 1.2.

The intermediate behavior between large surface bubbles and open channels is not necessarily beneficial for oxidation resistance, rather it can form pockets within the oxidation layers. When the borosilicate stiffening mechanisms (devitrification or boron loss) occur after bubble popping, leveling of the rims and crater will be slowed. However, a new bubble may still be growing in the new borosilicate at the crater bottom. This new bubble will grow and pop, again leaving behind an excessively stiff borosilicate rim. Accumulation of the rigid rims from multiple bubbles in the same crater will pinch-off the location of consecutive bubbling by impeding outward growth of the bubble walls. Continued growth will occur in towards the bulk and horizontally beneath the borosilicate layer. With the accumulation of the rigid rims and subsequent stiffening of many regions on the surface, the volume loss associated with oxidation of the underlying Mo-Si-B will lead to a separation between the bulk and borosilicate layer as can be seen in Figure 7.8.

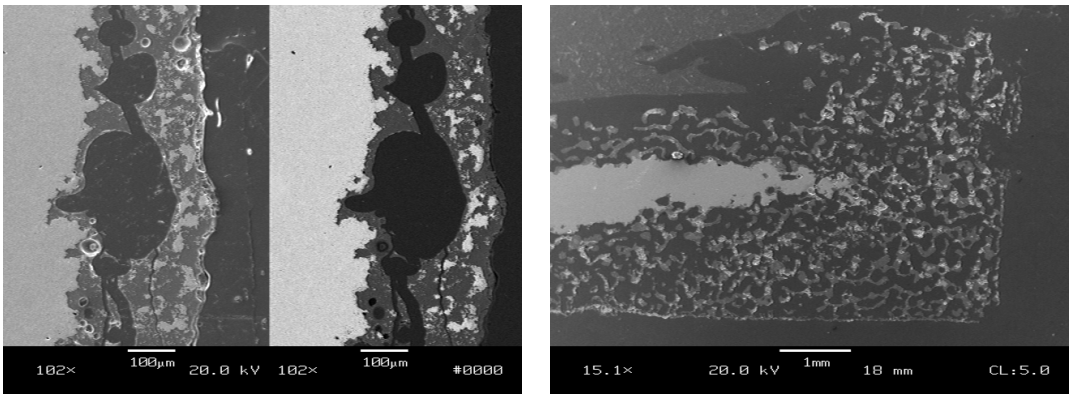

Figure 7.8: Images of large entrained pockets within the borosilicate oxidation layer formed during stage two. Left: side by side secondary and back-scatter images of the same large MoO_3 pockets under a mostly dense borosilicate. The extensive surface-parallel fracture which occurs upon cooling is apparent. The sample (cobalt modified with Si/B ratio of 1.6) was oxidized for 90 minutes at 1300℃. Right: the full cross section of a iron modified sample (Si/B ratio of 1.2) after 20 hours at 1300℃. Repeated pocket formation under newly formed borosilicate resulted in layers of borosilicate that nearly retained the original sample dimensions. The upper right portion was fractured and displaced during sample preparation.

7.1.4 Stage Two Transition

The transition between stage two and stage three oxidation occurs when MoO_3 vapor no longer forms beneath the borosilicate layer. With a fixed atmospheric oxygen concentration and relatively constant diffusion of oxygen within the bulk, lowering of oxygen activity at the borosilicate to substrate interface is caused by both thickening of the borosilicate and reducing its oxygen permeability. The first factor, the thickness of the borosilicate layer, is dependent upon how long stage two operates. The second factor, oxygen permeability, is also primarily time dependent as the boria content of the borosilicate dictates its permeability just as it does the viscosity [101, 65]. The volatilization of boron does have some dependence upon both gas velocity and moisture content (HBO_2 has the highest partial pressure at 1300℃), the relative influences of which are discussed in Section 7.2. Regardless of the details, the critical aspect of successful transition to stage three oxidation is that the borosilicate thickening and boria loss simultaneously approach the desired values. If not, the material will develop non-resistant surface structures as described previously.

7.1.5 Stage Three

Stage three oxidation has the lowest oxidation rate and is entirely diffusion/permeation controlled. In many ways it is very similar to classic parabolic oxidation. Within the borosilicate oxygen and MoO_4^{-2} transport still occur, albeit at very slow rates due to substantial boria depletion of the borosilicate on the air side. On the other side of the borosilicate, in contact with the molybdenum species, the oxygen activity is very low. This is primary due to the protective borosilicate but also balanced by oxygen diffusion into the underlying Mo-Si-B material. Additionally, diffusion of silicon and boron from the bulk to the interface will react with oxygen, preventing molybdenum oxide formation.

Aside from the borosilicate surface layer and bulk Mo-Si-B material, four other reaction layers can form and are all present to some extent in Figure 7.9. The largest layer, which has always been seen in oxidized samples adjacent to the bulk, is composed of fine silica and boria particles within a αMo matrix. This layer arises from diffusion of oxygen into the bulk where it reacts with A15 and T2 grains forming silica and boria. The oxygen activity is too low however, to oxidize the molybdenum. MoO_2 does form in another reaction layer which is always located just beneath the surface borosilicate. Although it is bounded by stability values of the oxygen activity gradient, the origin of this layer is unclear. Its microstructure does not reflect the bulk and tends instead to be thick, coarse grained, and with few secondary phases. A possible formation mechanism is a continuous liquid molybdate which reduces to MoO_2 by inward oxygen transport. During stage three, this layer seems to reduce in size, probably from higher internal oxygen diffusion than through the protective borosilicate.

The final two reaction layers are likely associated with the decomposition of the MoO_2 layer, and exist between it and the internally oxidized A15 and T2. These layers have only occasionally been observed and are, (1), a thin but mostly continuous borosilicate separating the MoO_2 and internal oxidation and, (2), fine αMo grains attached to the MoO_2 layer but extending into the thin borosilicate (1). It is believed that after long oxidation times, the inward oxygen diffusion through a very high silica protective layer is exceedingly slow. Internal silicon and boron diffusion will exceed that of the oxygen. The

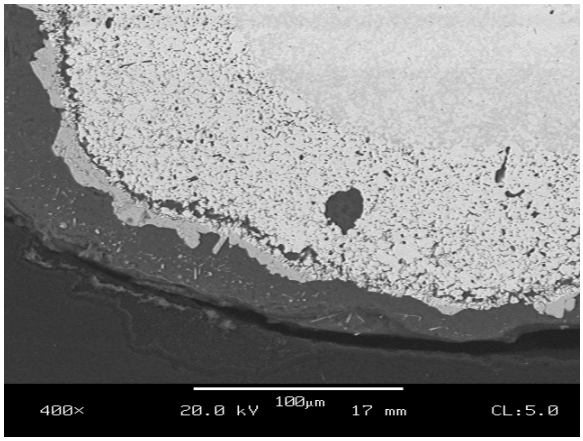

Figure 7.9: SEM-backscatter image of a sample oxidized for 20 hours at 1300℃ experiencing stage three oxidation. The borosilicate is well adhered around the corner. From the air-side inward the layers present are: borosilicate, gray MoO_2, some αMo grain on the back-side of the MoO_2, borosilicate, internal oxidation of αMo with isolated borosilicate pockets, and the bulk.

behavior at the MoO_2 layer will become dominated by silicon and boron flux to it, rather than oxygen passing through. This results in silicon and boron reducing the preexisting MoO_2, creating layers (1) and (2) as described above. Ultimately, the MoO_2 layer will be fully consumed, the borosilicate beneath it will merge with the overlying borosilicate, and the small αMo grains will remain trapped but protected within the borosilicate. In cross section of oxidation samples this appears as only two layers, the protective borosilicate and internal oxidation, but with a small line of αMo particles partway through the borosilicate.

7.2 Environment Interaction

The mechanisms associated with the development of oxidation resistance in Mo-Si-B composites can be quite sensitive to the oxidation environment, occasionally with surprising results. Each of the three stages and the transitions between them can respond differently to various environmental conditions. This has been shown experimentally, to a limited extent, in the change in oxidation resistance between static and flowing air, see Section 6.2.8. However, it is difficult to experimentally isolate individual environmental factors such as gas flow rates, partial pressures, and boundary layer thicknesses and doing so was beyond the scope of this work which focused primarily on composite composition. In spite of the limited data, the details of the three stage theory of oxidation do provide a framework for

understanding the sometimes unusual environmental dependencies.

Within the framework of the three stage theory, the primary divergence among the various oxidation results presented here was the behavior during the later portion of stage two. Generally samples quickly passed through stage one and entered into stage two bubbling. However, in most samples which did not ultimately have oxidation resistance, the bubbles persisted as holes or channels and the third stage of oxidation never occurred. Figure 7.10 shows schematic weight loss as a function of time for the different behaviors frequently seen here. The difference between successful resistance and the often seen open channels is manifested in the divergence during stage two.

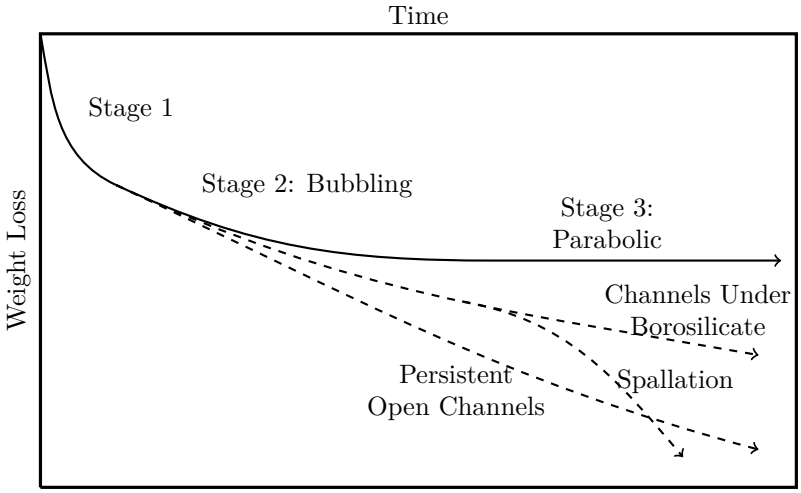

Figure 7.10: Schematic of weight loss during high temperature oxidation. The solid line represents an oxidation resistant behavior while the dashed lines are characteristic of failing to transition between stages two and three.

Instrumental in the differing behaviors shown in Figure 7.10 are the boron content and thickness of the borosilicate melt as they dictate if and when the transition to stage three oxidation occurs. These control both the oxygen activity beneath the borosilicate layer and its viscosity, what are in effect the driving force and mobility of MoO_3 bubbles respectively. Suppression of the bubbling behavior ends the second stage oxidation and results in the parabolic oxidation mechanism becoming dominant, referred to here as stage three. The boron content and borosilicate layer thickness are both highly dependent upon interactions with the environment. High temperature boron volatility is well known [66, 111, 108]

and is necessary to reduce the surface layer permeability and increase its viscosity. The borosilicate layer thickness is directly dependent upon the removal of molybdenum (by MoO_3 evaporation) which would otherwise impede the formation of a dense and continuous layer. The relative rates of these two processes can either lead to oxidation resistance or form the channels and high weight losses shown as dashed lines in Figure 7.10.

Figure 7.11 schematically details the rates and effects of borosilicate thickness and boron volatility. On the left side of Figure 7.11, the concurrent increase in borosilicate thickness and reduction in oxygen activity underneath this layer are shown. The borosilicate thickness is approximately interchangeable with weight loss from molybdenum evaporation. The underlying oxygen activity is dependent upon both the thickness of the borosilicate and its oxygen permeability. Additionally, the oxygen activity determines the formation of MoO_3 which will tend to grow as bubbles. The permeability and bubble behavior are dependent upon the boron content which is shown as the boron loss and resulting increase in viscosity in Figure 7.11 on the right. The higher viscosity is in turn associated with reduced oxygen permeability and an inability to level the borosilicate melt surface after popping of a MoO_3 bubble. Two critical points can be defined on these plots; one for the oxygen activity below which MoO_3 does not form, and another below which the borosilicate melt can't level and heal from bubble popping. If the oxygen activity drops below the critical value before the melt looses its ability to heal, then the transition from stage two to three oxidation will occur and the material will be oxidation resistant. If, on the other hand, the borosilicate looses its ability to heal before the underlying oxygen activity reaches the critical value, then continued MoO_3 formation in open channels will occur and the material will not be oxidation resistant.

The thickness of the borosilicate layer can be simply related to the weight loss if the fraction of condensed molybdenum oxides is negligible. In most of the compositions evaluated here, the hypothetical oxidation process of removing molybdenum and forming a residual borosilicate, causes a volume reduction of 55 to 60%. For approximate densities of 9.6 $^{g}/_{cc}$ for the bulk and 2.5 $^{g}/_{cc}$ for the glass and a surface area of $1cm^2$, this corresponds to $2^{mg}/_{cm^2}$ for every $1\mu m$ of borosilicate. The rate at which this process occurs is most

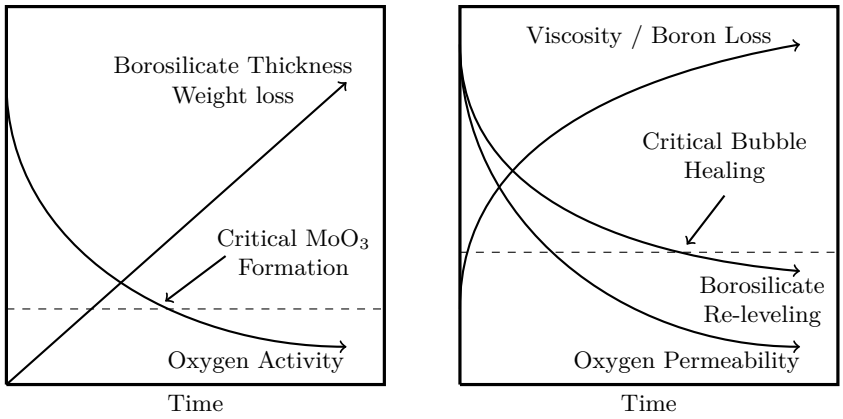

Figure 7.11: Schematic time dependent changes in borosilicate and MoO_3 behavior during theoretical Mo-Si-B oxidation.

likely limited by the gas transport to and from the surface through a gas boundary layer. This applies to both the removal of MoO_3 and the supply of O_2 to form the various oxides. In general, the mass transfer of these species is related to the partial pressure differential across the boundary layer and the size of the boundary layer itself [119, 89]. Of particular significance here is the boundary layer thickness which is inversely proportional to the gas velocity raised to the 0.5 or 0.8 power for laminar and turbulent flows respectively [89]. Oxidation in a flowing atmosphere will thus thin the gas boundary layer, accelerate the surface-vapor reactions, and increase the rate of growth of the surface borosilicate.

Whereas the hydrated vapor species of molybdenum (H_2MoO_4) becomes less significant than the polymerized MoO_3 species at elevated temperatures, the evaporation of boron is increased in moist gases due to the high equilibrium vapor pressure of HBO_2 and H_3BO_3 [75, 120]. While the environmental dependence of the left schematic in Figure 7.11 is primarily air flow velocity, the boron loss on the right is strongly related to the flow velocity, air moisture content, and the boria distribution in the borosilicate layer. In observations of some silicate glass melts, this last factor dominates the volatile losses through the formation of a high silica, high viscosity surface layer which limits viscous transport of boria or soda species to the melt-atmosphere interface [120, 86, 26].

In the case of Mo-Si-B composites, the gas flow rate, water vapor content, viscous diffusion of boria, and borosilicate bubbling during stage two all have complex and some

competing influences on the boron loss rate. Compounded by the difficulty in measuring boron contents and distributions within the oxidation layer, there is considerable uncertainty as to the overall boron behavior. However, given that oxidation resistance of Mo-Si-B materials can occur at all, and that many samples show better performance in flowing air than static, the window for obtaining the critical borosilicate layer thickness prior to dropping below the critical boron content must exist and be within the first 10 minutes at 1300℃ for the testing setup employed here.

7.3 Design for Oxidation Resistance

Drawn from the oxidation results and developed theories presented previously, the following general approach to designing Mo-Si-B composites with oxidation resistance is proposed. While both microstructure and composition factor into general composite design, the work here focused entirely on compositional variations and utilized processing with little room for modifying microstructures. Thus, this discussion will consider only the composition of Mo-Si-B composites and assume a consistent microstructure composed of relatively fine (nominally 5 μm) and equiaxed grains, well mixed phases, and a continuous αMo matrix. Given the additional requirements on mechanical properties and the larger size scale on which oxidation operates, limiting to this general microstructure is reasonable and will have minimal effect upon the oxidation behavior. Far more significant to the development of oxidation resistance is the compositional aspect of the composite design. This is divided into three sections: the silicon to boron ratio, minor refractory oxide or transition metal additions, and the matrix volume fraction. These three are primarily concerned with the borosilicate melt viscosity, ability to cover the composite surface, and the amount of bulk material that must oxidize prior to become protected.

7.3.1 Ratio of Silicon to Boron

The ratio of silicon to boron in Mo-Si-B composites is arguably the most significant factor in tailoring the composition for oxidation resistance. Upon oxidation, the surface silica and boria are responsible for forming the majority of the highly polymerized melt which both coats and protects the material. As the composition of this surface layer shifts to

higher silica fractions, the viscosity increases along with a decrease in both the oxygen permeability and the ability of the borosilicate to level/heal upon popping of any MoO_3 bubbles. Balancing the permeability and leveling behavior is crucial to developing oxidation resistance and thus the silicon to boron ratio is key to composite design.

While the silicon to boron ratio directly dictates the borosilicate composition and viscosity upon initial oxidation, the time dependent change due to boron volatility also plays a significant role in the overall oxidation behavior. Selection of the silicon to boron ratio thus depends upon not only the operation temperature but also the humidity of the atmosphere and the gas velocity. While the work here only explored a small range of these conditions, a silicon to boron ratio around 2.5 was found to be best for oxidation at 1300℃ in moderate flow rates of laboratory air. This corresponds to a borosilicate of 83 mol% SiO_2. At higher and lower temperatures, the optimal silicon to boron ratio would be expected to be lower and higher respectively, to compensate for the temperature dependence of the viscosity. Additionally, under conditions of higher boron volatility (higher gas velocities and moister contents), a lower silicon to boron ratio may be needed to prevent premature loss of the borosilicate's ability to heal upon bubble popping. However, given that the rate of molybdenum removal (and the borosilicate thickening) would also be higher, additional boron may not be necessary. Future investigations into this specific trade off would yield considerable insight into the general oxidation behavior of Mo-Si-B composites.

7.3.2 Minor Additions

7.3.2.1 Transition Metals

The addition of transition metals has been found, both here and in the literature, to have a profound effect upon the oxidation of Mo-Si-B composites at 1300℃. Cobalt, iron, manganese, and nickel were all found to substantially improve the oxidation resistance during the first 10 minutes. Their effect is related to aiding initial borosilicate coverage of the surface with fewer open holes being present. However, beyond this initial period the beneficial effects become superseded by extensive devitrification and spallation. The degree of devitrification and the severity of the spallation depends upon both the amount of the

addition present as well as which element is used. In this work manganese was found to be the only one of these transition metal additions for which a beneficial concentration was found that did not lead to devitrification and spallation. Samples with manganese added to 1.9 mol% MnO in the equivalent glass had excellent oxidation resistance at 1300℃ in both static and flowing air. Based upon the results of other samples, both higher and lower manganese contents are likely also viable.

7.3.2.2 Refractory Oxides

Similar to the transition metals above, the minor addition of certain refractory oxides is believed to improve Mo-Si-B oxidation resistance. While the exact mechanisms by which any of these additions aid oxidation are not clear, refractory oxides maybe included to fulfill two distinct roles. First, yttria, and potentially various lanthanides, can be added at low amounts to improve initial oxidation in the same manner as the transition metals described above. Samples containing 0.46 mol% yttria in the equivalent glass were found to have very low weight losses after 10 minutes of oxidation. The second role for refractory oxide additions is in modifying the borosilicate along the lines of traditional glasses. Alumina and alkaline-earth oxides can act as network formers and modifiers in borosilicates affecting the tenancy for phase separation, oxygen permeability, and solubility of other species [121, 117, 50, 65]. Within the work here, one volume percent $SrAl_2Si_2O_8$ (SAS) added to a manganese modified Mo-Si-B composition resulted in improved oxidation resistance both at 1300℃ and during the evaluation of pre-oxidation for protection at 800℃, Figure 6.39.

7.3.3 Matrix Volume Fraction

The final Mo-Si-B composite design factor considered here is the volume fraction of the αMo matrix. While this has little effect upon the long term oxidation behavior, which is controlled by the surface borosilicate composition, increasing the matrix volume fraction does raise the initial weight loss associated with forming a borosilicate layer. The greater volume of MoO_3 removal needed to free the borosilicate places more stringent demands upon the borosilicate's ability to heal upon bubble popping. However, these aspects of oxidation resistance must be balanced against the mechanical properties of the composite in order for

it to be viable as a structural material. Increasing the matrix volume fraction dramatically lowers the constraint upon its plasticity from the high fraction of hard phases and will result in a corresponding increase in toughness [69]. The general material design approach will be to tailor the borosilicate melt composition per the above factors and then include their source phases in the bulk at a minimum fraction necessary for oxidation resistance so as to limit the impact upon mechanical properties. Unfortunately, very little work has been done exploring the role of matrix volume fraction on the oxidation behavior. Figure 6.29 does show a proof of concept comparison between two samples with equivalent borosilicate compositions but differing matrix volume fractions. Its believed that continued increases in the matrix fraction would shift to higher initial weight losses but not effect the subsequent behavior. The practical limit to this and the optimal for engine applications are avenues of further investigations.

CHAPTER 8

CONCLUSIONS

The development of novel, high temperature materials has great potential for increasing gas turbine efficiency by raising the peak operating temperature. As with any engineering material, a combination of requirements must be met including high temperature oxidation resistance, creep resistance, and strength and fracture toughness over the full temperature range seen in service. Mo-Si-B composites aim to meet these demands through their refractoriness, formation of a protective borosilicate surface scale, and crack trapping within an αMo matrix.

Aside from the αMo matrix, the Mo-Si-B composites of interest here contain a large volume fraction of Mo_3Si (A15) and Mo_5SiB_2 (T2) phases. The A15 and T2 intermetallic grains provide both creep resistance and a surface borosilicate upon exposure to oxygen, which then leads to oxidation resistance. The αMo matrix is the phase which gives Mo-Si-B composites an advantage over other high temperature materials, such as SiC-SiC composites and bulk intermetallics. Crack trapping, blunting, and bridging by the αMo grains greatly increases the fracture toughness and fatigue strength due to plasticity mechanisms not present in the other high temperature material candidates.

The very different properties of αMo and the two intermetallics complicates material development because the optimizations for strength and oxidation resistance compete. Research into Mo-Si-B composites requires a framework for the development of some properties without neglecting others. The theoretical framework presented here reflects the critical role of the αMo matrix by placing all the oxidation resistance demands upon the 45 volume%, or less, of the hard, intermetallic phases. Specifically, the borosilicate composition formed upon oxidation of these phases must be able to coat the composite surface during initial oxidation and then subsequently be an oxygen barrier for long term resistance. However, this 45v% of intermetallics must have a minimal effect upon the αMo phase so that it does

not lose the plasticity necessary for inhibiting crack growth.

Within this framework, this dissertation investigated the relationship between oxidation resistance and the composition of the intermetallic fraction, with minor additions, for samples produced in a manner which minimally impacted the αMo matrix. The Mo-Si-B composite processing built upon the previously developed powder processing with silicon and boron nitrides that allows for a low oxygen content and sintering of fine starting powders [78]. Adjustments were made to the firing cycle based upon dew point measurements made during the hydrogen de-oxidation stage. Under a relatively high gas flow, 90% of the total water generated occurred during a ramp of $2^{\circ}C/_{min}$ between 450 and 800℃ followed by a hold of 30 minutes.

Although improvements to de-oxidation during processing minimized any premature oxidation of silicon and boron, which could create slight composition changes, the pressureless sintering still required temperatures near 1600℃. Processing to this high a temperature has two negative consequences. First, it results in a silicon supersaturation that raises the brittle to ductile transition temperature (BDTT) to 1000-1100℃ and, second, volatile loss of manganese precludes its use as a minor modifier for oxidation resistance. As an alternative, hot isostatic pressing (HIP) at 1300℃ was demonstrated as a viable consolidation technique. By firing *and* HIP'ing to only 1300℃, the silicon solubility was reduced and added manganese was retained. However, due to contamination issues, titanium cans had to be used instead of low-carbon steel. Further development of material handling and canning in titanium should be a focus of future work to produce and evaluate the mechanical properties, both at high temperatures and to identify the degree by which the BDTT is lowered by HIP processing.

Beyond the processing development, this dissertation addressed the active mechanisms during oxidation and the role of composition. Analysis of both samples with and without oxidation resistance gave insight into the series of steps by which a borosilicate scale forms, spreads, and becomes protective. This investigation into oxidation resistance has resulted in four conclusions. First, the borosilicate compositions which lead to oxidation resistance at 1300℃ are not necessarily the same as those reported in the literature. The 33 mol%

boria borosilicate of Mo-3wt%Si-1wt%B was not oxidation resistant in the testing here. Instead, increasing the silica fraction to 80 to 85% was found to be necessary so that the borosilicate would have a sufficiently high viscosity and low permeability. Within the Mo-Si-B composition this corresponds to a Si/B atomic ratio of 2.3 to 3. Higher (more viscous) compositions failed due to spallation of the poorly attached, high silica scales. Lower compositions failed from continuous oxidation, either through open channels or repetitive MoO_3 bubble growth and popping.

The second conclusion from the oxidation investigations was that minor additions of certain transition metals are critical during the initial stage of oxidation at 1300℃. Iron, nickel, cobalt, yttrium, and manganese were all identified as dramatically improving the short term oxidation when present at 0.3 to 1.5 mol% within the borosilicate. Both diminished weight loss and improved surface coverage were observed. However, these additions tended to cause substantial devitrification and spallation at later points during oxidation testing. This eliminated the use of all but manganese, which was the sole additive to not cause large scale spallation and resulted in samples with long term oxidation rates below -0.05$^{mg}/_{cm^2 \cdot hr}$.

The third conclusion from the oxidation testing resulted from a change to the testing methodology. By performing oxidation under forced air, the long term oxidation resistance was improved, even for compositions which performed poorly in static environments. The improved long term resistance came about after a higher weight loss during the initial phase of oxidation. Both of these are a consequence of the more aggressive oxidation in flowing air. Supply of oxygen and removal of MoO_3 vapors increases the rate by which molybdenum is oxidized and removed, which is linked to the total amount of borosilicate generated on the sample surface. Once the borosilicate layer formed, it was thicker and thus a better oxidation barrier. Additionally, the flowing air increased the rate at which boria was removed from the borosilicate surface. As the initially formed borosilicate is intended to coat the surface, it has a relatively high oxygen permeability. By evaporating boria from the surface, the borosilicate layer becomes less permeable and more protective.

The final conclusion of the oxidation results was the development of a theory by which

oxidation resistance occurs. While the initial and long term oxidation stages are similar to those found within the literature, the addition of another, intermittent stage provided valuable insight into how the observed structures form. Also, considering the factors associated with transitioning between these three stages provides a framework by which many observed failures can be understood. The borosilicate thickening by MoO_3 bubbling during stage two was identified as the point where most of the non-oxidation resistance compositions tested here deviated from the ideal pathway. Open and closed channels and large scale spallation from devitrification arose from the material behavior during stage two when the borosilicate was either excessively fluid or viscous.

The understanding of oxidation resistance established here serves more as a key step in Mo-Si-B composite development than as an end in itself. Within the context of the three stages of oxidation, and with the variety of oxidation structures observed, Mo-Si-B samples can be more quickly and throughly understood. Future work can thus focus upon the mechanical properties of these composites. However, investigating the mechanical behavior will require a larger volume of material both due to the number of samples needed and requirements upon their size. Therefore the three following points are recommended for future development of continuous αMo, Mo-Si-B composites.

1. Consolidation of Mo-Si-B powders by hot isostatic pressing at 1300℃ has the dual advantages of low silicon solubility and retention of added manganese. However, because this consolidation must follow the de-oxidation and nitride decomposition/reaction processing steps, a procedure must be developed to transfer the fired powder, or compact, into a titanium can. Preventing oxygen contamination during this transfer is a challenge as the powder (pre-fired to 1300℃) will have high open porosity and surface area.

2. The main mechanical property of interest is the brittle to ductile transition temperature (BDTT). Ductile behavior is the advantage held by Mo-Si-B composites over other high temperature material such as SiC-SiC composites and bulk intermetallics.

The high BDTT of molybdenum with excessive silicon supersaturation must be addressed for Mo-Si-B composites to be of use. HIP'ing at 1300℃ will reduce the silicon solution, however the extent the BDTT can be lowered needs to be identified. Additionally, improvements in the lower temperature toughness may be associated with a loss of high temperature creep resistance. Measurements of both the BDTT and high temperature creep resistance should be made on the same material to understand the trade-off and, potentially, identify the relative roles of grain boundary strength and dislocation slip.

3. As stated above, and within the theoretical framework used here, the mechanical behavior of Mo-Si-B composites is critical but strongly restricted by oxidation resistance requirements. These requirements can be greatly reduced by first, treating the bulk oxidation resistance as a mechanism for damage tolerance and second, developing coating systems to provide the environmental protection for the majority of a component's life. Promising candidates include T1-based, pack-cemented coatings and thermal sprayed or sintered Ba/Sr aluminosilicates (BSAS). These coatings should be evaluated under thermal cycles, moist atmospheres, and with regard to their interaction with the bulk oxidation products upon localized failure.

REFERENCES

[1] Abuluwefa, H. T., "Thermodynamics and Kinetics of Surface Oxidation of Steels during Annealing in H2-N2 Atmospheres," in *Proceedings of the International Multi-Conference of Engineers and Computer Scientists*, vol. 2, 2012.

[2] Akinc, M., Meyer, M., Kramer, M., Thom, A., Huebsch, J., and Cook, B., "Boron-doped molybdenum silicides for structural applications," *Materials Science and Engineering A*, vol. 261, pp. 16–23, Mar. 1999.

[3] Amberc, C., "Effect of Molybdenum and Other Oxides on Surface Tension of Silicate Melts and on Properties of Refractories and Abrasives," *Journal of the American Ceramic Society*, vol. 29, no. 4, pp. 87–93, 1946.

[4] Bansal, N. P., "Solid state synthesis and properties of monoclinic celsian," *Journal of Materials Science*, vol. 33, no. 19, pp. 4711–4715, 1998.

[5] Beerkens, R. G., "Modeling the kinetics of volatilization from glass melts," *Journal of the American Ceramic Society*, vol. 84, no. 9, pp. 1952–1960, 2001.

[6] Belton, G. and Jordan, A., "The volatilization of molybdenum in the presence of water vapor," *The Journal of Physical Chemistry*, vol. 69, no. 6, pp. 2065–2071, 1965.

[7] Berczik, D., "Oxidation resistant molybdenum alloy," Dec. 1997. Patent US 5693156.

[8] Birks, N. and Pettit, F., "Environmental effects during application of materials at temperatures above 1200C," *Materials Science and Engineering: A*, vol. 143, no. 1, pp. 187–195, 1991.

[9] Boike, M., Hilpert, K., and Müller, F., "Thermodynamic activities in B2O3-SiO2 melts at 1475K," *Journal of the American Ceramic Society*, vol. 76, no. 11, pp. 2809–2812, 1993.

[10] Brewer, L. and Lamoreaux, R., "The Mo-O system (Molybdenum-Oxygen)," *Journal of Phase Equilibria*, vol. 1, no. 2, pp. 85–89, 1980.

[11] Burk, S., Gorr, B., Trindade, V. B., and Christ, H.-J., "Effect of Zr Addition on the High-Temperature Oxidation Behaviour of Mo-Si-B Alloys," *Oxidation of Metals*, vol. 73, pp. 163–181, Aug. 2009.

[12] Burk, S., *Hochtemperaturoxidation Molybdan-basierter Legierungen unter Berucksichtigung von Einflussen aus Umgebungsatmosphare und legierungstechnischen MaBnahmen*. PhD thesis, Zugl.: Siegen, Universitat Siegen, Diss., 2011, 2011.

[13] Burk, S. and Christ, H. J., "High-Temperature Oxidation Performance of Mo-Si-B Alloys: Current Results, Developments and Opportunities," *Advanced Materials Research*, vol. 278, pp. 587–592, July 2011.

[14] Burk, S., Gorr, B., and Christ, H.-J., "High temperature oxidation of Mo-Si-B alloys: Effect of low and very low oxygen partial pressures," *Acta Materialia*, vol. 58, pp. 6154–6165, Oct. 2010.

[15] Bygden, J., Sichen, D., and Seetharaman, S., "A thermodynamic study of the molybdenum-oxygen system," *Metallurgical and Materials Transactions B*, vol. 25, no. 6, pp. 885–891, 1994.

[16] Calas, G., Le Grand, M., Galoisy, L., and Ghaleb, D., "Structural role of molybdenum in nuclear glasses: an EXAFS study," *Journal of Nuclear Materials*, vol. 322, pp. 15–20, Oct. 2003.

[17] Caurant, D., Majerus, O., Fadel, E., Quintas, A., Gervais, C., Charpentier, T., and Neuville, D., "Structural investigations of borosilicate glasses containing MoO3 by MAS NMR and Raman spectroscopies," *Journal of Nuclear Materials*, vol. 396, pp. 94–101, Jan. 2010.

[18] Caurant, D., Majerus, O., Fadel, E., Lenoir, M., Gervais, C., and Pinet, O., "Effect of Molybdenum on the Structure and on the Crystallization of SiO2-Na2O-CaO-B2O3 Glasses," *Journal of the American Ceramic Society*, vol. 90, pp. 774–783, Mar. 2007.

[19] Chanmuang, C., Naksata, M., Chairuangsri, T., Jain, H., and Lyman, C. E., "Microscopy and strength of borosilicate glass-to-Kovar alloy joints," *Materials Science and Engineering: A*, vol. 474, no. 1, pp. 218–224, 2008.

[20] Chouard, N., Caurant, D., Majérus, O., Dussossoy, J.-L., Ledieu, A., Peuget, S., Baddour-Hadjean, R., and Pereira-Ramos, J.-P., "Effect of neodymium oxide on the solubility of MoO3 in an aluminoborosilicate glass," *Journal of Non-Crystalline Solids*, vol. 357, no. 14, pp. 2752–2762, 2011.

[21] Chychko, A., Teng, L., and Seetharaman, S., "MoO3 evaporation Studies from binary systems towards choice of Mo precursors in EAF," *Steel Research International*, vol. 81, no. 9, pp. 784–791, 2010.

[22] Cochran, J., Daloz, W., and Marshall, P., "Oxidation resistant Mo-Mo2B-silica and Mo-Mo2B-silicate composites for high temperature applications," *JOM*, vol. 63, no. 12, pp. 44–49, 2011.

[23] Cockeram, B., "The role of stress state on the fracture toughness and toughening mechanisms of wrought molybdenum and molybdenum alloys," *Materials Science and Engineering: A*, vol. 528, pp. 288–308, Nov. 2010.

[24] Cockeram, B. and Chan, K., "In-situ fracture studies and modeling of the toughening mechanism present in wrought low-carbon arc-cast molybdenum, titanium-zirconium-molybdenum, and oxide-dispersion-strengthened molybdenum flat products," *Metallurgical and Materials Transactions: A*, vol. 39, no. 9, pp. 2045–2067, 2008.

[25] Cockeram, B., Smith, R., and Snead, L., "The influence of fast neutron irradiation and irradiation temperature on the tensile properties of wrought LCAC and TZM molybdenum," *Journal of Nuclear Materials*, vol. 346, no. 2, pp. 145–164, 2005.

[26] Conradt, R. and Scholze, H., "Zur verdampfung aus glasschmelzen," *Glastechnische Berichte*, vol. 59, no. 2, pp. 34–52, 1986.

[27] Daloz, W., *Developing a High Temperature, Oxidation Resistant Molybdenum - Silica Composite*. Ph.D. Dissertation, Georgia Institute of Technology, Atlanta GA, 2015.

[28] Das, J., Mitra, R., and Roy, S. K., "Effect of Ce addition on the oxidation behaviour of Mo-Si-B-Al ultrafine composites at 1100C," *Scripta Materialia*, vol. 64, no. 6, pp. 486–489, 2011.

[29] Dheeradhada, V., Johnson, D., and Dayananda, M., "Diffusional analysis of a multiphase oxide scale formed on a Mo-Mo3Si-Mo5SiB2 alloy," *Journal of Phase Equilibria and Diffusion*, vol. 27, no. 6, pp. 582–589, 2006.

[30] Dimiduk, D. M. and Perepezko, J. H., "Mo-Si-B Alloys: Developing a revolutionary turbine-engine material," *MRS Bulletin*, vol. 28, no. 9, 2003.

[31] Doremus, R. H., "Viscosity of silica," *Journal of Applied Physics*, vol. 92, no. 12, p. 7619, 2002.

[32] Downs, I. P., Perepezko, J. H., Sakidja, R., and Choi, S. R., "Suppressing CMAS attack with a MoSiB-based coating," *Surface and Coatings Technology*, vol. 239, pp. 138–146, Jan. 2014.

[33] Eaton, H. E. and Linsey, G. D., "Accelerated oxidation of SiC CMC's by water vapor and protection via environmental barrier coating approach," *Journal of the European Ceramic Society*, vol. 22, no. 14-15, pp. 2741–2747, 2002.

[34] Edgeworth, R., Dalton, B., and Parnell, T., "The pitch drop experiment," *European Journal of Physics*, vol. 5, no. 4, p. 198, 1984.

[35] Gardner, R. A., "The kinetics of silica reduction in hydrogen," *Journal of Solid State Chemistry*, vol. 9, no. 4, pp. 336–344, 1974.

[36] Gokhale, A. B. and Abbaschian, G. J., "The Mo-Si (Molybdenum-Silicon) system," *Journal of Phase Equilibria*, vol. 12, pp. 493–498, Aug. 1991.

[37] Guillermet, A. F., "The Fe- Mo (Iron- Molybdenum) system," *Bulletin of Alloy Phase Diagrams*, vol. 3, no. 3, pp. 359–367, 1982.

[38] Gulbransen, E. A., Andrew, K. F., and Brassart, F. A., "Oxidation of Molybdenum 550 to 1700C," *Journal of The Electrochemical Society*, vol. 110, pp. 952–959, Sept. 1963.

[39] Gulbransen, E. A., Andrew, K. F., and Brassart, F. A., "Vapor Pressure of Molybdenum Trioxide," *Journal of The Electrochemical Society*, vol. 110, no. 3, pp. 242–243, 1963.

[40] Gupta, K. P., "The Co-Mn-Mo (cobalt-manganese-molybdenum) system," *Journal of Phase Equilibria and Diffusion*, vol. 25, no. 3, pp. 292–295, 2004.

[41] Gupta, T. K. and Jean, J.-H., "Origin of cristobalite formation during sintering of a binary mixture of borosilicate glass and high silica glass," *Journal of Materials Research*, vol. 9, no. 04, pp. 999–1005, 1994.

[42] Hassomeris, O., Schumacher, G., Kruger, M., Heilmaier, M., and Banhart, J., "Phase continuity in high temperature Mo-Si-B alloys: A FIB-Tomography Study," *Intermetallics*, vol. 19, no. 4, pp. 470–475, 2011.

[43] Heilmaier, M., Saage, H., Kruger, M., Jehanno, P., Boning, M., and Kestler, H., "Current Status of Mo-Si-B Silicide Alloys for Ultra-High Temperature Applications," in *MRS Proceedings*, vol. 1128, pp. 1128–U07, Cambridge Univ Press, 2008.

[44] Helmick, D. A., Meier, G. H., and Pettit, F. S., "The development of protective borosilicate layers on a Mo-3Si-1B (weight percent) alloy," *Metallurgical and Materials Transactions A*, vol. 36, pp. 3371–3383, Dec. 2005.

[45] Helmick, D. A., *High Temperature Oxidation of Mo-Si-B Base Alloys*. PhD thesis, University of Pittsburgh, 2003.

[46] Hiraoka, Y., Ogusu, T., and Yoshizawa, N., "Decrease of yield strength in molybdenum by adding small amounts of Group VIII elements," *Journal of Alloys and Compounds*, vol. 381, no. 1, pp. 192–196, 2004.

[47] Hiraoka, Y., Yoshimura, S., and Takebe, K., "Effects of complex additions of Re or Ti with C on the strength and ductility of recrystallized molybdenum," *International Journal of Refractory Metals and Hard Materials*, vol. 12, no. 5, pp. 261–268, 1994.

[48] Hryha, E., Dudrova, E., and Nyborg, L., "Critical aspects of alloying of sintered steels with manganese," *Metallurgical and Materials Transactions A*, vol. 41, no. 11, pp. 2880–2897, 2010.

[49] Hryha, E., Dudrova, E., and Nyborg, L., "On-line control of processing atmospheres for proper sintering of oxidation-sensitive PM steels," *Journal of Materials Processing Technology*, vol. 212, no. 4, pp. 977–987, 2012.

[50] Hudon, P. and Baker, D. R., "The nature of phase separation in binary oxide melts and glasses. I. Silicate systems," *Journal of Non-Crystalline Solids*, vol. 303, no. 3, pp. 299–345, 2002.

[51] Hwang, K. S. and Huang, H. S., "Identification of the segregation layer and its effects on the activated sintering and ductility of Ni-doped molybdenum," *Acta Materialia*, vol. 51, no. 13, pp. 3915–3926, 2003.

[52] Jacob, K. T., Kale, G. M., and Iyengar, G. N. K., "Phase equilibria and thermodynamic properties in the system Ni-Mo-O," *Journal of materials science*, vol. 22, no. 12, pp. 4274–4280, 1987.

[53] Jacob, K. T. and Varamban, S. V., "Phase equilibria and thermodynamic properties of ternary oxides in the system Co-Mo-O," *Journal of alloys and compounds*, vol. 280, no. 1, pp. 138–146, 1998.

[54] Jacobson, N., Farmer, S., Moore, A., and Sayir, H., "High-Temperature Oxidation of Boron Nitride: I, Monolithic Boron Nitride," *Journal of the American Ceramic Society*, vol. 82, no. 2, pp. 393–398, 1999.

[55] Jain, P. and Kumar, K., "Tensile creep of Mo-Si-B alloys," *Acta Materialia*, vol. 58, pp. 2124–2142, Apr. 2010.

[56] Jean, J.-H. and Gupta, T. K., "Devitrification inhibitors in borosilicate glass and binary borosilicate glass composite," *Journal of materials research*, vol. 10, no. 05, pp. 1312–1320, 1995.

[57] Kangsadan, T., *On the Reduction/de-oxidation of MoO2/Mo with Hydrogen During Second-stage Production of Mo Powder*. PhD thesis, Colorado School of Mines, 2004.

[58] Kim, G.-S., Lee, Y. J., Kim, D.-G., and Do Kim, Y., "Consolidation behavior of Mo powder fabricated from milled Mo oxide by hydrogen-reduction," *Journal of Alloys and Compounds*, vol. 454, no. 1, pp. 327–330, 2008.

[59] Konijnendijk, W. L. and Stevels, J. M., "The structure of borate glasses studied by raman scattering," *Journal of Non-Crystalline Solids*, vol. 18, no. 3, pp. 307–331, 1975.

[60] Kruger, M., Franz, S., Saage, H., Heilmaier, M., Schneibel, J., Jehanno, P., Boning, M., and Kestler, H., "Mechanically alloyed Mo-Si-B alloys with a continuous alpha-Mo matrix and improved mechanical properties," *Intermetallics*, vol. 16, pp. 933–941, July 2008.

[61] Kruger, M., Saage, H., Heilmaier, M., Boning, M., and Kestler, H., "Influence of processing on the microstructure and mechanical behaviour of Mo-Si-B alloys," *Journal of Physics: Conference Series*, vol. 240, p. 012087, July 2010.

[62] Kruger, M., Schliephake, D., Jain, P., Kumar, K. S., Schumacher, G., and Heilmaier, M., "Effects of Zr Additions on the Microstructure and the Mechanical Behavior of PM Mo-Si-B Alloys," *JOM*, vol. 65, no. 2, pp. 301–306, 2013.

[63] Kumar, A. and Eyre, B. L., "Grain Boundary Segregation and Intergranular Fracture in Molybdenum," *Proceedings of the Royal Society of London. Series A, Mathematical and Physical Sciences*, vol. 370, pp. 431–458, Apr. 1980.

[64] Kumar, K. S. and Alur, A. P., "Deformation behavior of a two-phase Mo-Si-B alloy," *Intermetallics*, vol. 15, no. 5, pp. 687–693, 2007.

[65] Lamkin, M. A., Riley, F. L., and Fordham, R. J., "Oxygen mobility in silicon dioxide and silicate glasses: A review," *Journal of the European Ceramic Society*, vol. 10, no. 5, pp. 347–367, 1992.

[66] Lamoreaux, R. H., Hildenbrand, D. L., and Brewer, L., "High-Temperature Vaporization Behavior of Oxides II. Oxides of Be, Mg, Ca, Sr, Ba, B, Al, Ga, In, Tl, Si, Ge, Sn, Pb, Zn, Cd, and Hg," *Journal of Physical and Chemical Reference Data*, vol. 16, no. 3, pp. 419–443, 1987.

[67] Lange, A., Heilmaier, M., Sossamann, T. A., and Perepezko, J. H., "Oxidation behavior of pack-cemented Si-B oxidation protection coatings for Mo-Si-B alloys at 1300C," *Surface and Coatings Technology*, vol. 266, pp. 57–63, 2015.

[68] Lee, K. N., Fox, D. S., and Bansal, N. P., "Rare earth silicate environmental barrier coatings for SiC/SiC composites and Si3N4 ceramics," *Journal of the European Ceramic Society*, vol. 25, no. 10, pp. 1705–1715, 2005.

[69] Lemberg, J. A. and Ritchie, R. O., "Mo-Si-B Alloys for Ultrahigh-Temperature Structural Applications," *Advanced Materials*, vol. 24, no. 26, pp. 3445–3480, 2012.

[70] Lemberg, J. A., Middlemas, M. R., Weingartner, T., Gludovatz, B., Cochran, J. K., and Ritchie, R. O., "On the fracture toughness of fine-grained Mo-3Si-1B (wt.%) alloys at ambient to elevated (1300 C) temperatures," *Intermetallics*, vol. 20, no. 1, pp. 141–154, 2012.

[71] Majumdar, S., Schliephake, D., Gorr, B., Christ, H.-J., and Heilmaier, M., "Effect of yttrium alloying on intermediate to high-temperature oxidation behavior of Mo-Si-B alloys," *Metallurgical and Materials Transactions A*, vol. 44, no. 5, pp. 2243–2257, 2013.

[72] Majumdar, S., Donges, B., Gorr, B., Christ, H.-J., Schliephake, D., and Heilmaier, M., "Mechanisms of oxide scale formation on yttrium-alloyed Mo-Si-B containing fine-grained microstructure," *Corrosion Science*, vol. 90, pp. 76–88, 2015.

[73] Martineau, C., Michaelis, V. K., Schuller, S., and Kroeker, S., "Liquid-Liquid Phase Separation in Model Nuclear Waste Glasses: A Solid-State Double-Resonance NMR Study," *Chemistry of materials*, vol. 22, no. 17, pp. 4896–4903, 2010.

[74] Mendiratta, M. G., Parthasarathy, T. A., and Dimiduk, D. M., "Oxidation behavior of alphaMo-Mo3Si-Mo5SiB2 (T2) three phase system," *Intermetallics*, vol. 10, pp. 225–232, Mar. 2002.

[75] Meschi, D. J., Chupka, W. A., and Berkowitz, J., "Heterogeneous reactions studied by mass spectrometry. I. Reaction of B2O3 (s) with H2O (g)," *The Journal of Chemical Physics*, vol. 33, no. 2, pp. 530–533, 1960.

[76] Meyer, M., Thom, A., and Akinc, M., "Oxide scale formation and isothermal oxidation behavior of Mo-Si-B intermetallics at 600-1000C," *Intermetallics*, vol. 7, pp. 153–162, Feb. 1999.

[77] Middlemas, M., *Fabrication, Strength and Oxidation of Molybdenum-Silicon-Boron Alloys from Reation Synthesis*. Ph.D. Dissertation, Georgia Institute of Technology, Atlanta GA, May 2009.

[78] Middlemas, M. and Cochran, J., "Dense, fine-grain Mo-Si-B alloys from nitride-based reactions," *Journal of the Minerals, Metals and Materials Society*, vol. 60, pp. 19–24, July 2008.

[79] Middlemas, M. R. and Cochran, J. K., "The microstructural engineering of Mo-Si-B alloys produced by reaction synthesis," *Journal of the Minerals, Metals and Materials Society*, vol. 62, pp. 20–24, Oct. 2010.

[80] Miller, M. and Bryhan, A., "Effect of Zr, B and C additions on the ductility of molybdenum," *Materials Science and Engineering: A*, vol. 327, no. 1, pp. 80–83, 2002.

[81] Mousa, M., Wanderka, N., Timpel, M., Singh, S., Kruger, M., Heilmaier, M., and Banhart, J., "Modification of Mo-Si alloy microstructure by small additions of Zr," *Ultramicroscopy*, vol. 111, pp. 706–710, May 2011.

[82] Mueller, A., Bianco, R., and Buckman, R., "Evaluation of oxide dispersion strengthened (ODS) molybdenum and molybdenum–rhenium alloys," *International Journal of Refractory Metals and Hard Materials*, vol. 18, no. 4, pp. 205–211, 2000.

[83] Nagae, M., Yoshio, T., Takada, J., and Hiraoka, Y., "Improvement in recrystallization temperature and mechanical properties of a commercial TZM alloy through microstructure control by multi-step internal nitriding," *Materials Transactions*, vol. 46, no. 10, pp. 2129–2134, 2005.

[84] Nowotny, H., Dimakopoulou, E., and Kudielka, H., "Investigation of the Ternary Systems Mo-Si-B and W-Si-B and of the system VSi2-TaSi2," *Monatshefte fuer Chemie*, vol. 88, no. 2, 1957.

[85] Nunes, C. A., Sakidja, R., Dong, Z., and Perepezko, J. H., "Liquidus projection for the Mo-rich portion of the Mo-Si-B ternary system," *Intermetallics*, vol. 8, pp. 327–337, Apr. 2000.

[86] Oldfield, L. and Wright, R., "The volatilization of constituents from borosilicate glass at elevated temperatures," *Glass Technology*, vol. 3, no. 2, pp. 59–68, 1962.

[87] Olds, L. E. and Rengstorff, G. W. P., "Effects of Oxygen, Nitrogen, and Carbon on the Ductility of Cast Molybdenum," *Journal of Metals*, vol. 8, pp. 150–155, 1956.

[88] Opila, E. J., "Volatility of common protective oxides in high-temperature water vapor: Current understanding and unanswered questions," in *Materials Science Forum*, vol. 461, pp. 765–774, Trans Tech Publ, 2004.

[89] Opila, E. J., Jacobson, N. S., Myers, D. L., and Copland, E. H., "Predicting oxide stability in high-temperature water vapor," *Journal of the Minerals, Metals and Materials Society*, vol. 58, no. 1, pp. 22–28, 2006.

[90] Parthasarathy, T. A., Mendiratta, M. G., and Dimiduk, D. M., "Oxidation mechanisms in Mo-reinforced Mo5SiB2(T2)-Mo3Si alloys," *Acta Materialia*, vol. 50, pp. 1857–1868, Apr. 2002.

[91] Paswan, S., Mitra, R., and Roy, S., "Oxidation behaviour of the Mo-Si-B and Mo-Si-B-Al alloys in the temperature range of 700-1300C," *Intermetallics*, vol. 15, pp. 1217–1227, Sept. 2007.

[92] Perepezko, J. and Sakidja, R., "Oxidation-resistant coatings for ultra-high-temperature refractory Mo-based alloys," *Journal of the Minerals, Metals and Materials Society*, vol. 62, no. 10, pp. 13–19, 2010.

[93] Riebling, E., "Structure of borosilicate and borogermanate melts at 1300C; a viscosity and density study," *Journal of the American Ceramic Society*, vol. 47, no. 10, pp. 478–483, 1964.

[94] Rioult, F., Imhoff, S., Sakidja, R., and Perepezko, J., "Transient oxidation of Mo-Si-B alloys: Effect of the microstructure size scale," *Acta Materialia*, vol. 57, pp. 4600–4613, Sept. 2009.

[95] Roy, B., Das, J., and Mitra, R., "Transient stage oxidation behavior of Mo76Si14B10 alloy at 1150C," *Corrosion Science*, vol. 68, pp. 231–237, 2013.

[96] Saage, H., Kruger, M., Sturm, D., Heilmaier, M., Schneibel, J., George, E., Heatherly, L., Somsen, C., Eggeler, G., and Yang, Y., "Ductilization of Mo-Si solid solutions manufactured by powder metallurgy," *Acta Materialia*, vol. 57, pp. 3895–3901, Aug. 2009.

[97] Saitton, B. and Rosen, E., "Gibbs Energies of Formation of Mn2Mo3O8 and MnMoO4 in the Temperature Range 1100-1400 K," *Acta Chemica Scandinavica*, vol. 49, pp. 709–709, 1995.

[98] Sakidja, R. and Perepezko, J. H., "Alloying and microstructure stability in the high-temperature Mo-Si-B system," *Journal of Nuclear Materials*, vol. 366, no. 3, pp. 407–416, 2007.

[99] Sakidja, R., Perepezko, J., Kim, S., and Sekido, N., "Phase stability and structural defects in high-temperature Mo-Si-B alloys," *Acta Materialia*, vol. 56, pp. 5223–5244, Oct. 2008.

[100] Sakidja, R., Sieber, H., and Perepezko, J., "The formation of mo precipitates in a supersaturated Mo5SiB2 intermetallic phase," *Philosophical magazine letters*, vol. 79, no. 6, pp. 351–357, 1999.

[101] Schlichting, J., "Oxygen transport through glass layers formed by a gel process," *Journal of Non-Crystalline Solids*, vol. 63, pp. 173–181, Feb. 1984.

[102] Schneibel, J. H., "High temperature strength of Mo-Mo3Si-Mo5SiB2 molybdenum silicides," *Intermetallics*, vol. 11, no. 7, pp. 625–632, 2003.

[103] Schneibel, J. H., Kramer, M. J., and Easton, D. S., "A Mo-Si-B intermetallic alloy with a continuous alpha-Mo matrix," *Scripta Materialia*, vol. 46, pp. 217–221, Feb. 2002.

[104] Schulmeyer, W. V. and Ortner, H. M., "Mechanisms of the hydrogen reduction of molybdenum oxides," *International Journal of Refractory Metals and Hard Materials*, vol. 20, no. 4, pp. 261–269, 2002.

[105] Smedskjaer, M. M., Youngman, R. E., and Mauro, J. C., "Principles of Pyrex® glass chemistry: structure–property relationships," *Applied Physics A*, vol. 116, no. 2, pp. 491–504, 2014.

[106] Smolik, G. R., Petti, D. A., McCarthy, K. A., and Schuetz, S. T., "Oxidation, volatilization, and redistribution of molybdenum from TZM alloy in air," Tech. Rep.

INEEL/EXT-99-01353, Idaho National Engineering and Environmental Lab., Idaho Falls, ID (US), 2000.

[107] Sossaman, T., Sakidja, R., and Perepezko, J., "Influence of minor Fe addition on the oxidation performance of Mo-Si-B alloys," *Scripta Materialia*, vol. 67, pp. 891–894, Dec. 2012.

[108] Soulen, J. R., Sthapitanonda, P., and Margrave, J. L., "Vaporization of inorganic substances: B2O3, TeO2 and Mg3N2," *The Journal of Physical Chemistry*, vol. 59, no. 2, pp. 132–136, 1955.

[109] Spear, K. E. and Wang, M. S., "Thermodynamic modeling of the molybdenum-boron system," *Calphad*, vol. 5, no. 2, pp. 109–113, 1981.

[110] Spear, K. and Liao, P., "The B-Mo (boron-molybdenum) system," *Journal of Phase Equilibria*, vol. 9, no. 4, pp. 457–466, 1988.

[111] Speiser, R., Naiditch, S., and Johnston, H. L., "The Vapor Pressure of Inorganic Substances. II. B2O3," *Journal of the American Chemical Society*, vol. 72, no. 6, pp. 2578–2580, 1950.

[112] Stephens, J. R. and Witzke, W. R., "Alloy hardening and softening in binary molybdenum alloys as related to electron concentration," *Journal of the Less Common Metals*, vol. 29, no. 4, pp. 371–388, 1972.

[113] Strobel, P. and Le Page, Y., "Growth and morphology of single crystals of hexagonal molybdates (IV) M2Mo3O8 (M= Mn, Fe, Co, Ni)," *Journal of Crystal Growth*, vol. 61, no. 2, pp. 329–338, 1983.

[114] Sturm, D., Heilmaier, M., Schneibel, J., Jehanno, P., Skrotzki, B., and Saage, H., "The influence of silicon on the strength and fracture toughness of molybdenum," *Materials Science and Engineering: A*, vol. 463, pp. 107–114, Aug. 2007.

[115] Supatarawanich, V., Johnson, D. R., and Liu, C. T., "Effects of microstructure on the oxidation behavior of multiphase Mo-Si-B alloys," *Materials Science and Engineering: A*, vol. 344, no. 1, pp. 328–339, 2003.

[116] Trinkle, D. R. and Woodward, C., "The chemistry of deformation: How solutes soften pure metals," *Science*, vol. 310, no. 5754, pp. 1665–1667, 2005.

[117] Urbain, G., Bottinga, Y., and Richet, P., "Viscosity of liquid silica, silicates and alumino-silicates," *Geochimica et Cosmochimica Acta*, vol. 46, pp. 1061–1072, June 1982.

[118] Urbain, G., Millon, F., and Cariset, S., "Viscosities of some silica rich liquids in the system SiO2-B2O3," *Comptes Rendu Hebdomadaires des Seances de l'Academie des Sciences, Series C: Chim. Centrale Revues*, vol. 290, no. 8, pp. 137–40, 1980.

[119] van Limpt, H., Beerkens, R., and Verheijen, O., "Models and Experiments for Sodium Evaporation From Sodium-Containing Silicate Melts," *Journal of the American Ceramic Society*, vol. 89, no. 11, pp. 3446–3455, 2006.

[120] van Limpt, J. A. C., *Modeling of evaporation processes in glass melting furnaces*. PhD thesis, Eindhoven University of Technology, Netherlands, 2007.

[121] Volf, M., *Chemical Approach to Glass*. No. 7 in Glass Science and Technology, Elsevier, New York, 1984.

[122] Wang, F., Shan, A., Dong, X., and Wu, J., "Oxidation behavior of Mo-12.5Si-25B alloy at high temperature," *Journal of Alloys and Compounds*, vol. 459, no. 1, pp. 362–368, 2008.

[123] Wesemann, I., Hoffmann, A., Mrotzek, T., and Martin, U., "Investigation of solid solution hardening in molybdenum alloys," *International Journal of Refractory Metals and Hard Materials*, vol. 28, pp. 709–715, Nov. 2010.

[124] Woodard, S. R., Raban, R., Myers, J. F., and Berczik, D. M., "Oxidation resistant molybdenum," Nov. 2003. Patent US 6652674.

[125] Yoshimi, K., Nakatani, S., Suda, T., Hanada, S., and Habazaki, H., "Oxidation behavior of Mo5SiB2-based alloy at elevated temperatures," *Intermetallics*, vol. 10, pp. 407–414, May 2002.

[126] Zheng, Q., Youngman, R. E., Hogue, C. L., Mauro, J. C., Potuzak, M., Smedskjær, M. M., and Yue, Y., "Structure of boroaluminosilicate glasses: Impact of Al2O3/SiO2 ratio on the structural role of sodium," *Physical Review B*, vol. 86, no. 5, p. 054203, 2012.

[127] Zumbrunnen, A. and Fitzpatrick, J., "Grain refinement and improved ductility in molybdenum by small boron additions," *Journal of the Less Common Metals*, vol. 7, no. 5, pp. 356–367, 1964.